THERMAL HYDRAULIC MODELING OF DISCRETELY FRACTURED GEOTHERMAL RESERVOIRS

A Dissertation

Presented to the Faculty of the Graduate School

of Cornell University

in Partial Fulfillment of the Requirements for the Degree of

Doctor of Philosophy

by

Don Bruce Fox

February 2016

© 2016 Don Bruce Fox
ALL RIGHTS RESERVED

THERMAL HYDRAULIC MODELING OF DISCRETELY FRACTURED GEOTHERMAL RESERVOIRS

Don Bruce Fox, Ph.D.

Cornell University 2016

Enhanced/Engineered Geothermal Systems (EGS) have the potential to provide a significant amount of base load electricity and heat and to displace fossil fuel consumption globally. To determine the potential for the expansion of direct use geothermal energy, a detailed analysis of U.S. energy consumption was performed to estimate the amount of primary energy consumed as a function of its utilization temperature from 0 to 260 °C. The analysis revealed that about 34 EJ annually, more than 30% of the U.S. annual energy demand is used for direct thermal use applications in the temperature range of 0 to 260 °C.

Both analytical and numerical models of discretely fractured reservoirs were developed to probe the thermal hydraulic behavior of model EGS reservoirs and quantify factors controlling performance. An analytical model for discrete, fixed aperture, rectangular fractures with specified uniform flow was used to illustrate the renew ability of EGS reservoirs with a ratio of production to renewal times of about 0.2 to 0.33. Fracture structure and connectivity were also shown to affect reservoir performance in modeling studies. In general, fracture connectivity is more important than aperture variations within the fractures. Flow channeling in fractures with spatially varying aperture fields were simulated using a developed numerical model. An ensemble of fracture realizations were used to illustrate how the magnitude of aperture variations lead to flow structures that often inhibit rather than enhance subsurface heat exchange.

Finally, both conservative and reactive tracers were used to determine the spatially varying thermal field during heat extraction in a discrete fracture with variable aperture. Reduced order modeling of the fracture was used to create a tractable framework for inferring reservoir structure. Tracers revealed the capability to predict a reservoir's production temperature versus time, with reactive tracers providing better results. However, difficulties in accurately predicting the aperture field led to a non-unique outcome where more than one reservoir realization matched both the tracer curve and production temperature.

BIOGRAPHICAL SKETCH

Don Fox was born and raised in Hidalgo County, Texas and graduated from Pharr-San Juan-Alamo North High School. Before enrolling at Cornell University, he earned an undergraduate degree in chemical engineering from the Massachusetts Institute of Technology. He successfully defended his dissertation during the fall 2015 semester.

To my parents.

ACKNOWLEDGEMENTS

It is impossible to acknowledge all those that have helped me throughout my time here at Cornell University. Forgive me for any omissions. I would like to first thank the members of my committee, specifically Donald Koch and Jefferson Tester. During these past few months, I was amazed at the amount of time they have put into getting me to the point of defending my research. Thank you for the time you devoted to me and your patience; I was not always the best student, but I hope you think it was worth it. Polly Marion, Jeff Tester's assistant, was a great resource for answering my questions and helping me with administrative matters. Steve Gallow, the head of IT at Snee Hall, helped me with my computer resource needs and was an excellent source for answering my random computer questions. I would like to thank the Tester group for their useful discussions and input over my research. Adam Hawkins provided good discussions and I always found his opinions over my work useful. In addition, it was a great pleasure to work with him in writing our successful Department of Energy research grant proposal. Much thanks to José Cano and Calvin Whealton, both from the civil and environmental engineering department, for helping me with the genetic algorithm and answering my numerous statistical questions, respectively. Deborah Sills and Mitchell Ishmael served as close friends that I would feel comfortable talking about both work and personal matters. Thank you for listening and I hope you benefited from me as well. Finally, I would like to thank Jennifer, my significant other, for not only proofreading the chapters of my dissertation, but believing in me and giving me the encouragement to accomplish this body of work.

TABLE OF CONTENTS

Biographical Sketch . . . iii
Dedication . . . iv
Acknowledgements . . . v
Table of Contents . . . vi
List of Tables . . . ix
List of Figures . . . x

1 Introduction and Background 1
1.1 The Case for Renewable Energy Sources . . . 1
1.2 Geothermal Energy and Thermal Hydraulic Modeling . . . 4

2 Objectives and Approach 19

3 U.S. Thermal Spectrum 24
3.1 Introduction . . . 24
3.2 Methodology . . . 27
3.2.1 Residential Sector . . . 28
3.2.2 Commercial Sector . . . 30
3.2.3 Industrial Sector . . . 30
3.2.4 Electrical Systems Energy Losses . . . 32
3.3 Results and Discussion . . . 33
3.4 Conclusion . . . 43

4 Sustainable Heat Farming 51
4.1 Introduction . . . 51
4.2 Analytical Model . . . 55
4.2.1 First Extraction Phase . . . 58
4.2.2 Validity of 1-D Conduction . . . 59
4.2.3 First Recovery Phase . . . 60
4.2.4 Second Extraction Phase . . . 65
4.2.5 Subsequent Extraction and Recovery Phases . . . 67
4.2.6 Multifracture EGS reservoir . . . 68
4.2.7 Alternate Strategies . . . 69
4.3 TOUGH2 Numerical Model . . . 70
4.4 Results and Discussions . . . 75
4.4.1 Single Fracture Simulations . . . 75
4.4.2 Multiple Fractures Simulations . . . 79
4.5 Conclusions and Recommendations . . . 87

5 DFN Analytical Model **94**
5.1 Introduction . . . 94
5.2 Discrete Fracture Network Model Description . . . 98
5.2.1 Fluid Flow in the Discrete Fracture Network . . . 99
5.2.2 Fracture Surface Temperature Field . . . 102
5.2.3 Automating the Calculation of Fluid Velocity and Temperature in a Network . . . 110
5.3 Numerical Validation . . . 111
5.4 Case Study 1: Aperture Uncertainty . . . 118
5.4.1 First Fracture Network . . . 121
5.4.2 Second Fracture Network . . . 126
5.5 Case Study 2: Fracture Structure Uncertainty . . . 129
5.6 Conclusion . . . 138

6 FEM and BIE Numerical Model **149**
6.1 Introduction . . . 149
6.2 Numerical Model Description . . . 152
6.2.1 Fluid Flow . . . 153
6.2.2 Heat Transport . . . 156
6.2.3 Particle Transport . . . 159
6.3 Numerical Model Showcase . . . 161
6.3.1 Circular Fracture with Dipole Flow . . . 162
6.3.2 Thermal Recovery . . . 169
6.3.3 Natural Convection . . . 172
6.3.4 Intersecting Fractures . . . 176
6.4 Conclusion . . . 180

7 Spatial Aperture Variations **187**
7.1 Introduction . . . 187
7.2 Modeling of Mass, Momentum, and Heat Transport . . . 191
7.2.1 Self-affine Aperture Field . . . 192
7.2.2 Fluid Flow and Heat Transport . . . 194
7.3 Results for One Fracture . . . 195
7.3.1 Varying Strength of Aperture Fluctuations . . . 197
7.3.2 Varying the Hurst Coefficient . . . 204
7.3.3 Varying Wellbore Separation . . . 206
7.4 Results for Multiple Fractures . . . 209
7.4.1 Varying Strength of Aperture Fluctuations . . . 211
7.4.2 Three Fracture System . . . 216
7.4.3 Flow Control . . . 217
7.5 Conclusion . . . 221

8 Inverse Methods with Conservative and Reactive Tracers 230
8.1 Introduction . . . 230
8.2 Inverse Problem Description . . . 238
8.2.1 Fracture Aperture Field . . . 239
8.2.2 Tracer Test . . . 241
8.2.3 Thermal Performance of a Reservoir . . . 244
8.3 Inversion Algorithm . . . 245
8.3.1 Principal Component Analysis . . . 245
8.3.2 Genetic Algorithm . . . 250
8.4 Inversion Results Using Conservative Tracers . . . 254
8.5 Inversion Results Using Reactive Tracers . . . 268
8.6 Conclusion . . . 274

9 Conclusions and Recommendations 286
9.1 Summary of Research . . . 286
9.2 Recommended Future Work . . . 288

A FEM Formulation 299
A.1 Fluid Flow . . . 299
A.2 Heat Transfer . . . 300
A.3 Particle Transport . . . 301
A.4 Applying Essential Boundary Conditions . . . 302

B Generating Self-affine Aperture Variations 304

C Genetic Algorithm 306

LIST OF TABLES

5.1 List of key assumptions and limitations of the model 109
5.2 Percentage of flow paths and the median dimensionless production temperature for networks with the specified number of flow paths . 132
5.3 PAWN sensitivity indices T for the uncertainty of structure and aperture of the fracture network 136

6.1 List of values used in the simulations 161

7.1 Thermal performance with varying the Hurst coefficient 205
7.2 Thermal performance with varying wellbore spacing 207

8.1 The correlation coefficient of the l^2-norm error of tracer and aperture field and the tracer and the production temperature 258
8.2 Correlation coefficient of the l^2-norm error of the aperture field and dimensionless temperature drawdown 267

LIST OF FIGURES

1.1 Increase in atmospheric carbon dioxide levels from the late 1950s to 2015 . . . 3
1.2 Global annual mean surface air temperature change since 1880 . . 4
1.3 Idealized depiction of two different geothermal systems 7

3.1 Possible applications for direct thermal use of geothermal energy (Líndal diagram) . . . 27
3.2 Breakdown of the industrial sector energy consumption in 2006 . . 33
3.3 Total low-temperature thermal energy demand of the three demand sectors . . . 35
3.4 Thermal energy use temperature distribution from without ESEL . 39
3.5 Thermal energy use temperature distribution with ESEL 40
3.6 Continuous approximation of the energy demand distribution density with ESEL . . . 41
3.7 Cumulative thermal energy demand with and without ESEL 42
3.8 Energy cascade system providing both power and thermal energy . 43

4.1 Conceptualized multifracture EGS reservoir 56
4.2 TOUGH2 mesh used for single and multifracture simulations . . . 72
4.3 Dimensions of the simulation space used in TOUGH2 73
4.4 First extraction comparison results (lower flow) 76
4.5 First extraction comparison results (higher flow) 77
4.6 Comparison of first recovery results 78
4.7 Second extraction results comparison 79
4.8 Second recovery results comparison 80
4.9 Outlet temperature of multifractured reservoirs during extraction and recovery . . . 81
4.10 Percent of enthalpy extracted and exergy retained 83
4.11 Outlet temperature results for parallel multifracture reservoir . . . 85
4.12 Second extraction efficiency in terms of enthalpy 86
4.13 Second extraction efficiency in terms of exergy 87

5.1 Sample discrete fracture network 100
5.2 Idealized depiction of a single rectangular fracture 104
5.3 Sample fracture network with the directionality of the flow identified 108
5.4 A discrete fracture network composed of six segments 113
5.5 A discrete fracture network composed of fourteen segments 113
5.6 The TOUGH2 computational domain and mesh used for the simulations . . . 114
5.7 A comparison of the analytical equation and TOUGH2 for the first network . . . 115
5.8 A comparison of the analytical equation and TOUGH2 for the second network . . . 116

5.9 Dimensionless temperature fields at the end of extraction from the TOUGH2 model . . . 117
5.10 Histogram of dimensionless production temperature . . . 122
5.11 The median and interquartile range of the dimensionless production temperature for a range of the dimensionless standard deviation of the aperture . . . 123
5.12 The median and interquartile range of the ratio of time it took to reach the drawdown criteria . . . 124
5.13 Boxplot of dimensionless production temperatures by applying the reservoir pressure drop criteria. . . . 125
5.14 The median and interquartile range of the dimensionless production temperature for a range of the dimensionless standard deviation of the aperture . . . 126
5.15 The median and interquartile range of the ratio of time it took to reach the drawdown criteria of the base case time for a range of the dimensionless standard deviation of the aperture . . . 127
5.16 Boxplot of dimensionless production temperatures for the two different fracture networks . . . 128
5.17 Four examples of possible fracture networks that can occur by sampling the number of fractures, their directionality, and position . . 131
5.18 A histogram of the dimensionless production temperature due to the uncertainty in the fracture network structure. . . . 132
5.19 Histograms of the dimensionless production temperatures for the generated ensemble of fracture networks . . . 133

6.1 Fracture network of the Soultz, France EGS project . . . 151
6.2 Idealized fracture in a geothermal reservoir . . . 153
6.3 Numerical model results for a monopole in an unconfined fracture . 159
6.4 Mesh used for the variable wellbore spacing study . . . 164
6.5 Dimensionless fracture surface temperature for a circular fracture . 165
6.6 Thermal drawdown curves for various wellbore spacings . . . 166
6.7 Reservoir life as a function of wellbore spacing . . . 166
6.8 Mean dimensionless fracture surface temperature versus time . . . 167
6.9 Drawdown curves for an elliptically shaped fracture . . . 168
6.10 Dimensionless fracture surface temperature for an elliptical and constant aperture field . . . 168
6.11 Thermal recovery curves for different wellbore spacings . . . 170
6.12 Dimensionless fracture surface temperature during recovery . . . 171
6.13 Dimensionless production temperature drawdown curves with buoyancy effects . . . 175
6.14 Dimensionless fracture surface temperature for with and without buoyancy effects . . . 176
6.15 Dimensionless fracture surface temperature for a parallel intersection system . . . 178

6.16 Dimensionless fracture surface temperature for a perpendicular intersection system 179
6.17 Drawdown curves for several intersecting fracture systems 180

7.1 Dimensionless fracture surface temperature. 199
7.2 Histogram of the dimensionless production temperature 200
7.3 Mean dimensionless production temperature as a function of the dimensionless standard deviation of the aperture 202
7.4 Standard deviation of the dimensionless production temperature as a function of the dimensionless standard deviation of the aperture . 203
7.5 Fraction of fractures exhibiting thermal performance enhancement as a function of the dimensionless standard deviation of the aperture 204
7.6 The fracture aperture profile for various values of the Hurst coefficient. 206
7.7 Boxplot of dimensionless production temperatures for various wellbore spacing. 208
7.8 Histogram of the thermal performance of the two fracture system . 211
7.9 Histogram of the fractional flow split of the two fracture system . . 212
7.10 Dimensionless production temperature as a function of fractional flow split 213
7.11 The standard deviation of the dimensionless production temperature standard deviation of the fraction flow split 214
7.12 The fraction of two fracture system exhibiting thermal performance enhancement 215
7.13 Fitted Gaussian probabilty density function of dimensionless production temperature for one, two, and three fracture system. 217
7.14 Boxplot of dimensionless production temperatures for, no flow control, 50/50 flow split, and the optimal flow split 219
7.15 The change of production temperature, using an equal flow split strategy as a function of the original flow split fraction. 220
7.16 The fraction of reservoirs exhibiting thermal performance enhancement with equal flow as a function of the dimensionless standard deviation of the aperture 221

8.1 Examples of residence time distributions 243
8.2 Principal component modes for a circular fracture 249
8.3 Fracture aperture field for various number of PCA modes 250
8.4 Boxplots l^2-norm error of the genetic algorithm output using various number of PCA modes 257
8.5 Comparison of the genetic algorithm output results for the tracer curves and the production temperature 258
8.6 The accuracy and precision of the dimensionless production temperature 260
8.7 Comparison of the output aperture field from the inversion algorithm with the true, full order, aperture field 263

8.8 Comparison of the output aperture field from the inversion algorithm with the true, full order, aperture field 264
8.9 Inversion algorithm results, using twenty-four modes, for five different target fractures 266
8.11 Boxplots of the l^2-norm error for the reactive tracer results 274

B.1 Sample generated self-affin aperture field 305

C.1 Genetic algorithm flowchart 309

CHAPTER 1

INTRODUCTION AND BACKGROUND

1.1 The Case for Renewable Energy Sources

The capability of humans to harness and control a range of accessible and affordable energy sources has enabled us to become the most dominant specie this planet has ever seen. Through the domestication of plants and animals, implementation of agriculture, burning of woody biomass, and the exploitation of small scale hydro and wind power, early humans were able to form societies and cultures. Through these societies and cultures, humanity has produced oral and written traditions, formed the foundation in which we understand mathematics and science, and established economies and markets, the very things that make us distinct among the rest of life on Earth. Our advances in civilization and industrialization have given us the capability to increase our geographical range and our standards of living.

The use of fossil fuels in the past 200 to 300 years, of which the past 150 years has been the most significant, has helped humanity to accelerate our expansion and dominance upon this planet. The high energy density found in coal, natural gas, and petroleum are without equal compared to earlier forms of energy upon which humanity relied. However, the pursuit of evermore progress and population growth has come at a cost. Apart from the immediate ecological damage from extracting fossil fuels, the burning of fossil fuels has led to a substantial increase in atmospheric levels of carbon dioxide (CO_2). The amount of atmospheric CO_2 has increased from 275 to 285 ppm (Intergovernmental Panel on Climate Change, 2007) during the years preceding the industrial revolution to about 400 ppm in 2015 (Tans and Keeling, 2015). However, as illustrated in Figure 1.1, atmospheric

levels have dramatically increased from less than 320 ppm to about 400 pm in the past 60 years. Since CO_2 is a green house gas, the rise in atmospheric CO_2 has been associated with an increase in global mean temperatures by intensifying the Greenhouse Effect. As shown in Figure 1.2, the global temperature has risen by 0.8 °C (1.4 °F) since 1880 and has increased at a higher rate since about the 1960s. The Intergovernmental Panel on Climate Change (2014) has stated that climate change attributed to humans has already resulted in alteration of hydrological systems by changing precipitation patterns and melting snow and ice, changes to terrestrial, freshwater, and marine species through modifying their geographic range, seasonal activities, and abundance, and furthermore, has had negative impacts on crop yields. Apart from climate change, humanity also faces challenges in meeting the growing resource demand for food, manufactured goods, shelter, and mobility. It has been estimated that our resource use is unsustainable; we currently use about 1.5 Earths to sustain us and we are projected to require the resources of two planet Earths by the year 2030 (World Wildlife Fund, 2010).

Not all countries have been able to rely on the consumption of fossil fuels for the same period of time as developed countries. Nations like the United States and those in Western Europe have had a 200 to 300 year head start in the usage of fossil fuels to pull their populations out of poverty. As a result, developed countries constitute 46% of the global energy use but only comprise 18% of the world's population (U.S. Energy Information Administration, 2013). Understandably, developing countries view fossil fuels as the quickest way to develop their countries, reduce poverty, and give their populations a standard of living closer to that of the U.S. or Western Europe. However, unlike the U.S. and Western Europe, it will take less time than 200 to 300 years for countries like Indian and China to reach per capital energy consumption levels on par with developed nations. It is pro-

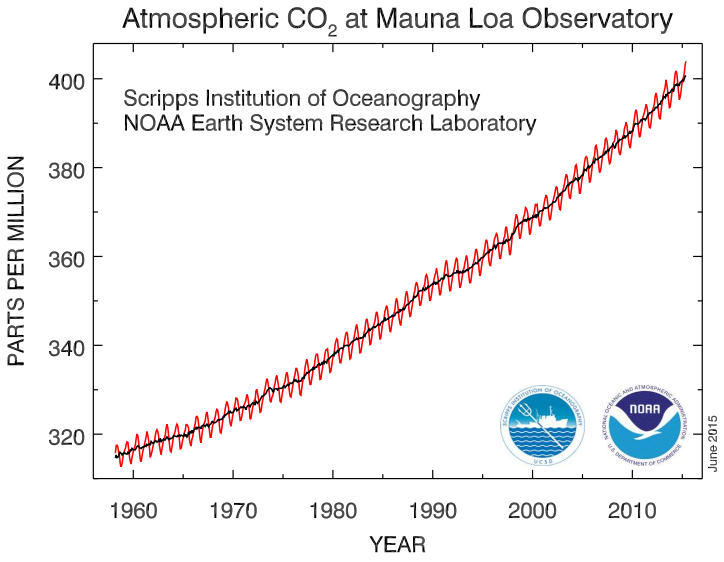

Figure 1.1: Increase in atmospheric CO_2 levels from the late 1950s to 2015 taken from the Mauna Loa Observatory in Hawaii. The red curve represents the dry mole fraction defined as the number of molecules of CO_2 divided by the number of molecules of dry air multiplied by one million (ppm). The black curve is the seasonally corrected data. The figure was retrieved from Earth System Research Laboratory web page: `http://www.esrl.noaa.gov/gmd/ccgg/trends/`.

jected that developing countries will contribute 65% of the world's annual energy use by 2040 (U.S. Energy Information Administration, 2013). This change in the world's energy consumption pattern is expected to come from countries like India and China through both an increase in population and per capita energy use.

It is clear that the current rate of our fossil fuel use is unsustainable. Thus, it is imperative to develop and deploy sustainable and renewable sources of energy to improve the lives of people and to ensure a viable future for not only the 7 billion people and counting, but for all living things on Earth. The immediate question that arises is how does one define what constitutes a sustainable energy source. Tester et al. (2006) defined sustainable energy as "a dynamic harmony between the equitable availability of energy-intensive goods and services to all people and the

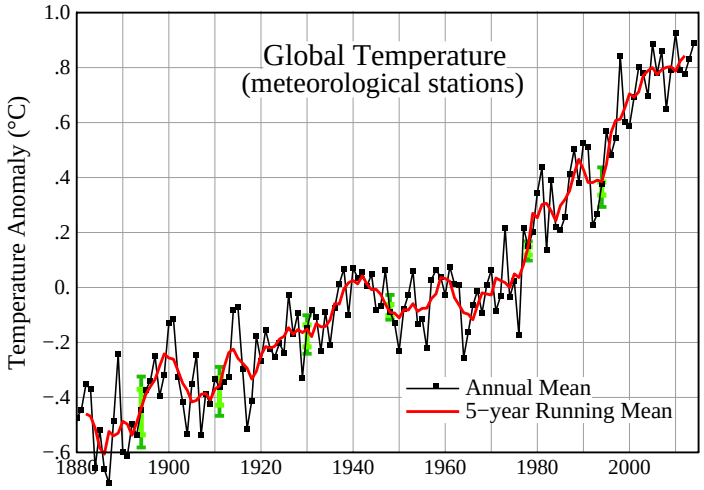

Figure 1.2: Global annual mean surface air temperature change since 1880. Uncertainty bars (in green), based on a 95% confidence interval, are shown for the annual and five year means. The figure was retrieved from NASA Goddard Institute for Space Studies' web page: `http://data.giss.nasa.gov/gistemp/graphs_v3/`.

preservation of the earth for future generations." In order to solve the our current reliance on unsustainable energy sources, we must continue to develop renewable energy sources like solar, wind, and geothermal energy.

1.2 Geothermal Energy and Thermal Hydraulic Modeling

Geothermal energy is the stored thermal energy within the earth. It has the advantage over solar and wind is that it can provide both base load power and heat. There are three different classes of geothermal energy: ground source heat pumps, hydrothermal systems, and Enhanced/Engineered Geothermal Systems (EGS). Geothermal heat pumps use the shallow ground as both a source and sink of heat, depending if cooling or heating is required (Omer, 2008). Hydrothermal

systems are hot aquifers (up to 350 °C) usually located at depths of 1 to 4 km in permeable and porous geological formations (Tester et al., 2012). Since most hydrothermal systems' heat sources originate from magmatic intrusions or shear heating, high-grade geothermal sources are often found in areas of volcanism and tectonic plate boundaries. Furthermore, since geysers and hot springs are surface manifestations of hydrothermal systems, they were the first to be identified and developed.

Unfortunately, nature does not always provide geological sites with ideal attributes for the development of hydrothermal systems. EGS employ technology that is implemented in areas with low permeability and/or dry rock with small amounts of in situ water or steam to provide a means for extracting the earth's stored thermal energy. An EGS reservoir is engineered, or enhanced, by creating an active reservoir, i.e., opening existing weakly sealed fractures or inducing new ones to facilitate the circulation of water into and out of the fractured reservoir to "farm" or extract a portion of the thermal energy. Since EGS technology complements or enhances sites to enable development of geothermal energy, the practical extraction of stored geothermal energy is no longer restricted to the relatively limited number of hydrothermal sites. Figure 1.3 depicts a hydrothermal and an Enhanced/Engineered Geothermal System (EGS). There have been several EGS pilot projects, beginning with the Fenton Hill project in New Mexico in the 1970s, followed by the Rosemanowes project in England in the 1980s (Parker, 1999), and current projects including the project in Soultz-sous-Forêts (Schill et al., 2015) and the Rittershoffen project in France (Maurer et al., 2015), the Cooper Basin site in Australia (Hogarth and Bour, 2015), and the Newberry caldera in Oregon (Cladouhos et al., 2012).

In 2014, the U.S. consumed about 100 EJ of primary energy, of which approximately 80 EJ were from fossil fuels and only about 10 EJ came from renewable sources, mostly from hydro energy (U.S. Energy Information Administration, 2015). Solar, wind, and biomass receive a disproportionate amount of attention, compared to geothermal energy. This may be partly due to humanity's early experience and reliance upon solar, wind, hydro and woody biomass. For example, early civilizations took advantage of solar energy and biomass for heating and relied on wind and water, which are ultimately powered by the sun, for mechanical energy. In 2014, geothermal energy contributed 220 PJ of primary energy in the U.S., only about 2% of the renewable energy total (U.S. Energy Information Administration, 2015). Not only does renewable energy need to continue to displace fossil fuel consumption, but geothermal energy sources must be further deployed to accelerate the offset and make up a larger part of our energy use portfolio.

A 2006 assessment study led by MIT examined the potential of geothermal energy to provide renewable electricity and concluded that the U.S. geothermal resource base was about 14 million EJ (at depths ranging from 3 to 10 km) of which 2.8 to 5.6 million EJ may be technically recoverable (Tester et al., 2006). Additionally, the study panel examined the feasibility of EGS to provide 100 GW of electricity, or 10% of the U.S. generating capacity by 2050 with a "reasonable investment in [research and development] and a proactive level of deployment" (Tester et al., 2006). Internationally, geothermal energy use has been predicted to contribute 140 to 160 GW electric and 800 GW thermal by the year 2050, constituting 3% and 5% of the global demand for electricity and heat, respectively (Intergovernmental Panel On Climate Change, 2011). According to Armstead and Tester (1987), the ideal reservoir must provide the greatest heat production at the longest possible life and with the lowest capital and operating costs. The goal is

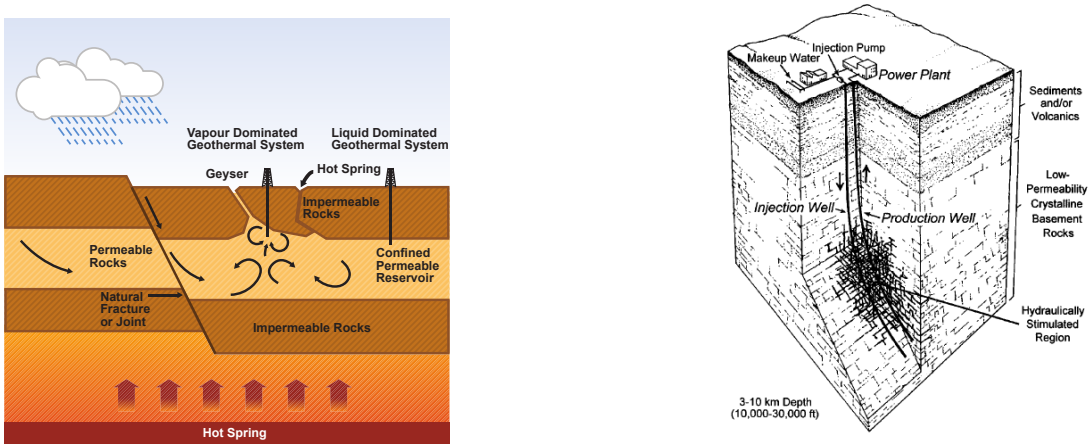

(a) (b)

Figure 1.3: Idealized depiction of two different geothermal systems. The left image is from the geothermal chapter of the IPCC Special Report on Renewable Energy Sources and Climate Change Mitigation (Intergovernmental Panel On Climate Change, 2011) while the image on the right comes from Tester et al. (2012). (a) Hydrothermal system. (b) Enhanced/Engineered Geothermal System.

to be able to utilize the reservoir for 25 to 30 years, producing 16 to 42 MW_{th} with a flow rate of 40 to 100 kg/s per well pair (Armstead and Tester, 1987). For comparison, The Geysers hydrothermal field in northwestern California has a total of 21 power plants with an installed generating capacity of 1400 MW of electricity, about 70 MW per power plant (Glassley, 2011). Given the need for renewable energy sources with low or no CO_2 emissions, there needs to be more research on geothermal energy, specifically EGS, in order to ensure that it will fulfill its reported potential. To that end, geothermal energy can become part of the solution to the multifaceted challenges involved with finding scalable, sustainable energy sources that will have substantially lower impacts on the environment.

There are several areas of ongoing research that promise to mature EGS and ti help EGS to realize its full potential. Much work has been done in terms of determining the best sites for geothermal development. These studies use bottom hole temperature data to create regional and national resource maps containing

temperature at depth and heat flow (Frone and Blackwell, 2010; Blackwell et al., 2011). These geothermal resource maps subsequently provide a tool by which to study the development of geothermal energy. Reber et al. (2014), for example, relied on geothermal resource maps to identify regions in New York and Pennsylvania where implementation of geothermal district heating from EGS would be feasible. They showed the potential of geothermal energy to provide cost effective space and water heating. Recent improvements in drilling cost analysis (Lukawski et al., 2014) allow for determining more accurate project costs, while alternate approaches to drilling, such as hydrothermal jet drilling, can potentially decrease drilling costs (Augustine and Tester, 2009; Hillson and Tester, 2015). Software programs like Geophires (Beckers et al., 2014) provide the capability to estimate the levelized cost of electricity and direct-use heat of geothermal projects. However, in order to accurately determine the viability of a geothermal project, one must first consider what is occurring in the subsurface, specifically, the thermal hydraulic behavior of the reservoir.

The thermal hydraulic performance of a reservoir refers to fluid flow in the subsurface and the evolution of the temperature field of a geothermal reservoir. Knowledge of the thermal hydraulic behavior of a geothermal reservoir is needed in order to accurately determine the techno-economic prospect of a project and to properly utilize the resource. In order to model the thermal hydraulic behavior of the subsurface, an appropriate set of constitutive equations is required for the transport of mass, momentum, and heat. One needs to solve these equations, which are often coupled, to begin to understand the behavior of the subsurface. There is a wide range of complexity for the governing physics and one must decide what to include, emphasize, simplify, or omit in the modeling process. For example, one can model the flow, by assuming Darcy flow, like what is often assumed in

porous media reservoirs such as those found in hydrothermal systems, or model the flow by using some form of the Navier-Stokes equations. In addition, one must also understand the limitations of their model and consequence of their modeling approach over a different set of assumptions. Some key reservoir characteristics to model are:

- the flow distribution in the fracture network
- the pressure of the system and flow impedance
- possible water loss to the subsurface
- the transient spatial temperature field
- the drop in production temperature with time
- the temperature field of the subsurface post energy extraction

The flow distribution is an important characteristic to model because convective heat transport is the mechanism by which the thermal energy of the subsurface is extracted. The extent of the flow in the subsurface determines the size of the active reservoir, the area withing the subsurface which is accessed for energy extraction. The fluid flow within the fractures determine how well the fluid is sweeping across the face of the fractures and ultimately, the rate of energy extraction from the subsurface. In order to model the fluid flow distribution in the reservoir, the locations, sizes, and connectivity of the fractures need to be identified, along with the constitutive equations that describe the transport of mass and momentum of fluid in the subsurface.

Techniques to identify fractures include measurement of microseismic events, vertical seismic profiling, and well logging (Dorbath et al., 2009; Sausse et al., 2010). Microseimic measurements of the subsurface result in a cloud of locations

of hydraulic activity and possible activation of faults and fractures (Dorbath et al., 2009). Sausse et al. (2010) have used techniques like microseimicity, vertical seismic profiling, and logging tools, like borehole televiewers, to map out the fracture network in the geothermal project in Soultz. However, these subsurface mapping techniques do not give a definitive description of the subsurface. Geophysical tools can only identify fractures near the wellbores and microseismic activity clouds do not explicitly identify fractures. Nonetheless, tools like well logging and microseismic measuresments can provide a useful basis for both analytical and numerical tools to model the possible thermal hydraulic behavior of the reservoir and to guide the modeling effort. For example, if the reservoir is characterized by a dense set of small fractures, rather than a few large and dominant fractures, one can take a porous media approach or a hybrid approach that considers both flow in and outside of the fractures. Even knowledge of the fracture connectivity is not sufficient to model the thermal hydraulics of the system. For instance, spatial aperture variations in the fractures will cause the flow to deviate, compared to modeling the fractures, as having smooth surfaces and affect convective heat transport in the reservoir. Thermal hydraulic modeling can be used to understand effects like fracture surface variations which are difficult to determine using geophysical tools.

The pressure drop in the reservoir is crucial to model because it contributes to the parasitic losses of the geothermal operation. Once the fluid flow in the reservoirs has been solved, the pressure drop throughout the system is easily determined by knowing the pressure at the wellheads. The amount of power required to pump the fluid through the reservoir is equal to the product of the pressure drop and the volumetric flow rate. Thus, having too large of a pressure drop in the system will reduce the net electricity produced for power generation and affect the economic viability of any project. By keeping the pressure drop small, it will be possible to

reach the economic flow rate of 50 to 100 kg/s per well pair (Tester et al., 2006). The pressure drop of the system is often reported as a flow impedance that is equal to the pressure drop divided by the mass flow rate. High flow impedance has been an issue in past geothermal projects, like the Rosemanowes project in England during the 1980s. The project had a target flow impedance of less than 0.1 MPa/kg, but only achieved a sustained impedance of 0.46 MPa/kg (Batchelor, 1987). The current Desert Peak project in northern Nevada was able to increase its economic viability by dropping the flow impedance in one of its well pairs, from 10 MPa/kg to 0.052 MPa/kg, through further reservoir stimulation (Benato et al., 2015).

EGS rely on pumping water from the surface to the subsurface in a closed loop manner. However, water losses to the subsurface will occur and require a makeup stream on the surface. The water loss occurs due to the high pressure of the flowing water, finite permeability and porosity of the host rock, and fractures that conduct flow away from the main fracture network. Water loss is inevitable, but having a loss rate of greater than 5% is not acceptable (Armstead and Tester, 1987). The Fenton Hill project suffered from high water loss rates at high injection pressures. The water lose was lower when the flow rate was dropped, but the resulting flow rate was lower than what was desired (Armstead and Tester, 1987). The Rosemanowes project also suffered from high water loss, having a sustained water loss of 22% (Batchelor, 1987). Additionally, geothermal projects in arid and drought prone areas will be more sensitivity to water loss due to the scarcity and cost of water in those regions.

The most important characteristic to model in a reservoir is the change in production temperature with time. Fracture dominated geothermal reservoirs,

like those found in EGS, can only access the stored thermal energy within the small region surrounding the fractures because of the low thermal diffusivity of the host rock. These reservoirs can be classified as "conduction limiting" because convective heat transport in the fracture is limited by the conductive heat transfer from the surrounding bulk rock. As a result, extended use of a discretely fractured reservoir will lead to localized cooling of the host rock that will result in a drop in the production temperature, often referred to as thermal drawdown. The Fenton Hill project experienced significant drawdown in the first phase of the project due to the size of the reservoir, precipitating the need for reservoir expansion in future stages of the project (Dash et al., 1983).

Early production temperature results are unreliable in predicting future thermal performance. Rather, forecasting the production temperature of the reservoir requires simulating the thermal hydraulics of the reservoir by modeling the mass and heat transport in the subsurface using information like the fracture network, temperature at depth, and the thermophysical properties of the host rock. Depending on the end use of the thermal energy, different applications can allow for different degrees of thermal drawdown. Applications like electricity production are more sensitive to drops in production temperature, while direct thermal use applications are less sensitive. However, for any application, premature and unpredictable decline in temperature will be a problem. In addition to the production temperature, the evolving spatial temperature in the subsurface is also important to model. The subsurface temperature field can help in determining how effectively the stored thermal energy is being extracted. If the systems needs to be expanded, optimal well placement will require identification of regions of the rock that have not experienced thermal drawdown, as well as targeting well placement in fractures that will result in the expansion of the heat transfer area of the reservoir.

Once the production temperature has dropped below the critical threshold, redrilling and further reservoir stimulation is required to expand the system to extract thermal energy in "fresh" rock. However, the abatement of extraction in the thermally depleted region will allow for the reservoir to naturally recharge, since the cooled zone is localized and surrounded by hot rock, allowing for conduction back into the depleted zone. It is expected that the rate of conduction in the cooled region would easily exceed the ambient continental heat flow of 65 mW/m^2 (Pollack et al., 1993), due to the steep temperature gradients induced by cooling of the rock. For example, for a temperature differential with respect to the host rock of 50 °C, a thermal conductivity of the rock of 3 W/m/K, and the length scale of the depleted zone of 25 m, the initial heat flux back into the zone will be around 6 W/m^2, two orders of magnitude greater than the average ambient continental heat flux. Reusing previously cooled regions of the subsurface provides an opportunity to optimally use natural resources and improve the economics by avoiding the costs of drilling additional wells and stimulating the reservoir. Thus, it is important to develop the tools to model the thermal recharge in geothermal reservoirs.

Every geothermal reservoir is unique due to the complexity of the subsurface and our knowledge of the system is limited and incomplete. The thermal hydraulic behavior of the reservoir is dependent on the structure and properties of the subsurface. However, we can use our limited knowledge as a guide in modeling the thermal hydraulics of the system to determine important reservoir characteristics, especially those that cannot be readily measured during the early stages of energy production. In addition, thermal hydraulic modeling can determine the effect of incomplete knowledge of the subsurface and ultimately, serves as an effective guide for the best management practices for the geothermal system. Increased accuracy

in determining the thermal hydraulics of the geothermal reservoir is vital for the advancement of EGS technology to offset current unsustainable energy sources.

Bibliography

Armstead, H. and Tester, J. W. (1987). *Heat Mining*. E. & F.N. Spon, London, New York.

Augustine, C. and Tester, J. W. (2009). Hydrothermal flames: From phenomenological experimental demonstrations to quantitative understanding. *The Journal of Supercritical Fluids*, 47(3):415–430.

Batchelor, A. (1987). Development of hot-dry-rock geothermal systems in the UK. *Physical Science, Measurement and Instrumentation, Management and Education - Reviews, IEE Proceedings A*, 134(5):371–380.

Beckers, K. F., Lukawski, M. Z., Anderson, B. J., Moore, M. C., and Tester, J. W. (2014). Levelized costs of electricity and direct-use heat from Enhanced Geothermal Systems. *Journal of Renewable and Sustainable Energy*, 6(1).

Benato, S., Hickman, S., Davatzes, N. C., Taron, J., Spielman, P., Elsworth, D., Majer, E. L., and Boyle, K. (2015). Conceptual model and numerical analysis of the Desert Peak EGS project: Reservoir response to the shallow medium flow-rate hydraulic stimulation phase. *Geothermics*. In press.

Blackwell, D., Richards, M., Frone, Z., Batir, J., Ruzo, A., Dingwall, R., and Williams, M. (2011). Temperature-at-depth maps for the conterminous U.S. and geothermal resource estimates. *Geothermal Resources Council Transactions*.

Cladouhos, T. T., Osborn, W. L., Petty, S., Bour, D., Iovenitti, J., Callahan, O., Nordin, Y., Perry, D., , and Stern, P. L. (2012). Newberry volcano EGS demonstration - Phase I results. In *Proceedings of the Thirty-Seventh Workshop on Geothermal Reservoir Engineering, Stanford University, January 30-February 1, 2012*, Stanford, CA.

Dash, Z., Murphy, H., Aamodt, R., Aguilar, R., Brown, D., Counce, D., Fisher, H., Grigsby, C., Keppler, H., Laughlin, A., Potter, R., Tester, J., Trujillo Jr., P., and Zyvoloski, G. (1983). Hot dry rock geothermal reservoir testing: 1978 to 1980. *Journal of Volcanology and Geothermal Research*, 15(1–3):59–99.

Dorbath, L., Cuenot, N., Genter, A., and Frogneux, M. (2009). Seismic response of the fractured and faulted granite of Soultz-sous-Forêts (France) to 5 km deep massive water injections. *Geophysical Journal International*, 177(2):653–675.

Frone, Z. and Blackwell, D. (2010). Geothermal map of the northeastern United States and the West Virginia thermal anomaly. *Geothermal Resource Council Transactions*, 34:339–344.

Glassley, W. (2011). *Geothermal Energy: Renewable Energy and the Environment*. CRC Press, Boca Raton, FL.

Hillson, S. D. and Tester, J. W. (2015). Heat transfer properties and dissolution behavior of barre granite as applied to hydrothermal jet drilling with chemical enhancement. In *Proceedings of the Fortieth Workshop on Geothermal Reservoir Engineering, Stanford University, January 26-28, 2015*, Stanford, CA.

Hogarth, R. A. and Bour, D. (2015). Flow performance of the Habanero EGS closed loop. In *Proceedings of the World Geothermal Conference, April 19–24, 2015*, Melbourne, Australia.

Intergovernmental Panel on Climate Change (2007). *Climate Change 2007: The Physical Science Basis. Contribution of Working Group I to the Fourth Assessment Report of the Intergovernmental Panel on Climate Change*. Cambridge University Press, Cambridge, United Kingdom and New York, NY, USA.

Intergovernmental Panel On Climate Change (2011). *Special Report on Renewable Energy Sources and Climate Change Mitigation*, chapter Geothermal Energy. Cambridge University Press, Cambridge, United Kingdom and New York, NY, USA.

Intergovernmental Panel on Climate Change (2014). *Climate Change 2014: Impacts,Adaptation, and Vulnerability. Contribution of Working Group II to the Fifth Assessment Report of the Intergovernmental Panel on Climate Change*. Cambridge University Press, Cambridge, United Kingdom and New York, NY, USA.

Lukawski, M. Z., Anderson, B. J., Augustine, C., Capuano Jr., L. E., Beckers, K. F., Livesay, B., and Tester, J. W. (2014). Cost analysis of oil, gas, and geothermal well drilling. *Journal of Petroleum Science and Engineering*, 118(0):1–14.

Maurer, V., Cuenot, N., Gaucher, E., Grunberg, M., Vergne, J., Wodling, H., Lehujeur, M., and Schmittbuhl, J. (2015). Seismic monitoring of the Rittershoffen EGS project (Alsace, France). In *Proceedings of the World Geothermal Conference, April 19–24, 2015*, Melbourne, Australia.

Omer, A. M. (2008). Ground-source heat pumps systems and applications. *Renewable and Sustainable Energy Reviews*, 12(2):344–371.

Parker, R. (1999). The Rosemanowes HDR project 1983–1991. *Geothermics*, 28(4–5):603–615.

Pollack, H. N., Hurter, S. J., and Johnson, J. R. (1993). Heat flow from the earth's interior: Analysis of the global data set. *Reviews of Geophysics*, 31(3):267–280.

Reber, T. J., Beckers, K. F., and Tester, J. W. (2014). The transformative potential of geothermal heating in the U.S. energy market: A regional study of New York and Pennsylvania. *Energy Policy*, 70(0):30–44.

Sausse, J., Dezayes, C., Dorbath, L., Genter, A., and Place, J. (2010). 3D model of fracture zones at Soultz-sous-Forêts based on geological data, image logs, induced microseismicity and vertical seismic profiles. *Comptes Rendus Geoscience*, 342(7–8):531–545.

Schill, E., Cuenot, N., Genter, A., and Kohl, T. (2015). Review of the hydraulic development in the multi-reservoir/multi-well EGS project of Soultz-sous-Forêts. In *Proceedings of the World Geothermal Conference, April 19–24, 2015*, Melbourne, Australia.

Tans, P. and Keeling, R. (2015). Recent monthly average Mauna Loa carbon dioxide. www.esrl.noaa.gov/gmd/ccgg/trends/. Accessed: June 2015.

Tester, J. W., Anderson, B. J., Batchelor, A. S., Blackwell, D. D., DiPippo, R., Drake, E. M., Garnish, J., Livesay, B., Moore, M. C., Nichols, K., Petty, S., Toksoz, M. N., Veatch, R. W., Baria, R., Augustine, C., Murphy, E., Negraru, P., and Richards, M. (2006). The future of geothermal energy. Technical Report DOE Contract DE-AC07-05ID14517, Massachusetts Institute of Technology.

Tester, J. W., Drake, E. M., Golay, M. W., Driscoll, M. J., and Peters, W. A. (2012). *Sustainable Energy: Choosing Among Options*. The MIT Press, Cambridge, MA, 2nd edition.

U.S. Energy Information Administration (2013). International energy outlook 2013. Technical report, U.S. Department of Energy.

U.S. Energy Information Administration (2015). Monthly energy review, June 2015. Technical report, U.S. Department of Energy.

World Wildlife Fund (2010). Living planet report 2010, biodiversity, biocapacity and development. Technical report, World Wildlife Fund.

CHAPTER 2

OBJECTIVES AND APPROACH

The overall goal of my research is to develop a better understanding of the thermal hydraulic behavior of fractured geothermal reservoirs, such as those often encountered in Enhanced/Engineered Geothermal Systems (EGS). A focus of the research will be to develop analysis tools and modeling techniques that can be used to learn more about the performance of EGS and to better plan the development of such systems. A key expected outcome of using these techniques is to better predict the lifetime of such systems. Hydrothermal systems' long history of development has resulted in economically competitive electricity and heat production on a large scale at a number of sites worldwide. The long term behavior of operating hydrothermal systems has been well characterized and, in some cases, is fully understood. If geothermal energy is to be a major source of both electricity and direct thermal use, EGS technology needs to reach a level of technoeconomic maturity of hydrothermal systems. Thus, my research goals are aimed at developing analysis tools and modeling techniques that can be used to learn more about the performance of EGS and to better plan the development of such systems. Specifically, my research approach is to:

1. Determine the domestic market for the expansion of geothermal energy for direct thermal use
2. Quantify the renewability of EGS by determining how the temperature field recovers after a period of no sustained heat extraction in model reservoir systems
3. Develop analytical and numerical models to probe how fundamental reservoir characteristics including aperture distribution, fracture intersections,

and other rock properties affect thermal hydraulic performance

4. Develop the methodology of using conservative and reactive tracers to determine flow characteristics
5. Validate the role of tracer modeling to predict thermal behavior

The chapters that follow document my research and how it accomplishes the dissertation objectives. The structure and arrangement of the dissertation and the content of each chapter is described below. Each chapter can be considered a separate study, aimed at one aspect of the research objectives. In combination, they are all linked through each individual contribution to the overall research goals.

Chapter 3 documents a study of the spectrum of direct thermal energy use in the United States. The energy spectrum displays the amount of direct thermal energy use by its characteristic end use temperature for the U.S. By determining the thermal energy spectrum, one can easily understand the U.S. energy practices and determine the market for expansion of geothermal energy for direct use, as opposed to electricity production. The study was conducted in collaboration with Daniel Sutter, a visiting masters student from ETH Zürich, and was published in the journal *Energy and Environmental Science* in 2011, and was fully documented in an Cornell Energy Institute report (Fox et al., 2011a,b).

Chapter 4 deals with determining the sustainability and renewable capacity of discretely fractured geothermal reservoirs. Unlike hydrothermal systems, EGS reservoirs, which are conduction limited, are more susceptible to thermal drawdown due to localized cooling of the rock around the fractures. Using both analytical and numerical models, the study evaluates the sustainability of EGS reservoirs

through simulation of the extraction and thermal recovery process. The study was carried out in collaboration with Koenraad Beckers and Maciej Łukawski, both Cornell chemical engineering Ph.D. students, as well as with Daniel Sutter. It was published in the journal *Geothermics* in 2013 (Fox et al., 2013).

Chapter 5 centers around the development of an analytical model for the fluid flow and heat transport in a discretely fractured geothermal reservoir. The analytical model relies on some of the tools and framework from the analytical models presented in Chapter 4. The purpose of the study was to fill the gap between simple analytical models that do not consider interconnected discrete fractures and numerical codes that do. Furthermore, this study serves to demonstrate the capabilities of the model such as how to determine the effect uncertainty in fracture aperture and fracture network connectivity/structure have on the thermal performance of discretely fractured geothermal reservoirs. Results from this particular study will be submitted for publication. The study may be combined with results from a parallel effort led by Morgan Ames, a Ph.D. student at Stanford University working in Professor Roland Horne's research group. Ames and Horne are currently using the analytical discrete fracture model for the temperature derived in Chapter 5 in order to determine the capability of reactive tracers to identify the subsurface fracture structure and connectivity.

Chapter 6 details the development of a numerical model for the fluid flow and heat transport in discrete fractures. The purpose of the chapter is to create a numerical framework to be utilized in later studies. The chapter details how fluid flow, heat transport, and tracer particle transport are modeled and showcases the capability of the code to simulate the thermal hydraulics of geothermal reservoirs.

Chapter 7 focuses on modeling the effect of fracture surface aperture variations

on the thermal performance of a reservoir. The study relies on the developed numerical model in Chapter 6 to simulate a reservoir's thermal performance. The purpose of the chapter is to help understand the importance of modeling fracture surface features and to quantify its effect on important reservoir parameters like production temperature and reservoir life. The study has been accepted for publication to the journal *Geothermal Energy* (Fox et al., 2015).

Chapter 8 is centered around determining a spatially varying aperture field in a fracture using both conservative and reactive tracer data. Additionally, this study strikes to use the determined aperture field in order to predict the reservoir's production temperature with time. The task of determining the aperture field is framed as an inverse problem using the genetic algorithm and reduced order modeling. The work in the chapter utilizes the numerical model developed in Chapter 6 and from which simulated tracer data is generated for a given known fracture aperture distribution.

Chapter 9 summaries the contributions of the dissertation and provides, subsequently, specific recommendations for future work. In doing so, it ties together all the studies presented in the dissertation with respect to the goals and objectives of this research.

Bibliography

Fox, D. B., Koch, D. L., and Tester, J. W. (2015). The effect of spatial aperture variations on the thermal performance of discretely fractured geothermal reservoirs. *Geothermal Energy*, 3(1):1–29.

Fox, D. B., Sutter, D., Beckers, K. F., Lukawski, M. Z., Koch, D. L., Anderson,

B. J., and Tester, J. W. (2013). Sustainable heat farming: Modeling extraction and recovery in discretely fractured geothermal reservoirs. *Geothermics*, 46(0):42–54.

Fox, D. B., Sutter, D., and Tester, J. W. (2011a). The thermal spectrum of low-temperature energy use in the United States. *Energy Environmental Sciences*, 4(10):3731–3740.

Fox, D. B., Sutter, D., and Tester, J. W. (2011b). The thermal spectrum of low-temperature use in the united states. Technical Report 1, Cornell Energy Institute, Ithaca, NY.

CHAPTER 3

THE THERMAL SPECTRUM OF LOW-TEMPERATURE ENERGY USE IN THE UNITED STATES

3.1 Introduction

Fossil fuels have remarkable properties as energy carriers such as high specific energy density (e.g. lower heating value of gasoline is 43 MJ/kg) and high combustion temperatures ranging from 1000 to 2500 °C, depending on fuel-air composition, combustor design, and other factors. These characteristics enable fossil fuels to meet extreme energy demands of sophisticated machines such as jet engines and gas turbines and allow for highly efficient energy conversion to electricity in today's combined cycle power plants.

The laws of thermodynamics teach us much about what happens to energy as it is transferred or transformed and finally used to provide a specific energy service. For example, many end-uses currently powered by fossil fuels do not necessarily require the higher grade characteristics inherent to these energy sources. As a result, fossil fuel energy is downgraded to meet these thermodynamically lower grade demands. The metric used to quantify these losses is known as exergy or availability, which corresponds to the maximum work-producing potential of an energy source. The combustion temperatures of fossil fuels are too high for various thermal end-uses. In U.S. residential buildings, 93.5% of the energy used for space heating is provided by natural gas, fuel oil, liquefied petroleum gas, and kerosene (U.S. Energy Information Administration, 2009). A logical energy use scheme would close the gap between source and process end-use temperature and would reserve the high grade fossil energy sources for combustion processes that require

high temperatures. Correspondingly, a more efficient energy utilization approach would be to tailor the energy source used to the temperature needs of the process.

In 2008, the U.S. used 104.8 EJ (99.3 quadrillion Btu) of primary energy, 84% of which came from fossil fuels as reported by the U.S. Energy Information Administration (U.S. Energy Information Administration, 2009). The primary energy demand can generally be divided into two categories, one used for thermal energy and the other for mechanical drive. About 40% of U.S total primary energy is used for electricity generation (U.S. Energy Information Administration, 2009). Electricity, in turn, also provides thermal or mechanical energy for specific end-uses. Primary energy demand is typically divided into four end use sectors: residential, commercial, industrial, and transportation.

The International Energy Agency reports that electricity production has received most of the attention with regards to the use of renewable energy (International Energy Agency, 2007). As a result of this and other factors such as the generally low capital cost of gas and oil furnaces for buildings, policies and incentives in the U.S. aimed at encouraging direct thermal use of renewables or fossil-fired co-generation have not been deployed to the same extent as those for electricity generation. In order to evaluate the potential market for lower temperature energy sources, the actual demand for thermal energy as a function of process temperature needs to be quantified. This creates a thermal spectrum of energy demand that could, in principle with the right infrastructure in place, be supplied from energy sources such as geothermal, solar thermal, and waste heat.

These lower grade energy sources would be more valuable from both a sustainability and economic perspective when used for direct thermal applications rather than incur the significant thermodynamic losses incurred in upgrading them to

electricity.

Literature in the field of direct thermal energy use from renewable sources includes the famous Líndal diagram shown in Figure 3.1. It presents a number of possible applications for direct thermal use along with typical end-use temperatures. The idea of the Líndal diagram has been taken up by other authors, such as Kalogirou, who shows a variation with a focus on solar thermal rather than geothermal (Kalogirou, 2003). The Líndal diagram illustrates the opportunity but does not quantify the potential of direct use, since it does not provide how much thermal energy is used for each end use shown. The recent worldwide review of direct thermal application of geothermal energy quantifies current worldwide use, but again, misses the existing potential within the thermal spectrum (Kalogirou, 2003). Another study included work that looked at the potential of providing thermal energy from renewable sources but did not specify the exact temperatures required by the potential end-uses (Vannoni et al., 2008). In 2004, 40-50% of the total worldwide energy demand in residential, commercial, and industrial sectors was used for heating and cooling (Philibert, 2006). Thus, there is a need to not only quantify the magnitude of the thermal demand, but also the demand temperatures to better understand how much of the current demand could be replaced by renewables such as geothermal and solar thermal. Thirty-five years ago, Reistad (1975) quantified the low-temperature thermal energy consumption and correlated it with end-use temperatures. This important study quantified the situation for the U.S. based on 1968 energy consumption data. Much has changed in the U.S. with respect to energy demand in the last 42 years due to an increase in population as well as structural changes in the manufacturing, transportation, and housing sectors. In addition, end-use or process temperatures might have changed due to technological development. A primary motivation for our work was to evaluate the

situation as it now exists in the United States.

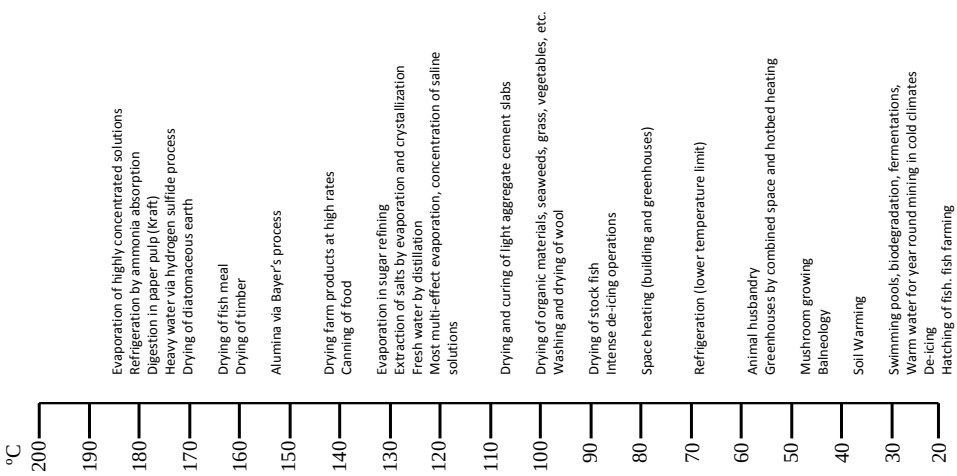

Figure 3.1: Industrial and other possible applications for direct thermal use of geothermal energy suggested by Líndal (1973), as cited by Armstead (1978).

3.2 Methodology

We focused on the lower temperature range 0 to 260 °C (0 to 500 °C) of energy use because resources at higher temperatures would be used for electricity production to exploit the higher 2nd Law efficiencies before supplying lower temperature heat for direct thermal use. A 20 °C temperature bin size was chosen to allow for coarse graining and to acknowledge that certain processes can be undertaken over a range of temperatures rather than requiring a specific temperature.

The EIA issues an Annual Energy Review (AER) for the United States that defines four demand sectors, i.e. residential, commercial, industrial, and transportation sectors and provides information about their yearly energy consumption (U.S. Energy Information Administration, 2009). The transportation sector was left aside because its consumption of energy is for mechanical drive. For all four

demand sectors, the EIA issues sector specific reports on a rotating basis such that a report for each sector is released every four years (U.S. Energy Information Administration, a,b,c). While the AER provides useful general information, only the sector specific consumption surveys give details about end-use specific energy demand. Consequently, both reports were used for each sector. Extrapolation was applied because the sector specific surveys are not issued in the same years. 2008 was selected as the base year because it is the year of the most recent AER.

Our general approach was to break energy consumption down to specific end-uses in order to quantify their energy demand, to determine their thermal and non-thermal character, and to estimate their required end-use temperature based on reported practices. The relative fractions of energy demand for each end-uses could then be extrapolated to the base year, for which the total consumption of the demand sectors is given in the AER. For more detailed information on the methodology including all assumptions and numerical values for the energy consumption, interested readers are invited to look at the supplementary information provided or the Cornell Energy Institute report (Fox et al., 2011).

3.2.1 Residential Sector

Space heating, appliances, water heating, and air conditioning are the major end-uses in the residential sector. The appliances were carefully examined to only consider the ones requiring thermal energy for their end-use. Thermal use appliances consisted of refrigerators, clothes dryers, freezers, range tops, dishwashers, ovens, microwaves, clothes washers, pools/hot tubs/spa heaters, coffee makers, waterbed heaters, large heated aquariums, and humidifiers. The main source of information about the specific energy use of common appliances also came from the EIA (U.S.

Energy Information Administration, 2001). Generally, temperatures around and above 50 °C (122 °F) are used in space heating, but using temperatures as low as 40 °C (104 °F) is feasible (Bloomquist, 2003). Therefore, space heating is included in the 40 to 60 °C (104 to 140 °F) range. Although many U.S. house- holds set their water heaters to a higher temperatures, the U.S. Department of Energy (U.S. Department of Energy, 1995) points out that a temperature of 48.9 °C (120 °F) is sufficient as opposed to most manufacturers' setting of 60 °C (140 °F). Therefore, the temperature category for water heating is chosen to be 40 to 60 °C. Dishwasher thermal energy contribution was also placed in the same bin because dishwashing draws its energy primarily from the household hot water heaters (U.S. Department of Energy, 1995).

The temperature assigned to air conditioning and refrigeration is based on the temperature requirements to run an absorption or adsorption cooling system. For residential air conditioning, a heat source temperature of 60 to 80 °C (140 to 176 °F) is considered to be sufficient to operate such systems (Wang et al., 2009). Higher temperatures would allow for higher coefficients of performance (COP), which increases the economic competitiveness of these cooling systems.

The temperature range for refrigeration and freezers was based on a review of Fan et al. (2007) and was chosen to be 100 to 120 °C (212 to 248 °F) and 120 to 140 °C (248 to 284 °F), respectively. The temperature for the clothes drying end-use varies from 40 to 120 °C for different literature sources (International Energy Agency, 2007; Conde, 1997; Bansal et al., 2010; Yadav and Moon, 2008; Bansal et al., 2001). The temperature range of 80 to 100 °C (176 to 212 °F) was ultimately chosen.

Energy requirements of pools/hot tubs/spa heaters, waterbed heaters, and large

aquariums were collectively binned at 20 to 40 °C (68 to 104 °F). For cooking applications, the range tops and conventional ovens were all placed in the 240 to 260 °C range (464 to 500 °F) while microwave oven energy consumption was binned at 100 to 120 °C (212 to 248 °F) to reflect the nature of usage of the microwave ovens. Due to their need to boil water, coffee makers and humidifiers were placed in the 100 to 120 °C bin.

3.2.2 Commercial Sector

Energy consumption in the commercial buildings sector is made up of space heating, lighting, air conditioning, water heating, refrigeration, ventilation, cooking, computers, office equipment, and other appliances. Of the listed end-uses, spacing heating, air conditioning, water heating, refrigeration, and cooking were considered thermal end-uses, similar to that of the residential sector. The end-use temperature designations for the five thermal end-uses are the same as for the residential sector.

3.2.3 Industrial Sector

The industrial sector consists of the following types of activities, categorized in the North American Industrial Classification System (NAICS) with their respective code in parenthesis (U.S. Energy Information Administration, 2009).

- Agriculture, Forestry, Fishing and Hunting (11)
- Mining (21)

- Construction (23)
- Manufacturing (3133)

The EIA provides a specific survey with the detailed information needed for this study only for the manufacturing sector, i.e. NAICS codes 3133, in its Manufacturing Energy Consumption Survey (MECS) (U.S. Energy Information Administration, c). For the three most recent MECS of 1998, 2002, and 2006, the manufacturing sector covers 84 to 90% of the industrial consumption.

Thermal energy consumption in the other industrial activities was estimated and found to be small compared to the manufacturing energy consumption. Due to the lack of detailed EIA data, only manufacturing activities were considered. Figure 3.2 shows a graphical representation of the breakdown of the industrial sector energy consumption to the end-uses of interest. For the quantification of the thermal energy demand, only process steam, process cooling, and HVAC were investigated. The temperature distribution was investigated for the five subsectors with the highest energy demand for process steam:

- Petroleum and Coal Products Manufacturing (324)
- Chemical Manufacturing (325)
- Paper Manufacturing (322)
- Food Manufacturing (311)
- Primary Metals Manufacturing (331)

The above manufacturing sectors are responsible for 76% of the total manufacturing fuel consumption and for 87% of the process steam fuel demand. Their

weighted (by steam energy demand) average distribution of process steam temperature is assumed to be representative for the remaining 16 manufacturing subsectors and used to quantify the thermal energy distribution of the remaining "other" manufacturing sectors. Because process steam is often used at different temperature ranges, the process steam temperature distribution for each of the five main manufactures was individually determined using multiple sources (Resource Dynamics Corporation, 2002; Ozalp and Hyman, 2007; Brown et al., 1985; Lund et al., 1980).

Quantifying process cooling and HVAC, as with process steam, was done by consulting the MECS. The HVAC contribution was broken down into space heating and air condition whose temperature bin was chosen to be the same as the residential sector. For process cooling, the temperature range was increased to reflect industrial refrigeration processes demand characterized by typically lower cooling temperatures compared to refrigeration in homes. Therefore, the end-use temperature for industrial cooling and refrigeration was increased to 120 to 140 °C compared to 100 to 120 °C for residential refrigeration.

3.2.4 Electrical Systems Energy Losses

If one Joule of electricity consumption is eliminated, the entire fuel energy that had to be invested for generating that Joule of electricity would be saved. Hence, losses in the electricity generation system in the U.S. were also considered in this work. The AER (U.S. Energy Information Administration, 2009) accounts for losses in the generation, transmission, and distribution of electricity in a category called Electrical System Energy Losses (ESEL). The category Electricity Retail Sales (ERS) covers the electricity sold to the ultimate customers by the utilities (U.S. Energy Information Administration, 2009). The overall system efficiency,

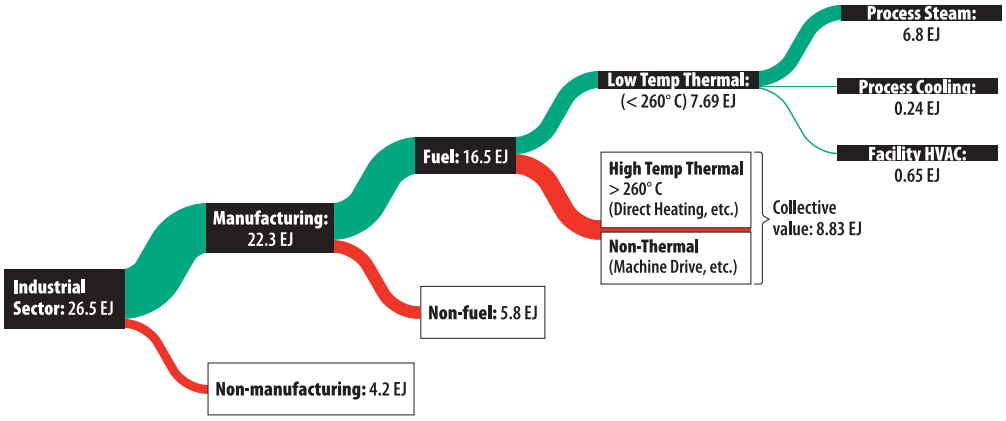

Figure 3.2: Breakdown of the industrial sector energy consumption in 2006 presented in the form of a Sankey diagram. The energy flows in red were not considered in the analysis, only the last three energy flows in green on the far right were considered.

η_{el}, can be calculated based on ERS and ESEL:

$$\eta_{el} = \frac{ERS}{ERS + ESEL} \tag{3.1}$$

The overall system efficiency for electricity in the U.S. in 2008 was 31.67%.

3.3 Results and Discussion

Figure 3.3 illustrates the distribution of the total low-temperature thermal energy use among the three demand sectors, residential, commercial, and industrial. It is important to note that this work assess the consumption of primary energy to provide heat for thermal end-uses in the year 2008 and does not include the transportation sector. Meeting the energy demand of some non-transportation end-uses using geothermal, solar thermal, or waste heat resources would not necessarily require the same amount of primary energy. Hence, in order to estimate

the amount of thermal energy that would have to be generated from renewable sources to cover all low-temperature thermal energy demands, the technological implementation would have to be investigated in detail for each end-use. For example, for sorption cooling, the COP would be required. The presented estimates for the actual energy consumption however represent a valuable estimate of how much conventional energy could be saved by switching to renewable thermal energy sources.

Figure 3.3b includes the 11.4 EJ (10.8 quads) of Electrical System Energy Losses (ESEL) related to the 5.27 EJ (5.00 quads) of Net Electricity included in Figure 3.3a, a 51% increase of the total. The area of the circles in Fig. 3 is proportional to the total. The 33.5 EJ (31.7 quads) in (b) represent 32% of the total U.S. energy consumption of 105 EJ (99.3 quads) in 2008 (U.S. Energy Information Administration, 2009). As shown in Fig. 3, the share of energy demand for the industrial sector drops when ESEL is considered while it increases for the residential and commercial sectors. The change in the distribution is due to the residential and commercial sector having more end-uses powered by electricity than the industrial sector, whose low-temperature thermal demand is comprised mostly of process steam.

The residential sector has the highest potential for direct use of low-temperature thermal energy but the decentralized nature of the residential sector complicates large scale geothermal, solar, or waste heat recovery projects. Investments are too high for single households while infrastructure needs, such as district heating networks, are enormous. Therefore, local communities should be encouraged to pursue such solutions. Geothermal heat pumps and flat plate solar collectors present small scale alternatives for single houses. The thermal end-uses in the commercial sector

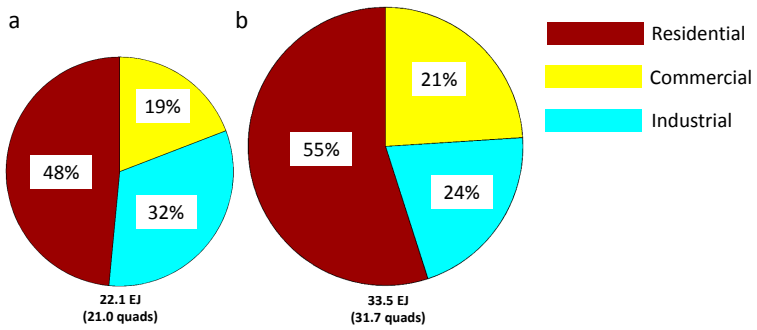

Figure 3.3: (a) Total low-temperature thermal energy demand and share of the three demand sectors: residential, commercial, and industrial without Electrical System Energy Losses (b) includes Electrical System Energy Losses.

have very similar requirements to the residential sector. Commercial buildings are generally larger and more centralized.

The EIA data show that the residential and commercial sectors' energy demand has been increasing following an almost linear trend for the past 40 years, whereas industrial demand decreased from its 1997 high to levels comparable to the demand in the mid 1970s. In 40 years, the U.S. population has increased from 200 million in 1968 to just over 300 million in 2008 while the U.S. total energy consumption has risen from 63.8 EJ to about 100 EJ, a 4% increase in per capita energy consumption. Reistad's work indicates that in 1968, 26.4 EJ (40% of the total consumption) was used for direct thermal applications below 250 °C while in 2008 33.5 EJ were used for applications below 260 °C (32% of the total consumption). The decrease in percentage of energy being consumed for low temperature applications can be attributed to an increase in electricity consumption, especially with the rise of personal computers and other personal electronics as well as improved efficiencies in heating applications. Although a shift of manufacturing to other countries is largely responsible for the sector's decrease from its 1997 high, they have the effect of increasing the importance of providing energy

to the residential and commercial sectors.

In 2008, 25% of the total manufacturing industry's energy demand, including ESEL, powered thermal end-uses below 260 °C. Additionally, regions in the U.S. with moderate to high geothermal temperature gradients might be able to attract energy intensive industries to create tax revenue and jobs. A prominent example is the use of renewable electricity for aluminum production in Iceland. The availability of low cost geothermal electricity made it attractive to have bauxite shipped long distances to be processed into aluminum (Hreinsson, 2007).

A more important example is Iceland's radical transformation from a nation that had no native fossil fuels to one that utilized their indigenous renewable energy supply in less than 50 years. Iceland made use of their high grade geothermal resources to provide 95% of their heating demand that includes not only space heating but also ice melting, fish farming, and greenhouses.

Figure 3.4 relates the thermal energy demand with its associated end-use temperature range using 20 °C wide temperature bins. The industrial sector process steam demand is sub-divided into the five key manufacturing sectors and "Other Manufacturing". The end-uses with the largest contributions are annotated.

By far the largest energy use is in the temperature range from 40 to 60 °C, with space and water heating as major contributors. When ESEL are not considered, space heating accounts for a demand of 8.46 EJ (8.02 quads). This corresponds to 38% of the total energy demand for low-temperature thermal use and 8% of the total U.S. energy consumption in 2008. Water heating makes up 2.80 EJ (2.66 quads). Figure 3.4 incorporates ESEL to the appropriate end-uses such as air conditioning, refrigeration, and cooking. Interestingly, most of the thermal energy

consumption in the investigated region from 0 to 260 °C occurs in the lower half of the temperature range. Besides cooking, all residential and commercial contributions require end-use temperatures below 140 °C. Industrial process steam and cooking are the only end-uses above 140 °C. Figure 3.4 and 3.5 resemble the results from Reistad's study; the thermal spectrum is largely distributed at lower half of the temperature range (¡120 °C) and with industrial applications mostly filling the demand at the higher temperature range (120 to 260 °C). Figure 3.6 shows a continuous functional approximation of the discrete data of Figure 3.5. The figure approximates Figure 3.5 as if the resolution was set to an infinitesimal value as opposed to the discrete 20 °C bins. A piecewise cubic Hermite polynomial (PCHIP) was used by employing the built-in pchip-function from MATLAB. The values of Figure 3.5 were plotted at the mean value of each temperature bin and then a PCHIP was applied to obtain the smooth graph. The smooth, continuous representation shown in Figure 3.6 takes into account that the end-use temperature of each process might vary slightly and the temperature ranges are not sharply confined but rather overlap and merge. Effectively, Figure 3.6 provides a continuous distribution function that can be easily integrated to provide estimates of total energy use to a particular temperature. The total area under the curve in Figure 3.6 corresponds to the cumulative thermal energy demand up to 260 °C. To relate energy use temperature to geothermal resource depths, average geothermal temperature gradients can be used. Gradients ranging from about 20 to 60 °C/km are representative of a large portion of the U.S. In Figure 3.6, the dashed horizontal line corresponds to an assumed maximum economic drilling depth of 6 km (Tester et al., 2005) where temperatures would be 135 °C for the 20 °C/km gradient resource, 255 °C for 40 °C/km, and 375 °C for 60 °C/km. Even with the lowest gradient, the temperature at 6 km would be sufficient for space and water heating,

air conditioning, and refrigeration applications. The cumulative thermal energy with and without ESEL is shown in Figure 3.7. The change of the demand within the 20 °C temperature bins was assumed to be linear. For example, the value at 20 °C is zero, and the value linearly increases to match the whole demand of the 20 to 40 °C temperature bin at 40 °C. The scale on the right shows the proportion of the U.S. total energy demand excluding the transportation sector. Note that a temperature of 150 °C would be sufficient to supply more than 35% of the U.S. industrial, commercial, and residential energy demand. A temperature of 150 °C can be reached within the 6 km drilling depth limit for most regions in the U.S. where average geothermal temperature gradients are higher than 22 °C/km.

An alternative technology that has the capability to cover space heating, water heating, and cooling is geothermal groundsource heat pumps (GHPs). Typically, GHPs have a coefficient of performance (COP) of 4 or more, meaning that 4 units of thermal energy are transferred for every 1 unit of electrical energy (Tester et al., 2005). Thus using GHP systems to provide residential and commercial space heating, water heating, and air conditioning would replace significant amounts of fossil fuel use, but would increase electricity consumption. In contrast, the use of thermal energy in other applications requiring electric power would actually free up generating capacity for use in other applications.

Meeting thermal energy demands at different temperatures does not necessarily require multiple thermal energy sources. A single thermal energy source can supply end-uses over a range of temperatures in a cascaded heat supply system (Figure 3.8). Armstead and Tester (1987) illustrate the general idea of high efficiency combined heat and power utilization in a cascaded system. They show how a single geothermal source of a given temperature could supply all of the ther-

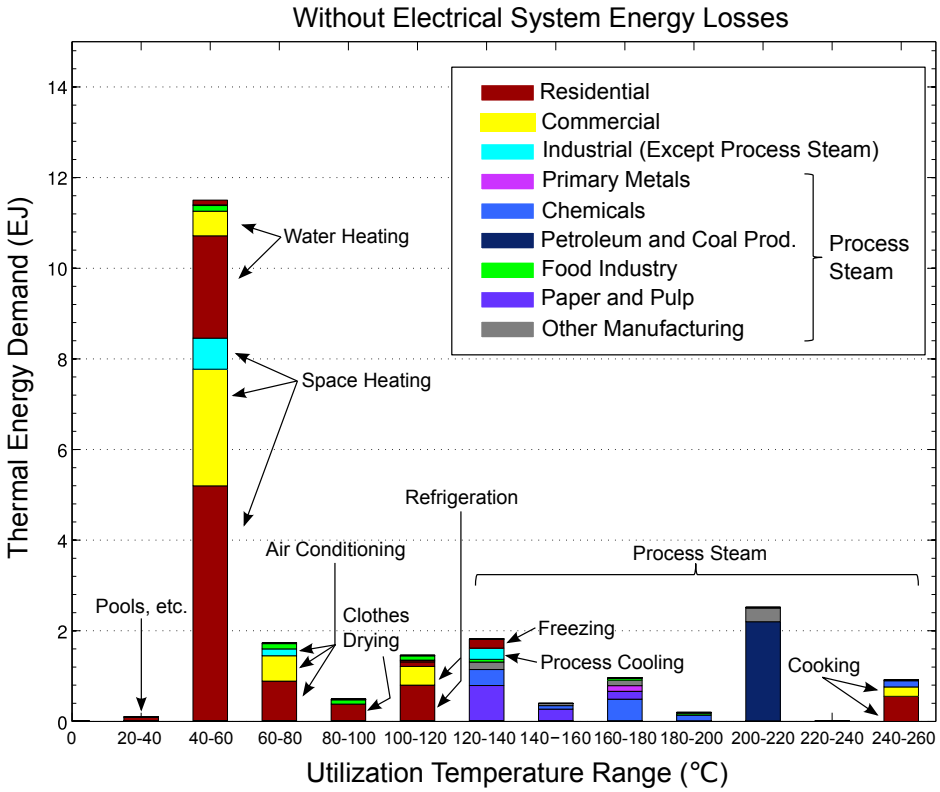

Figure 3.4: Thermal energy use temperature distribution from 0 to 260 °C without Electrical System Energy Losses. The end-uses with the largest contribution are annotated. The total thermal energy demand from 0 to 260 °C in 2008 was 22.1 EJ (20.9 quads). Refer to the Cornell Energy Institute report (Fox et al., 2011) for tabulated values of each temperature bin.

mal and electrical energy needs of a hypothetical market. Armstead and Tester's example demonstrates the importance of knowing the thermal energy demand of a given market to effectively plan an energy use scheme. The same approach can be applied to the U.S. heat market. According to Figure 3.5 the residential and commercial thermal energy demand for space heating, water heating, and air conditioning makes up 17.4 EJ (16.5 quads). A cascaded district heating system would be able to serve most or all these demands, and generate sufficient electrical power to meet applications that cannot be displaced with thermal energy such as lighting, electronic appliances and computers. Consider a heat source at 200 °C.

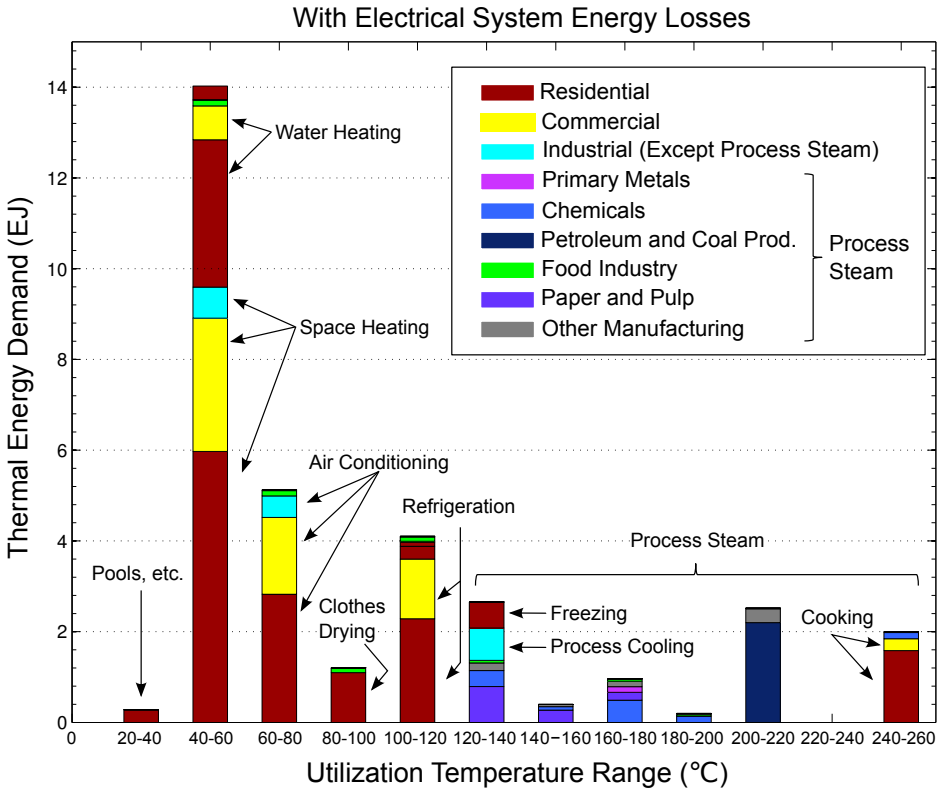

Figure 3.5: Thermal energy use temperature distribution from 0 to 260 °C with Electrical System Energy Losses (ESEL). The end-uses with the largest contribution are annotated. The total thermal energy demand from 0 to 260 °C in 2008 was 33.5 EJ (31.7 quads). Refer to the electronic supplemental information or the Cornell Energy Institute (Fox et al., 2011) for tabulated values of each temperature bin.

The working fluid would first be introduced to a turbine to generate electricity. To enable air conditioning in a sorption cooling system, the fluid should leave the turbine at about 80 °C, resulting in a Carnot efficiency of $\eta_c = 0.25$. The exhausted fluid would be used for cooling via a sorption cycle and could then cascade further down to provide any hot water needs. Depending on the seasonal need, the waste heat from power production could also be used for space heating. The remaining energy could be used for snow melting, soil warming, or other end-uses below 40 °C. Similar cascaded systems have already been implemented, specifically the geothermal power plant in Neustadt-Glewe, Germany, which has an electric and

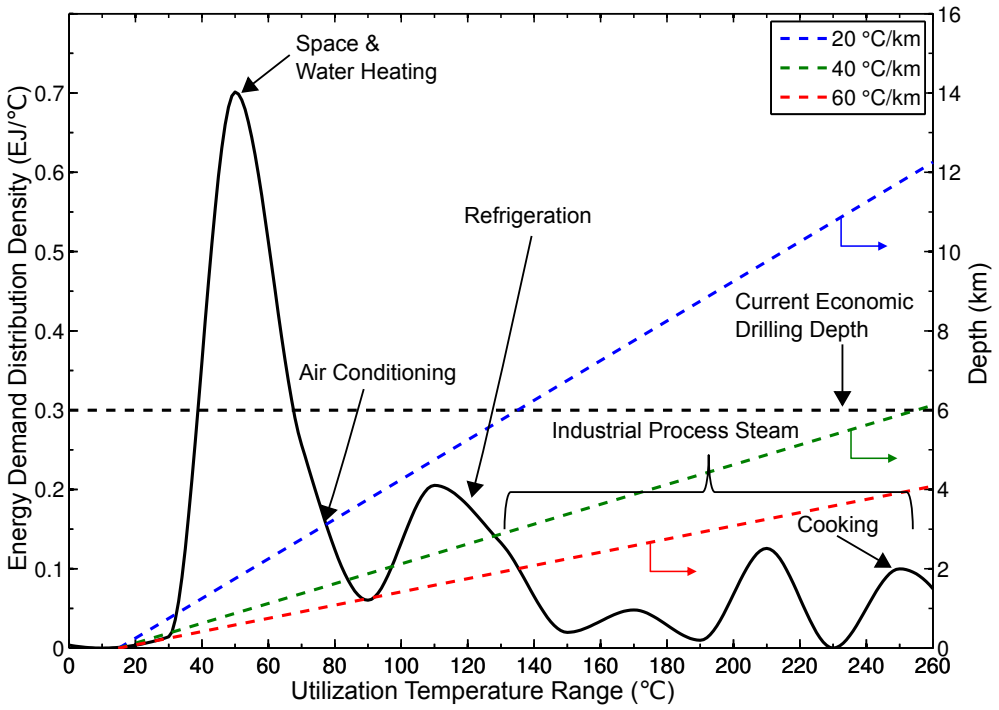

Figure 3.6: Continuous approximation of the energy demand distribution density with Electrical System Energy Losses (ESEL). The energy demand is normalized by the temperature, i.e. the total area under the curve represents the total thermal energy demand. The scale on the right-hand side indicates the depth needed to achieve the corresponding temperature for three different temperature gradients (20, 40, 60 °C/km). The dashed horizontal line presents the current maximum economic drilling depth.

thermal capacity of 230 kWe and 6 MWt, respectively (Lund et al., 2005). Heat systems can also be cascaded bottom up, i.e. for preheating in certain processes. Cascaded heat systems generally minimize the earlier criticized temperature gap between the source of heat and the process temperature.

As discussed in the industrial sector methodology section, byproducts are used as fuel to help improve the economics of a process by reducing the amount of imported energy. One might argue that these byproducts should not be considered in the potential for the discussed renewable, low-temperature thermal energy sources

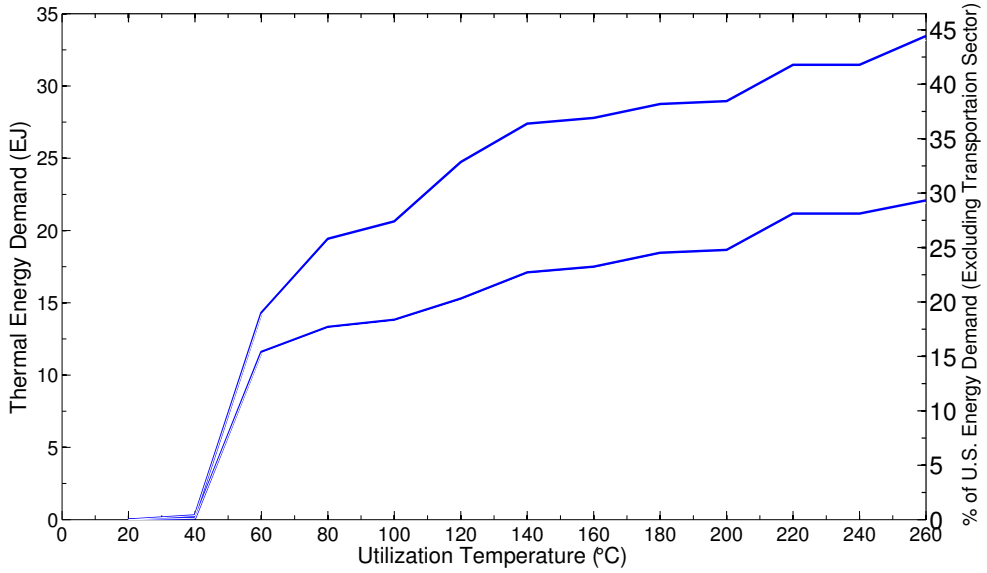

Figure 3.7: Cumulative thermal energy demand with and without Electrical System Energy Losses (ESEL).

because the byproducts should not be wasted. However, these byproducts could be used to meet other energy requirements, especially those that cannot be displaced by low- temperature direct thermal energy use such as electricity generation, machine drive, or direct fired processes. Transportation fuel production is another option for byproducts that become abundant, as their former thermal end-use is met by the mentioned renewable sources. Forest industry byproducts from paper manufacturing, for example, could be used to generate biofuels. The goal should be to shift byproduct use to applications that make use of their relatively high exergy and combustion temperatures to generate electricity or power mechanical drives as well as process heat in cascaded or co-generation systems, and thus, implement a more efficient energy use scheme.

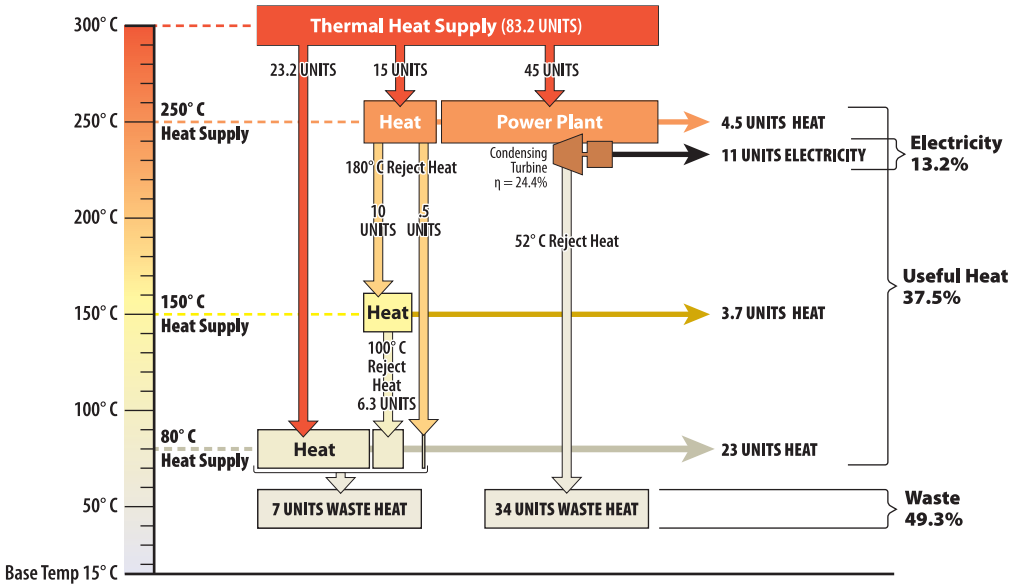

Figure 3.8: Energy cascade system that provides power and thermal energy at three different end-use temperatures, 250, 150, and 80 °C. Without energy cascading, the total thermal demand for the system would have been 100 units. Modified from Armstead and Tester (1987).

3.4 Conclusion

By evaluating U.S. thermal energy consumption over a range of temperatures from 0 to 260 °C, the magnitude of potential markets for thermal energy was quantified. When electrical system energy losses are included, the cumulative thermal energy demand below 260 °C in 2008 was found to be 33.5 EJ (31.7 quads) which is slightly greater than 30% of total U.S. energy demand in 2008.

Detailed information about the distribution of this energy consumption with end-use temperatures suggests significant potential for deploying district heating and cooling systems to increase efficiency and enable the use of renewable thermal

sources in a dispatachable mode. Almost 80% of the total is used to provide heat below 150 °C. Space and water heating and air conditioning in residential and commercial buildings are the end-uses with the largest thermal energy demand. More than half of that demand (55%) is from the residential sector. The results show that there is a large potential for utilizing low enthalpy geothermal, solar thermal, and waste heat resources to meet these demands in the U.S. which if deployed at scale would replace a substantial amount of natural gas and oil that is consumed today to supply heat in this range. Such a transformation from discrete fossil energy use in buildings to a district renewable energy supply of thermal energy would have immediate environmental benefits as well in terms of reducing airborne emissions including CO_2 from these point sources.

While it is clear that significant opportunities exist for providing thermal energy using geothermal, solar, and waste heat sources, it would be misleading to presume that these resources could technically supply the thermal energy for *all* end-uses below 260 °C. Obviously, appliances such as blow dryers, toaster ovens, and coffee makers would be unwieldy and impractical, if their thermal energy was supplied by anything else besides electricity. Note that these appliances do not contribute significantly to the total thermal demand as toaster ovens and coffee makers only contribute 0.0245 and 0.087 EJ, respectively, while the EIA data does not track energy usage of blow dryers. Other examples, such as clothes dryers, whirlpools, and hot tubs, would be clearly feasible from a technical point of view, but the capital costs to install needed infrastructure might make these applications uneconomical. Technical feasibility and economics of the single thermal end-uses should be investigated, most importantly for those that have the highest thermal energy demand. To reflect the difference between technical and economic feasibility one may move the allocations one bin higher from those used in Figures 3.4 and

3.5. For example, one may want to redistribute space heating to the 60 to 80 °C temperature bin.Further information about the technical and economic requirements for widespread deployment for low enthalpy renewable heat supply options is needed to overcome the anticipated barriers to implementation.

The geographical availability of solar, geothermal, and waste heat energy is an important issue, but exceeds the scope of this study. The quality of the solar resources varies depending on latitude and incident solar irradiation. For geothermal energy, thermal gradients and other geologic conditions are important. However, since a large portion of the thermal demand spectrum occurs at temperatures below 120 °C, lower grade geothermal resources can be effectively utilized over a large region of the United States. The availability of large waste heat resources also varies widely and will require infrastructure changes to make them usable.

In general, the availability of existing or new infrastructure and the scale of the thermal demand lead to different scenarios. A housing community already connected to a district heating or cooling grid presents a different situation than a single home in a rural area. The interruptible nature of solar energy requires storage or backup energy sources. Further research should also investigate the geographical correlation of high industrial thermal energy demands and suitable sites for geothermal plants. Waste incineration plants located close to urban centers could provide both electricity and thermal energy in the form of steam or hot water as has been widely implemented in Sweden and other European countries. Clearly, there are multiple sustainable options for meeting the low-temperature thermal energy demand in the U.S. that would both increase performance and reduce carbon emissions.

Different resources often complement each other suggesting a portfolio approach

to deliver the best solution. City and regional planning should aim at establishing communities whose heat markets are best served with the use of the locally available resources, including the application of cascaded heat systems. Both the thermal structure and location of the heat market relative to the supply have significant impact on the feasibility and economics of any alternative thermal energy sources. The economic attractiveness of using renewable or waste heat thermal energy are not specifically covered in this work. Of course, they depend heavily on prevailing fossil fuel prices which might be affected by CO_2 management policies in the future. A CO_2 tax or cap and trade system would create additional incentives for companies and communities to invest in alternatives. Although time constraints prevented a more detailed analysis of the individual industrial sectors, the general approach and methodology presented in this study could be applied to a specific sector or even specific plant or operation with greater resolution and less coarse graining. The analysis could generate specific thermal energy use temperature distribution data similar to Figures 3.4 and 3.5. The thermal energy use temperature distribution information would then enable to find solutions optimized for the specific industry or plant.

The agricultural and mining industries were not considered in this study because the EIA database does not include these sectors. Other sources indicate that agricultural and mining industries' thermal energy demand appears to be relatively low compared to the manufacturing industries. Nonetheless, some of the most prominent applications of direct geothermal heat, nowadays, are greenhouses and drying processes in agriculture. One may want to undertake a sector specific analysis to determine the potential for the mentioned alternative energy sources in these sectors.

The EIA does not collect data about thermal energy use specifically. Their data had to be carefully analyzed and additional assumptions had to be made to quantify the thermal energy demand. The differences in sector definitions between the AER and the sector specific surveys burdened the analysis of the EIA data. End-use temperature information was collected from various sources. Especially for the industrial sector, information about typical process steam temperature distributions of single industrial branches is rare. Additional analysis that considers this area would be worthwhile.

More research focused on the U.S. thermal energy market and infrastructure requirements is needed to provide a complete picture of opportunities and capital cost requirements for retrofitted and new applications. Research results would enable informed policy and investment decisions to be made for the U.S. as it transforms its energy supply system.

Bibliography

Armstead, H. (1978). *Geothermal Energy*. E. & F. Spon Ltd., London, 1 edition.

Armstead, H. and Tester, J. W. (1987). *Heat Mining*. E. & F.N. Spon, London, New York, first edition.

Bansal, P., Sharma, K., and Islam, S. (2010). Thermal analysis of a new concept in a household clothes tumbler dryer. *Applied Energy*, 87(5):1562–1571.

Bansal, P. K., Braun, J. E., and Groll, E. A. (2001). Improving the energy efficiency of conventional tumbler clothes drying systems. *International Journal of Energy Research*, 25(15):1315–1332.

Bloomquist, R. G. (2003). Geothermal space heating. *Geothermics*, 32(4-6):513–526.

Brown, H. L., Hamel, B. B., Hedman, B. A., Koluch, M., Gajanana, B. C., and Troy, P. (1985). *Energy Analysis of 108 Industrial Processes*. U.S. Department of Energy.

Conde, M. R. (1997). Energy conservation with tumbler drying in laundries. *Applied Thermal Engineering*, 17(12):1163–1172.

Fan, Y., Luo, L., and Souyri, B. (2007). Review of solar sorption refrigeration technologies: Development and applications. *Renewable & Sustainable Energy Reviews*, 11(8):1758–1775.

Fox, D. B., Sutter, D., and Tester, J. W. (2011). The thermal spectrum of low-temperature use in the united states. Technical Report 1, Cornell Energy Institute, Ithaca, NY.

Hreinsson, E. (2007). Deregulation, environmental and planning policy in the icelandic renewable energy system. In *International Conference on Clean Electrical Power*, pages 283–291, Capri, Italy.

International Energy Agency (2007). Renewables for heating and cooling - untapped potential. Technical report, International Energy Agency.

Kalogirou, S. A. (2003). The potential of solar industrial process heat applications. *Applied Energy*, 76(4):337–361.

Líndal, B. (1973). *Industrial and Other Applications of Geothermal Energy*, volume 12 of *Geothermal Energy*. Unesco Paris.

Lund, J. W., Allen, E., Higbee, C., Lienau, P., Phillips, W., and Shreve, J. (1980). Assessment of the geothermal potential within the bpa marketing area. Technical Report DE-AC79-79BP15325, Geo-Heat Utilization Center - Oregon Institute of Technology.

Lund, J. W., Freeston, D. H., and Boyd, T. L. (2005). Direct application of geothermal energy: 2005 worldwide review. *Geothermics*, 34(6):691–727.

Ozalp, N. and Hyman, B. (2007). Allocation of energy inputs among the end-uses in the U.S. petroleum and coal products industry. *Energy*, 32(8):1460–1470.

Philibert, C. (2006). Barriers to technology diffusion: The case of solar thermal technologies. Technical report, International Energy Agency (IEA).

Reistad, G. M. (1975). Analysis of potential nonelectrical applications of geothermal energy and their place in the national economy. Technical report, Lawrence Livermore Laboratory.

Resource Dynamics Corporation (2002). Steam system opportunity assessment for the pulp and paper, chemical manufacturing, and petroleum refining industries. Technical Report DOE/GO-102002-1639, U.S. Department of Energy - Office of Energy Efficiency and Renewable Energy.

Tester, J. W., Drake, E. M., Golay, M. W., Driscoll, M. J., and Peters, W. A. (2005). *Sustainable Energy: Choosing Among Options*. The MIT Press, Cambridge, MA.

U.S. Department of Energy (1995). Energy-efficient water heating. Technical Report DOE/GO-10095-063, U.S. Department of Energy.

U.S. Energy Information Administration (2001).

End-Use Consumption of Electricity. URL: http://www.eia.doe.gov/emeu/recs/recs2001/enduse2001/enduse2001.html.

U.S. Energy Information Administration (2009). Annual energy review 2008. Technical Report DOE/EIA-0384(2008), U.S. Department of Energy (DOE). URL: http://www.eia.doe.gov/emeu/aer/pdf/aer.pdf.

U.S. Energy Information Administration (a). *Residential Energy Consumption Survey (RECS)*. U.S. Departement of Energy (DOE). Online Database URL: http://www.eia.doe.gov/emeu/recs/contents.html.

U.S. Energy Information Administration (b). *Commercial Buildings Energy Consumption Survey (CBECS)*. U.S. Departement of Energy (DOE). Online Database URL: http://www.eia.doe.gov/emeu/cbecs/contents.html.

U.S. Energy Information Administration (c). *Manufacturing Energy Consumption Survey (MECS)*. U.S. Departement of Energy (DOE). Online Database URL: http://www.eia.doe.gov/emeu/mecs/contents.html.

Vannoni, C., Battisti, R., and Drigo, S. (2008). Potential for solar heat in industrial processes. Technical report, University of Rome "La Sapienza".

Wang, R. Z., Ge, T. S., Chen, C. J., Ma, Q., and Xiong, Z. Q. (2009). Solar sorption cooling systems for residential applications: Options and guidelines. *International Journal of Refrigeration*, 32(4):638–660.

Yadav, V. and Moon, C. G. (2008). Modelling and experimentation for the fabric-drying process in domestic dryers. *Applied Energy*, 85(5):404–419.

CHAPTER 4

SUSTAINABLE HEAT FARMING: MODELING EXTRACTION AND RECOVERY IN DISCRETELY FRACTURED GEOTHERMAL RESERVOIRS

4.1 Introduction

The practical utilization of geothermal energy requires extracting or mining the stored thermal energy contained in the Earth's crust, often several kilometers deep. Today, geothermal energy reservoirs exploit naturally occurring hydrothermal aquifers with high permeability and porosity and sufficient quantities of water or steam. Unfortunately, nature does not always provide these ingredients in locations with large temperature gradients. Engineered or Enhanced Geothermal Systems (EGS) offer technologies that can be implemented in areas with low permeable and/or porous rock formations that do not contain enough water and/or steam or lack sufficient interwell connectivity. In most EGS reservoirs, the rock formations must be stimulated, typically using hydraulic pumping resulting in fracturing or hydroshearing to open pre-exiting sealed fractures. In this manner, the reservoir is engineered, creating open fractures and connectivity where liquid water can then flow under increased pressure through the fracture system to extract heat by contacting regions of hot rock.

One important feature of any operating geothermal reservoir system is its anticipated production sustainability over the long term. In simple terms, the heat mining process removes the stored thermal energy faster than it can be supplied by steady state conduction. Although geothermal reservoirs will be depleted during production, with proper management, hydrothermal reservoirs have been shown

to be productive over long periods of time (Axelsson et al., 2005; Bromley et al., 2006). The situation is different for EGS as there is no record of long term field testing and as a result, the renewability of EGS is often questioned. Axelsson et al. (2001) define the renewability of a geothermal resource as the ability to maintain the installed capacity indefinitely. Strictly speaking, to maintain capacity indefinitely, the reservoir would have to operate in steady state where the rate of heat extraction from the reservoir is equal to the rate of recharge of thermal energy coming back into the reservoir from the surrounding bulk rock. Unfortunately, due to practical requirements for production, plant needs, and operation costs, the renewable capacity is often too small for commercial development (Sanyal, 2005). Therefore, considerations about the sustainability of geothermal systems must also include the thermal recovery that occurs during a pause in heat extraction. Megel and Rybach (2000) explore the sustainability of a low temperature (62 °C) hydrothermal doublet used for district heating. By allowing for thermal recovery after a period of thermal extraction, they concluded that because the hydrothermal doublet renews itself on a time scale comparable to extraction, it can be operated in a sustainable manner. Sanyal (2005) defines the sustainable capacity of a geothermal reservoir as the capacity that can be economically maintained over the amortized life time of a power plant. In this study, we attempt to quantify the recovery of the reservoir on an absolute basis in terms of its thermal productivity irrespective of any power plant or surface installation life time considerations. Note that unfortunately, recovery is sometimes used as a synonym to thermal extraction (e.g., (Elsworth, 1989)) in the sense that thermal energy is recovered from the subsurface for use in the surface installation. To avoid confusion, in this study extraction is used to denote the process of removing heat from the subsurface while recovery describes the process of heat from the surrounding hot

rock transferring back into the reservoir after extraction has stopped.

Although exploiting an EGS reservoir at an economically useful rate eventually results in significant local cooling of the reservoir, there are valid reasons to consider such geothermal resource operations as sustainable. Complete recovery of the thermal energy is eventually guaranteed following the discontinuation of all production as heat is conducted and convected to the surrounding hot rock that contains the active reservoir. Even with recovery times of hundreds of years, the resource base is large enough to allow for long term sustainable energy production on a national or global scale (Tester et al., 2006). Additionally, geothermal resources can be considered renewable on time scales of technological/societal systems, 10-100 years, whereas fossil fuel reserves "renew" on geologic time scales of order hundreds of million years (Rybach et al., 2000). Furthermore, displacement of fossil fuel consumption with geothermal or other renewables would reduce environmental pollution and help to preserve hydrocarbons for future generations as raw materials and chemical feedstocks as well as for cleaner and more efficient power applications (Sanyal, 2005).

To guarantee the long term sustainability and renewability of a specific EGS reservoir or field development would require implementing a heat farming strategy. Under this approach, several EGS reservoirs would be used in a rotating manner. When the first reservoir is "depleted" to a point where it is no longer able to satisfy the thermal needs of the surface installation, production would be shifted to a new reservoir. The process would continue until the first reservoir has recovered sufficiently to be restarted or restimulated.

The main objective of this work is to evaluate how effectively model geothermal reservoirs recover following extraction. An analytical and numerical model were

used to characterize the transient thermal hydraulic behavior of a fractured EGS reservoir. The analytical model considers an idealized system with single and multiple parallel isolated fractures embedded in a large body of impermeable rock with uniform properties. In this situation, heat transfer is dominated by transient conduction perpendicular to the fracture surface coupled to convection of heat by the fluid flowing along the fracture. The TOUGH2 numerical code developed at the Lawrence Berkeley National Laboratory (Pruess et al., 1999) was used for modeling multiple parallel fractures with two-dimensional transient heat conduction within the rock to test the assumptions of the analytical model.

Although the parallel multi-fracture system is highly idealized and is impossible to replicate in practice, such a simple model was chosen to capture the basic behavior of a conduction dominated EGS reservoir undergoing alternating phases of extraction and recovery. This behavior is relevant to evaluating the sustainability of EGS and has been virtually ignored by other researchers. Although our model only represents thermal modeling of a very idealized, conduction dominated EGS reservoir, we feel it illustrates the limiting behavior one might expect in practice — therefore providing a conservative evaluation of sustainability. Real EGS reservoirs will, of course, contain nonlinear coupled thermal, hydraulic, mechanical, and chemical (THMC) processes. However, introducing these features into the analytical model would not result in tractable solutions relevant to the main objective of the paper.

Much research has been done in addressing nonlinear and coupled phenomena in EGS reservoirs. Kohl et al. (1995) modeled coupled THM processes in a single fracture using linear thermo-poroelastic effects and a logarithmic closer law and learned that these effects lead to significant long term reduction in impedance of

flow. Willis-Richards and Wallroth (1995) summarized the current EGS modeling at the time and emphasized the importance of accurately capturing the evolution of aperture near the injection and production well, large scale permeability enhancement through means of fracture extension, and heat conduction in the reservoir. Taron and Elsworth (2009) studied THMC coupling effects in a dual porosity media where porosity and permeability change as a result of change of stress and chemical precipitation and dissolution. Their numerical simulations indicate that mechanical effects dominate in the short term (days), while thermal effects are important in the intermediate term (months) and chemical effects are only important in the long term (years). Simulations also reveal that coupling of these effects are needed to explain observed phenomena that parallel reactive transport and geomechanic simulations cannot capture. Ghassemi and Zhou (2011) coupled fracture flow and heat transport to thermo-poroelastic deformation in a discretely fractured reservoir and found the resulting temperature, pressure, stress, and aperture at every time step. Their numerical model revealed that poroelastic effects are dominant at early stages while thermoelastic effects take over at later time and coincide with less leakoff to the far field and significant increase in fracture aperture.

4.2 Analytical Model

A representation of a parallel discretely fractured EGS reservoir, adapted from earlier works by Gringarten et al. (1975) and Wunder and Murphy (1978), is pictured in figure 4.1. For a single fracture model, the fracture spacing x_s goes to infinity. Although realistic reservoirs consist of a network of fractures, a single fracture model adequately captures the essential features of thermal extraction through heat conduction from the rock surrounding the fracture. A single rectangular, ver-

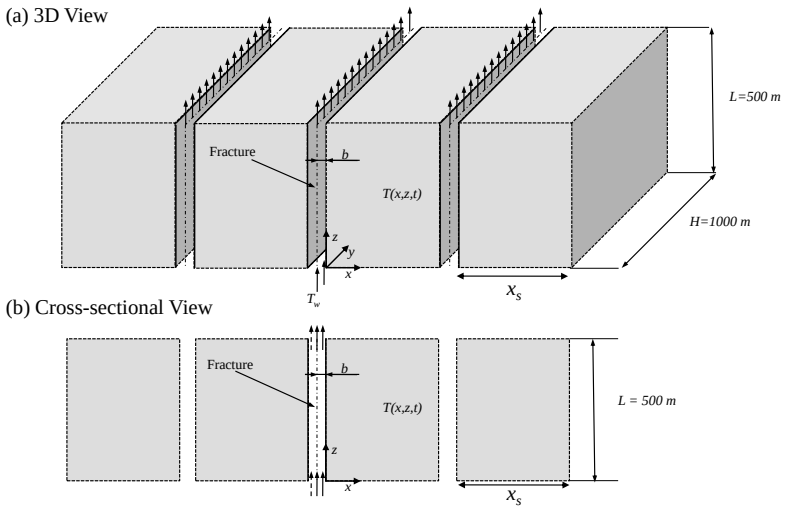

Figure 4.1: Conceptualized multifracture EGS reservoir. (a) Three-dimensional view of the multifracture EGS reservoir. x_s represents the spacing in between fractures. (b) Reduced two-dimensional view.

tical fracture of constant width $2b$ separates two blocks of homogeneous, isotropic, impermeable rock. The orientation of the fracture does not matter because buoyancy driven flow is not considered; however, hydraulic stimulation of a reservoir will usually yield vertically oriented fractures because fractures propagate in the direction normal to the plane of least principal stress. A Cartesian coordinate system has been placed such that $x, z = 0$ coincides with the inlet.

In the isolated fracture model, the rock is assumed to extend in x to $\pm\infty$. Both the rock and the fracture extend to infinity in the y direction. Initially ($t \leq 0$), this semi-infinite system is at a uniform temperature T_r. During the heat extraction phase, water is injected at $x, z = 0$ for all y at a constant temperature T_w and a constant mass flow rate. The water flows parallel through the fracture to the outlet at $x = 0$ and $z = L$. Furthermore, the following assumptions are made:

1. The temperature variation in x in the water is negligible, as the aperture of the fracture is very small compared to the diffusion length in x ($b \ll \sqrt{\alpha t}$). For all z, the water temperature is equal to the rock temperature at $x = 0$. In other words, all heat transfer resistance at the rock/water interface is neglected, which is a reasonable assumption for any practical case given the low thermal conductivity of the rock (Wunder and Murphy, 1978; Ogino et al., 1999).

2. Conduction in the vertical direction, z, in both the fracture and the rock formation is neglected. Because the aperture $2b$ of the fracture is small compared to the fracture extent in the y direction H, such that $2b/H \ll 1$, we can extend the y axis to $\pm\infty$ and ignore the heat transfer in the y direction, effectively reducing the heat transfer problem to two spatial dimensions. Heat transfer occurs only by conduction in the rock in the x direction and forced convection along the z direction in the fracture. Radiative heat transfer is also neglected.

3. No heat flux occurs at the rock/water interface during recovery when no fluid is circulating. This assumption is justified by the small volume, and hence, small overall heat capacity of the fluid filling the fracture compared to the total heat capacity of the rock that has been cooled during the preceding extraction phase.

4. The static fluid pressure in the fracture is set to exceed the vapor pressure of the water by a large enough margin to sustain single phase flow in the fracture. The pressure drop due to viscous forces is small and results in negligible temperature rise.

5. The thermophysical properties of both water and rock are constant and independent of temperature and position.

4.2.1 First Extraction Phase

A one-dimensional differential energy balance within the rock yields

$$\frac{\partial T}{\partial t} - \alpha \frac{\partial^2 T}{\partial x^2} = 0 \tag{4.1}$$

where T is the temperature and α is the rock thermal diffusivity, i.e., the ratio of its thermal conductivity k_r to the product of density ρ_r and specific heat capacity $c_{p,r}$. By applying a steady state energy balance to the water in the fracture over a differential length in z, the boundary condition for the rock/water interface is

$$\left(\rho_w c_{p,w} U b \frac{\partial T}{\partial z} = k_r \frac{\partial T}{\partial x} \right) \Bigg|_{x=0} \tag{4.2}$$

with U representing the flow velocity of the water, b the half width of the fracture, and ρ_w and $c_{p,w}$ the density and specific heat capacity of the water, respectively. With the initial and bulk temperature of the rock specified as T_r and the constant water temperature at the injection position taken as T_w, the additional boundary conditions are

$$T(0, 0, t) = T_w, \quad t > 0, \tag{4.3}$$

$$\lim_{x \to \infty} T(x, z, t) = T_r, \tag{4.4}$$

and the initial condition is

$$T(x, z, t \leq 0) = T_r. \tag{4.5}$$

The analytical solution is given in terms of the dimensionless, normalized temperature Θ and is based on the similarity solution of a classical transient heat transfer problem as presented by Carslaw and Jaeger (1959) and Arpaci (1966):

$$\Theta \equiv \frac{T(x, z, t) - T_w}{T_r - T_w} = \operatorname{erf}\left[\frac{x + \beta z}{2\sqrt{\alpha t}} \right], \tag{4.6}$$

where β is defined as

$$\beta \equiv \frac{2 k_r}{(\dot{m}/A) c_{p,w} L}. \tag{4.7}$$

Here, $\dot{m}/A$ is the mass loading of the fracture where A is defined as the one face area of the fracture and equals HL and L is the length of the fracture parallel to the flow. In terms of a temperature difference with respect to the bulk rock, the temperature profile in the reservoir is equal to

$$u(x,z,t) = u_0 \text{erfc}\left[\frac{x+\beta z}{2\sqrt{\alpha t}}\right], \tag{4.8}$$

where $u \equiv T(x,z,t) - T_r$ and $u_0 = T_w - T_r$. The relationship between u and Θ is thus $\Theta = 1 - u/u_0$. Eq. (4.6) can be evaluated for the temperature at the outlet, $x = 0$ and $z = L$, (for a fracture of length L) and rewritten in a more familiar form as

$$\Theta(0,L,t) = \text{erf}\left[\left(\frac{\dot{m}}{A}\right)^{-1} \frac{1}{c_{p,w}} \sqrt{\frac{k_r \rho_r c_{p,r}}{t}}\right]. \tag{4.9}$$

4.2.2 Validity of 1-D Conduction

The solution for the temperature field in the previous section neglects heat conduction parallel to the fracture. Conventional scaling analysis can be used to compare the order of magnitude of heat conduction in the two directions and to assess the assumption of negligible heat conduction in z. The terms in the governing equation for two-dimensional differential energy balance scale as

$$\frac{\partial^2 T}{\partial x^2} \sim \frac{\Delta T}{\delta_x^2} \quad \text{and} \quad \frac{\partial^2 T}{\partial z^2} \sim \frac{\Delta T}{\delta_z^2}, \tag{4.10}$$

where ΔT, δ_x , and δ_z are the appropriate characteristic quantities for temperature and length in x and z, respectively. Hence, we can define a dimensionless quantity $\mathcal{D}$ as

$$\mathcal{D} \equiv \frac{\text{heat conduction in } z}{\text{heat conduction in } x} = \left(\frac{\delta_x}{\delta_z}\right)^2 \tag{4.11}$$

In order to determine the relative importance of heat conduction in each direction, the characteristic length scales in both the x and z direction must be determined. δ_x and δ_z can be considered to be the penetration lengths of the thermal cooling front along the x and z axis, respectively. Defining the position of the thermal cooling front to be the value of x or z at which Θ equals an arbitrary value, the thermal penetration lengths are

$$\delta_x \sim \sqrt{\alpha t} \quad \text{and} \quad \delta_z \sim \frac{1}{\beta}\sqrt{\alpha t}. \tag{4.12}$$

Eq. (4.12) takes the typical form of penetration lengths of conduction dominated problems. From Eq. (4.12), our dimensionless quantity scales as follows

$$\mathcal{D} \sim \beta^2 \propto \left(\frac{A}{\dot{m}}\right)^2. \tag{4.13}$$

For $\dot{m} = 70$ kg/s, single face fracture area HL of 500,000 m^2 and typical thermophysical properties of water and rock, $\beta = 0.02$ and $\beta^2 = 4 \times 10^{-4}$. Thus, for typical flow rates, heat conduction in x is three orders of magnitude greater than in z, validating the approximation of neglecting heat conduction in z. The factor β^2 acts as a perturbation parameter in the full form of Eq. (4.1) and the solution presented in Eq. (4.8) is the $O(1)$ solution. Because there is no convective transport of heat in the z direction below the inlet and above the outlet, a boundary layer (in z) of thickness $\varepsilon \sim \sqrt{\alpha t}$ is present in these regions. As a result of the boundary layers, Eq. (4.8) solution is most accurate for z values between ε and $L - \varepsilon$.

4.2.3 First Recovery Phase

An approach using Green's functions was used to describe the temperature in the single fracture model analytically. Green's functions provide a systematic way to

solve linear partial differential equations with inhomogeneous terms. We consider a linear heat sink along the fracture, i.e., for all z at $x = 0$. The line sink represents the heat extraction by the flowing fluid in the fracture during the extraction phase and varies in both z and t. The energy balance including the heat sink becomes

$$\frac{\partial T}{\partial t} - \alpha \frac{\partial^2 T}{\partial x^2} = \frac{q(z,t)\delta(x)}{\rho_r c_{p,r}} \tag{4.14}$$

where $q(z,t)$ is the net heat flux from the fracture to the rock (which is typically negative) and $\delta(x)$ is the Dirac delta function. As mentioned before, the temperature at $x = 0$ is valid for both rock and water at the interface. We are now solving the problem in unbounded space with the initial condition for Eq. (4.14) again represented by Eq. (4.4) and two boundary conditions that the temperature goes to T_r at $x = \pm\infty$.

During the extraction phase, heat is conducted from the hot regions of rock into the moving fluid in the fracture at $x = 0$. The flux can be determined based on the temperature profile for the extraction in Eq. (4.6). No heat flux occurs at the rock/water interface during the recovery phase and thus $q(z,t)$ is identically zero. With t_1 being the time at the end of the extraction phase, we get

$$q(z,t) = \begin{cases} -2k_r \frac{\partial T}{\partial x}\big|_{x=0}, & 0 < t \leq t_1 \\ 0, & t > t_1. \end{cases} \tag{4.15}$$

The temperature solution during the first extraction, Eq. (4.8), is used to evaluate the flux in Eq. (4.15). The factor of two takes into account the two faces of the fracture. Eq. (4.14) was solved using the variable transformation u and the following Green's function (Duffy, 2001)

$$G(x - x', t - t') = \frac{H(t - t')}{\sqrt{4\pi\alpha(t - t')}} \exp\left[-\frac{(x - x')^2}{4\alpha(t - t')}\right], \tag{4.16}$$

where $H(t - t')$ is the Heaviside step function, which is equal to 1 for positive arguments and equal to 0 for negative arguments. The variable transformation u

results in homogeneous boundary and initial conditions and simplifies obtaining a solution. The transformations of Eq. (4.14) and its boundary and initial conditions are

$$\frac{\partial u}{\partial t} - \alpha \frac{\partial^2 u}{\partial t^2} = \frac{q(z,t)\delta(x)}{\rho_r c_{p,r}}, \tag{4.17}$$

$$\lim_{x \to \pm\infty} u(x,z,t) = 0, \tag{4.18}$$

and

$$u(x,z,t \leq 0) = 0. \tag{4.19}$$

The appropriate Green's function for the domain of $x \in \mathbb{R}$ and $t \in \mathbb{R}_0^+$ is shown in Eq. (4.16). Following the common approach for applying Green's functions, the solution to the PDE in Eq (4.17) is the integral

$$u(x,z,t) = \int_0^\infty \int_0^\infty G(x-x', t-t') \frac{q(x',z,t')\delta(x')}{\rho_r c_{p,r}} \mathrm{d}x' \mathrm{d}t'. \tag{4.20}$$

The $\mathrm{d}x'$ integral can be evaluated by applying the sifting property of the Dirac delta function and the upper integration boundary for t' can be reduced from $t' = \infty$ to $t = t$ because of the step function. The result is

$$u(x,z,t) = \int_0^t \frac{1}{\sqrt{4\pi\alpha(t-t')}} \exp\left[-\frac{x^2}{4\alpha(t-t')}\right] \frac{q(z,t')}{\rho_r c_{p,r}} \mathrm{d}t'. \tag{4.21}$$

Because the heat flux at the rock/water interface is piecewise continuous with respect to time, as seen in Eq. (4.15), Eq. (4.21) is best broken into two components, an integral from 0 to t_1 and a second integral from t_1 to t. The integral from t_1 to t is zero because there is no heat flux at the rock/water interface during recovery. The heat flux $q(z,t)$ during the extraction phase can be determined by taking the derivative of the temperature profile for the extraction in Eq. (4.6). The result is

$$q(z,t) = \frac{2k_r u_0}{\sqrt{\pi\alpha t}} \exp\left[-\frac{\beta^2 z^2}{4\alpha t}\right], \quad 0 < t \leq t_1. \tag{4.22}$$

Substituting the heat flux shown in Eq. (4.22) into Eq. (4.21), we get the integral solution for recovery,

$$u(x,z,t) = \frac{u_0}{\pi}\int_0^{t_1} \frac{1}{\sqrt{t'}\sqrt{t-t'}} \exp\left[-\frac{1}{4\alpha}\left\{\frac{x^2}{(t-t')} + \frac{\beta^2 z^2}{t'}\right\}\right] \mathrm{d}t'. \tag{4.23}$$

The integral in Eq. (4.23) has a closed form solution at the injection point $x, z = 0$ during the recovery ($t > t_1$):

$$\Theta(0,0,t) = \frac{2}{\pi}\tan^{-1}\left(\sqrt{\frac{t}{t_1}-1}\right). \tag{4.24}$$

The solution in Eq. (4.24) was derived earlier by Wunder and Murphy (1978).

Eq. (4.23) can be rewritten as

$$\frac{u(0,z,t)}{u_0} = \frac{1}{\pi}\int_0^{t_1} \frac{1}{\sqrt{t'}\sqrt{t}} \frac{1}{\sqrt{1-\frac{t'}{t}}} \exp\left[-\frac{\beta^2 z^2}{4\alpha t'}\right] \mathrm{d}t'. \tag{4.25}$$

Using the Taylor series expansion for the term $\sqrt{1-t'/t}$ about 0, Eq. (4.25) can be simplified to

$$\frac{u(0,z,t)}{u_0} = \frac{1}{\pi}\int_0^{t_1} \frac{1}{t^{n+\frac{1}{2}}} \sum_{n=0}^{\infty} \binom{n-\frac{1}{2}}{n} t'^{n-\frac{1}{2}} \exp\left[-\frac{\beta^2 z^2}{4\alpha t'}\right] \mathrm{d}t'. \tag{4.26}$$

The integral in each term of the summation in Eq. (4.26) can be expressed as an incomplete gamma function,

$$\frac{u(0,z,t)}{u_0} = \frac{1}{\pi}\sum_{n=0}^{\infty} \binom{n-\frac{1}{2}}{n} \left(\frac{t_1}{t}\right)^{n+\frac{1}{2}} \xi_r^{2n+1}(x,z,t_1)\Gamma\left(-\left\{n+\frac{1}{2}\right\}, \xi_r^2\right) \tag{4.27}$$

with the incomplete gamma function defined as

$$\Gamma(a,s) = \int_s^{\infty} \tau^{a-1} e^{-\tau} \mathrm{d}\tau. \tag{4.28}$$

Applying the substitution $\tau = x^2$, the incomplete gamma function can be evaluated using the following integral found in Gradshteyn and Ryzhik (2007),

$$\int_u^{\infty} \frac{e^{-p^2x^2}}{x^{2n}}\mathrm{d}x = \frac{(-1)^n 2^{n-1} p^{2n-1}\sqrt{\pi}}{(2n-1)!!}\mathrm{erfc}\,(pu) + \frac{e^{-p^2u^2}}{2u^{2n-1}} \sum_{k=0}^{n-1} \frac{(-1)^k 2^{k+1}(pu)^{2k}}{(2n-1)(2n-3)\ldots(2n-2k-1)}, \quad p > 0 \tag{4.29}$$

and substituted in Eq. (4.27) to yield an infinite series solution given by

$$\frac{u(0,z,t)}{u_0} = \frac{1}{\pi}\sum_{n=0}^{\infty}\binom{n-\frac{1}{2}}{n}\left(\frac{t_1}{t}\right)^{n+\frac{1}{2}}\left[\xi_r^{2n+1}\frac{(-1)^{n+1}2^{n+1}\sqrt{\pi}}{(2n+1)!!}\mathrm{erfc}\left(\xi_r\right) + \exp\left(-\xi_r^2\right)\sum_{k=0}^{n}\frac{(-1)^k 2^{k+1}\xi_r^{2k}}{(2n+1)(2n-1)\ldots(2n-2k+1)}\right] \tag{4.30}$$

where $\xi_r = \beta z/(2\sqrt{\alpha t_1})$ and $\binom{n-\frac{1}{2}}{n}$ is a binomial coefficient. Eq. (4.30) only applies to the recovery phase and the rock/fracture interface, i.e., for $t > t_1$ and $x = 0$. When the recovery time becomes large compared to the extraction time, $t/t_1 \gg 1$, the heat sink due to the extraction fluid resembles an impulsive point line sink at $t = 0$ and $x = 0$. The first term of the infinite series in Eq. (4.30) is

$$u^{(0)}(0,z,t) = \frac{2}{\pi}u_0\left(\frac{t_1}{t}\right)^{\frac{1}{2}}\left[\exp(-\xi_r^2) - \sqrt{\pi}\xi_r\mathrm{erfc}(\xi_r)\right]. \tag{4.31}$$

This is equivalent to an impulsive point source at $t = 0$ and $x = 0$ of magnitude

$$Q(z) = \int_0^{t_1} q(z,t)\mathrm{d}t = 4k_r u_0\left(\frac{t_1}{\pi\alpha}\right)^{1/2}\left[\exp(-\xi_r^2) - \sqrt{\pi}\xi_r\mathrm{erfc}(\xi_r)\right], \tag{4.32}$$

as Eq. (4.31) can be rewritten as

$$u^{(0)}(0,z,t) = \frac{Q(z)}{2\sqrt{\pi k_r\rho_r c_{p,r}}}\frac{1}{\sqrt{t}}, \tag{4.33}$$

where $Q(z)$ is the total heat extracted during the extraction phase at point z of the fracture.

If the recovery time is much larger than the period of the first extraction, then the temperature field depends only on the total heat extracted and not the temporal variations in the rate of extraction. Eq. (4.31) indicates that the temperature at the surface of the fracture will recover arbitrarily close to the initial rock temperature after a sufficient period of time. However, it also indicates that the deviation from the initial rock temperature retains a signature of the total heat extracted that is never forgotten. If multiple extraction phases were conducted, the long

time recovery temperature would depend on the total heat extracted in all the extraction phases.

4.2.4 Second Extraction Phase

For a geothermal reservoir undergoing three operational phases: extraction, recovery, and extraction, the heat flux at the rock/water interface ($x = 0$) is

$$q(z,t) = \begin{cases} -2k_r \frac{\partial u}{\partial x}\big|_{x=0}, & 0 < t \leq t_1 \\ 0, & t_1 < t \leq t_2 \\ -2k_r \frac{\partial u}{\partial x}\big|_{x=0}, & t > t_2, \end{cases} \tag{4.34}$$

where t_2 is the end of the first recovery phase. Using the Green's function and applying the sifting property of the Dirac delta function and the Heaviside step function, the temperature field is

$$u_3(x,z,t) = \int_0^t \frac{\exp\left[-\frac{x^2}{4\alpha(t-t')}\right]}{\sqrt{4\pi\alpha(t-t')}} \frac{q(z,t')}{\rho_r c_{p,r}} \mathrm{d}t'. \tag{4.35}$$

The subscript 3 in u_3 represents the temperature field during second extraction. Combining Eq. (4.34) with Eq. (4.35) yields

$$u_3(x,z,t) = \int_0^{t_1} \frac{\exp\left[-\frac{x^2}{4\alpha(t-t')}\right]}{\sqrt{4\pi\alpha(t-t')}} \frac{q(z,t')}{\rho_r c_{p,r}} \mathrm{d}t' + \int_{t_2}^t \frac{\exp\left[-\frac{x^2}{4\alpha(t-t')}\right]}{\sqrt{4\pi\alpha(t-t')}} \frac{q(z,t')}{\rho_r c_{p,r}} \mathrm{d}t'. \tag{4.36}$$

Since the first integral represents the integral solution for recovery with a duration of first extraction t_1, Eq. (4.36) can be rewritten as

$$u_3(x,z,t) = u_2(x,z,t;t_1) + \int_{t_2}^t \frac{\exp\left[-\frac{x^2}{4\alpha(t-t')}\right]}{\sqrt{4\pi\alpha(t-t')}} \frac{q(z,t')}{\rho_r c_{p,r}} \mathrm{d}t'. \tag{4.37}$$

At $x = 0$,

$$\left(k_r \frac{\partial u_3}{\partial x} = \rho_w c_{p,w} U b \frac{\partial u_3}{\partial z}\right)\Big|_{x=0} \tag{4.38}$$

which results in

$$u_3(x,z,t) = u_2(x,z,t;t_1) - \frac{1}{\beta}\sqrt{\frac{\alpha}{\pi}}\int_{t_2}^{t}\frac{\exp\left[-\frac{x^2}{4\alpha(t-t')}\right]}{\sqrt{(t-t')}}\frac{\partial u_3}{\partial z}(0,z,t')\mathrm{d}t'. \tag{4.39}$$

By only considering points along the fracture ($x = 0$), Eq. (4.39) simplifies to

$$u_3(0,z,t) = u_2(0,z,t;t_1) - \frac{1}{\beta}\sqrt{\frac{\alpha}{\pi}}\int_{t_2}^{t}\frac{1}{\sqrt{(t-t')}}\frac{\partial u_3}{\partial z}(0,z,t')\mathrm{d}t'. \tag{4.40}$$

Eq. (4.40) can be solved by applying Laplace transforms. The solution for $u_3(0,z,t)$ becomes

$$\begin{aligned} u_3(0,z,t) &= u_1(0,z,t''') + u_2(0,z,t;t_1) \\ &\quad + \frac{\beta}{\sqrt{\pi\alpha}}\int_0^{t'''}\int_0^{z}\left(\xi^2 - \frac{1}{2}\right)\frac{\exp\left(-\xi^2\right)}{\tau^{3/2}}u_2(0,z',t-\tau)\mathrm{d}z'\mathrm{d}\tau \end{aligned} \tag{4.41}$$

with

$$\xi = \frac{\beta(z-z')}{2\sqrt{\alpha\tau}} \tag{4.42}$$

and

$$t''' = t - t_2. \tag{4.43}$$

u_1 represents the first extraction phase given by Eq (4.8). The result indicates that the temperature during the second extraction is influenced by a delayed "fresh" extraction (i.e., a new extraction starting at $t''' = 0$ that proceeds as if no previous heat transfer had occurred), a continuing recovery, plus a convolution term involving the recovery temperature field. The convolution term represents the effect on the temperature field caused by the change in heat extraction rates during second extraction because the temperature field was not fully recovered before the extraction began. Thus, if the reservoir fully recovered, both the convolution term and u_2 would go to zero and Eq. (4.40) would reduce to Eq. (4.8), the solution for the first extraction.

4.2.5 Subsequent Extraction and Recovery Phases

One can follow a procedure analogous to that used in deriving the first recovery and second extraction phase to determine the temperature field for any extraction and recovery phase. For subsequent extractions, by using the Green's function, the appropriate piecewise heat flux $q(z,t)$ akin to Eq. (4.15) and (4.34), and by recognizing integral forms of the temperature field of previous operational phases, one arrives at

$$u_n(0,z,t) = u_{n-1}(0,z,t) - \frac{1}{\beta}\sqrt{\frac{\alpha}{\pi}}\int_{t_{n-1}}^{t} \frac{1}{\sqrt{(t-t')}}\frac{\partial u_n}{\partial z}(0,z,t')\mathrm{d}t'. \tag{4.44}$$

Odd values of n represent extraction phases while even values of n represent recovery phases. The parameter t_n represents the time at the end of the n^{th} phase. As was done for the second extraction, Laplace transforms are used to solve Eq. (4.44). The result is

$$\begin{aligned} u_n(0,z,t) &= u_1(0,z,t^{(n)}) + u_{n-1}(0,z,t) \\ &\quad + \frac{\beta}{\sqrt{\pi\alpha}}\int_0^{t^{(n)}}\int_0^{z}\left(\xi^2 - \frac{1}{2}\right)\frac{\exp\left(-\xi^2\right)}{\tau^{3/2}}u_{n-1}(0,z',t-\tau)\mathrm{d}z'\mathrm{d}\tau. \end{aligned} \tag{4.45}$$

where $t^{(n)} = t - t_{n-1}$ and $t^{(n)}$ represents a reset time such that time zero occurs at the beginning of the n^{th} operational phase. Similar to extraction, upon using Green's functions and recognizing integral forms, the recovery temperature field can be represented as

$$u_n(0,z,t) = u_{n-2}(0,z,t) - \frac{1}{\beta}\sqrt{\frac{\alpha}{\pi}}\int_{t_{n-2}}^{t_{n-1}} \frac{1}{\sqrt{(t-t')}}\frac{\partial u_{n-1}}{\partial z}(0,z,t')\mathrm{d}t'. \tag{4.46}$$

Here, the recovery temperature field is an explicit integral involving the previous extraction phase instead of a differential equation. By substituting Eq. (4.45) into Eq. (4.46) and recognizing the integral form of first recovery shown in Eq. (4.23),

the temperature for any recovery phase is

$$u_n(0,z,t) = u_2(0,z,t^{(n-1)};\Delta t_n) + u_{n-2}(0,z,t) + \frac{\beta}{\sqrt{\pi\alpha}}\int_0^{\Delta t_n}\frac{1}{\sqrt{t^{(n-1)}-t^{(n-2)}}} \times\left[\frac{\partial u_{n-2}}{\partial z}(0,z,t^{(n-1)}+t_{n-1}) + \frac{\partial F_n}{\partial z}(0,z,t^{(n-1)})\right]\mathrm{d}t^{(n-2)} \tag{4.47}$$

where

$$F_n(z,t^{(n)}) = \frac{\beta}{\sqrt{\pi\alpha}}\int_0^{t^{(n)}}\int_0^z\left(\xi^2-\frac{1}{2}\right)\frac{\exp\left(-\xi^2\right)}{\tau^{3/2}}u_{n-2}(0,z',t-\tau)\mathrm{d}z'\mathrm{d}\tau, \tag{4.48}$$

where Δt_n represents the duration of recovery and is equal to $t_n - t_{n-1}$.

The expression for the temperature along the fracture for subsequent recovery/extraction phases indicates that the temperature during extraction or recovery is dependent on a delayed fresh extraction or recovery plus the continuation of the previous recovery phase and finally a convolution integral involving the previous recovery phase. Although Eq. (4.47) gives us a more physical understanding, Eq. (4.46) is easier to implement numerically.

4.2.6 Multifracture EGS reservoir

To extend the analysis to a multifracture reservoir, one can imagine an infinite series of rectangular fractures evenly spaced by a distance x_s. Because of the resulting symmetry, the heat flux at $x = x_s/2$ (the midplane between two fractures) is equal to zero. Under this formulation, the boundary condition given by Eq. (4.4) is modified to $\partial T/\partial x = 0$ at $x = x_s/2$ and the temperature field can be solved via Laplace transforms. The solution for a multifracture system in Laplace space is

$$\bar{u}(x,z,s) = \frac{u_0}{s}\exp\left[-r\beta\tanh\left(\frac{1}{2}rx_s\right)z\right]\left\{\cosh(rx)+\tanh\left(\frac{1}{2}rx_s\right)\sinh(rx)\right\}, \tag{4.49}$$

where $r = \sqrt{s/\alpha}$. For the temperature at the outlet, the result becomes

$$\bar{u}(0, z, s) = \frac{u_0}{s} \exp\left[-r\beta \tanh\left(\frac{1}{2} r x_s\right) z\right]. \tag{4.50}$$

As the spacing between fractures, x_s, goes to infinity, the tanh term goes to 1, as expected, and the resulting temperature field resembles that of a single fracture, given by Eq. (4.8). Because δ_x determines the order of the extent of heat transfer that has taken place in the reservoir, the single fracture solution is valid when $\delta_x/x_s \ll 1$. We can conjecture that when $\delta_x/x_s \sim 1$, the solution for the single fracture should begin to deviate from the real solution as the fractures start to thermally interact with each other. Since an analytical inverse Laplace transform to Eq. (4.50) does not exist, we will rely on the numerical solution described below to characterize the conditions under which the heat extracted from a fracture is affected by interference by neighboring fractures.

4.2.7 Alternate Strategies*

Concurrent use of reservoirs provides additional operating strategies to manage geothermal reservoirs. One such strategy to promote recovery is to produce excess fluid from a second reservoir and to divert the excess production into a recovering reservoir. Thus, the recovering reservoir will not only have recovery via conduction from the bulk rock, which is slow, but will experience convection along the fracture, where the thermal depletion is concentrated. The solution for the temperature field resembles Eq. (4.40) and is

$$u_2^*(0, z, t) = u_0^* \mathrm{erfc}\left[\frac{\beta^* z}{2\sqrt{\alpha t''}}\right] + u_2(0, z, t) + \frac{\beta^*}{\sqrt{\pi\alpha}} \int_0^{t''} \int_0^z \left(\xi^2 - \frac{1}{2}\right) \frac{\exp\left(-\xi^2\right)}{\tau^{3/2}} u_2(0, z', t-\tau) \mathrm{d}z' \mathrm{d}\tau. \tag{4.51}$$

*This work did not appear in Fox et al. (2013) and has not been published

The asterisk identifies new values of the parameters under "reverse" extraction and $t'' \equiv t - t_1$. Eq. (4.51) assumes that the water temperature at the inlet is constant, but if we relax such assumption and let the temperature of the injected fluid follows that of Eq. (4.8), then the argument of the complimentary error function becomes $(\beta^* z + \beta' L)/(2\sqrt{\alpha t''})$, where the prime on β denotes the value of β under the flow conditions of the second reservoir.

Another operational strategy is to deploy a depleted reservoir as a preheater, which will delay thermal breakthrough of the second reservoir. Under the preheater strategy, the temperature field for second reservoir undergoing extraction in Laplace space is

$$\bar{u}(x, z, s) = \bar{u}_0(s) \exp\left[-\sqrt{\frac{s}{\alpha}}\,(x + \beta z)\right]. \tag{4.52}$$

Since the product of two function in Laplace space is the convolution of the two functions in real space,

$$u(x, z, t) = \frac{1}{2\sqrt{\alpha\pi}} \int_0^t u_0(t - \tau) \frac{(x + \beta z)}{\tau^{3/2}} \exp\left[-\frac{(x + \beta z)^2}{4\alpha\tau}\right] \, \mathrm{d}\tau, \tag{4.53}$$

where u_0 refers to the variable inlet temperature.

4.3 TOUGH2 Numerical Model

The TOUGH2 reservoir code developed at the Lawrence Berkeley National Laboratory (Pruess et al., 1999) was used for the numerical simulations of the extraction and recovery operational phases. TOUGH2 is a general purpose numerical simulation program for multidimensional non-isothermal flows of multiphase, multicomponent fluid mixtures in fractured and porous media. It employs an integral finite difference method (IFDM) in discretizing the medium, which has the advantage of

irregular discretization in multiple dimensions. Time is discretized fully implicitly as a first-order backward finite difference and fluxes are computed using upstream weighting (Pruess et al., 1999).

The computational cell in TOUGH2 was 1000 m in the x direction, 1600 m in the z direction, and 1 m in the y direction. Identical to the analytical solution, there is no heat or mass flow in the y direction and as a result, the dimension in y is arbitrary. Only half of the reservoir needs to be simulated because of symmetry along the yz plane. As a result, the total flow rate used in the simulation needs to be scaled down by a factor of $2H$. Hence, for our reservoir geometry, to represent a total flow of 70 kg/s into a fracture that is 1000 m long in y, a flow of 0.035 kg/s is used. Any confusion regarding the length of the y domain can be eliminated by using $\dot{m}/A$ where $\dot{m}$ refers to the total flow into the system spanning $\pm x$. The mesh is adequately sized with respect to x and z as the thermal penetration length δ_x in typically crystalline rocks with $\alpha \approx 10^{-6}$ m^2/s will only reach 1000 m after 10,000 years.

Figure 4.2 shows the mesh implemented. In order to simulate systems with single and multiple parallel fractures, a modular mesh was created. The mesh is called modular because by changing material properties of certain grid blocks, several different fracture scenarios can be simulated with only one mesh. The fractures are contained within a 200 m wide in x by 500 m long in z by 1 m in y simulation volume as seen in Figure 4.3. The fractures are 0.06 m wide. Because the mesh needs to be refined in regions of higher temperature gradients, such as near the fracture, a periodic logarithmic mesh spacing in x was used. For every 50 m in x, there are 27 grid blocks between each fracture which logarithmically increase from 0.06 m and then logarithmically decrease at the midpoint so that the

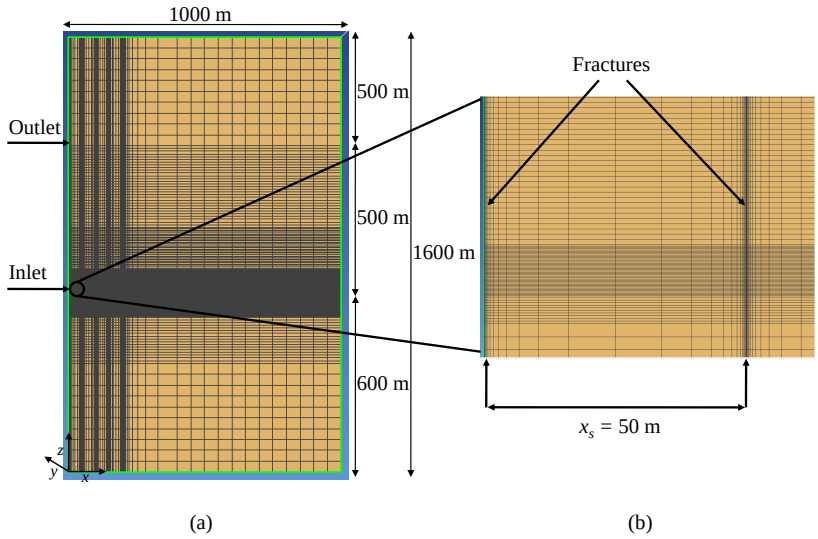

Figure 4.2: TOUGH2 mesh used for single and multifracture simulations. (a) Overview of the mesh with dimensions and inlet and outlet position identified. (b) Close-up to show the fractures in the mesh.

last grid block in the period before the next fracture is back at 0.06 m. Given the fracture spacing of 50 m, a total of 4.5 full fractures can be simulated. The half fracture results from the plane of symmetry cutting through the central fracture. Because of symmetry, the model can simulate nine full fractures in a reservoir. The mesh has 237 grid blocks in the z direction whose length varies as a step function. For example, near the inlet there are 40 0.250 m thick grid blocks followed by another 40 grid blocks but that are 1 m thick. Because heat and mass do not flow in the y direction, the mesh in y was not refined and only consists of one block. As seen in Figure 4.3, bulk rock was added above the production and below the injection well of the fracture to account for heat conduction beyond the fracture length. The bulk rock above and below the production and injection well will have the most effect in the recovery phases because conduction in z brings heat from the additional rock mass in the system to the thermally depleted zone.

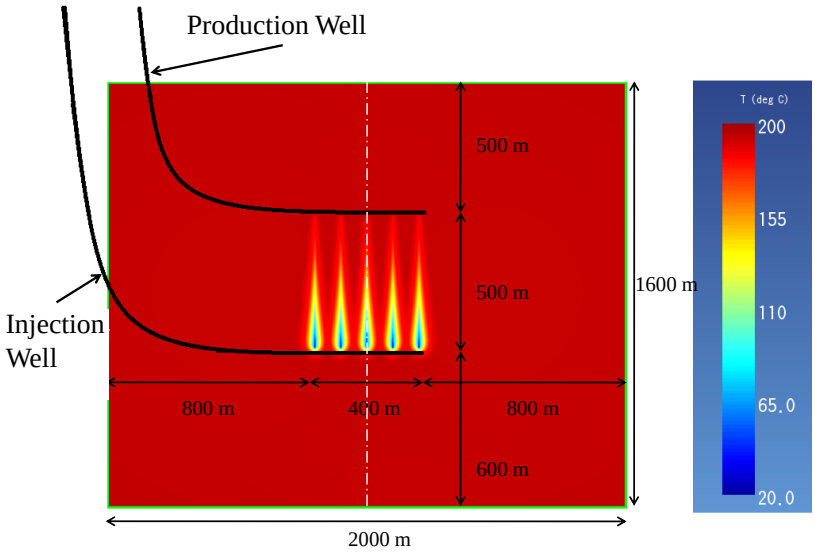

Figure 4.3: Dimensions of the simulation space used in TOUGH2. The dashed line down the middle indicates symmetry and thus only one side of the reservoir needs to be simulated. The presented reservoir has 5 fractures and has already undergone 10 years of extraction.

The mesh is primarily made up by two different materials named "rock" and "fracture". To model a scenario with fewer fractures, the material properties of the appropriate grid blocks that were designated as the fracture material are changed to the rock material. The permeability and porosity of the rock material was set to zero. Thus, no fluid can leave or enter the fracture grid blocks because the grid blocks adjacent to the fractures are designated as rock. The porosity of the fracture material was set to one to model the flow in an open fracture while the permeability was arbitrarily set to 10^{-9} m^2 to minimize the pressure drop. By keeping the pressure drop small with a relatively large permeability, single phase flow in the fracture will be ensured. The initial temperature and pressure are 200 °C and 20 bar.

The injection cell is represented by an extra cell superimposed over the first grid block of each fracture which supplies a specified source of fluid mass per unit

time at the injection temperature. The production cell is located 500 m further down from each injection cell. The cell directly above the production cell in z acts as a sink of mass and has zero thermal conductivity. Any mass and convective heat flow that enters this cell is removed from the system.

To model the recovery phase, the mass flow was simply set to zero and the initial conditions were set to the final field value of the previous extraction phase. The values of the thermophysical properties of the rock in the simulations are $\rho_r = 2700\,\mathrm{kg/m^3}$, $c_{p,r} = 1050\,\mathrm{J/(kg\,^\circ C)}$, $k_r = 2.9\,\mathrm{W/(m\,^\circ C)}$, $\alpha = 1.02\times10^{-6}\,\mathrm{m^2/s}$. TOUGH2 uses an equation of state to determine the thermophysical properties of water and as a consequence, will vary with temperature and pressure. This is in contrast with the analytical equations which assume constant thermophysical properties. Nonetheless, the only property of water of importance in comparing numerical and analytical results is the heat capacity which varies from 4493 J/(kg °C) at 200 °C to 4178 J/(kg °C) at 20 °C, all at 20 bar.

During extraction, it is to be expected that the temperature of the rock adjacent to the inlet $x, z = 0$ will quickly be reduced to the inlet temperature so that $\Theta = 0$. Figure 4.4 shows, that the temperature simulated with TOUGH2 at $x, z = 0$ remains at a non-zero value for an extended period of time. We found that this behavior was due to the difficulty of resolving the rapidly varying temperature field in the vicinity of the inlet. In particular, the deviation of the numerical from the analytical solution was found to scale as $\sqrt{\Delta z}$ when the grid spacing Δz near the inlet was reduced. By applying a fit of the form $\Theta(\Delta z, t) = \Theta(0, t) + a\sqrt{\Delta z}$ for $\Delta z = 0.250, 0.125, 0.0625$ m, and extrapolating the value of Θ at the inlet for an infinitely small grid, Θ was found to be as small as 10^{-3} after less than a month. The extrapolated temperature profile at the inlet is plotted as the black line in

Figure 4.4. At higher flow rates such as the value $\dot{m}/A = 4.8 \times 10^{-5}$ kg/(m^{2}s) presented in Figure 4.6, the convective heat transfer is strong enough so that the simulated inlet temperature decays to a very small value even without refining the grid.

4.4 Results and Discussions

4.4.1 Single Fracture Simulations

The single fracture simulations were first run with a flow rate of $\dot{m}/A = 1.6 \times 10^{-5}$ kg/(m^{2}s). The flow rate was chosen so that the thermal front remains within the reservoir so that the temperature varies within the fracture during much of the extraction phase. Figure 4.4 compares the numerical and analytical results for the normalized temperature Θ during a 30 year extraction period at 4 different positions along the fracture. Note that the simulated fluid pressure does not vary more than 10% from the initial condition, as intended in the problem formulation. In general, the numerical results show somewhat less thermal drawdown than the analytical model with the largest deviation occurring at positions near the inlet. The deviation is a result of two-dimensional conduction in TOUGH2. Dimensional effects on the rate of thermal drawdown have also been observed by Kolditz (1995) and Cheng et al. (2001) in which increased dimensions led to less drawdown.

Note that the analytical solutions only considers one-dimensional heat conduction and the error as a result of two-dimensional conduction scales as β^2. Using a flow rate that is three times higher, $\dot{m}/A = 4.8 \times 10^{-5}$ kg/(m^{2}s), β^2 is reduced by a factor of nine and the deviation between the analytical and numerical results

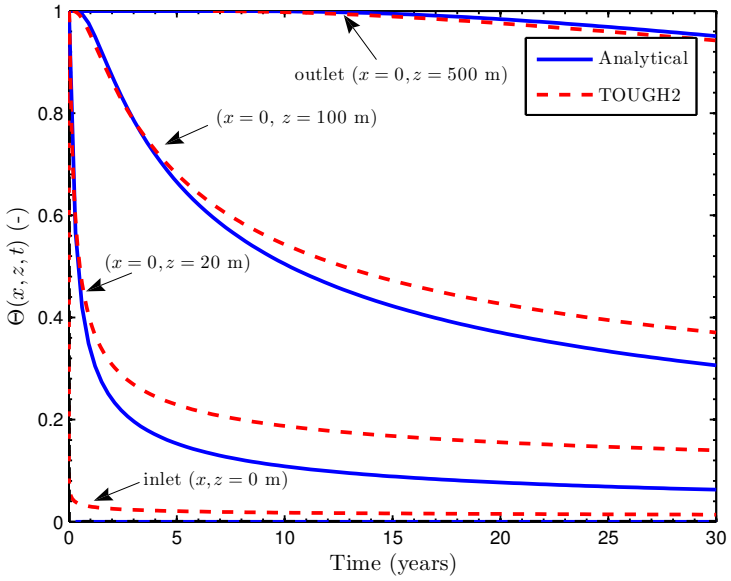

Figure 4.4: First extraction TOUGH2 numerical results compared to Eq. (4.6) at four different positions along the fracture for a 30 year extraction period and a mass loading of $\dot{m}/A = 1.6 \times 10^{-5}$ kg/(m^{2}s). The black dashed line represents the mesh convergence fit as $\Delta z \to 0$

should be minimized. Figure 4.5 demonstrates the effect of β^2 and confirms the expectation based on the scaling analysis. As before, the temperature from the simulation results are higher in the simulations. The remaining two-dimensional conduction at small β may result primarily from conduction from the bulk rock below the fracture. Indeed, we found that setting the thermal conductivity of a row of grid blocks below the injection points to zero caused the simulation results to nearly coincide with the analytical solution. The agreement between the simulation and analytical results signifies that in a real reservoir, heat conduction parallel to the fracture is negligible compared to the heat transfer perpendicular to the fracture.

Figure 4.6 shows the first recovery simulation results compared with those obtained from Eq. (4.30). As expected, the bulk rock above the outlet has enhanced

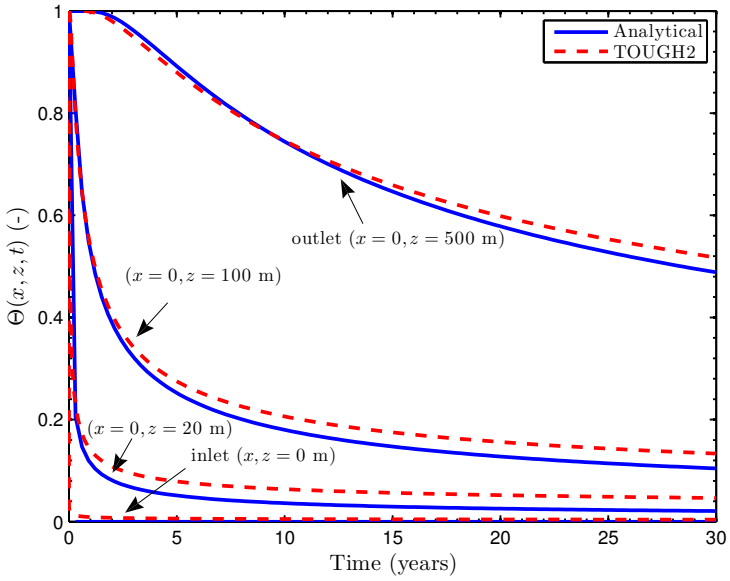

Figure 4.5: First extraction TOUGH2 numerical results compared to Eq. (4.6) at four different positions along the fracture for a 30 year extraction period and an area normalized flow rate of $\dot{m}/A = 4.8 \times 10^{-5}$ kg/(m^{2}s).

recovery. During extraction, forced convection in the fracture kept the ratio of conduction in z to conduction in x small. The convective heat transport rate along the fracture was balanced by the conductive heat transfer rate from the rock into the fracture in the x direction. During recovery, the forced convection is absent. Conduction in z would be expected to have less of an effect in the middle of the fracture where the variation of temperature with z is smaller than near the inlet and outlet and indeed the deviation of the numerical results from the analytical model is smaller at intermediate z in Figure 4.6. As was discussed previously with respect to the analytical equation for recovery, the reservoir does not recover completely. The bulk of recovery occurs within a time period equal to that of the preceding extraction. After this time period, the deviation of the temperature from the bulk rock decays with a slow $1/\sqrt{t}$ behavior characteristic of an impulsive line sink of heat. As a result, the additional gains from allowing the reservoir to recover for time periods greater than about 3 to 5 times the extraction

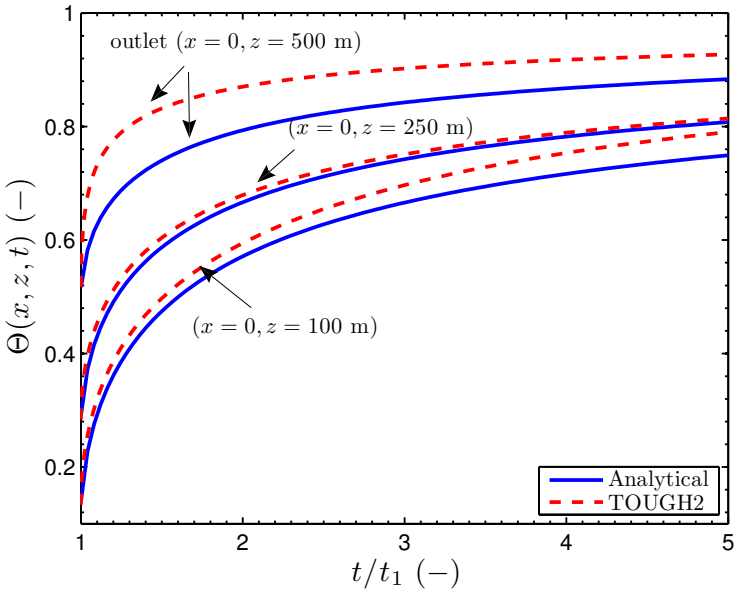

Figure 4.6: Comparison of first recovery results from TOUGH2 and Eq. (4.30) (with 100 terms) at three different positions along the fracture. The recovery occurred after 30 years of extraction with an area normalized flow rate of $\dot{m}/A = 4.8 \times 10^{-5}$ kg/(m^{2}s). Note that recovery starts at t_1 where $t/t_1 = 1$ represents the start of recovery.

time are small.

The purpose of letting a reservoir recover is to be able to use the reservoir for extraction again with a similar performance as obtained in the first extraction. Figure 4.7 validates the accuracy of the second extraction solution provided by Eq. (4.40). As discussed earlier, the added bulk rock had the effect of enhancing recovery near the outlet. However, these gains are quickly lost during a renewed extraction phase. Once the extraction starts, the temperature at the outlet is controlled by the heat convected from the middle of the fracture whose recovery is accurately predicted by the analytical model. According to Figure 4.7, the difference in the outlet temperature between second extraction and the delayed fresh extraction is decreasing with time. The same conclusion is reached by looking at Eq. (4.40) where the second extraction is dominated by the delayed fresh extraction

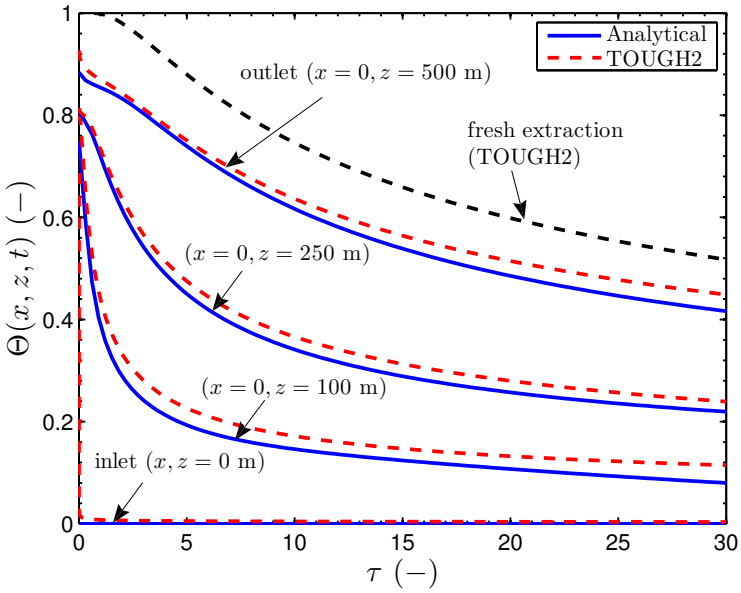

Figure 4.7: Second extraction TOUGH2 numerical results compared to Eq. (4.40) at four different positions along the fracture and for a 30 year extraction period and an area normalized flow rate of $\dot{m}/A = 4.8 \times 10^{-5}$ kg/(m^{2}s). The black dashed curve represents the temperature of a fresh reservoir undergoing its first extraction phase.

at larger times when both the recovery and convolution terms have decayed.

Figure 4.8 shows a similar behavior for the second recovery as that observed during the first recovery phase. The bulk of the recovery occurs early on and deviation between the analytical and numerical simulation results are small except near the ends of the fracture.

4.4.2 Multiple Fractures Simulations

A multiple parallel fractured reservoir is a more realistic representation of an EGS reservoir than a single fracture reservoir (Armstead and Tester, 1987). Multiple fractures have the effect of spreading out the mass loading into the reservoir and

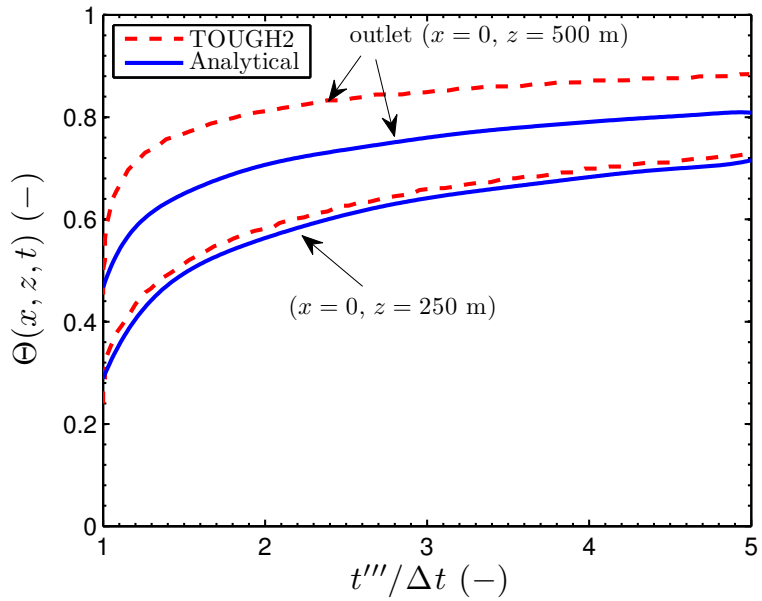

Figure 4.8: Comparison of second recovery results from TOUGH2 and Eq. (4.30) at two different positions along the fracture. The recovery occurred after a 30 year second extraction period with an area normalized flow rate of $\dot{m}/A = 4.8 \times 10^{-5}$ kg/(m^{2}s). Note that $t''' = t - t_2$ and second extraction starts at t_2 while second recovery starts at t_3 with $\Delta t = t_3 - t_2$ (the duration of the second extraction phase). $t'''/\Delta t = 1$ represents the start of second recovery.

thus increasing the effective heat transfer area. Thus, one would expect longer production lifetime for a multifracture EGS reservoir.

In our simulations the total flow rate in TOUGH2 was set to 70 kg/s corresponding to a total mass loading of 1.4×10^{-4} kg/(m^{2}s) for a fracture system with a one side area of 500,000 m^2 (500 m long and 1000 m wide). Economic total flow rates for EGS are estimated to range from 50 to 150 kg/s for a single reservoir (Tester et al., 2006). Note we are only modeling only half of the fracture system due to symmetry. In our case, each fracture receives $0.14/n$ kg/s where n is the number of fractures accounting for symmetry. The extraction phase was set to 10 years while the recovery phase was set to 20 years.

Figure 4.9 shows the results of the TOUGH2 multifracture simulations. The

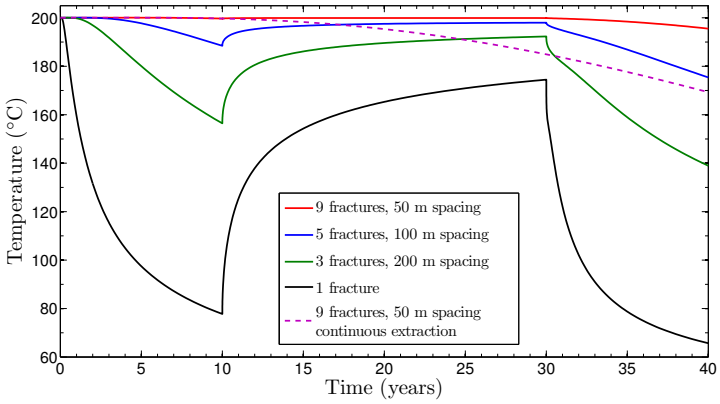

Figure 4.9: Average of the outlet temperatures of the fractures during 10 years of extraction and 20 years of recovery. Because of a low drawdown rate for the 9 fracture reservoir, a 40 year continuous extraction was plotted.

temperature at the outlet of the middle fractures and the outer fractures within any given reservoir does not vary more than one percent. This indicates that the temperature behaves in a manner similar to the infinite array of fractures used in formulating Eq. (4.50).

As expected, the decrease in the mass loading per fracture as one increases the number of fractures slows the rate of drawdown. In going from one ($x_s = \infty$) to three fractures ($x_s = 200$ m) the outlet temperature after 10 years of extraction increases from 80 °C to about 160 °C. With 5 ($x_s = 100$ m) and 9 fractures ($x_s = 50$ m), the drawdown remains within acceptable levels, from the point of view of power conversion, even at the end of the first extraction phase. A 20-year recovery phase is able to raise the outlet temperature sufficiently to begin a new extraction phase. However, as might be expected, the second extraction suffers from a more rapid drawdown, putting a burden on the surface installation to adapt more quickly to lower temperatures. Nonetheless, the recovery curves indicate that there would be no substantial gain for extending recovery beyond 30 years and that the ratio of recovery time to extraction time should fall between 2

and 4.

Another way to interpret the production results is to look at the total thermal energy content (enthalpy) and the maximum electrical work (exergy) of the fluid produced from the reservoir. Exergy or availability is the maximum possible work obtained from bringing a heat source to equilibrium with the surroundings at a specified temperature and pressure "dead state". Because exergy relates to the maximum work, it is the appropriate thermodynamic quantity for power generation while for direct use, enthalpy is more relevant. Figure 4.10 shows the enthalpy extracted as a percentage of the enthalpy (above the inlet water temperature) available in the reservoir region, defined to be 400 m x 500 m x 1000 m (0.20 km^3) volume. The exergy produced is expressed as a percentage of that which would be produced if the produced water reached the bulk rock temperature. The dead state was defined as 20 °C and 20 bar. Figure 4.10 reveals that for the given flow rate and fracture distribution investigated, the amount of enthalpy and exergy extracted for 5 fractures is nearly the same as in the case of 9 fractures. For the 5 and 9 fracture reservoir, breakthrough has yet to reach the outlet and thus there is no benefit with regards to outlet temperature to having more fractures beyond 5. In such a situation, an increase in $\dot{m}/A$ would differentiate the amounts of extracted enthalpy and exergy for 5 and 9 fractures. Comparison of the single fracture and 3 fracture reservoirs shows that the increase in the total extracted enthalpy per fracture has a trade-off in terms of decreased quality of extracted heat. A threefold increase in the mass loading per fracture for the single fracture reservoir as compared to the 3 fracture model resulted in considerable drop in the specific exergy of the fluid. Proper management of the EGS reservoir will require balancing the total extracted enthalpy and the specific exergy of the produced fluid with respect to anticipated production lifetime of the reservoir. This balance

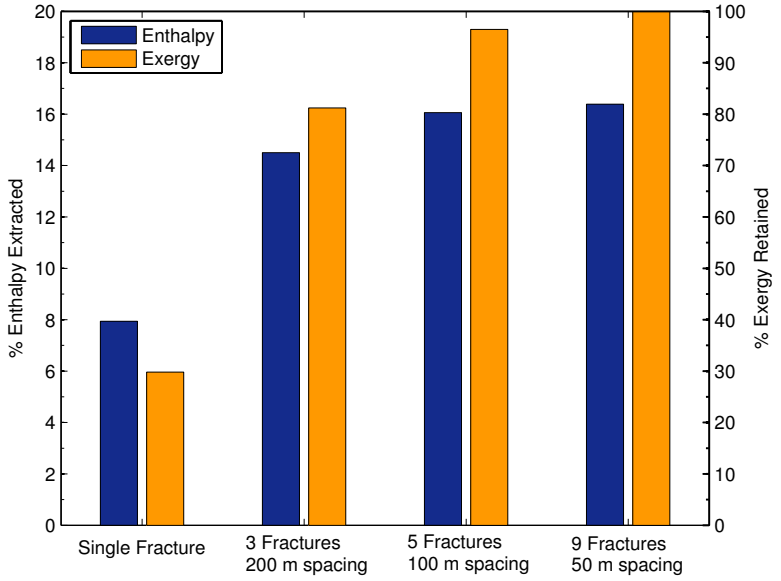

Figure 4.10: Percent of enthalpy extracted and exergy retained by a total $\dot{m}/A = 1.4 \times 10^{-4}$ kg/(m^{2}s) from an EGS reservoir normalized by the initial enthalpy of the entire reservoir. The reservoir is defined to be 400 m x 500 m x 1000 m (0.20 km^3) and the reference temperature and pressure was defined as 20°C and 20 bar.

would be achieved by adjusting the mass flow into the reservoir depending on its size and the surface infrastructure operation.

Figure 4.11 is a plot of the multifracture analytical solution presented in Eq. (4.50) along with with the results from the multifracture simulations. In the figure, the results indicate a close agreement between Eq. (4.50) and the numerical results. The small deviation is caused by two-dimensional heat conduction. From the numerical model, the temperature of each fracture was nearly identical. In particular, the outer fracture with one neighbor had a similar temperature profile to the middle fracture with two neighbors. The uniformity among the temperature profiles within the fractures suggests that the fractures are not thermally interfering with one another. Interestingly, the analytical solution for a single fracture outlet temperature with the same $\dot{m}/A$ as each fracture in a multifracture EGS reser-

voir results in a set of curves indistinguishable from those derived from Eq. (4.50). Because the two sets of curves are effectively identical, there is no measurable thermal interaction for the entire set of fracture spacings and flow rates investigated in this study as noted earlier. Lack of thermal interaction is seen in Figure 4.3 where the thermal depletion zone for each fracture is clearly distinguishable and has yet to overlap. The corresponding values of δ_x/x_s with $\delta_x = 2\sqrt{\alpha t}$ for 50 m, 100 m, and 200 m are 0.71, 0.36, and 0.18 respectively after 10 years of extraction. Although δ_x/x_s for fracture spacings of 50 m and 100 m are of order 1, the outlet temperature has not been effected by the thermal interaction even though $\delta_x \sim x_s$. As δ_x gets closer to x_s, temperatures will first start to deviate from the single fracture case in the injection region ($z \approx 0$) but do not propagate to the outlet. Additionally, when thermal penetration in the x direction at points near the inlet region starts to interfere with the thermal disturbance of the adjacent fracture, the thermal disturbance near the outlet is much smaller than the fracture spacing and the temperature field behaves as if the fractures were infinitely separated. Thus, points near the outlet are not effected by the thermal disturbance caused by the adjacent fracture.

For fracture spacings of 50 m, 100 m, and 200 m, a 5% production temperature deviation with respect to the single fracture solution occurs after 35, 46, and 120 years, respectively. These times correspond to δ_x/x_s values of 1.3, 0.76, and 0.62, respectively, all of order 1. Thermal interaction is not exclusively a function of δ_x/x_s but depends on β as well. For the cases of 1, 3, 5, and 9 fractures, the β values are 0.0020, 0.0059, 0.099, and 0.18, respectively. These results indicate that for systems with sufficient fracture spacings, parallel fractures do not interact thermally and one can model them using a single fracture model with β or $\dot{m}/A$ based on the flow rate passing through each fracture.

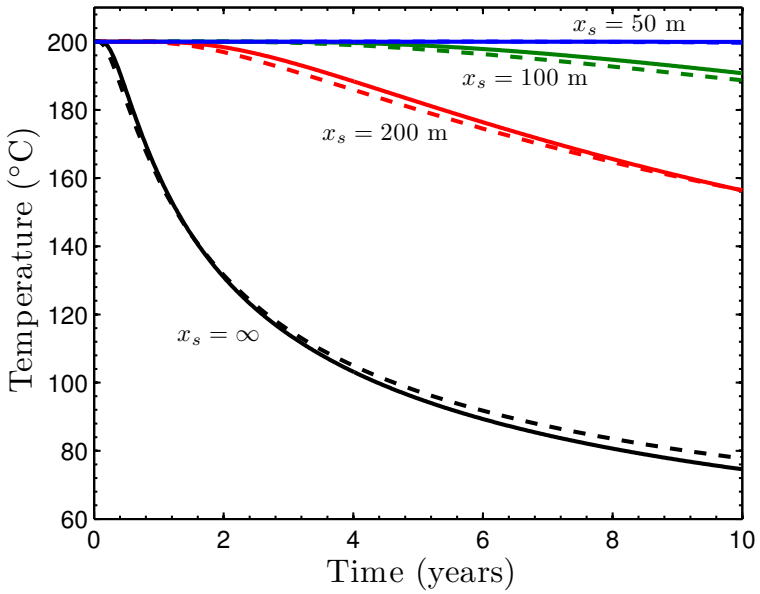

Figure 4.11: Outlet temperature results obtained from a parallel multifracture reservoir modeled in TOUGH2 (dashed curves) compared to multifracture solution (solid curves) from Eq. (4.50).

We can define an efficiency that describes how effective recovery was in restoring the farmed thermal energy of the reservoir and effecting the success of a second extraction phase. The efficiency η can be defined with either enthalpy or exergy. It is important to be able to predict how much less energy one will extract due to an incomplete recovery and make the appropriate surface installation adjustments. The efficiency of the second extraction is the ratio of the enthalpy or exergy extracted during the second extraction phase to that extracted during the first extraction phase. The efficiency was calculated using the analytical equations for a single fracture for flows corresponding to the 1, 3, and 5 fracture reservoirs. Figures 4.12 and 4.13 depict the two differently defined efficiencies under 5, 10, 15, and 20 year extraction periods as a function of the ratio of recovery to extraction time.

The results demonstrate that the second extraction efficiency is a function of

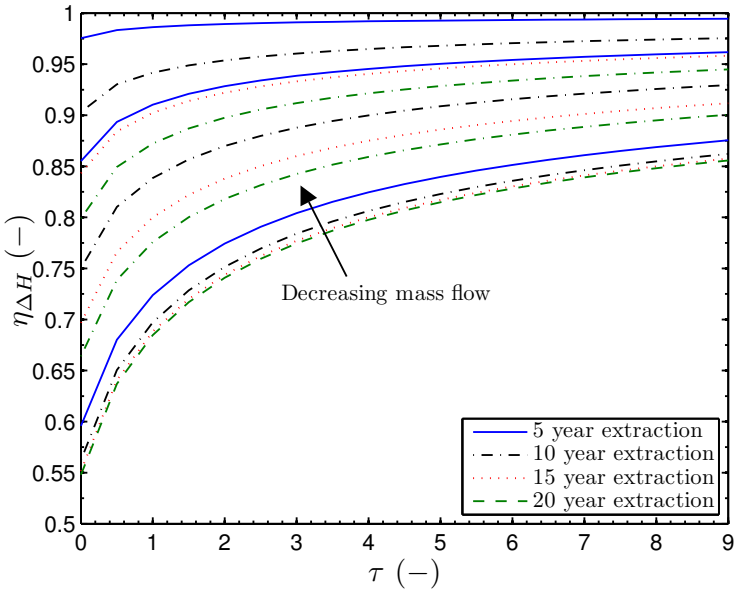

Figure 4.12: Second extraction efficiency in terms of enthalpy for a 5, 10, 15, and 20 year extraction period as a function of the duration of recovery to extraction, τ. A τ value of zero represents a recovery duration of zero while one represents equal recovery and extraction durations. Because colors are repeated, the first instance of a particular color, from the bottom to the top of the figure, represents the single fracture case while the second and third represent the 3 and 5 fracture reservoir, respectively.

not only of the ratio of recovery to extraction time but also the mass flow into the reservoir. As was seen in the graphs of temperature during recovery and second extraction, Figures 4.12 and 4.13 also suggest that little is gained for letting a reservoir recover beyond a ratio of recovery to extraction time of 4.

At higher flow rates or fewer fractures, the different extraction duration curves are grouped closer, revealing that there will be only a small increase of efficiency by reducing the extraction period. At smaller flow rates or more fractures, the grouping is much larger and shorter extraction periods yield second extraction rates closer to the first extraction period. Under these conditions, shorter extraction periods are favored because they result in higher second extraction efficiencies.

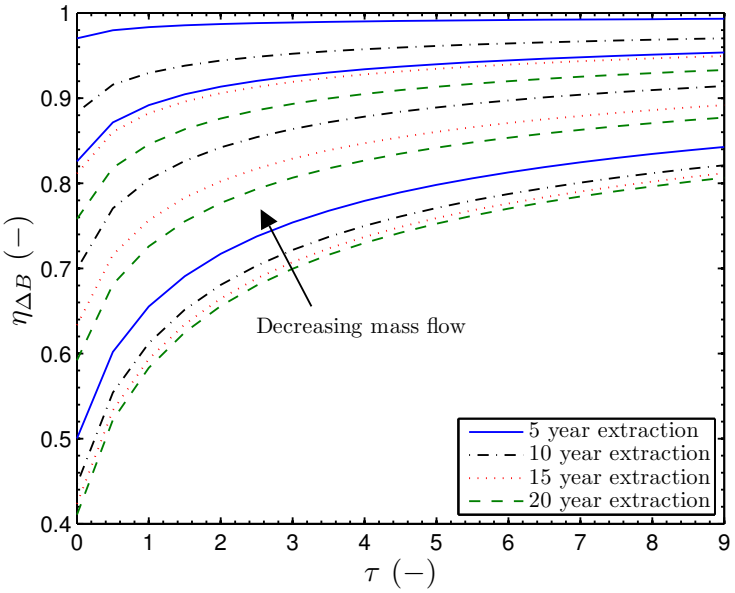

Figure 4.13: Second extraction efficiency in terms of exergy for a 5, 10, 15, and 20 year extraction period as a function of the duration of recovery to extraction, τ. A τ value of zero represents a recovery duration of zero while one represents equal recovery and extraction durations. Because colors are repeated, the first instance of a particular color, from the bottom to the top of the figure, represents the single fracture case while the second and third represent the 3 and 5 fracture reservoir, respectively.

4.5 Conclusions and Recommendations

The ability of conductively dominated EGS reservoirs to recover their thermal energy after ceasing production was assessed using both analytical and numerical methods. The assessment is important to demonstrate how Enhanced or Engineered Geothermal Systems could sustainably supply energy over a range of scales from a specific reservoir to a set of reservoirs operating sequentially in a field. With such modular systems operating successfully, one can envision how EGS could provide a significant portion of our global energy needs in a sustainable manner. This important characteristic provides a rationale for further field testing of EGS under commercial scale production conditions.

Analytical equations were derived for the temperature along a single rectangular fracture of an EGS reservoir during alternating periods of thermal extraction and recovery using a Green's function solution of the transient one-dimensional heat conduction in the rock. The analytical equations were shown to agree well with a numerical solution obtained using TOUGH2 of the energy conservation including two-dimensional conduction. The analytical equations can therefore be used as an alternative to a numerical model and as a zeroth order model to explore a particular facet of EGS operations such as thermal recovery.

The majority of the equations derived here are for a single fracture, but under certain conditions, the single fracture model can be used to model a system of parallel fractures, specifically, under typical fracture spacings and time scales of extraction. If the fracture spacing is large enough then the fractures do not thermally interact and the fractures behave independently. The single fracture model can be used for multiple parallel fractures as long the mass flow or β is scaled on a per fracture basis. With multiple fractures present, the rate of drawdown is significantly reduced. The slower rate of drawdown and the recoverability of the reservoir enhance the renewability and sustainability of conduction dominated EGS reservoirs.

Although conduction dominated EGS reservoirs do not have recovery times as small as those with substantial convective or advective drive, this study has shown that even these EGS reservoirs can be operated sustainably. Significant amount of their original thermal energy will be restored following a defined production period if they are allowed to recovery for two to four times the initial extraction time. The time scales of recovery are within the life time of surface installations which could allow for the recycling of an old reservoir. This study affirms classification

of EGS reservoirs as renewable and capable of sustainable energy production.

The investigated models can be considered a conservative representation of a worst case because they do not account for recharge by convection. Even though a low permeability EGS reservoir may not initially contain measurable amounts of fluid, water that had been introduced into the fracture system will lead to convective or advective flows. Fluid loss to the far field occurs because rock outside the fracture zone has a finite permeability and porosity. Because reservoir fluid pressures are expected to exceed the *in situ* pore pressures in EGS reservoirs with injection pumps, the injected water will have a tendency to migrate out of the fractures zones into the rock matrix during extraction. During recovery or after reducing production pressures, the "lost" fluid will flow back into the active reservoir region and accelerate recovery via the addition of convectively driven hot water. Additionally, since cooler regions of the reservoir will exhibit larger apertures caused by thermal contraction of the rock, these regions will receive the majority of the flow and expedite recovery in places where it is needed the most.

Along with neglecting convection, the idealized approach used in this study did not consider non-parallel or intersecting fractures or buoyancy driven flow, which are important features in real EGS reservoirs (Harlow and Pracht, 1972; McFarland and Murphy, 1976; Armstead and Tester, 1987). Furthermore, as was discussed in the introduction, our model does not include some of the coupled thermal, hydraulic, mechanical, and chemical physics that will surely effect how the system behaves. These features could either increase or reduce extraction and/or recovery times depending on their extent. The effect of these features have on the rate of recovery is unknown and should be investigated in the future.

The optimal operational strategy of an EGS reservoir will vary with the end-

use of the surface installation. For example, a district heating system can allow for somewhat greater thermal drawdown compared to a binary power plant which is more sensitive to temperature changes in the production fluid. Additionally, the best strategy may involve different cycle times and variable flow rates and include tandem use of reservoirs. The models developed in this study can be used as a basis for exploring the optimal strategies for using EGS reservoirs for specific applications.

Bibliography

Armstead, H. and Tester, J. W. (1987). *Heat Mining*. E. & F.N. Spon, London, New York, 1st edition.

Arpaci, V. S. (1966). *Conduction Heat Transfer*. Addison-Wesley, Reading, England.

Axelsson, G., Gudmundsson, A., Steingrímsson, B., Pálmason, G., Ármannsson, H., Tulinius, H., Flóvenz, O., Björnsson, S., and Stefánsson, V. (2001). Sustainable production of geothermal energy: Suggested definition. *IGA-News*, Quarterly No. 43(January-March):1–2.

Axelsson, G., Stefánsson, and Björnsson, G. (2005). Sustainable utilization of geothermal resources for 100–300 years. In *Proceedings of the World Geothermal Congress*, Antalya, Turkey.

Bromley, C., Mongillo, M., and Rybach, L. (2006). Sustainable utilization strategies and promotion of beneficial environmental effects-having your cake and eating it too. In *New Zealand Geothermal Workshop*.

Carslaw, H. and Jaeger, J. (1959). *Conduction of Heat in Solids*. Oxford University Press, Oxford, 2nd edition.

Cheng, A. H. D., Ghassemi, A., and Detournay, E. (2001). Integral equation solution of heat extraction from a fracture in hot dry rock. *International Journal for Numerical and Analytical Methods in Geomechanics*, 25(13):1327–1338.

Duffy, D. G. (2001). *Green's Functions with Applications*. Studies in Advanced Mathematics. Chapman & Hall/CRC, Washington, D.C.

Elsworth, D. (1989). Theory of thermal recovery from a spherically stimulated hot dry rock reservoir. *Journal of Geophysical Research*, 94(B2):1927–1934.

Fox, D. B., Sutter, D., Beckers, K. F., Lukawski, M. Z., Koch, D. L., Anderson, B. J., and Tester, J. W. (2013). Sustainable heat farming: Modeling extraction and recovery in discretely fractured geothermal reservoirs. *Geothermics*, 46(0):42–54.

Ghassemi, A. and Zhou, X. (2011). A three-dimensional thermo-poroelastic model for fracture response to injection/extraction in enhanced geothermal systems. *Geothermics*, 40(1):39–49.

Gradshteyn, I. and Ryzhik, I. (2007). *Table of Integrals, Series, and Products*. Academic Press, New York, 7th edition.

Gringarten, A. C., Witherspoon, P. A., and Ohnishi, Y. (1975). Theory of heat extraction from fractured hot dry rock. *Journal of Geophysical Research*, 80(8):1120–1124.

Harlow, F. H. and Pracht, W. E. (1972). A theoretical study of geothermal energy extraction. *Journal of Geophysical Research*, 77(35):7038–7048.

Kohl, T., Evansi, K., Hopkirk, R., and Rybach, L. (1995). Coupled hydraulic, thermal and mechanical considerations for the simulation of hot dry rock reservoirs. *Geothermics*, 24(3):345–359.

Kolditz, O. (1995). Modelling flow and heat transfer in fractured rocks: Dimensional effect of matrix heat diffusion. *Geothermics*, 24(3):421–437.

McFarland, R. D. and Murphy, H. D. (1976). Extracting energy from hydraulically-fractured geothermal reservoirs. 11th Intersociety Energy Conversion Engineering Conference, State Line, NV. ASME,.

Megel, T. and Rybach, L. (2000). Production capacity and sustainability of geothermal doublets. In *Proceedings of the World Geothermal Congress*, pages 849–854, Kyushu - Tohoku, Japan. World Geothermal Congress.

Ogino, F., Yamamura, M., and Fukuda, T. (1999). Heat transfer from hot dry rock to water flowing through a circular fracture. *Geothermics*, 28(1):21–44.

Pruess, K., Oldenburg, C., and Moridis, G. (1999). Tough2 user's guide, version 2.0. Technical report, Lawrence Berkeley National Laboratory.

Rybach, L., Megel, T., and Eugster, W. (2000). At what time scale are geothermal resources renewable? In *Proceedings of the World Geothermal Congress*, Kyushu-Tohoku, Japan.

Sanyal, S. K. (2005). Sustainability and renewability of geothermal power capacity. In *Proceedings of the World Geothermal Congress*, Antalya, Turkey.

Taron, J. and Elsworth, D. (2009). Thermalhydrologicmechanicalchemical processes in the evolution of engineered geothermal reservoirs. *International Journal of Rock Mechanics and Mining Sciences*, 46(5):855–864.

Tester, J. W., Anderson, B. J., Batchelor, A. S., Blackwell, D. D., DiPippo, R., Drake, E. M., Garnish, J., Livesay, B., Moore, M. C., Nichols, K., Petty, S., Toksoz, M. N., Veatch, R. W., Baria, R., Augustine, C., Murphy, E., Negraru, P., and Richards, M. (2006). The future of geothermal energy. Technical report, Massachusetts Institute of Technology.

Willis-Richards, J. and Wallroth, T. (1995). Approaches to the modelling of HDR reservoirs: A review. *Geothermics*, 24(3):307–332.

Wunder, R. and Murphy, H. (1978). Thermal drawdown and recovery of singly and multiply fractured hot dry rock reservoirs. Informal Report W-7405-ENG. 36, Los Alamos Scientific Laboratory of the University of California.

CHAPTER 5

AN ANALYTICAL THERMO-HYDRAULIC MODEL FOR DISCRETELY FRACTURED GEOTHERMAL RESERVOIRS

5.1 Introduction

For discretely fractured geothermal reservoirs like those found in Enhanced/Engineered Geothermal Systems (EGS), knowledge of the fracture network is important to understanding the thermal hydraulics, i.e., the fluid flows in the system and resulting temporal evolution of the subsurface temperature. EGS reservoirs are developed in hot rock with low permeability and porosity to extract a portion of the stored thermal energy contained in rock mass. A reservoir is stimulated by hydraulic pressurizaton to open existing sealed fractures (hydroshearing) or induce new ones by hydraulic fracturing. Following simulations, water may be pumped into and out of the fractured reservoir using a connected set of injection and production wells to "farm" or extract the stored thermal energy in the rock mass. A reservoir's thermal performance during fluid circulation, defined by the temperature of the produced fluid and the production rate, will determine the longevity and economic prospect of the system. Information about the location, number, and size of the fractures is needed to develop an accurate forecast of a reservoir's thermal performance. Researchers have used a combination of microseismicity and wellbore imaging techniques to characterize discrete fracture networks (Dorbath et al., 2009; Sausse et al., 2010). However, these imaging techniques cannot capture the complete description of the subsurface and researchers must rely on analytical and numerical tools to help understand how uncertainty in reservoir features and properties impact a reservoir's thermal performance. For

example, well logging imaging techniques will only identify fractures that intersect the wellbores and microseismic clouds cannot reveal the precise location, number, and orientation of fractures. Investigators may want to explore different reservoir configurations based on incomplete data on the fracture network. The purpose of this study is to develop an analytical model of the fluid flow and heat transport in a discretely fractured network with a specified geometry that can be used for a wide range of modeling applications such as determining the range of a reservoir's thermal behavior given the uncertainty of a reservoir parameter.

Research on fluid flow in discrete fracture networks has been motivated by its application in oil and gas reservoirs (Li and Lee, 2008), solute transport (Bruderer-Weng et al., 2004; Wellman et al., 2009), and safe storage of nuclear material (Cacas et al., 1990; Nordqvist et al., 1992). Nonetheless, numerical codes have been developed to model discretely fractured geothermal reservoirs, as well. Juliusson and Horne (2013) used the numerical code FEFLOW to optimize injection rates in multiwell discretely fractured reservoirs while Held et al. (2014) relied on FRACTure (Kohl and Hopkirk, 1995) to conduct an economic analysis of the Soultz-sous-Forêts Enhanced/Engineered Geothermal System. Previous analytical studies have led to solutions for idealized geothermal reservoirs with rectangular (Gringarten et al., 1975; Nicol and Robinson, 1990), cylindrical (Yang and Yeh, 2009), and circular fractures (Heuer et al., 1991), but these solutions only model parallel multifracture systems, not an interconnected fracture network. Thus, there is a need to develop an analytical model to describe the fluid flow and the temperature along the fracture surfaces in discretely fractured geothermal systems. Such a solution would bridge the gap between the previously derived analytical solutions and sophisticated numerical codes and provide researchers with an efficient tool for modeling discretely fracture networks in geothermal reservoirs.

An analytical equation for the temperature of a discrete fracture network would be useful for various reasons. First of all, it can provide a computationally fast model compared to numerical codes which often rely on the finite element, finite difference, or finite volume methods. If one is content with the simplifications that come along with deriving a tractable analytical solution, then the model can be used to easily explore the consequence of reservoir characteristics. For example, one can model the sensitivity of thermal performance to parameters like aperture, fracture length, wellbore positioning, etc. Having a closed form solution also allows for a wider range of analysis tools, particularly those that require a closed form solution, such as derivative dependent optimization techniques. A closed form solution would also make it possible to easily identify key parameters, as well as their coupled effects, to readily understand how they affect the system. Furthermore, having an analytical equation could provide a benchmark to validate numerical models that simulate discretely fractured networks. By comparing an analytical equation against a numerical code, one can contrast the two in order to understand how important it is to model physics that the analytical model simplifies or omits.

Another application of an analytical equation for a discrete fracture network is for use as the basis of solving inverse problems to determine the fracture network and subsurface temperature field using reactive tracers tests. Chemically reactive tracers have been proposed as a tool to probe the subsurface (Robinson et al., 1988), since these tracers have reaction rates that are a function of temperature. The results of a reactive tracer test contain information about the fluid flow as well as the temperature in the subsurface and need to be deconvoluted to map out the thermal structure of the subsurface. In order to simulate these reactive tracers, one needs to know the temperature field along the fracture surface. An inverse search

to determine the fracture network required at least 10^3 to 10^4 model evaluations to obtain an answer. For this reason, relying exclusively on a numerical code may not be practical. A computational bottleneck would detract from the proof of concept of reactive tracers and the identification of optimal inverse algorithms and procedures. Instead, one can use a hybrid approach in which the inverse algorithm uses the analytical equation and only switches over to a more computationally expensive model once the inverse search has whittled away bad solutions and is now in the search space near the optimal reservoir structure.

For this paper, we will first explain our proposed fracture network made up of rectangular fractures with unidirectional flow. By specifying the structure of the fractures in the network, the connectivity and size of the fractures, we derive the fluid flow in the system. With information on the flow in the network, we describe how to implement the model and readily generate the temperature of the fracture surface in an arbitrary network. The temperature in the fracture is solved by coupling convective heat transport in the fracture with one dimensional heat conduction perpendicular to the fracture. Then, we validate the derived equation for the temperature using the established TOUGH2 reservoir simulator. Finally, we showcase the capabilities of the discrete fracture model for two different case studies. The first case study focuses on the effect of aperture value uncertainty for the fractures on thermal performance. An ensemble of fracture networks are generated when the aperture values are sampled from a log-normal distribution and the resulting distribution of thermal performance is calculated. The second case study considers the consequence of having only incomplete information on the structure of a fracture network on the uncertainty in the thermal performance of the reservoir. In the network, only two fractures are identified, the fractures that intersect the injection and production wells. The number of additional fractures,

their position in the network, and their directionality are sampled from a distribution to generate different fractures networks with different levels of connectivity and reservoir size. An ensemble set of fracture networks are generated and the distribution of thermal performance is calculated to illustrate the range of possible reservoir thermal behavior. The case study ends with demonstrating the use of sensitivity analysis tools to determine the relative importance of network structure versus fracture aperture variations on the thermal performance of a discretely fractured geothermal reservoir.

5.2 Discrete Fracture Network Model Description

Researchers have modeled the fractures in the subsurface as disks, but often the flow is simplified as unidirectional and the flow network is treated as a system of planar fractures (Cacas et al., 1990; Nordqvist et al., 1992; Bruel et al., 1994). Others have taken a more detailed approach to modeling the flow in the fracture. Andersson and Dverstorp (1987) solve the Laplacian of the pressure for each fracture using the boundary element method, while Lough et al. (1998) modeled the flow in both the surrounding matrix and the fractures by using Darcy flow in the matrix and treating the fractures as planar sources. Some researchers simplified modeling of the flow by considering the different length scales of the fractures. Lee et al. (2001) and Li and Lee (2008) both applied a hierarchical approach based on fracture lengths by treating short fractures as an enhanced matrix permeability and modeling medium and larger fractures using either the boundary element or finite volume method. However, in order to derive an analytical solution for the fluid flow and the temperature of the geothermal reservoir, a simple approach to modeling the fluid flow is required akin to the methods used by (Cacas et al., 1990;

Nordqvist et al., 1992; Bruel et al., 1994).

For the proposed discrete fracture network model, the fractures were considered to be rectangles each having one of their sides aligned in a neutral direction with the other sides forming a set of interconnected lines drawn on a 2D space. The flow in each fracture is static and unidirectional. An example of a discrete fracture network used in our model is shown in Figure 5.1.

We first describe how we calculate the fluid flow in the system given the connectivity and sizes of the fractures, the injected mass, and the pressure at either the injection or production well. With the flow in the system described, we then show how we can model the coupled convective and conductive heat transport in a single fracture of the system and use the interconnectivity of the network to derive an equation describing the temperature along all the fractures. Although a more complicated flow model could have been developed like those mentioned earlier, the model was kept simple in order to have a tractable solution for the temperature in the network. The thermal model of the network is based on rectangular fractures where the flow is unidirectional and the conductive heat transport is perpendicular to the fracture.

5.2.1 Fluid Flow in the Discrete Fracture Network

A discrete fracture network can be reduced to a set of segments and nodes. Nodes are points in the network that are connected by segments, where segments are portions of a fracture that have been discretely identified. The nodes in the system may be populated where one fracture ends and another begins or where multiple fractures intersect. The resulting discretization of the fractures by the nodes yield

the segments in the system. In graph theory, segments are known as edges, nodes are known as vertices, and the network is referred to as the graph. See Figure 5.1 for an example of a discrete fracture network with its nodes and segments. Each network has one node designating the injection well and another node representing the production well.

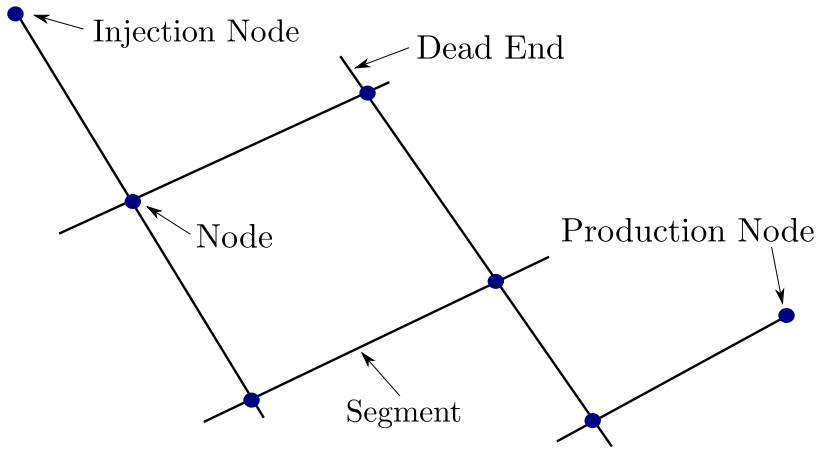

Figure 5.1: Sample discrete fracture network with segments, nodes, injection node, production node, and dead ends identified.

To determine the flow throughout the fracture network, one needs to apply a mass balance around each node in the system. By assuming viscous, pressure-driven flow, the ultimate result is a linear set of algebraic equations for the pressure at each node in the system. Additionally, the pressure needs to be specified at one node, typically either the node representing the injection or production well. The mass balance around node k is equal to

$$\sum_{i \in S_k} \dot{m}_i = f_k, \tag{5.1}$$

where $\dot{m}_i$ is the mass flow in segment i of the network and S_k is the set of segments that have node k as one of their two nodes. The term f_k on the right hand side of the above equation represents any mass lost or gained in the node from an injection

or production well. The mass in segment i of the network is equal to

$$\dot{m}_i = \rho_w v_i A_c, \tag{5.2}$$

where ρ_w is the density of the water, v_i is the velocity, and A_c is the cross sectional area of the segment. The cross sectional area is the product of the fracture width w_i and thickness H, which is kept constant for all fractures. The thickness of the fracture is defined as the dimension orthogonal to the flow or the dimension into the page. If the fluid velocity is modeled as Poiseuille flow, then the mean cross sectional velocity in the segment is equal to

$$v_i = -\frac{w_i^2}{12\mu}\frac{\Delta P}{L_i}, \tag{5.3}$$

where μ is the dynamic viscosity, L_i is the length of the segment, and ΔP is the pressure drop in the segment. The pressure drop ΔP is defined as $\Delta P \equiv P_k - P_{[k]}$ where P_k is the pressure of node k and $P_{[k]}$ is the other node in the segment that is not node k. Putting Eq. (6.2) and (5.3) together, the mass flow in each segment becomes

$$\dot{m}_i = -C_i \Delta P, \tag{5.4}$$

where C_i is the conductance of the flow and is given by

$$C_i = \frac{\rho_w w_i^3 H}{12\mu L_i}. \tag{5.5}$$

The segments in the network can be viewed as "resistors" where the pressure drop along a segment is analogous to the voltage drop and the conductance is the inverse of the electrical resistance.

Except for the node where the pressure is specified, the mass balance around each node in the system is applied to generate $n-1$ equations, where n is the number of nodes in the system. An additional equation is generated by applying

the specified pressure condition, $P_p = P_0$, where P_p is the pressure of the node with the specified condition and P_0 is the value of the specified pressure. With the specified pressure condition, there are n equations. The system of algebraic equations can be represented as

$$\mathbf{Dp} = \mathbf{f}, \tag{5.6}$$

where the matrix $\mathbf{D}$ is the coefficient matrix, $\mathbf{p}$ is the pressure at each node, and $\mathbf{f}$ equals any mass gained or lost in the system at each node. The dimensionality of $\mathbf{D}$, $\mathbf{f}$, and $\mathbf{p}$, is $n \times n$, $n \times 1$, and $n \times 1$, respectively, where n is the number of nodes in the system. The pressure at each node is easily solved by inverting Eq. (5.6) to solve for $\mathbf{p}$. With the pressure at each of the nodes determined, the inlet (upstream) and outlet (downstream) nodes of each segment can be identified as well as the directionality of flow. The inlet and outlet nodes of each segment are simply the node with the highest and lowest pressure in the segment, respectively, and flow travels from higher to lower pressure.

5.2.2 Fracture Surface Temperature Field

For a single rectangular fracture geothermal reservoir the governing equation for 1D conduction in the bulk rock is

$$\frac{\partial \Theta}{\partial t} - \alpha \frac{\partial^2 \Theta}{\partial x^2}, \tag{5.7}$$

where Θ is the dimensionless temperature defined as $\Theta \equiv (T - T_w)/(T_r - T_w)$, T is temperature of the reservoir, T_r is the original reservoir temperature, T_w is the injected water temperature, x is defined as the direction into the rock mass, t is time, and α is the thermal diffusivity of the host rock. The dimensionless temperature Θ ranges from zero to one, with a value of zero representing complete

drawdown when the temperature is equal to the injected water temperature, while a value of one indicates no deviation from the original rock temperature, or no drawdown. A depiction of the geometry of the problem is shown in Figure 5.2. The boundary and initial conditions are

$$\Theta(\infty, z, t) = 1, \tag{5.8}$$

$$\Theta(0, 0, t) = 0, \tag{5.9}$$

and

$$\Theta(x, z, 0) = 1. \tag{5.10}$$

Eq. (5.9) describes the injected temperature of the water which is equal to zero by the definition of the dimensionless temperature. There is an additional boundary condition relating the heat transport at the fracture surface given by

$$\left(\rho_w c_w w U \frac{\partial \Theta}{\partial z} = 2k_r \frac{\partial \Theta}{\partial x}\right)\Bigg|_{x=0}, \tag{5.11}$$

where ρ_w is the density of water, c_w is the heat capacity, U is the velocity of the fluid, w is the aperture of the fracture, and the direction z is the dimension along the fluid streamline. Thermal conduction inside the fracture is neglected because the Péclet number is much larger than one. For typical values of $U \sim 0.1$ m/s, $w \sim 1 \times 10^{-3}$ m, and $\alpha_w \sim 1 \times 10^{-7}$ m^2/s, and a Péclet number defined as $\mathrm{Pe} \equiv Uw/\alpha_w$, the Péclet number is on the order of 1×10^3. Eq. (5.11) says that the rate of convection along the fracture surface is equal to the conduction into the fracture from the surrounding bulk rock. The temperature field has been solved using Laplace transforms (Lauwerier, 1955; Arpaci, 1966; Carslaw and Jaeger, 1959; Gringarten et al., 1975) and is equal to

$$\Theta(x, z, t) = \mathrm{erf}\left[\frac{x + \beta z}{2\sqrt{\alpha t}}\right], \tag{5.12}$$

where β is a dimensionless parameter grouping defined as

$$\beta \equiv \frac{2k_r H}{\dot{m} c_w}. \tag{5.13}$$

Note that the final solution depends on the mass flow rate $\dot{m} = \rho_w U w H$ but not on the fracture aperture w and velocity U separately.

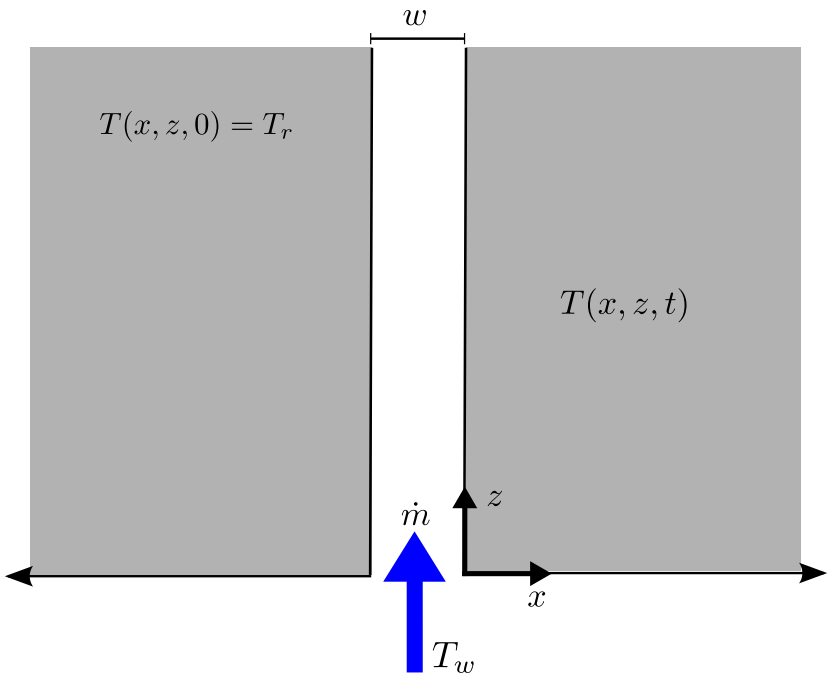

Figure 5.2: Idealized depiction of a single rectangular fracture. Water is pumped at a mass rate of $\dot{m}$ at a constant temperature T_w and the original and far field temperature of the reservoir is T_r. The scale of the fracture width is exaggerated and $x = 0$ corresponds to the fracture surface.

To determine the temperature in a discrete fracture network, one needs to first consider an isolated segment in the system and generalize the inlet fluid temperature condition of the single rectangular model. For this isolated segment, the Laplace transform of the dimensionless temperature along the fracture ($x = 0$) is equal to

$$\bar{\Theta}_i(z, s) = \frac{1}{s} - \frac{1}{s}\left(1 - s\bar{\Theta}_0\right) \exp\left[-\beta_i z \sqrt{s/\alpha}\right], \tag{5.14}$$

where the overbar denotes the Laplace transform, s is the Laplace space variable, $\bar{\Theta}_0$ is the Laplace transform of the dimensionless inlet temperature, and $z = 0$

corresponds to the upstream node position of the segment. Eq. (5.14) represents the penultimate form of the temperature along the fracture, before applying the inlet temperature condition and taking the inverse Laplace transform. If the inlet temperature is constant with time, then the Laplace transform of the constant inlet temperature is equal to zero and the inverse Laplace transform of Eq. (5.14) simply becomes the single rectangular fracture solution.

If one knows how the inlet temperature varies with time, then one can construct the temperature along the segment of interest. To determine $\bar{\Theta}_0$, one must look immediately upstream from the segment of interest and determine the temperature of the feed segment(s), the segment immediately upstream, at its corresponding outlet node ($z = L_i$). If there is more than one feed segment, then a mixing cup or weighted average based on the mass flow is used to determine the inlet temperature.

The outlet temperature of the feed segments will also take the form of Eq. (5.14) but with their respective values of β_i and $z = L_i$. Since β is a function of the mass flow, each segment will potentially have different values of β. Under a recursive approach, one backtracks from the segment of interest, keeping track of all unique paths, to the node corresponding with the injection well where the fluid temperature is constant. The consequence of the backtracking is a multiplicative form of all the upstream segments that contribute to the inlet temperature. The form is

$$\bar{\Theta}_i(z,s) = \frac{1}{s} - \frac{1}{s}\sum_{k}^{n_p}\left(\prod_{j\in S_k}\chi_j \exp(-\bar{\xi}_j)\right)\exp\left(-\beta_i z\sqrt{s/\alpha}\right), \tag{5.15}$$

where k represents a path to get to segment i from the total number of paths n_p, S_k represents the set of segments j in path k, $\bar{\xi}_j = \beta_j L_j\sqrt{s/\alpha}$, while χ_j is the fraction of fluid from segment j that contributed to the flow in the immediate downstream segment. For diverging nodes where the flow is split, the value of χ is equal to one

since all the flow from the branching segments came from the upstream segment. However, for converging nodes, χ will have a value other than one and can be expressed more precisely as

$$\chi_j = \dot{m}_j / \sum_{l \in J_p} \dot{m}_l, \tag{5.16}$$

where J_p is the set of segments that converge into the downstream segment of j. For example, segments 2, 3, and 4 converge and supply the flow of segment 5. If the mass flow for segments 2, 3, and 4 are 15, 25, and 10 kg/s, respectively, then their respective χ values are equal to 0.3, 0.5, and 0.2. As a check, the summation of each χ_j term in the set of S_k, i.e., $\sum_{j \in S_k} \chi_j$, should be equal to the mass flow in segment k divided by the total mass flow rate of the system.

By applying the multiplicative relationship of exponents, Eq. (5.15) can be expressed as simply a sum of terms in the form of $\exp(-a\sqrt{s})/s$, which can be analytically inverted from the Laplace space to time. As with the single rectangular fracture solution, the resulting equation is expressed using the error function and is equal to

$$\Theta_i(z,t) = \sum_{k}^{n_p} \left(\prod_{j \in S_k} \chi_j \right) \operatorname{erf} \left[\sum_{j \in S_k} \xi_j + \frac{\beta_i z}{2\sqrt{\alpha t}} \right], \tag{5.17}$$

where ξ_j is the inverse Laplace transform of $\bar{\xi}_j$ and is equal to

$$\xi_j = \frac{\beta_j L_j}{2\sqrt{\alpha t}}. \tag{5.18}$$

In the derived equation, we see how it is built with the temperature solution of the single rectangular fracture. Additionally, the equation shows the influence of upstream segments in each path through the parameter ξ and the consequence of converging streams through the product of χ. The resulting fracture temperature is a function of the aperture and length of each of the segments in the network. Although the aperture values do not appear explicitly in Eq. (5.17), they control

the mass distribution through the cubic relationship shown in Eq. (5.5) and will affect the values of both χ and β. The influence of the length of the segments is seen more clearly since L appears directly in Eq. (5.17) through ξ but also influences β due to the inverse relationship with the segment's conductance shown in Eq. (5.5). The implementation of Eq. (5.17) is quick, for example, it takes 30 and 60 seconds to calculate the temperature for ten thousand networks with two and six paths, respectively, using a computer with 4 GB of RAM and a 2.67 GHz processor.

Eq. (5.17) involves multiple summations and a product of a sequence and consequently, can be confusing to apply. To illustrate how it is applied, consider the network shown in Figure 5.3 where the injected fluid first travels through one fracture and then splits into two other fractures before converging into one fracture that leads to the production well. The paths to segment 5 that contain the production well are $S_1 = \{1, 3\}$ and $S_2 = \{1, 2, 4\}$, where the numbers correspond to the segments involved in each path. The temperature in the last segment leading to the production well is equal to

$$\Theta_5(z,t) = \chi_1\chi_2\chi_4 \text{erf}\left[\xi_1 + \xi_2 + \xi_4 + \frac{\beta_5 z}{2\sqrt{\alpha t}}\right] + \chi_1\chi_3 \text{erf}\left[\xi_1 + \xi_3 + \frac{\beta_5 z}{2\sqrt{\alpha t}}\right]. \quad (5.19)$$

There are two distinct paths from the injection to production well and the two paths manifest themselves via the two term summation. Because the outlet node of segment 1 is a diverging/splitting node and is the only feed segment to segments 2 and 3, χ_1 is equal to one. To evaluate the temperature at the production well, set $z = L_5$, as z represents the distance from the upstream to the downstream node of the segment of interest.

The solution, as with the single rectangular fracture solution, only models 1D heat conduction in the direction perpendicular to the flow. However, Fox et al. (2013) showed that β^2 was the perturbation parameter in 2D conduction and can

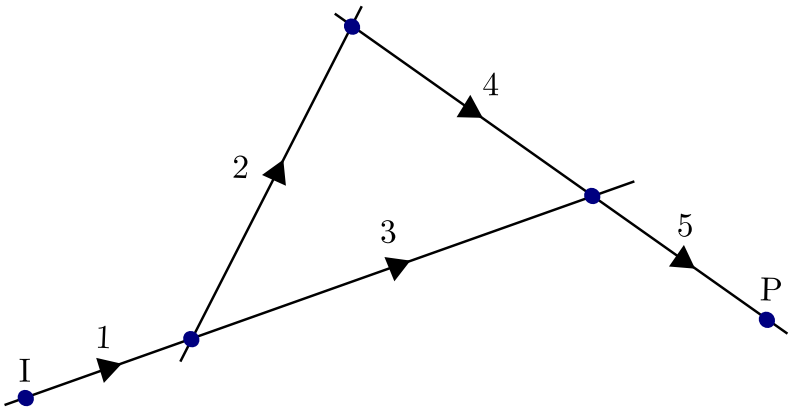

Figure 5.3: Sample fracture network with the directionality of the flow identified. The injection and production nodes are represented by the letters "I" and "P" and the direction of the flow is shown by the arrows in the middle of each segment. The network has two flow paths from the injection to production well.

be neglected when $\beta^2 \ll 1$. The economic flow rate has been assessed to be 50 to 100 kg/s per well pair (Tester et al., 2006) and for typical values of thermophysical properties, $\beta^2 \approx 2 \times 10^{-4}$ when the reservoir thickness ranges from 500 to 1000 m. However, since β is inversely proportional to the mass flow and is defined as the mass flow of the segment and not of the entire system, the flow in a highly fractured, dense network would result in segments that violate the $\beta^2 \ll 1$ criteria because the mass flow in each fracture will be low. When the flow within a fracture is only 1 or 2 kg/s, $\beta^2 \approx 0.1$ when the reservoir thickness is 500 or 1000 m. On the other hand, the smaller fractures in the network may not play an important part in the thermal processes because they will take less flow. In this case, the analysis can just focus on the highly conductive fractures. One can apply an approach similar to that of Maryška et al. (2005), who simplified discrete fractured network by moving, stretching, and merging intersections.

The equation we have derived does not model thermally interacting fractures but this will not be a problem when the fracture spacing is greater than $\sqrt{\alpha t}$, the

Table 5.1: List of key assumptions and limitations of the model.

Assumption	Comment
only convective heat transport inside the fracture	valid when Pe $\gg 1$, which will be typical
constant thermal physical properties	required to obtain solution
unidirectional flow	spatial aperture variations can be partially considered by using a fracture's hydraulic aperture (see Section 5.4)
1D heat conduction	multidimensional effects negligible for $\beta^2 \ll 1$
no thermal interference	valid for fractures spaced larger than $\sqrt{\alpha t}$

thermal penetration distance due to conduction, as is typically the case. It may be a problem in modeling highly dense fracture networks. For the ideal reservoir life of ten to thirty years, $\sqrt{\alpha t}$ ranges from 20 to 30 m. Nicol and Robinson (1990) reported a spacing of 10 to 25 m for major flowing zones in the Rosemanowes EGS project in England while Evans et al. (2005) observed a spacing of 50 m for fractures with major flow in the Soultz reservoir. These reported fracture spacing values is on the order thermal penetration distance. The derived solution can be adapted to incorporate fracture interference by changing the kernel $\exp(-\beta_i z\sqrt{s/\alpha})$ in Eq. (5.15) to be $\exp(-\beta_i z\sqrt{s/\alpha}\tanh[0.5x_s\sqrt{s/\alpha}])$, where x_s is the fracture spacing. The modified kernel was derived for a reservoir with an infinite array of parallel fractures with a fracture spacing of x_s (Fox et al., 2013), and one can used the mean fracture spacing of the network as an appropriate value for x_s. Using the modified kernel prevents one from analytically inverting the resulting temperature equation back into the time domain, and Laplace numerical inversion schemes must be utilized. Like the single rectangular fracture equation, Eq. (5.17) assumes the thermophysical quantities are constant. A list of the key assumptions and limitations of the model are listed in Table 5.1.

5.2.3 Automating the Calculation of Fluid Velocity and Temperature in a Network

Automation is required to implement the model in an investigation that is generating many different fracture networks. To carry out this out, one first needs to solve the mass flow distribution using Eq. (5.6), which can be readily constructed for any arbitrary network by using the concepts of the finite element method (FEM) including matrix assembly and applying essential (Dirichlet) boundary conditions. Under the FEM framework, each segment is considered an element with an elemental $\mathbf{D}^e$ matrix given by

$$\mathbf{D}^e = C_i \begin{bmatrix} 1 & -1 \\ -1 & 1 \end{bmatrix}. \tag{5.20}$$

From the elemental matrices, a global conductance matrix $\mathbf{D}$ is constructed by applying the assembly algorithm, which considers how the elements/segments are connected to each other. This connectivity matrix is of dimension $m \times 2$, where m is the number of segments. Each row corresponds to a segment in the network and the first and second columns represent the inlet and outlet node, respectively. The next step is to apply the specified pressure condition that is needed to form a complete set of independent equations, often called the essential boundary condition in FEM literature, and invert the matrix in Eq. (5.6) to solve for $\mathbf{p}$. The description of the assembly and essential boundary condition algorithms can be found in most FEM sources like Smith and Griffiths (1988); Cook et al. (2001); Fish and Belytschko (2007).

The second step is to determine all paths to each segment of interest. The fracture network should be free of dead end segments. A dead end segment has no flow due to equal pressure of the inlet and outlet nodes. These segments are

easily determined once the flow distribution is calculated and should be removed to ease analysis. To determine the paths to reach each segment, a graph traversal algorithm like depth-first search is needed (Bondy and Murty, 2010; Even and Even, 2011). Starting with the inlet node of a segment, the search follows upstream all the way to the injection node. The directionality of the network is determined by the pressure at each node, since fluid flows from higher to lower pressure and the injection node will have the highest pressure in the network. The algorithm records the segments visited as well as any branching nodes. Once the injection well is reached, the algorithm goes back to the last branching node and proceeds to once again travel upstream to reach the injection node via a different path. The search stops when the algorithm accounts for all branching nodes. The search algorithm will be easier to implement if all dead ends have been removed.

A path matrix P_{ij} can be used to readily identify the participating segments for all the flow paths in the network. The number of rows and columns are equal to the number paths and segments in the network, respectively. If segment j is in path i, then $P_{ij} = 1$, otherwise $P_{ij} = 0$. The segments in path i can be easily determined by checking row i. Similarly, the paths passing through segment j are identified by looking up column j. The final step is to calculate the required parameters like β_i and χ_i. Finally, for a given segment with all its paths identified, Eq. (5.17) can now yield the temperature along the segment.

5.3 Numerical Validation

Eq. (5.17) was validated using TOUGH2 for two different fracture networks, differing in the number of flow paths. TOUGH2 is a reservoir code developed at

the Lawrence Berkeley National Laboratory and is a general purpose numerical simulation program for multidimensional non-isothermal flows of multiphase, multicomponent fluid mixtures in fractured and porous media (Pruess et al., 1999). It employs an integral finite difference method (IFDM) in discretizing the medium, which has the advantage of irregular discretization in multiple dimensions. Time is discretized fully implicitly as a first order backward finite difference and fluxes are computed using upstream weighting (Pruess et al., 1999).

The networks modeled are depicted in figures 5.4 and 5.5. The first network has two paths from the injection to the production well while the second network has six. Given the numbering scheme of the segments shown in the figures, the paths from the injection to production well for the first network are $S_1 = \{1, 3, 5, 6\}$ and $S_2 = \{1, 2, 4, 6\}$. For the second network, the paths are $S_1 = \{1, 4, 9, 12, 13, 14\}$, $S_2 = \{1, 4, 7, 10, 13, 14\}$, $S_3 = \{1, 4, 7, 8, 11, 14\}$, $S_4 = \{1, 2, 5, 8, 11, 14\}$, $S_5 = \{1, 2, 5, 10, 13, 14\}$, $S_6 = \{1, 3, 6, 11, 14\}$. For each network, the temperature drawdown curves were calculated at each node in the system. The parameters used were $\dot{m} = 50$ kg/s, k_r=2.7 W/(m °C), $\rho_r = 2700$ kg/m^3, $c_r = 1050$ W/(m °C), and $c_w = 4300$ W/(m °C).

The computational domain in TOUGH2 is 1000 m by 1000 m by 10 m. There is a no mass and energy flux at all the boundaries of the domain. The third dimension (10 m) is perpendicular to the plane of the fracture network and is arbitrary since there is no heat or mass transfer in that direction. This dimension corresponds to the reservoir thickness H in the analytical model. Thus, to model an injected mass of 50 kg/s for a reservoir with $H = 500$ m in the TOUGH2 model with $H = 10$ m, the injected mass needs to be scaled down to 1 kg/s. The fracture network only extends 700 m by 500 m and is centered in the domain. The domain

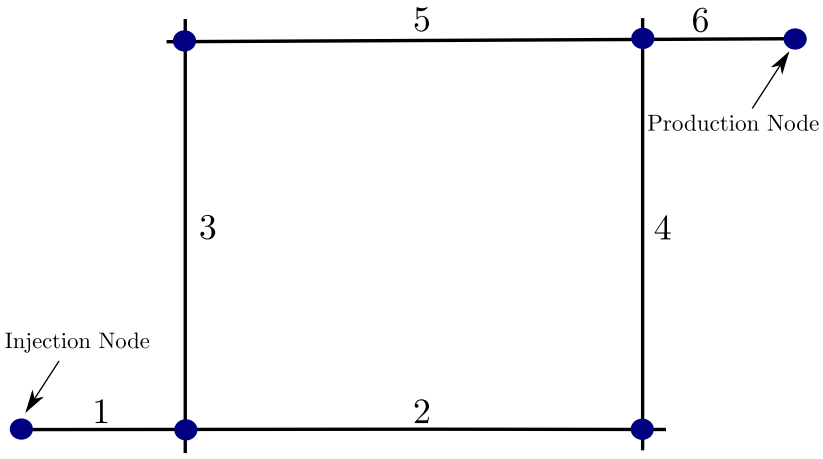

Figure 5.4: A discrete fracture network composed of six segments. All segments are 500 m except for segments 1 and 6, which are 100 m. The injection and production wells are represented by the inlet node of segment 1 and the the outlet node of segment 6, respectively.

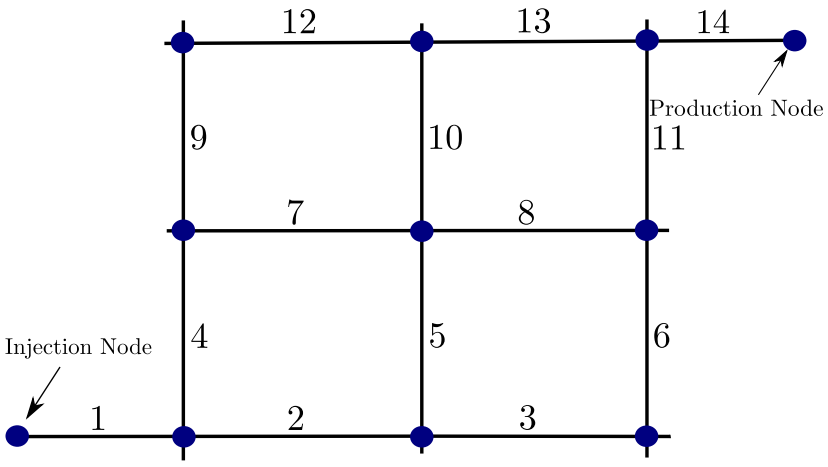

Figure 5.5: A discrete fracture network composed of fourteen segments. All segments are 250 m except for segments 1 and 14, which are 100 m. The injection and production wells are represented by the inlet node of segment 1 and the outlet node of segment 14.

is appropriately sized because the injection well is located 150 m away from the edge of the domain and the thermal penetration depth will only reach the edge after 200 years, ensuring that the heat transfer is not affected by the finite size of the computational domain.

The model is composed of two materials, "fracture" and "rock". The porosity of the fracture is one, while it is zero for the rock. Thus, the flow is completely contained within the fracture cells. Since the region near the fractures will experience high temperature gradients, the mesh is more refined around the fractures. Overall, the model is composed of 67,591 cells. The two fracture networks were modeled using the same TOUGH2 mesh by changing the material of certain cells from "fracture" to "rock". The fracture permeability was set to 10^{-9} m^2 and the pressure drop inside the system is low enough to maintain single phase liquid flow. The initial temperature and pressure is 200 °C and 20 MPa, respectively. Both the injection and production wells are represented by a single cell, where the mass rate injected and produced are set to 1 kg/s for 10 m reservoir thickness, equivalent to 50 kg/s for a 500 m thick reservoir. The computation model and mesh is shown in Figure 5.6.

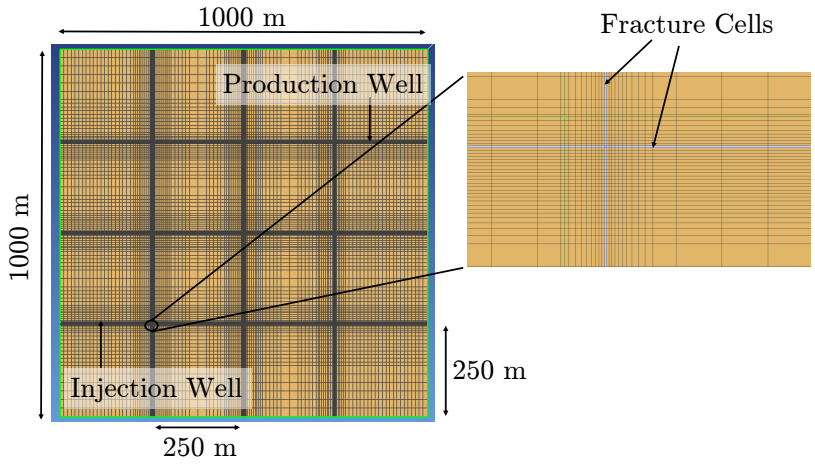

Figure 5.6: The TOUGH2 computational domain and mesh used for the simulations. The left hand figure shows an overview while the right hand figure zooms in to show the fracture cells (colored cyan).

Figure 5.7 shows the dimensionless drawdown curves at different positions in the fracture network depicted in Figure 5.4 for a period of 20 years. Time is nondimensionalized by τ, where $\tau \equiv k_r \rho_r c_r / (c_w \dot{m} / A)^2$. The dimensionless time

considers the relationship between time and mass flow rate in Eq. (5.17), specifically, $1/(\dot{m}\sqrt{t})$. Thus, the analytical equation produces the same drawdown curve by keeping the dimensionless time the same. There is close agreement with the analytically derived results and TOUGH2 for all points in the reservoir with the TOUGH2 results being slightly lower. The dimensionless production temperature from TOUGH2 after 20 years is 0.0043 (0.78 °C dimensionally) lower. The fact that the two sets of drawdown curves are similar indicates that the assumption that there is little thermal interaction among the fractures was valid.

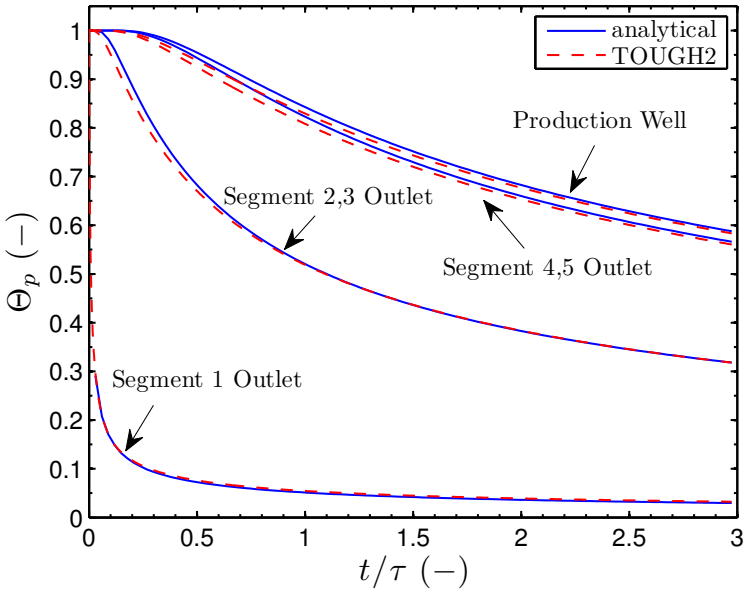

Figure 5.7: A comparison of the analytical equation and TOUGH2 for the dimensionless temperature drawdown for various segments of the discrete fracture network shown in Figure 5.4.

If we increase the fracture density of the system, we should anticipate more fracture thermal interaction. Plotted in Figure 5.8 is the analytical dimensionless production temperature drawdown curve for the network in Figure 5.5 compared against two drawdown curves from TOUGH2. The two TOUGH2 curves use a different set of mass flow and extraction period that keeps the dimensionless time the same, the first uses 50 kg/s and 40 years while the second uses 100 kg/s and

10 years. The results show that the TOUGH2 production temperatures are lower than the values derived from Eq. (5.17). The TOUGH2 results start to deviate from each other at around $t/\tau = 0.8$, or 11 years and 2.8 years for the 50 kg/s and 100 kg/s results, respectively. The 100 kg/s mass flow TOUGH2 results had the least deviation form the analytical drawdown curve.

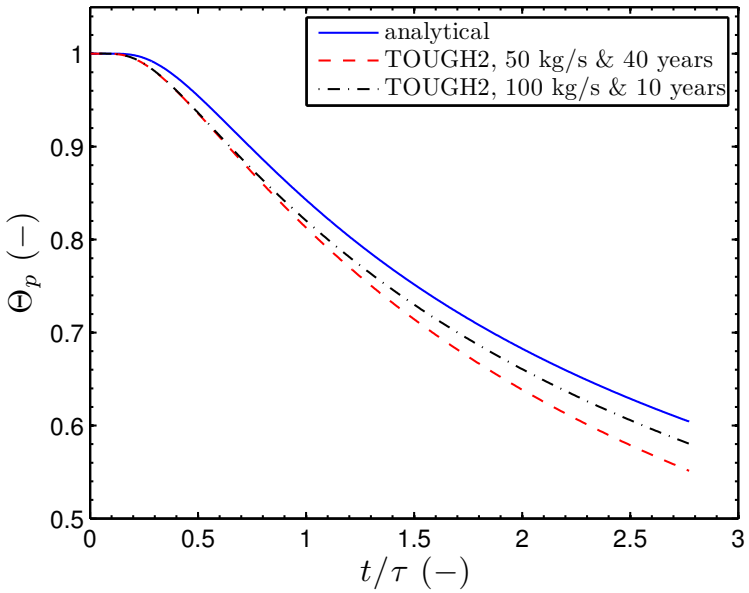

Figure 5.8: A comparison of the analytical equation and TOUGH2 results of the dimensionless production temperature Θ_p as a function of dimensionless time t/τ for the fracture network drawn in Figure 5.5. The solid blue curve represents the production temperature using the analytical equation, while the dashed curve and the dash-dot curve represent the production temperature from TOUGH2 using a mass flow and extraction period of 50 kg/s and 40 years and 100 kg/s and 10 years, respectively.

The deviation from the analytical solution can be explained by thermal interference among the fractures in the network. Figure 5.9 shows the results from TOUGH2 of the dimensionless temperature field for the simpler fracture network and for the more complicated network under the two different operating conditions. For the simpler network, it is clear that fractures do not thermally interfere but that is not the case for the more complicated network when extraction times are

long. However, for the results for operating conditions of 100 kg/s and 10 years, the area in between the fractures is less thermally depleted and as a result, there is less thermal interference and the production temperature is closer to the analytical results. Since the thermal penetration distance is estimated by $2\sqrt{\alpha t}$, the ratio $\delta_t/(0.5x_s)$ can be used to estimate the level of thermal interference, where x_s is the fracture spacing. When the ratio is much less than one, there will be negligible thermal interference. For the simpler network, the ratio is equal to 0.2 but is equal to 0.6 and 0.3 for the more complicated network under the 50 kg/s and 40 year and 100 kg/s and 10 year operating conditions, respectively. The comparison of the analytical model and TOUGH2 results shows how Eq. (5.17) is capable of modeling the temperature field of discretely fractured reservoirs and despite the error, the deviation is systematic and the analytical model still captures the behavior of the temperature drawdown curve.

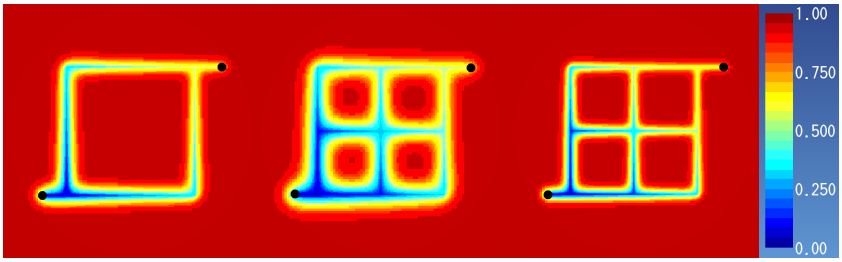

Figure 5.9: Dimensionless temperature fields at the end of extraction from the TOUGH2 results for the discrete fracture networks shown in figures 5.4 (first temperature field) and 5.5 (the second and third temperature fields). The mass flows and extraction times are 50 kg/s and 20 years for the first field, 50 kg/s and 40 years for the second, and 100 kg/s and 10 years for the third. The first reservoir has a fracture surface area of 1.1 km^2 while the second and third have an area of 1.6 km^2. The color scale is given on the right and ranges from 0 to 1. The injection and production wells are denoted by a black dot.

5.4 Case Study 1: Aperture Uncertainty

The derived discrete fracture model can be used to study the effect of reservoir property uncertainty on the thermal performance of the reservoir. Two cases are presented that focus on different reservoir property uncertainty. The first case study examined here focuses on a reservoir where the network configuration is known but the aperture values are not. Since the conductance of a fracture is proportional to the cube of the aperture, uncertainty in the aperture values of the network will result in a distribution of flow in the reservoir and consequently, a distribution of thermal performance. This case study aims to quantify the thermal performance distribution by sampling the aperture values from a given distribution.

Fracture aperture values from core samples have been shown to have either a normal (Glover et al., 1998; de Dreuzy et al., 2013) or log-normal (Moreno et al., 1988; Watanabe et al., 2008; Hooker et al., 2009) distribution. Since log-normal distributions do not produce negative values, we have chosen to sample the aperture from a log-normal distribution. The range chosen for the dimensionless standard deviation of the aperture σ_w/w_0 was from 0.01 to 0.4, where w_0 represents the mean aperture and the value of the base case, 1 mm. This range was chosen in order to model a wide class of scenarios. Core samples from natural fractures have revealed values of σ_w/w_0, from as low as 0.042 (Xiong et al., 2011), 0.26 (Yeo et al., 1998), 0.35 (Xiong et al., 2011), and as high as 0.42 (Hakami and Larsson, 1996). However, core samples are effectively point measurements of the reservoir, in contrast to the length scale of the dominant fractures in geothermal reservoirs. Thus, it is difficult to say how representative a core sample is of the entire reservoir and it is important to model a large range of values for the standard deviation of the sampled aperture.

Since the fluid flow model assumes unidirectional flow, it cannot model local aperture variations in the fracture because aperture variations alter the otherwise unidirectional flow. These aperture variations have been shown to generate preferential fluid flow channels (Brown, 1987; Tsang and Tsang, 1989; Glover et al., 1998; Drazer and Koplik, 2000; Méheust and Schmittbuhl, 2001; Auradou et al., 2006; Watanabe et al., 2008; Koyama et al., 2009). Zimmerman and Bodvarsson (1996) point out the mean aperture of the fracture with spatially varying apertures cannot be used as a direct substitute for the cubic law governing discrete fracture flow. Instead, the hydraulic aperture w_H is used rather than the spatial mean aperture. The hydraulic aperture is the effective aperture of a fracture given its conductance or transmissivity. In other words, it is the value of w to use in the equation for conductance. For a given fracture, isotropic spatial aperture variations will cause the hydraulic aperture to be lower than the mean aperture. Values for the cube of the ratio of (w_h/w) have been modeled using quadratic (Zimmerman and Bodvarsson, 1996) and exponential (Patir and Cheng, 1978; Brown, 1987) fits, and the the ratio (w_h/w) typically ranges from 0.5 to 0.95 (Brown, 1987; Glover et al., 1998). However, the work of Méheust and Schmittbuhl (2000, 2001, 2003) showed how the flow may either be inhibited or enhanced depending on the orientation of the applied pressure drop for a particular fracture. Unless one complicates the modeling by including two dimensional flow, the effects of intrafracture flow channeling, due to aperture variations in each fracture, can be incorporated by using the hydraulic aperture. Thus, the range of σ_w/w_0 used in the analysis can be considered as already incorporating the hydraulic effect that surface aperture variations have on the flow distribution in each fracture of the network. However, since the flow is still being modeled as unidirectional, the model cannot consider the effect flow variations in each individual fracture have on the coupled convective-conductive

heat transfer.

For each value of σ_w/w_0 in the range from 0.01 to 0.4, ten thousand different fracture network realizations were generated and their thermal performance was calculated. Each realization has a different set of aperture values sampled from a log-normal distribution defined by σ_w/w_0, where σ_w and w_0 are the standard deviation and mean of the distribution. The analysis is first carried out in the fracture network shown in Figure 5.4 and then on the network shown in Figure 5.5, which has more flow paths. The resulting distribution of dimensionless production temperatures is analyzed by using the interquartile range and comparing it against the base case fracture network, where the aperture is the same throughout the fractures. The interquartile range is a measure of variability of a distribution where the lower value is the first quartile (25% quantile) and the upper value is the third quartile (75% quantile). The dimensionless production temperature of each network realization was calculated next for the same reservoir extraction time, the time required for the base case to reach $\Theta_p = 0.8$. For the thermophysical properties used in the validation exercise and a mass flow of 50 kg/s, the base case reaches $\Theta_p = 0.8$ after 8.2 years. Additionally, we report the distribution of reservoir lifetime based on the time energy extraction must be halted when a reservoir's dimensionless production temperature drops below 0.8. Since the pressure drop across the injection and production well is a known value in a geothermal operation, the reservoir's pressure drop can help narrow the distribution of likely production temperatures. We apply our procedure for aperture uncertainty for an additional case by only considering fracture networks that have a pressure drop close to the base case pressure drop. We then compare the new distribution of thermal performance that considers pressure drop with the distribution that does not.

5.4.1 First Fracture Network

Figure 5.10 shows a histogram of the thermal performance of the ten thousand network ensemble when $\sigma_w/w_0 = 0.25$. There are no network realizations with a dimensionless production temperature greater than the base case, $\Theta_p = 0.8$. The base case has an aperture value of 1 mm throughout the network. Because no network had a production temperature higher than the base case, the optimal aperture distribution for the system is when all the segments of the network have the same aperture value. Any unequal flow distribution in the network results in diminished thermal performance. The equal flow split is the optimal value because both paths to the production well have the same heat transfer area in this particular network. If the different paths had different heat transfer areas, the optimal flow split values will have the longer path accepting more of the flow.

The resulting distribution of the production temperature is controlled by the distribution in flow split fractions. For a network with two flow paths, the flow split fraction for path A is equal to $1/(1 + (w_A/w_B)^3)$ where the subscripts refer to the aperture of the respective flow path. The flow split for path B is simply one minus the split of path A, due to the conservation of mass. The dimensionless production temperature is $\Theta_p \sim \chi_A \text{erf}(1/\chi_A) + (1-\chi_A)\text{erf}(1/(1-\chi_A)$. The inverse of the flow split is due to β being inversely proportional to the mass flow rate of a path. The resulting distribution of thermal performance is not intuitive and a log-normal distribution in apertures does not lead to a log-normal distribution in production temperatures.

Plotted in Figure 5.11 are the median and interquartile range of the dimensionless production temperature for the range of σ_w/w_0 investigated. As expected, as the standard deviation of the sampled distribution of aperture values increases,

the range of possible production temperature values increases. While the median production temperature only drops about 5% compared to the base case value, there is a wide distribution of likely production temperatures, especially when $\sigma_w/w_0 > 0.25$.

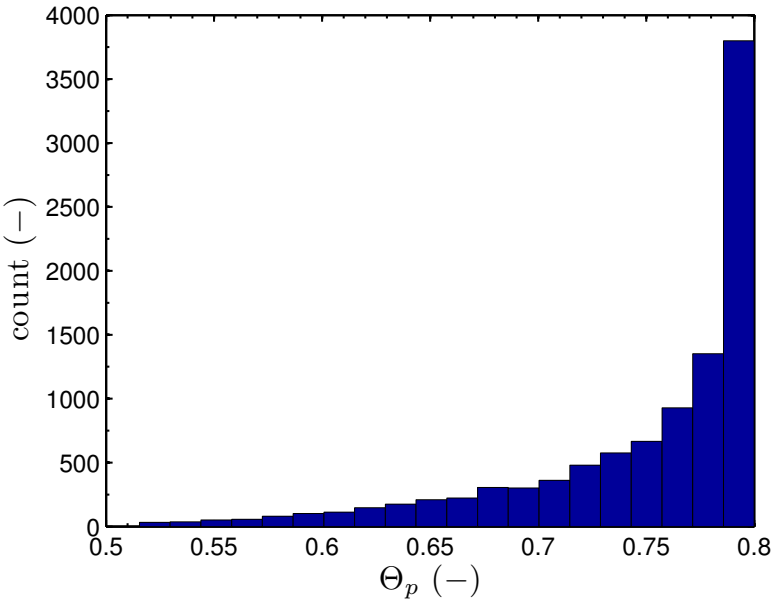

Figure 5.10: Histogram of dimensionless production temperature Θ_p when the dimensionless standard deviation of the aperture σ_w/w_0 is equal to 0.25. The results are for the network shown in Figure 5.4 and the base case value (uniform aperture) corresponds to $\Theta_p = 0.8$.

If the geothermal operation has to be halted after the production temperature drops below a critical value, then this faster than expected drawdown will result in a shorter reservoir life. For normal drilling costs to depths of 3 to 6 km, using a reservoir's anticipated lifetime is a major indicator of the economic viability of a geothermal project. Plotted in Figure 5.12 is the distribution of the reservoirs' life t_l given a halting criteria of $\Theta_p = 0.8$. The results show that the dimensionless standard deviation of fracture apertures must be greater than 0.26 for the majority of the cases to have an effective reservoir lifetime less than 90% of the base case value. For $\sigma_w/w_0 > 0.36$, the majority of the realizations had a reservoir life time

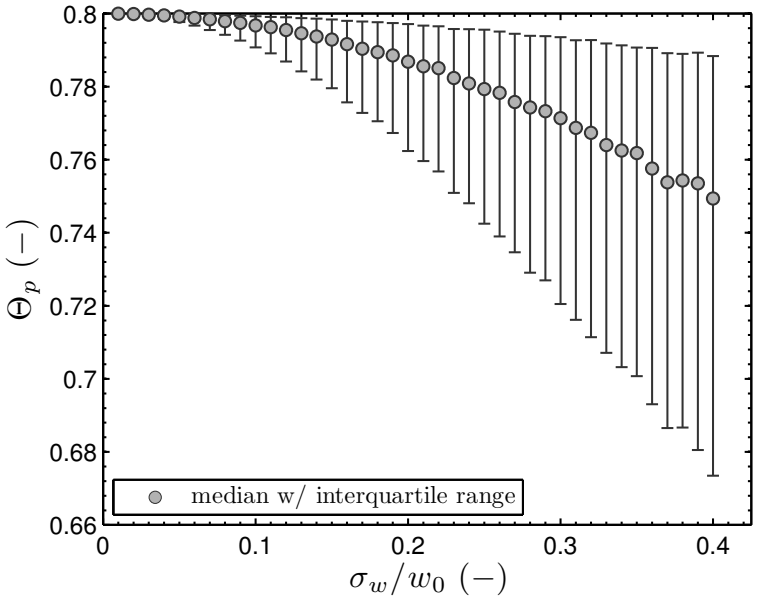

Figure 5.11: The median (circle) and interquartile range (lower and upper bars) of the dimensionless production temperature Θ_p for a range of the dimensionless standard deviation of the aperture σ_w/w_0. The results are for the network shown in Figure 5.4 and the base case value (uniform aperture) corresponds to $\Theta_p = 0.8$, after 8.2 years of extraction with a mass flow rate of 50 kg/s.

less than 80% of the base case. However, as with the production temperature, the interquartile range for the reservoir's life is still large.

The pressure drop in a reservoir provides additional information that may help bracket the thermal performance. One can generate only reservoirs that adhere to a pressure drop criteria. We have repeated the process of generating ten thousand network realizations but now generate only networks with a pressure drop with less than a 10% difference from the base case. In terms of the hydraulic aperture, the percent error is about 3%. Unfortunately, given that the cross correlation for w_H of the reservoir and Θ_p is never greater than 0.15, corresponding to $\sigma_w/w_0 = 0.4$, and using the hydraulic aperture may not narrow the possible values of the production temperature. A boxplot comparing the distribution of thermal performances when $\sigma_w/w_0 = 0.1, 0.2, 0.3,$ and 0.4 is shown in Figure 5.13. For comparison, the figure

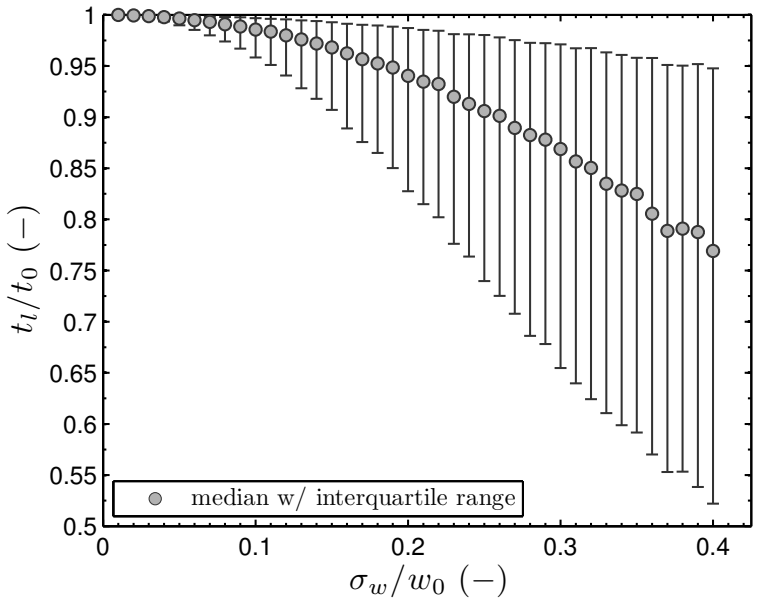

Figure 5.12: The median (circled) and interquartile range (lower and upper bars) of the ratio of time it took to reach the drawdown criteria t_l to the base case time t_0 (uniform aperture distribution) for a range of the dimensionless standard deviation of the aperture σ_w/w_0. The drawdown criteria is when the reservoir's dimensionless production temperature reaches 0.8. The results are for the network shown in Figure 5.4.

contains the boxplot of the thermal performance results without the pressure drop criteria. The comparison between the distributions shows that using the pressure criteria to narrow down possible outcomes is not effective. For values of $\sigma_w/w_0 < 0.3$, the distributions are nearly identical. When $\sigma_w/w_0 > 0.3$, the two populations for Θ_p can be differentiated; the distribution is shifted to slightly lower production temperatures. When $\sigma_w/w_0 = 0.4$, the median dimensionless temperature drops from 0.749 (no pressure criteria) to 0.732. However, the distributions are essentially the same and are qualitatively similar.

The pressure drop in the reservoir is dependent on the absolute value of the aperture. On the other hand, the temperature field is not for the model. Instead, the temperature field is a function of the relative aperture values which determine

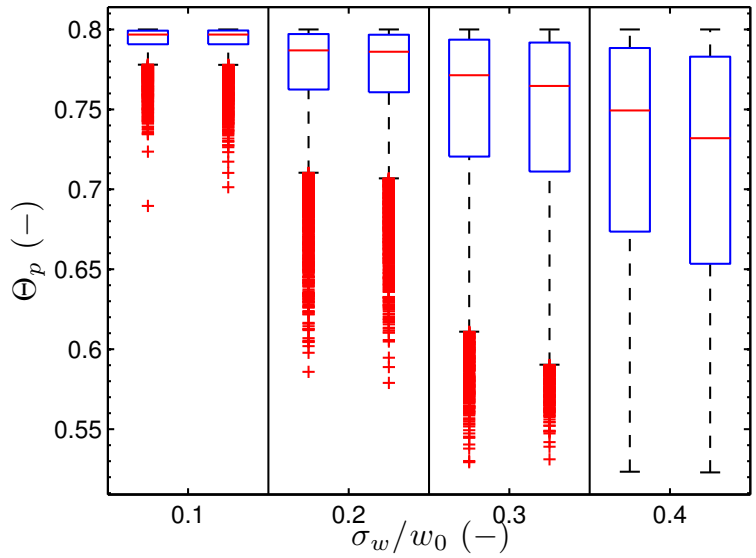

Figure 5.13: Boxplot of dimensionless production temperatures Θ_p by applying the reservoir pressure drop criteria. The boxplots are arranged in four pairs separated by a black divider, one pair for each value of the dimensionless standard deviation σ_w/w_0 of the sampled aperture. The first boxplot in each pair represents the distribution from the set of network realizations that do not consider the pressure drop criteria while the second boxplot represents the data set the does consider the pressure drop criteria. The lower and upper part of the box represents the first and third quartiles while the solid red line represents the median value. The lower and upper whiskers of the boxplot are defined as 1.5 times the first and third quartile value, respectively, and the red plus signs represent the outliers.

the flow distribution in the network. Thus, a reservoir in which all the aperture values are increased or decreased by the same factor will have a different pressure drop but will still have the same thermal behavior. The hydraulic aperture or the overall reservoir pressure drop is not useful in obtaining a better prediction of thermal performance. Consequently, the use of conservative and reactive tracers is imperative for subsurface characterization. Residence time distribution curves of conservative tracer tests will contain information regarding the flow paths and can be used to determine the flow in the reservoir (Robinson and Tester, 1984, 1986).

5.4.2 Second Fracture Network

The analysis of generating a distribution of thermal performances due to uncertainty in fracture aperture was repeated for the more complicated network shown in Figure 5.5. The second network has six rather than two flow paths from the injection to the production well and the base case reservoir reaches $\Theta_p = 0.8$ in 17 years. As with the first network, the optimal production temperature occurs when the flow is the same in all paths because all flow paths are the same length. Figures 5.14 and 5.15 show the distribution of the thermal performance and reservoir life, respectively. As with the simpler network, there are no cases with a higher production temperature than the base case. When $\sigma_w/w_0 > 0.2$, the majority of the networks have a reservoir life of 90% lower than the base case and 80% lower when $\sigma_w/w_0 > 0.29$.

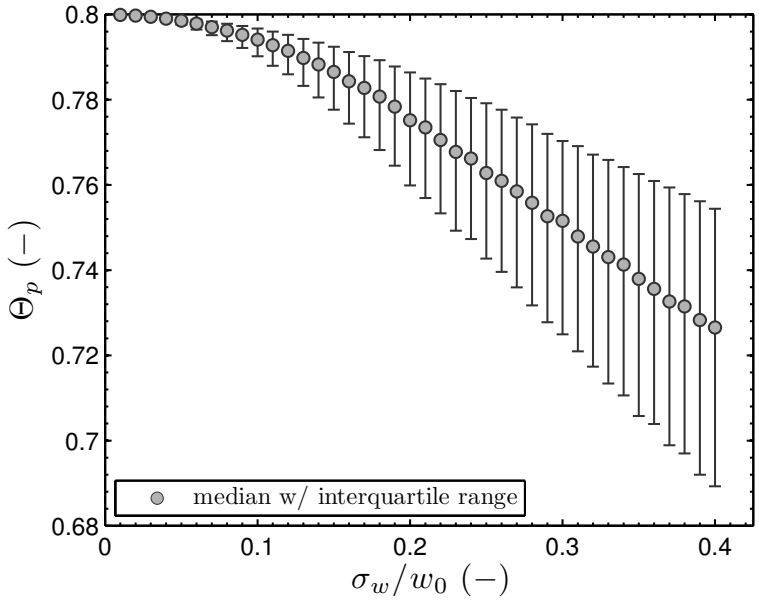

Figure 5.14: The median (circle) and interquartile range (lower and upper bars) of the dimensionless production temperature Θ_p for a range of the dimensionless standard deviation of the aperture σ_w/w_0. The results are for the network shown in Figure 5.5 and the base case value (uniform aperture) corresponds to $\Theta_p = 0.8$, after 17 years of extraction with a mass flow rate of 50 kg/s.

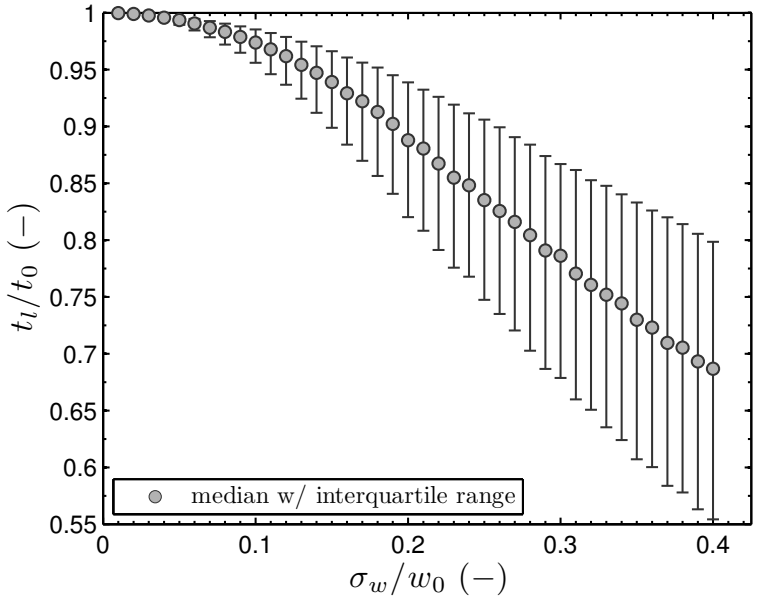

Figure 5.15: The median (circle) and interquartile range (lower and upper bars) of the ratio of time it took to reach the drawdown criteria of the base case time (uniform aperture) for a range of the dimensionless standard deviation of the aperture σ_w/w_0. The results are for the network shown in Figure 5.5.

Compared to the simpler network, the median dimensionless temperature is lower but production temperatures are less widely distributed. Figure 5.16 has a side by side comparison of the boxplots of the dimensionless production temperatures of the two fracture networks for several values of σ_w/w_0. The distributions are noticeably different when $\sigma_w/w_0 \geq 0.2$, with the more complicated network being less spread out. The interquartile range for the more complicated network is smaller than that of the simpler network. There are six possible paths from the injection to the production well. By having more flow paths, the reservoir is more insulated to adverse thermal performance. When there is blockage of flow in one path, the reservoir can still rely on the other paths to more evenly distribute the flow in the system and prevent fast thermal drawdown. However, the boxplots show that when $\sigma_w/w_0 = 0.4$, the outliers for the more complicated network extend further out than the simpler network. Having more flow paths can help insulate a

network when one path is not accepting a lot of flow, however, it is still possible to have a situation where all paths but one are nearly blocked. The apertures of the other paths can be too small to accept any flow and the all the fluid is channeled into just one path. Since the extraction time of the base case is more than twice as long for the more complicated network, the production temperature for the more complicated network having effectively one flow path will be lower than if it had occurred in the simpler network. Since the distribution is made up of a large number of realizations, ten thousand, it becomes likely to sample the described scenario multiple times.

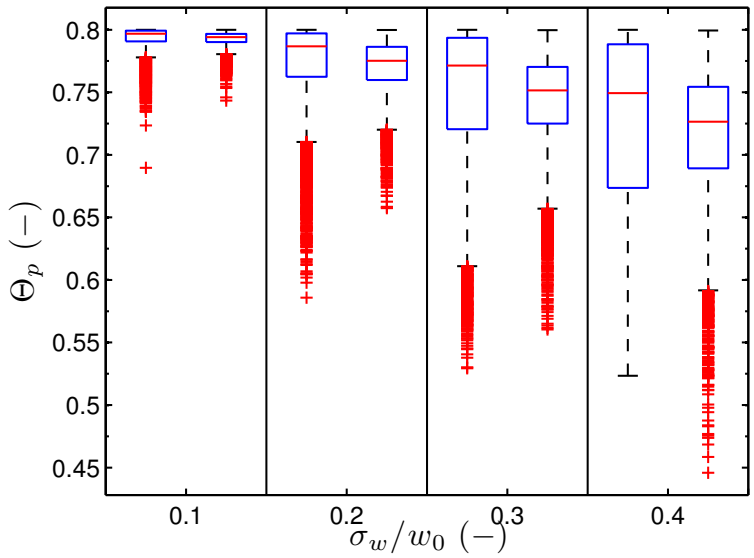

Figure 5.16: Boxplot of dimensionless production temperatures Θ_p for the two different fracture networks. The boxplots are arranged in four pairs separated by a black divider, one pair for each value of the dimensionless standard deviation σ_w/w_0 of the samepled aperture. The first boxplot in each pair represents the distribution from the simpler network depicted in Figure 5.4 while the second boxplot represents the more complicated network depicted in Figure 5.5. The lower and upper part of the box represents the first and third quartiles while the solid red line represents the median value. The lower and upper whiskers of the boxplot by applying the reservoir pressure drop criteria are defined as 1.5 times the first and third quartile value, respectively, and the red plus signs represent the outliers.

5.5 Case Study 2: Fracture Structure Uncertainty

Another scenario of interest to apply the developed discrete fracture model is when the structure of the fracture network is unknown. Under this scenario, one has not identified all fractures in the network, but only the fractures intersecting the injection and production well. The structure of a network refers to both the connectivity or the arrangements of the fractures and the size of the fractures. Downhole tools can easily identify the fractures that intersect the wells, but it is more difficult to identify the "interwell" fractures. The uncertainty in the exact network structure will result in different possible network models, each with its own thermal performance. For this case study, we have generated a set of ten thousand fracture networks by sampling the number of interwell fractures, their orientation, and position and simulated their thermal performance to measure the consequence of fracture network uncertainty.

All networks generated have two fractures whose orientation, position, and length is known; they are the fractures that are connected to the injection well and production well. These two fractures are 500 m long, parallel, and separated by 500 m. The injection well is located at the bottom of one of the fractures while the production well is located at the top, resulting in the wells being separated by 707 m. These fractures are referred to as the injection and production well fractures or collectively as the wellbore fractures. The wellbore fractures form a hydraulic connection via the interwell fractures. Depictions of possible fracture network configurations for this case study are shown in Figure 5.17.

The mean number of interwell fractures was set to 4.3. For each network realization, the number of fractures that intersect the injection well fracture was sampled from a Poisson distribution with a mean of 4. The Poisson distribution

takes on integer values of the number of "events" occurring independently at a constant rate over a fixed time period. Only realizations with at least one interwell fracture are generated to allow for hydraulic connectivity from the injection to production well. By discarding networks with zero interwell fractures, the mean number of fractures from the resulting truncated Poisson distribution was 4.3. The position of the interwell fractures are sampled from a uniform distribution on the entire length of the injection fracture.

The fracture orientations are sampled using the von Mises probability distribution, a continuous distribution on a circle that is symmetric about the mean. The distribution is given by

$$f(\theta) = \frac{\exp\left[\kappa \cos\left(\theta - \mu\right)\right]}{2\pi I_0(\kappa)}, \tag{5.21}$$

where θ is the angle, κ is a measure of the distribution's concentration, μ is the mean direction, and I_0 is the modified Bessel function of order zero. The distribution is more diffuse for larger values of κ, and more concentrated for smaller values. Cacas et al. (1990) fitted a natural set of fractures to the von Mises distribution and others have used the distribution to sample fracture orientations (Nordqvist et al., 1992; Bruel et al., 1994; Maryška et al., 2005). These studies have used a range of κ values from 3 to 30. For this study, we have chosen $\kappa = 20$ and $\mu = 0$ (direction perpendicular to the wellbore fractures). For $\kappa = 20$, the interquartile range of the fracture orientation is -0.05π to 0.05π.

The length of the interwell fractures are determined by their position along the injection well and their orientation; they extend until they reach the horizontal position of the production well fracture. Some of the interwell fractures may not intersect the production well fracture because the production well fracture has a finite length of 500 m. However, interwell fractures that do not intersect the pro-

duction fracture may still contribute to the hydraulic connectivity of the network by intersecting other interwell fractures. Only networks that form a hydraulic connection from the injection to production well are allowed for the analysis; the angle of the interwell fractures are resampled until there is a hydraulic connection. Resampling the angles ensures that the mean number of interwell fractures remains at 4.3. The aperture of the fractures are all set to 1 mm.

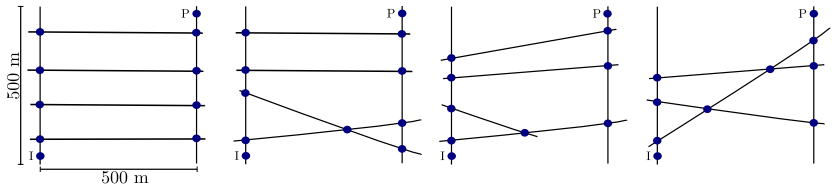

Figure 5.17: Four examples of possible fracture networks that can occur by sampling the number of fractures, their directionality, and position. The vertical fractures are connected to the injection well and production well. The nodes representing the injection and production wells are denoted by an "I" and a "P".

Figure 5.18 shows the distribution of the dimensionless production temperature as a result of sampling different reservoir structures. The distribution is multimodal with four different populations of production temperatures. The multimodal behavior can be attributed to the different number of possible flow paths in the system. Table 5.2 breaks down the percentage of flow paths in the ensemble of fracture networks along with their respective median dimensionless production temperature. The median number of flow paths is five with the most frequent number of flow paths being two. Although, the mean number of interwell fractures is four, the orientation of the fractures will influence the ability of the fractures to form a hydraulic connection across the wellbore fractures. This decreases the number of flow paths. In general, reservoirs with more paths have more heat transfer area and higher production temperatures. Figure 5.19 shows the distribution of dimensionless production temperatures by isolating the networks by their number of paths. One can clearly see how the different populations in the histogram shown

Table 5.2: Percentage of flow paths in the ensemble of fracture networks and the median dimensionless production temperature for networks with the specified number of flow paths.

flow paths	percentage	median Θ_p
1	13.3	0.35
2	14.6	0.55
3	9.8	0.69
4	9.2	0.58
5	9.6	0.69
6	6.6	0.78
7	4.8	0.82
8	4.0	0.77
9	3.9	0.79
>10	24.5	0.86

in Figure 5.18 are a result of the populations based on the number of flow paths. The one flow path networks populate the lowest production temperatures while the networks with five or more flow paths are located in the higher temperature region of the histogram.

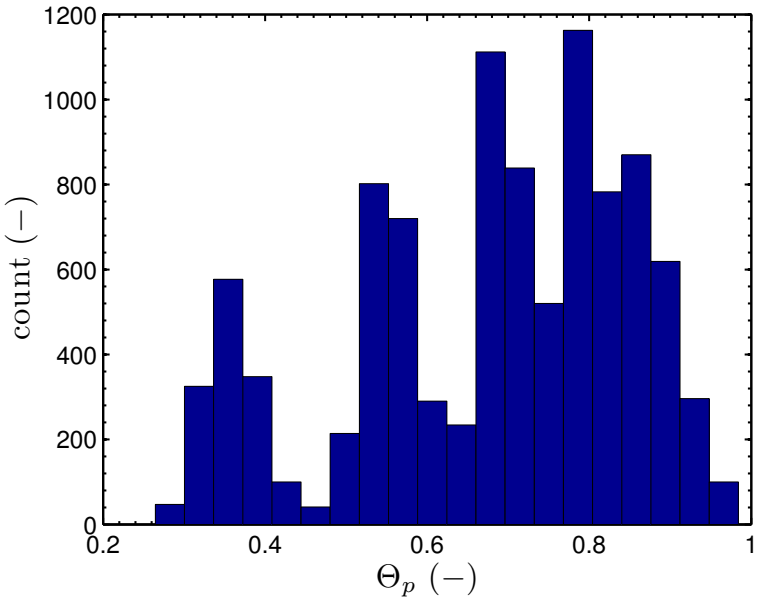

Figure 5.18: A histogram of the dimensionless production temperature Θ_p due to the uncertainty in the fracture network structure.

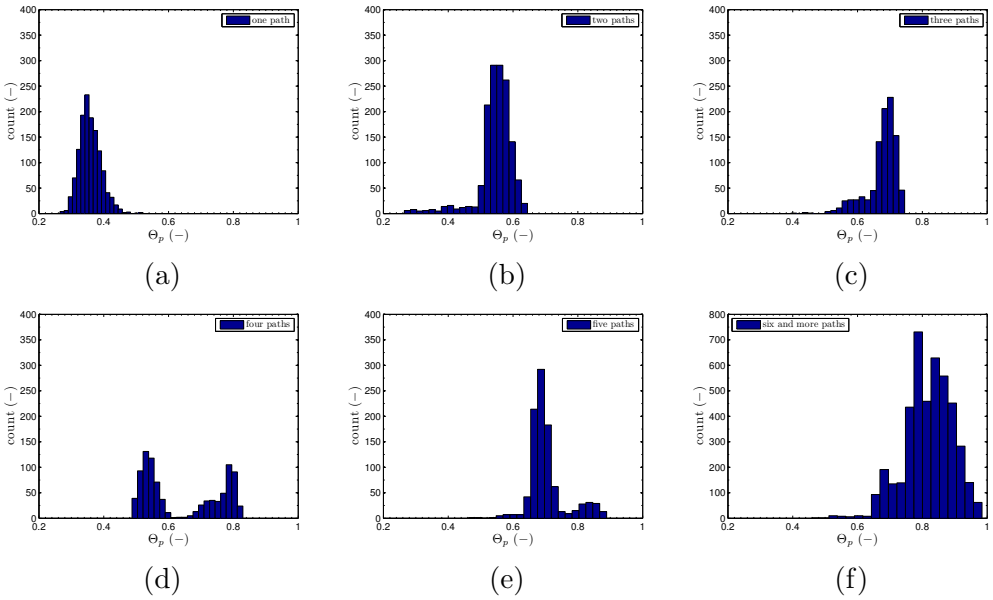

Figure 5.19: Histograms of the dimensionless production temperatures Θ_p for the generated ensemble of fracture networks. The subpopulations are based on the number of paths from the injection to production well in the networks where (a) is the subpopulation for one path, (b) two paths, (c) three paths, (d) four paths, (e) five paths, and (f) six or more paths.

A wide range of thermal behavior is possible given the uncertainty in the structure of a reservoir. The dimensionless production temperature is controlled by both the number of flow paths in the system and the heat transfer area available in the network. The equation for Θ in Eq. (5.17) shows both the dependence on the flow paths and the heat transfer area. The influence of the flow paths on the temperature is seen by the summation operator that results in n_p terms, where n_p is the number of paths from injection to production well. The dependence on the heat transfer area is seen through the summation operator of the sequence of ξ_i, which is linearly proportional to $L_i H$, the heat transfer area of segment i. Thus, it is important to be able to quantify both the number of flow paths and heat transfer area of a reservoir. Information on these properties can be obtained from tracer tests.

As was shown previously, the uncertainty of the aperture values of the fractures led to a distribution of thermal performances. We can relax the assumption of uniform aperture in the network and sample the apertures from a log-normal distribution. Now the thermal performance is dependent on the generated network and the aperture values and a sensitivity analysis can be used to assess the relative importance of these two reservoir parameters.

A sensitivity analysis is a tool to measure the relative contributions of the uncertainty of various inputs on the variability of the output. Most sensitivity analysis tools are variance based and may not be adequate when the model output distribution is highly skewed or is multimodal. As was shown, the distribution for the production temperatures was both multimodal and highly skewed for the network and the aperture uncertainty study, respectively. Instead of a variance based method, we use a sensitivity analysis method called PAWN (acronym based on the creators' names) that is based on the cumulative distribution of the output (Pianosi and Wagener, 2015) and uses the Kolmogorov-Smirnov test. The Kolmogorov-Smirnov test compares two continuous probability distributions (CDF) and returns the largest value of the difference of the two CDFs, called the K-S statistic. If the K-S statistic is larger than a critical value c, then the test rejects, at a given confidence interval, the null hypothesis that the two distributions are statistically the same . The critical value is a function of the desired confidence interval and the the number of samples of the two distributions. The PAWN algorithm uses the Kolmogorov-Smirnov test to compare two distributions, the unconditional distribution and a conditional distribution. The unconditional distribution is generated by sampling all the parameters of the model from their respective distributions. The conditional distribution is obtained by keeping one of the parameter values constant but sampling the non-fixed parameters. Thus,

if there is little difference between the CDFs of the unconditional and conditional distributions, the parameter has little influence on the output of the model and the K-S statistic is small and near or below the critical value. A set of conditional distributions for the fixed parameter are created by repeating the process but by using a different value of the fixed parameter. A new statistical value T is generated for each model parameter by taking the median of all of the KS statistics from the set of conditional distributions. The value of T ranges from zero to one and if the value of T is less than a critical value c, the input is said to be non-influential.

The dimensionless production temperature can be expressed as

$$\Theta_p = f(N, \boldsymbol{\theta}, \mathbf{z}, \mathbf{w}), \tag{5.22}$$

where N refers to the number of interwell fractures, $\boldsymbol{\theta}$ are the values of the directionality of the interwell fractures, $\mathbf{z}$ are the locations of the interwell fractures along the injection well fracture, and $\mathbf{w}$ are the aperture values of all the fractures in the network. Of those parameters, N, $\boldsymbol{\theta}$, and $\mathbf{z}$ can be grouped together because they control the structure of the system. Thus, $\Theta_p = f(\text{strc}, \mathbf{w})$, where "strc" is short for the structure of the network. In generating the conditional distributions for the structure, the number of interwell fractures are sampled along with a set of values for their position and orientation and are used to form a network with a specific structure. For the conditional distributions for $\mathbf{w}$, a set of values for the fracture aperture are sampled and assigned to the fractures of the network.

Table 5.3 displays the results from the PAWN sensitivity analysis using six sets of parameters of the von Mises distribution parameter κ, which influences the fracture structure, and the dimensionless standard deviation of the sampled aperture σ_w/w_0. In general, the results show that under all sets of parameters, the fracture structure dominates in controlling the reservoir's thermal performance.

Table 5.3: PAWN sensitivity indices T for the uncertainty of structure and aperture of the fracture network under different sets of the von Mises directionality parameter κ and the standard deviation of the sampled fracture aperture σ_w/w_0. For comparison, the critical value of sensitivity index is 0.14 and the 95% confidence intervals are derived using resampling based on the bootstrapping method.

κ	σ_w/w_0	T_{strc}	$T_{\mathbf{w}}$
2	0.25	0.57 ± 0.02	0.10 ± 0.01
20	0.25	0.55 ± 0.03	0.12 ± 0.01
200	0.25	0.52 ± 0.02	0.15 ± 0.01
2	0.4	0.48 ± 0.02	0.12 ± 0.01
20	0.4	0.47 ± 0.02	0.15 ± 0.01
200	0.4	0.42 ± 0.02	0.19 ± 0.01

On the other hand, the aperture uncertainty is often below or slightly above the critical value and only is statistically significant when $\sigma_w/w_0 = 0.4$ and $\kappa = 200$. The influence of aperture uncertainty increases for increasing values of κ because larger κ values reduces the variability in the sampled directionality of the interwell fractures. When the directionality of the interwell fractures are similar, it is more likely the generated reservoirs will have the same connectivity and not form a wide range of reservoir structures.

The structure of the reservoir establishes the number of flow paths in the system and the heat transfer area of those paths. The fracture apertures can be viewed as having a secondary effect as it controls the flow distribution among the paths created by the connectivity of the network. In the equation for Θ, the connectivity sets the number of terms in the summations and the relative aperture values control the weighting of those paths. The results from the sensitivity analysis should not be interpreted to mean that aperture variability plays no role in a reservoir's thermal performance; the results in the previous section showed how it produces a wide range of production temperatures even when the fracture structure was completely identified. Instead, the results indicate that, when it exists, uncertainty in the

structure of the reservoir is the primary factor driving the uncertainty in thermal performance.

Constraining the variability of the structure can increase the relative importance of aperture uncertainty but it is dependent on how sensitive the new population of structures is to the aperture variability. For example, if the network can only have one interwell fracture, the aperture variability will have no influence on the thermal performance because there will only be one flow path. If we reduce the uncertainty of the structure by only generating networks with four interwell fractures, the PAWN indices change from $T_{\text{strc}} = 0.55 \pm 0.03$ and $T_{\mathbf{w}} = 0.12 \pm 0.01$ to $T_{\text{strc}} = 0.40 \pm 0.03$ and $T_{\mathbf{w}} = 0.19 \pm 0.01$ when $\kappa = 20$ and $\sigma_w/w_0 = 0.25$. The effect is more pronounced when $\sigma_w/w_0 = 0.4$ as the new indices are now equal to $T_{\text{strc}} = 0.27 \pm 0.02$ and $T_{\mathbf{w}} = 0.24 \pm 0.02$ when $\kappa = 20$, and the thermal performance is now equally controlled by the structure and aperture variability. When the number of interwell fractures is known to be four, the thermal performance of the reservoir becomes more dependent on the aperture uncertainty over the case when the number of interwell fractures is not precisely known. The relative importance of the aperture variability and structure will be dependent on the level of information one has on each of those parameters for the system of interest. For example, the fracture network structure may be highly constrained if one believes one has identified all the major fractures that contribute to the flow.

For this sensitivity analysis, the individual elements controlling the structure were not decoupled and their respective importance was not quantified. The same is the case for the aperture values; for a given network, some fracture apertures may have a greater control over the reservoir's thermal performance because they modulate the flow to a large portion of the heat transfer area. Nonetheless, the

purpose of this case study was to show the capability of the derived analytical model to reveal the relative importance of certain properties of discrete fractured networks.

5.6 Conclusion

The purpose of the study was to demonstrate the usefulness of an analytical model for fluid flow and heat transfer in a discrete fracture network that would fill the gap between simpler analytical models that do not treat interconnected fracture networks and numerical simulators for discrete fracture networks. The study first presents the derivation of the model and compares the results of the model with an established reservoir code. Subsequently, we use the model in two different case studies to exhibit the model's capability to probe how certain reservoir characteristics affect thermal performance.

For an idealized two dimensional discrete fracture model, we have derived the fluid flow throughout the system by calculating the pressure at each node in the network. The flow in each segment was modeled by using a linear relationship with the pressure drop, and constructing a system of algebraic equations describing the pressure at each node by applying conservation of mass around each node in the network. The resulting flow is specified to be unidirectional within each fracture and independent of time. The temperature field in the network was derived by modeling each segment of the network as an isolated rectangular fracture, where the convective heat transport within the fracture aperture is coupled with conduction in the rock mass perpendicular to the flow. The injected water temperature entering each segment varies with time according to the development of the thermal

field upstream from each segment. By knowing the structure and the mass flow through each part of the network, we were able to describe a systematic method to build an expression for the temperature of the fracture surface of the network. The resulting equation is a function of the number of flow paths in the network and the heat transfer area. The equation assumes one dimensional heat conduction and negligible thermal interference between fractures. These assumptions are reasonable for typical flow conditions in reservoirs dominated by large fractures. The resulting analytical model runs in the order of 100 seconds for ten thousand evaluations on a computer with 4 GB of RAM and a 2.67 GHz processor, while typical run times for numerical codes like TOUGH2 vary strongly with the mesh resolution and may be on the order of minutes or hours for a single run.

The derived equation for the temperature was validated using the TOUGH2 reservoir code for mass and heat transfer in porous media. The analytical model was better at modeling the temperature when the fracture spacing is larger than the thermal penetration distance and for shorter extraction periods undergoing higher flow rates. When modeling a reservoir with six flow paths, the results from the analytical model deviated by a small, but non-negligible, amount but the error was systematic by being consistently higher than the TOUGH2 results. The results of the analytical equation assume negligible thermal interference between the fractures and thus, results in slightly higher temperature values for the specific cases considered in this study. Additionally, the temperature drawdown from the analytical model captured the same qualitative behavior of the TOUGH2 results; there is a time lag in which the production temperature stays nearly constant before declining.

For the first case study, the effect of aperture value uncertainty was deter-

mined by generating an ensemble set of fracture networks where the apertures were sampled from a log-normal distribution but the fracture configuration was kept the same. The resulting distributions of production temperatures were highly skewed towards lower production temperatures and the optimal reservoir production temperature occurred when the network had a uniform aperture value. The distribution of reservoir performance increases with larger values of the standard deviation of the sampled aperture. Networks with more flow paths resulted in a thermal performance distribution with less variability since, if one flow path is receiving little flow, there are still more paths to avoid highly uneven overall network flow distribution. The case studied provided additional insight to fractured networks by illustrating how variations in fracture aperture can cause large variations in thermal performance and reservoirs with less flow paths are more susceptible to aperture variations.

The second case study focused on modeling the effect of not knowing the network configuration of a reservoir. The number of fractures and their position and directionality were sampled from a given distribution. Based on the sampled values of the position and fracture direction, the reservoir production temperature was widely distributed. The distribution was multimodal and was made up of several subpopulations characterized by the number of paths from the injection to production well. When the assumption of uniform aperture was relaxed, a sensitivity analysis determined that the uncertainty in the network structure had more control over the reservoir's thermal performance than the uncertainty in aperture values of the fractures. In addition, if one constrains the variability of network configurations, aperture uncertainty will play a larger role in production temperature uncertainty. The case study establishes the role of both reservoir structure and fracture uncertainty in affecting thermal performance as well as the methodology

to study the coupling of both phenomena.

The analytical solution for the temperature explicitly shows the dependence of reservoir characteristics like the number of flow paths, the heat transfer area, and the flow distribution in the network. The model can be used as a basis for deriving alternate forms with added features. For example, the flow model can be generalized for fractures with tapering or expanding apertures for the purpose of modeling thermal contraction or hydraulic expansion of the fracture apertures. The flow can be modeled using the lubrication approximation to derive an alternate form for a fracture's conductance or to derive an expression for the hydraulic aperture of the fractures to use instead of the geometric aperture. In addition, one can easily generalize the derived model for systems with multiple injection and productions wells to model and optimize the injection and production rates of the wellbores. Details of the derivation of the model were included to facilitate possible future extensions and applications of the model. The case studies demonstrated how one can utilize the model to address important questions. Through the two case studies, we have shown the capabilities of the developed analytical model to explore more realistic situations such as the uncertainty of fracture apertures and network structure. Other possible case studies and applications could include using the the developed model for an inverse search using conservative and reactive tracers to characterize the subsurface and to better forecast the thermal performance of a discretely fractured geothermal reservoir.

Bibliography

Andersson, J. and Dverstorp, B. (1987). Conditional simulations of fluid flow in three-dimensional networks of discrete fractures. *Water Resources Research*,

23(10):1876–1886.

Arpaci, V. S. (1966). *Conduction Heat Transfer*. Addison-Wesley, Reading, England.

Auradou, H., Drazer, G., Boschan, A., Hulin, J.-P., and Koplik, J. (2006). Flow channeling in a single fracture induced by shear displacement. *Geothermics*, 35(5–6):576–588.

Bondy, A. and Murty, U. (2010). *Graph Theory*. Graduate Texts in Mathematics. Springer.

Brown, S. R. (1987). Fluid flow through rock joints: The effect of surface roughness. *Journal of Geophysical Research: Solid Earth*, 92(B2):1337–1347.

Bruderer-Weng, C., Cowie, P., Bernabé, Y., and Main, I. (2004). Relating flow channelling to tracer dispersion in heterogeneous networks. *Advances in Water Resources*, 27(8):843–855.

Bruel, D., Cacas, M. C., Ledoux, E., and de Marsily, G. (1994). Modelling storage behaviour in a fractured rock mass. *Journal of Hydrology*, 162(3-4):267–278.

Cacas, M. C., Ledoux, E., de Marsily, G., Tillie, B., Barbreau, A., Durand, E., Feuga, B., and Peaudecerf, P. (1990). Modeling fracture flow with a stochastic discrete fracture network: Calibration and validation: 1. The flow model. *Water Resources Research*, 26(3):479–489.

Carslaw, H. and Jaeger, J. (1959). *Conduction of Heat in Solids*. Oxford University Press, Oxford, England, 2nd edition.

Cook, R. D., Malkus, D. S., Plesha, M. E., and Witt, R. J. (2001). *Concepts and Applications of Finite Element Analysis*. Wiley, New York, NY, fourth edition.

de Dreuzy, J.-R., Pichot, G., Poirriez, B., and Erhel, J. (2013). Synthetic benchmark for modeling flow in 3D fractured media. *Computers & Geosciences*, 50(0):59–71.

Dorbath, L., Cuenot, N., Genter, A., and Frogneux, M. (2009). Seismic response of the fractured and faulted granite of Soultz-sous-Forêts (France) to 5 km deep massive water injections. *Geophysical Journal International*, 177(2):653–675.

Drazer, G. and Koplik, J. (2000). Permeability of self-affine rough fractures. *Physical Review E*, 62(6):8076–8085.

Evans, K. F., Genter, A., and Sausse, J. (2005). Permeability creation and damage due to massive fluid injections into granite at 3.5 km at Soultz: 1. Borehole observations. *Journal of Geophysical Research: Solid Earth*, 110(B4).

Even, S. and Even, G. (2011). *Graph Algorithms*. Cambridge University Press, Cambridge, England.

Fish, J. and Belytschko, T. (2007). *A First Course in Finite Elements*. Wiley, Chichester, England.

Fox, D. B., Sutter, D., Beckers, K. F., Lukawski, M. Z., Koch, D. L., Anderson, B. J., and Tester, J. W. (2013). Sustainable heat farming: Modeling extraction and recovery in discretely fractured geothermal reservoirs. *Geothermics*, 46(0):42–54.

Glover, P. W. J., Matsuki, K., Hikima, R., and Hayashi, K. (1998). Fluid flow in synthetic rough fractures and application to the Hachimantai geothermal hot dry rock test site. *Journal of Geophysical Research: Solid Earth*, 103(B5):9621–9635.

Gringarten, A. C., Witherspoon, P. A., and Ohnishi, Y. (1975). Theory of

heat extraction from fractured hot dry rock. *Journal of Geophysical Research*, 80(8):1120–1124.

Hakami, E. and Larsson, E. (1996). Aperture measurements and flow experiments on a single natural fracture. *International Journal of Rock Mechanics and Mining Sciences & Geomechanics Abstracts*, 33(4):395–404.

Held, S., Genter, A., Kohl, T., Koelbel, T., Sausse, J., and Schoenball, M. (2014). Economic evaluation of geothermal reservoir performance through modeling the complexity of the operating EGS in Soultz-sous-Forêts. *Geothermics*, 51(0):270–280.

Heuer, N., Küpper, T., and Windelberg, D. (1991). Mathematical model of a hot dry rock system. *Geophysical Journal International*, 105(3):659–664.

Hooker, J., Gale, J., Gomez, L., Laubach, S., Marrett, R., and Reed, R. (2009). Aperture-size scaling variations in a low-strain opening-mode fracture set, Cozzette Sandstone, Colorado. *Journal of Structural Geology*, 31(7):707–718.

Juliusson, E. and Horne, R. N. (2013). Optimization of injection scheduling in fractured geothermal reservoirs. *Geothermics*, 48(0):80–92.

Kohl, T. and Hopkirk, R. (1995). "FRACTure"- a simulation code for forced fluid flow and transport in fractured, porous rock. *Geothermics*, 24(3):333–343.

Koyama, T., Li, B., Jiang, Y., and Jing, L. (2009). Numerical modelling of fluid flow tests in a rock fracture with a special algorithm for contact areas. *Computers and Geotechnics*, 36(1-2):291–303.

Lauwerier, H. (1955). The transport of heat in an oil layer caused by the injection of hot fluid. *Applied Scientific Research, Section A*, 5(2-3):145–150.

Lee, S. H., Lough, M. F., and Jensen, C. L. (2001). Hierarchical modeling of flow in naturally fractured formations with multiple length scales. *Water Resources Research*, 37(3):443–455.

Li, L. and Lee, S. H. (2008). Efficient field-scale simulation of black oil in a naturally fractured reservoir through discrete fracture networks and homogenized media. *SPE Reservoir Evaluation & Engineering*, 11(4):750–758.

Lough, M., Lee, S., and Kamath, J. (1998). An efficient boundary integral formulation for flow through fractured porous media. *Journal of Computational Physics*, 143(2):462–483.

Maryška, J., Severýn, O., and Vohralík, M. (2005). Numerical simulation of fracture flow with a mixed-hybrid FEM stochastic discrete fracture network model. *Computational Geosciences*, 8(3):217–234.

Méheust, Y. and Schmittbuhl, J. (2000). Flow enhancement of a rough fracture. *Geophysical Research Letters*, 27(18):2989–2992.

Méheust, Y. and Schmittbuhl, J. (2001). Geometrical heterogeneities and permeability anisotropy of rough fractures. *Journal of Geophysical Research: Solid Earth*, 106(B2):2089–2102.

Méheust, Y. and Schmittbuhl, J. (2003). Scale effects related to flow in rough fractures. *Pure and Applied Geophysics*, 160(5–6).

Moreno, L., Tsang, Y. W., Tsang, C. F., Hale, F. V., and Neretnieks, I. (1988). Flow and tracer transport in a single fracture: A stochastic model and its relation to some field observations. *Water Resources Research*, 24(12):2033–2048.

Nicol, D. A. and Robinson, B. A. (1990). Modelling the heat extraction from the Rosemanowes HDR reservoir. *Geothermics*, 19(3):247–257.

Nordqvist, A. W., Tsang, Y. W., Tsang, C. F., Dverstorp, B., and Andersson, J. (1992). A variable aperture fracture network model for flow and transport in fractured rocks. *Water Resources Research*, 28(6):1703–1713.

Patir, N. and Cheng, H. (1978). An average flow model for determining effects of three-dimensional roughness on partial hydrodynamic lubrication. *Journal of Lubrication Technology*, 100:12–17.

Pianosi, F. and Wagener, T. (2015). A simple and efficient method for global sensitivity analysis based on cumulative distribution functions. *Environmental Modelling and Software*, 67:1–11.

Pruess, K., Oldenburg, C., and Moridis, G. (1999). TOUGH2 user's guide, version 2.0. Technical report, Lawrence Berkeley National Laboratory.

Robinson, B., Tester, J. W., and Brown, L. (1988). Reservoir sizing using inert and chemically reacting tracers. *SPE Formulation Evaluation*, 3:227–334.

Robinson, B. A. and Tester, J. W. (1984). Dispersed fluid flow in fractured reservoirs: An analysis of tracer-determined residence time distributions. *Journal of Geophysical Research*, 89:10374–10384.

Robinson, B. A. and Tester, J. W. (1986). Characterization of flow maldistribution using inlet-outlet tracer techniques: An application of internal residence time distributions. *Chemical Engineering Science*, 41(3):469–484.

Sausse, J., Dezayes, C., Dorbath, L., Genter, A., and Place, J. (2010). 3D model of fracture zones at Soultz-sous-Forêts based on geological data, image logs, induced microseismicity and vertical seismic profiles. *Comptes Rendus Geoscience*, 342(7–8):531–545.

Smith, I. M. and Griffiths, D. V. (1988). *Programming the Finite Element Method*. Wiley, Chichester, England, 2nd edition.

Tester, J. W., Anderson, B. J., Batchelor, A. S., Blackwell, D. D., DiPippo, R., Drake, E. M., Garnish, J., Livesay, B., Moore, M. C., Nichols, K., Petty, S., Toksoz, M. N., Veatch, R. W., Baria, R., Augustine, C., Murphy, E., Negraru, P., and Richards, M. (2006). The future of geothermal energy. Technical report, Massachusetts Institute of Technology.

Tsang, Y. W. and Tsang, C. F. (1989). Flow channeling in a single fracture as a two-dimensional strongly heterogeneous permeable medium. *Water Resources Research*, 25(9):2076–2080.

Watanabe, N., Hirano, N., and Tsuchiya, N. (2008). Determination of aperture structure and fluid flow in a rock fracture by high-resolution numerical modeling on the basis of a flow-through experiment under confining pressure. *Water Resources Research*, 44(6).

Wellman, T. P., Shapiro, A. M., and Hill, M. C. (2009). Effects of simplifying fracture network representation on inert chemical migration in fracture-controlled aquifers. *Water Resources Research*, 45(1).

Xiong, X., Li, B., Jiang, Y., Koyama, T., and Zhang, C. (2011). Experimental and numerical study of the geometrical and hydraulic characteristics of a single rock fracture during shear. *International Journal of Rock Mechanics and Mining Sciences*, 48(8):1292–1302.

Yang, S.-Y. and Yeh, H.-D. (2009). Modeling heat extraction from hot dry rock in a multi-well system. *Applied Thermal Engineering*, 29(8-9):1676–1681.

Yeo, I., de Freitas, M., and Zimmerman, R. (1998). Effect of shear displacement on the aperture and permeability of a rock fracture. *International Journal of Rock Mechanics and Mining Sciences*, 35(8):1051–1070.

Zimmerman, R. W. and Bodvarsson, G. S. (1996). Hydraulic conductivity of rock fractures. *Transport in Porous Media*, 23(1):1–30.

CHAPTER 6

FEM AND BIE NUMERICAL MODEL

6.1 Introduction

Thermal hydraulic modeling of Enhanced/Engineered Geothermal Systems is required to determine the anticipated performance of a reservoir. Of most significance is the evolution of both the subsurface temperature field and the production temperature throughout the operation of the reservoir. Modeling the thermal hydraulic behavior of the reservoir is needed because it is difficult to determine future reservoir performance from the early behavior of the reservoir. Although analytical models are useful in providing physical insight and providing zeroth or first order approximations, they are limited by simplifications or omissions of the physics controlling the system. Therefore, in order to compensate for this limitation, numerical modeling of the thermal hydraulic behavior of geothermal systems is needed in order to be able to expand the analysis in simulating more realistic reservoirs and to obtain better predictions of a reservoir's thermal performance. Modeling of geothermal reservoirs can include thermal, hydraulic, chemical, and mechanical considerations. The purpose of this chapter is to present the development of a numerical model in order to simulate the fluid flow, heat transport, and particle transport in discretely fractured geothermal reservoirs and to demonstrate the capabilities of the model.

Modeling approaches for EGS reservoirs can be divided into two classes, those that model the subsurface as discrete fractures or those that model the subsurface as a continuous permeable medium. Modeling hydrothermal reservoirs is usually done as a continuous permeable medium where the fluid flow follows Darcy's con-

stitutive equations. TOUGH2 and its sibling codes have been extensively used to model EGS reservoirs. Taron and Elsworth (2009, 2010) and Taron et al. (2009) developed a model with thermal-hydraulic-mechanical-chemical coupling using TOUGHREACT and FLAC3D, a geotechnical stress and deformation analysis software, to show the different impacts on the permeability of the reservoir. Although TOUGH2 can be used to model discrete fractures, it becomes cumbersome for more complex fracture systems because not only do the fractures need to be discretized, but the entire reservoir domain needs to be as well.

Professor Ahmad Ghassemi, of the Petroleum and Geological Engineering Department of Oklahoma University, and his research group have done extensive work on single discrete fractures. The bulk of their work is formulated using Green's functions and integral equation formulations. They have looked into rectangular (Cheng et al., 2001), circular, and arbitrary shaped fractures (Ghassemi et al., 2003) and have studied the thermal induced stresses that lead to aperture opening due to slippage (Ghassemi et al., 2005, 2007). They have also studied silica dissolution and precipitation (Ghassemi and Kumar, 2007), as well as poro-thermoelastic effects (Ghassemi et al., 2008) in rectangular fractures in order to derive a semi-analytical expression for the variation in aperture in space and time. Their work has culminated in thermo-porelastic analysis of a single fracture, using both finite and boundary element methods, and shows how poroelastic effects are dominant at early times but thermoelastic effects become more dominant at later times (Zhou et al., 2009; Ghassemi and Zhou, 2011).

Geophysical imaging techniques have been used to show that EGS reservoirs consist of a network of intersecting fractures. Sausse et al. (2010) used well logs, vertical seismic profiling, and microseismic data from the Soultz, France EGS

project to identify fifty-three structures around the six well system. Figure 6.1 shows the identified fracture network of the Soultz reservoir. The discrete fracture nature of the Soultz reservoir and other EGS reservoirs was the motivation for choosing to develop a numerical framework that models the reservoir as consisting of discrete fractures.

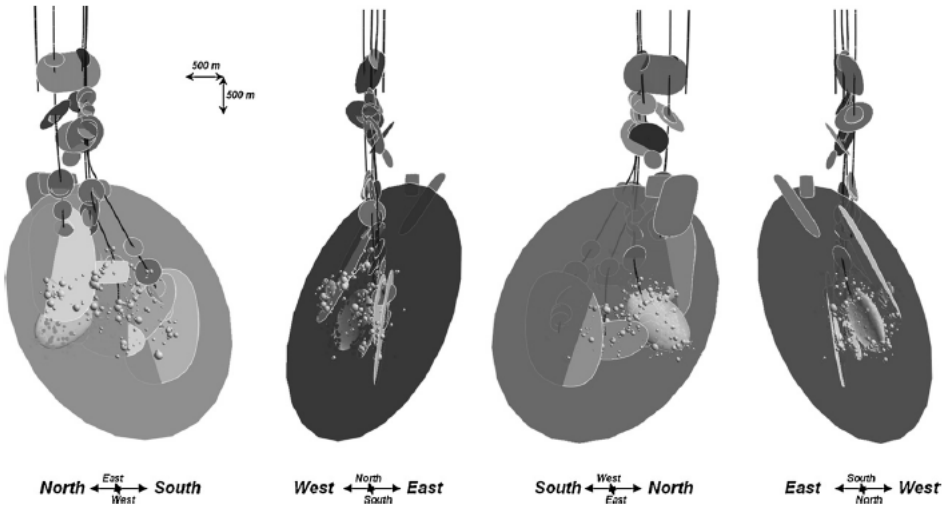

Figure 6.1: Four orientations of the identified fracture network using geophysical imaging techniques in the Soultz, France EGS project. The image was taken from Sausse et al. (2010)

.

The goals and objectives of the model are to simulate key features of EGS reservoirs and to provide an adequate forward model in order to calculate the temperature of the subsurface. This numerical model is influenced by the approaches of Professor Ahmad Ghassemi. The developed numerical model is a combination of the finite element method (FEM) and boundary integral equations (BIE) based

on Green's functions. The fluid flow is solved via the FEM, while the temperature field is solved by coupling the FEM inside the fracture with a boundary integral description of the transient conduction from the surrounding rock. The numerical model relies on 2D discretization of only the fracture surface, not the entire domain. If needed, once the surface heat flux has been quantified, the Green's function can be used to determine the temperature at any arbitrary point within the domain. The 2D discretization offers faster numerical run times as compared to a 3D discretization of the entire reservoir, and therefore, allows one to invest more computational effort on fracture scale details. The numerical model must be able to simulate reservoirs with intersecting fractures, heterogeneous aperture fields, thermal recovery of depleted reservoirs, natural convection, and the transport of tracer particles in the fracture.

6.2 Numerical Model Description

The following section describes the governing equations used to model the thermal hydraulics of discretely fractured geothermal reservoirs and the numerical approach used in solving those equations. In addition to describing how the fluid flow and heat transport in the fracture are solved, the section describes how the transport of particles within the system is modeled. Since both the heat and particle transport require solving for the velocity field, the treatment of the fluid flow in the geothermal system is presented first. Figure 6.2 shows an idealized fracture in a geothermal reservoir with an injection and production well.

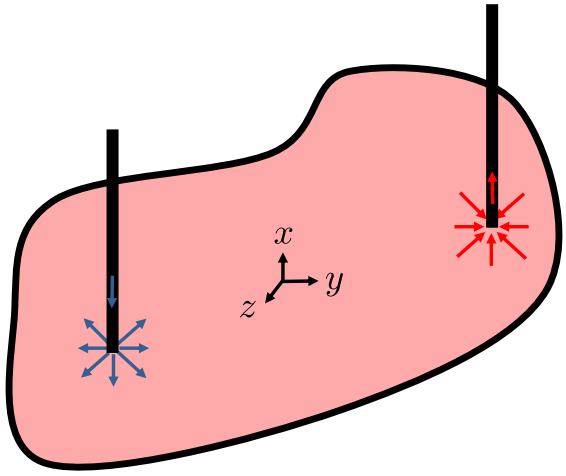

Figure 6.2: Idealized fracture in a geothermal reservoir. The x and y coordinates are in the plane of the fracture, while z is perpendicular to the fracture.

6.2.1 Fluid Flow

The fluid flow within the fracture aperture can be modeled as a flow of a Newtonian fluid in a thin channel. For fully developed laminar flow, if the aperture varies gradually, the Navier-Stokes equation is reduced to

$$\mu \nabla^2 \mathbf{v} = \boldsymbol{\nabla} P - \rho_w \mathbf{g}, \tag{6.1}$$

where P is the pressure, $\mathbf{v}$ is the velocity, ρ_w is the density of water, and μ is the dynamic viscosity. The conservation of mass can be expressed as

$$\boldsymbol{\nabla} \cdot (\rho_w w \langle \mathbf{v} \rangle) = \sum_l \dot{m}_l \delta (\mathbf{r} - \mathbf{r}_l) . \tag{6.2}$$

The summation on the right hand side refers to sources/sinks of mass, w is the local aperture or gap of the channel, and $\langle \mathbf{v} \rangle$ is the fluid velocity averaged across the gap. The sources and sinks of mass in the fracture come from the connection to the wellbores, the injection (source) and production (sink) wells. Poiseuille flow describes pressure driven laminar flow in a channel with a no slip condition applied at the walls of the channel. For Poiseuille flow, the velocity averaged across the

gap is

$$\langle \mathbf{v} \rangle = -\frac{w^2}{12\mu} \left(\boldsymbol{\nabla} P - \rho_w \mathbf{g} \right), \tag{6.3}$$

and this velocity is a function of the position $\mathbf{r}$ in the two-dimensional plane of the fracture. Combining Eq. (6.2) and Eq. (6.3) yields

$$-\boldsymbol{\nabla} \cdot \left(\frac{\rho_w w^3}{12\mu} \left[\boldsymbol{\nabla} P - \rho_w \mathbf{g} \right] \right) = \sum_l \dot{m}_l \delta(\mathbf{r} - \mathbf{r}_l), \tag{6.4}$$

where the gradient operator only applies in the plane of the fracture. Often, Eq. (6.4) is referred to as the Reynolds equation and is derived using an approximate lubrication analysis. As such, Eq. (6.4) is valid when $\mathrm{Re}(w/L_{x,y}) \ll 1$ and $w/L_{x,y} \ll 1$ (Deen, 1998). $L_{x,y}$ refers to the characteristic length scale of aperture variations in the x and y direction and may be considered a "wavelength" of aperture variations. Here, the Reynolds number is defined as $\mathrm{Re} \equiv (\rho_w U_c w)/\mu$, where U_c is the characteristic velocity. For a mass flow of 40 kg/s, a wellbore spacing of $L = 400$ m, a width of 1 mm, and a characteristic velocity of $U_c \sim \dot{m}/(\rho_w w L)$, then $\mathrm{Re} \sim 100$, well below the critical Reynolds number for turbulence transition. The lubrication criteria $\mathrm{Re}(w/L_{x,y}) \ll 1$ and $w/L_{x,y} \ll 1$ will also be satisfied when $\mathrm{Re} \sim 100$ if $L_{x,y} > 1$ m and for large scale aperture variations. Eq. (6.4) has been used extensively to model fluid flow in fractures (Brown, 1987; Zimmerman and Bodvarsson, 1996; Méheust and Schmittbuhl, 2001; Watanabe et al., 2008). Since the aperture is raised to the third power, flow modeled using Eq. (6.4) is sometimes said to follow the "cubic law".

The injection and production wells are modeled as circles in order to avoid singularities in pressure. A typical radius for a wellbore is 0.15 m. The mass flux is then evenly distributed along the circumference of the injection and production well. We specify a no mass flux condition on the boundary of the fracture and in the direction normal to the surface, in order to model the fracture with a limited

areal extent with no leak off, that is, the surrounding rock matrix is assumed to be impermeable. Under the FEM treatment, Eq. (6.4) is applied to all nodes in the system except for those representing Dirichlet (essential) boundary conditions. After applying the Dirichlet boundary conditions, a system of algebraic equations is formed for the pressure at each node. The Dirichlet condition will typically be the specification of the pressure for either the injection or production well. However, if one is not interested in the absolute pressure value, an arbitrary value at an arbitrary point in the system can be used since the velocity field only depends on the gradient of the pressure. After solving for the pressure using Eq. (6.4) with the finite element method, the velocity is then obtained using Eq. (6.3). The pressure drop across the system can therefore be determined by subtracting the pressure at the injection well from the pressure at the production well. Please refer to Appendix A for a complete description of the finite element treatment used in solving for the pressure field.

For reservoirs with fracture intersections, the governing equation found in Eq. (6.4) is not applied to the nodes of the fracture intersections. For systems with p intersections and n fractures, the resulting system of equations from the FEM treatment is $\sum_{i=1}^{n} N_i - 2\sum_{i=1}^{p} L_i$, where N_i and L_i refer to the number of nodes for the mesh of fracture i and for the number of nodes representing the fracture intersection p, respectively. Finally, the system of equations is completed by applying continuity of pressure and conservation of mass along the intersection. Numerically,

$$P_{\mathrm{A},l} = P_{\mathrm{B},l}, \tag{6.5}$$

and

$$f_{\mathrm{A},l} + f_{\mathrm{B},l} = 0. \tag{6.6}$$

Here, A and B refer to two different fractures that intersect with each other and

f is the mass flux of the intersection nodes. The conditions in Eq. (6.5) and (6.6) imply that the number of nodes along the intersection needs to be the same and located at spatially corresponding points for both fractures involved. These two constraints shown above complete the system of algebraic equations that describes the pressure at each node in the system.

6.2.2 Heat Transport

The numerical model for heat transport in discrete fractures uses a hybrid finite element and boundary element method. The three-dimensional heat conduction in the rock matrix is captured through a boundary element treatment, while the fluid flow and thermal convection are solved via the FEM. As stated earlier, the rock matrix surrounding the discrete fractures is assumed to be impermeable with respect to fluid flow. The numerical model relies on 2D discretization of only the fracture surface, not the entire domain.

The fluid energy balance inside the fracture is

$$\rho_w c_w w \frac{\partial T}{\partial t} + \rho_w c_w w \langle \mathbf{v} \rangle \cdot \boldsymbol{\nabla} T - k_w w \nabla^2 T = q_s, \tag{6.7}$$

where T is temperature, q_s refers to the surface heat flux, and c_w and k_w are the heat capacity and thermal conductivity of water, respectively. By neglecting the transient heat storage in the liquid contained by the fracture and thermal conduction in the liquid ($\mathrm{Pe} \equiv U_c L/\alpha_w \gg 1$), Eq. (6.7) becomes

$$\rho_w c_w w \langle \mathbf{v} \rangle \cdot \boldsymbol{\nabla} T = q_s. \tag{6.8}$$

Unfortunately, the preceding equation cannot be solved independently because the surface heat flux is unknown and coupled to transient conduction of the rock mass

surrounding the fracture. The surface heat flux is also related to the temperature of the system and can be represented by the 3D Green's function and the intensity of the source. Here, the source is the fracture surface heat flux. For a source located at z and confined by the extent of the fracture, the temperature of the system is expressed as

$$T(x,y,z,t) = T_r + \int_0^t \int_A G(x-x', y-y', z, t-t') \frac{q_s(x',y',t')}{\rho_r c_r} \, \mathrm{d}x' \, \mathrm{d}y' \, \mathrm{d}t', \quad (6.9)$$

$$\bar{T}(x,y,z,s) = \bar{T}_r + \int_A \bar{G}(x-x', y-y', z, s) \frac{\bar{q}_s(x',y',s)}{\rho_r c_r} \, \mathrm{d}x' \, \mathrm{d}y', \quad (6.10)$$

where G is the 3D Green's function for transient conduction and the overbar notation refers to the Laplace transform where s represents the Laplace space variable. The subscript r refers to the thermophysical properties of the rock, while T_r is the original reservoir rock temperature. The Laplace transform of the fracture heat balance equation is simply

$$\rho_w c_w w \langle \mathbf{v} \rangle \cdot \boldsymbol{\nabla} \bar{T} = \bar{q}_s. \quad (6.11)$$

For intersecting fractures, similar to what was done for the pressure, the temperature along the intersection of one fracture is equal to the temperature of its corresponding position within other fracture.

By working in the Laplace space, time discretization is explicitly avoided, along with singularities at $t = 0$ that lead to accuracy issues associated with early time discretization. Eq. (6.10) and (6.11) are solved simultaneously to obtain the surface heat flux and the temperature profile of the fracture for different time steps of interest. The inverse Laplace transform is computed using the Gaver-Stehfest algorithm (Stehfest, 1970a,b) which determines the value of $f(t)$ by computing several terms in a series involving $\bar{f}(s)$ at different values of s. Once the surface heat flux is computed for the time steps of interest, the temperature field within

the fracture is solved by returning to the FEM discretization of Eq. (6.8). To solve for the temperature at any point in the system, a numerical discretization of Eq. (6.9) is used. Please refer to Appendix A for more details on the finite element treatment of the heat transport in the reservoir.

The matrix $\bar{G}_{ij}(x-x', y-y', z)$ is computationally intensive to construct because every entry must be evaluated. The computational cost is $O(N^2)$ where N is the number of nodes. Computations can be greatly reduced by noticing that many of the entries in $\bar{G}_{ij}$ are virtually zero and can be skipped in populating $\bar{G}_{ij}$. For determining $\bar{G}_{ij}$ for a given s, entries that correspond to evaluating points that are farther than $20\sqrt{\alpha/s}$ are skipped where α refers to the thermal diffusivity of the rock. The computational intensity can be reduced to $O(N \log N)$. The value twenty is arbitrary and can be changed to adjust for accuracy. This method is akin to a single term Fast Multipole Method as described by Greengard and Rokhlin (1997). For a 2500 node mesh, the computational time was reduced by a factor of about twenty, with only a difference in the fifth significant figure for the outlet temperature.

Alternatively, since the conduction is dominated by the direction perpendicular to the fracture, the 1D Green's function can be used instead of the full 3D form. Doing so results in a less than 1% error and over a twenty-fold decrease in simulation time compared to the use of the truncation approximation of $\bar{G}_{ij}$. Additionally, the 1D simplification corresponds to a 400 fold decrease in simulation time compared to the fully populated $\bar{G}_{ij}$ matrix. Fox et al. (2013) showed that 1D conduction is a reasonable approximation when $\beta^2 \ll 1$. Here, β is a dimensionless parameter describing the ratio of the extent of thermal depletion normal to the plane of the fracture to the extent of depletion in the plane of the fracture. For

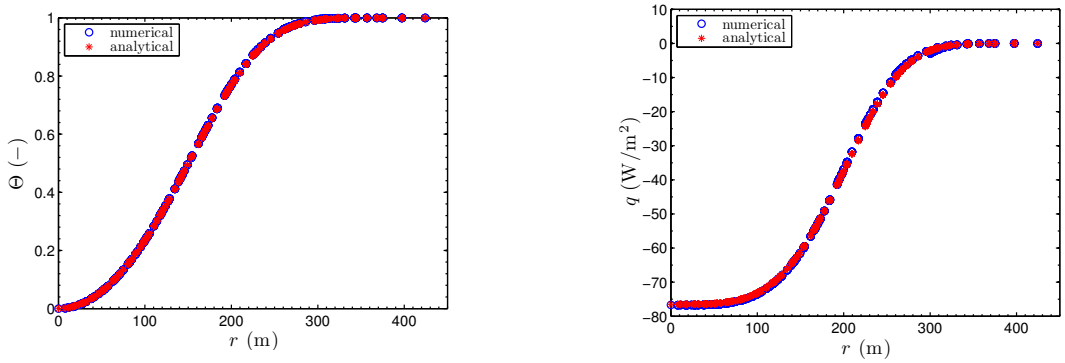

(a) (b)

Figure 6.3: Comparison of the numerical results to the results of the analytical solution for a monopole in an unconfined fracture. In these graphs, r represents the radial distance from the injection well. Eight terms were used in the Gaver-Stehfest inversion, along with a 961 node mesh. (a) Dimensionless temperature Θ. (b) Surface heat flux q.

dipole flow, β can be defined as $\beta = 2k_r L/(\dot{m}c_w)$, where L is the spacing between the injection and production wells. For typical flow conditions of 40 kg/s and a wellbore separation of 400 m, $\beta^2 = 2 \times 10^{-4}$. Nonetheless, for completeness, we used the 3D heat conduction Green's function for the simulations in this chapter.

As a test of the numerical model, results from the numerical model for the heat transport were compared against the case of a monopole in an unconfined fracture, which has an analytical solution for both the flow and temperature field. Figure 6.3 shows how the numerical results closely match the analytical values for both the temperature and the surface heat flux.

6.2.3 Particle Transport

The numerical model must be able to simulate the transport of passive particles in the subsurface in order to model the injection of tracers. The governing equation

for particle transport in the fracture is

$$w\frac{\partial C}{\partial t} + w\mathbf{v}\cdot\boldsymbol{\nabla}C - w\boldsymbol{\nabla}\cdot D\boldsymbol{\nabla}C = wr, \tag{6.12}$$

where C is the concentration of the particles, D is the particle diffusivity, and r is the reaction rate. As with Eq. (6.7), the w comes from the reduction of within the fracture from 3D to 2D transport within the fracture. The reaction rate can be due to a chemical reaction, decay, or any other volumetric loss or gain within the fracture. For a first order chemical reaction, for example, the reaction rate r is equal to $-k(T)C$, where k is the reaction constant and can be a function of temperature. The reaction term is needed when modeling chemically reactive tracers as opposed to conservative tracers that do not have a reaction term. Since the typical residence time of injected particles is on the order of hours or days and the typical time scale of energy extraction is months or years, it is appropriate to assume that the temperature of the subsurface does not change during a tracer test. Thus, one does not need to solve a coupled equation with the heat transport in order to solve for the concentration field. To solve for the particle or tracer concentration, the velocity field must first be solved, followed by the temperature field, if there is a temperature sensitive chemical reaction occurring. For fracture intersections, the same treatment is used as for the pressure; there is continuity of concentration and equal mass flux along the intersection. Eq. (6.12) is solved by using the finite element method. Please refer to the Appendix A for more details on the finite element formulation for solving for the particle concentration.

In modeling chemically reactive tracers, the Damköhler number Da becomes important to calculate. The Damköhler number is the ratio of the tracer's residence time to the time scale of the chemical reaction. If $\mathrm{Da} \ll 1$, then little reaction occurs during the time the particles are in the reservoir and the tracer will behave like a conservative tracer. When the opposite occurs, most of the tracer particles

Table 6.1: List of values used in the simulations.

parameter	value	units
c_w	4200	J/kg°C
ρ_w	1000	kg/m^3
k_r	2.4	W/m^2°C
c_r	1000	J/kg°C
ρ_r	2300	kg/m^3
T_r	200	°C
T_w	20	°C
$\dot{m}$	40	kg/s
R	500	m

will react in the subsurface. The ideal reactive tracer should have a reaction rate where Da $\sim$ 1 in order to get tracer results that will be most beneficial in determining the subsurface temperature.

6.3 Numerical Model Showcase

The capabilities of the developed numerical model are exhibited in the following sections. Although the numerical framework can model any arbitrary shaped fracture, the presented case studies use a circular fracture. Specifically, these sections showcase the results of simulating fractures with different wellbore spacing, fractures with varying aperture field, reservoirs undergoing thermal recovery, reservoirs with buoyancy, and reservoirs with intersecting fractures. Unless otherwise noted, Table 6.1 lists the thermophysical and reservoir property values used in the simulations.

6.3.1 Circular Fracture with Dipole Flow

The circular fracture case is considered to be a better representation of an EGS reservoir than the single rectangular model with unidirectional flow explored in Chapter 4. First of all, in the circular fracture model, the flow is induced by a point source (injection well) and a point sink (production well), resulting in spatially varying flow. For a circular fracture with a uniform aperture field, the complex velocity potential is given by Hertzsch et al. (2007) to be

$$W(z) = \phi + i\psi = \sum_i \frac{\dot{Q}_i}{2\pi} \left[\ln(z - \zeta_i) - \ln(R^2 - \zeta_i z)\right], \tag{6.13}$$

where $\dot{Q}_i$ is the volumetric flow rate of the sink/source, R is the fracture radius, ζ_i is the position of the sink/source in the complex plain given by complex number z, defined as $z = x + iy$. The real part of the complex potential is the flow potential ϕ and the imaginary part represents the stream line function ψ. Given the definition of the velocity potential, the velocity is simply

$$\mathbf{v} = -\boldsymbol{\nabla}\phi, \tag{6.14}$$

and there is no need to solve the pressure and velocity using the FEM.

Dimensionless variables allow for a simulation occurring under one set of variables to be equivalent to another set, so long as their set of dimensionless variables are the same. The Buckingham π theorem states that a physical process governed by $\mathcal{V}$ meaningful variables with $\mathcal{D}$ dimensions is a function of $\mathcal{G} = \mathcal{V} - \mathcal{D}$ dimensionless groups. For the circular fracture dipole,

$$\pi_1 = f(\pi_2, \pi_3, \pi_4, \pi_5). \tag{6.15}$$

A set of dimensionless groups is

$$\pi_1 = \frac{T - T_w}{T_r - T_w}, \quad \pi_2 = \frac{L}{2R}, \quad \pi_3 = \frac{\dot{Q}t}{L^3}, \quad \pi_4 = \frac{\alpha t}{L^2}, \text{ and } \quad \pi_5 = \frac{\alpha' t}{L^2}, \tag{6.16}$$

and consequently,

$$\Theta = f\left(\frac{L}{2R}, \frac{\dot{Q}t}{L^3}, \frac{\alpha t}{L^2}, \frac{\alpha' t}{L^2}\right). \tag{6.17}$$

In the equations above, α' is a convenient grouping of $k_r/(\rho_w c_w)$ and can be considered an effective thermal diffusivity. Given the relationship in Eq. (6.17), we can easily see the effects on the dimensionless temperature Θ on changing parameters such as flow and extraction duration. For example, Θ remains the same by doubling L, R, $\dot{Q}$, and quadrupling t, or by halving $\dot{Q}$, α, α', and doubling t.

Four different values of $L/(2R)$, 0.8, 0.6, 0.4, and 0.2, are explored for modeling energy extraction. Each reservoir is simulated until the dimensionless production temperature Θ_p reaches a value of 0.8 and 0.5. The mass flow and fracture radius used was 40 kg/s and 500 m, respectively. The mesh used in the simulations, along with a sample output of the fracture surface temperature, are shown in Figure 6.4 and 6.5. The mesh used has 2518 nodes and 2439 elements. Since the analytical velocity field is used instead of one solved from using the FEM, the injection and production wells can be represented by a single node, so long as the integration of elements for the convective term of the heat transport are treated properly using the Lachat-Watson integration scheme (Lachat and Watson, 1976). The same mesh is used to simulate other wellbore spacing by simply using a different set of nodes to represent the injection and production wells. Using a nearly doubly fine mesh showed only a less than 0.03% difference in temperature.

Figure 6.6 shows the combined results of the four different $L/(2R)$ values. The figure shows that a large wellbore separation distance slows the rate of drawdown. The flow is more spread out for larger values of $L/(2R)$, increasing the efficiency for harvesting the stored thermal energy in the subsurface and slowing the rate of temperature decrease at the production well. Figure 6.7 shows the relationship of a

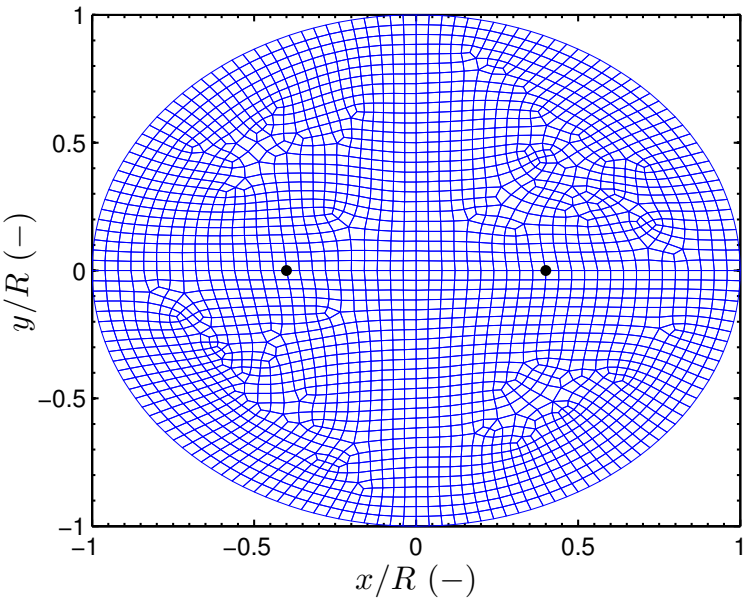

Figure 6.4: The mesh used for the variable $L/(2R)$ study. It contains 2518 nodes and 2439 elements. The width of each element is approximately 20 m. The location of the injection and production nodes are repositioned for simulations with different values of $L/(2R)$. The black markers represents the location of the injection and production well when $L/(2R) = 0.4$.

reservoir's life based on three different minimum dimensionless production temperature criteria, along with the wellbore spacing. The three different dimensioneless production temperature values used for the figure are 0.95. 0.8, and 0.5. The figure illustrates a quadratic relationship for $\Theta = 0.95$, with mostly linear relationships for greater drawdown criteria at intermediate to larger wellbore spacings.

The mean dimensionless fracture surface temperature $\langle\Theta\rangle$ is a measure of how much of the fracture has been thermally accessed and is equal to

$$\langle\Theta\rangle = \frac{\iint \Theta(x,y)\ \mathrm{d}A}{\iint\ \mathrm{d}A}. \tag{6.18}$$

For small values of $L/(2R)$, the mean fracture surface temperature should be large because much of the flow is concentrated in a smaller region of the fracture and does not effectively harvest the stored thermal energy in areas away from the region

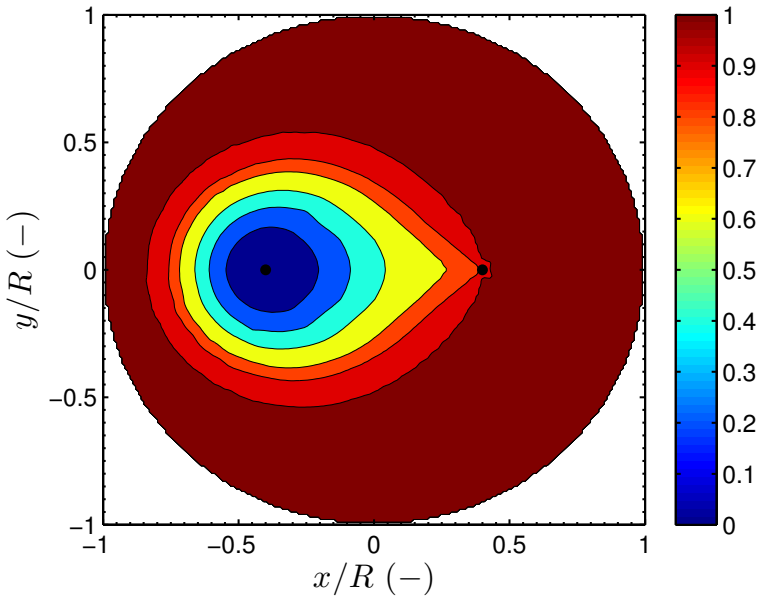

Figure 6.5: Dimensionless fracture surface temperature Θ for $L/(2R) = 0.4$, with a flow of 40 kg/s, and after 48 days of extraction. The Θ contours are 0, 0.2, 0.4, 0.6, 0.8, 0.9, and 0.99. The x and y axes are nondimensionalized by R and the black marker refers to the injection (-0.4, 0) and production well (0.4, 0).

surrounding both the injection and production well. Figure 6.8 shows the value of the mean dimensionless fracture surface temperature throughout the extraction process for various wellbore spacings. The figure shows a strong effect of the wellbore spacing on the mean fracture surface temperature. When $L/(2R) = 0.2$, the mean dimensionless fracture surface temperature stays relatively constant, compared to the other curves, remaining close to $\langle\Theta\rangle = 0.95$. The curves for different values of wellbore spacings are significantly spread out, in contrast to the production temperature drawdown curves displayed in Figure 6.6. The figure easily shows how important wellbore spacing is in affecting the subsurface heat exchange area and how the dimensionless mean fracture surface temperature is a good metric for the efficiency of the flow to sweep across the fracture surface.

An alternate to the uniform aperture field is an elliptical aperture field that mimics a fracture that is pinched off along the edges. Additionally, simple fracture

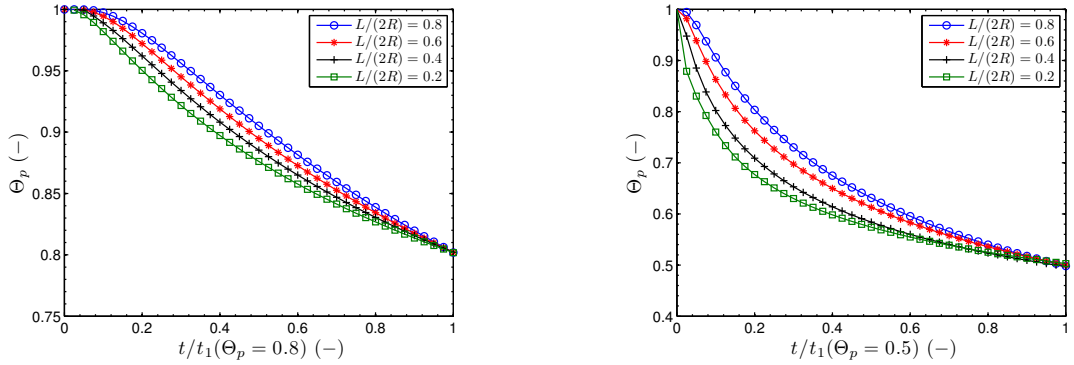

(a) (b)

Figure 6.6: Thermal drawdown curves for different end values of the dimensionless production temperature Θ_p, across various wellbore spacings. Time for each drawdown curve has been nondimensionalized by the duration of extraction t_1 for its respective wellbore spacing value so that all curves range from zero to one. (a) Extraction to $\Theta_p = 0.8$. (b) Extraction to $\Theta_p = 0.5$.

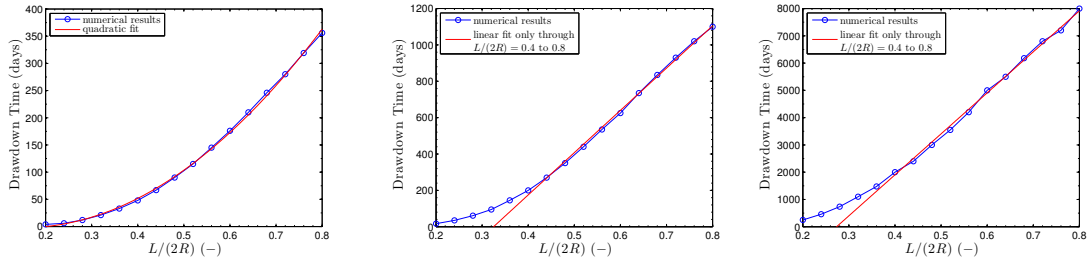

(a) (b) (c)

Figure 6.7: Reservoir life based on different drawdown criteria as a function of dimensionless wellbore spacing $L/(2R)$ (a) Drawdown to $\Theta_p = 0.95$ with a quadratic fit. (b) Drawdown to $\Theta_p = 0.8$ with a linear fit through $L/(2R) = 0.4 - 0.8$. (c) Drawdown to $\Theta_p = 0.5$ with a linear fit through $L/(2R) = 0.4 - 0.8$.

creation under pressurized fluid results in an elliptical fracture (Sneddon, 1946). The aperture is spatially described as

$$w(x, y) = w_0 \sqrt{1 - (x/R)^2 - (y/R)^2}, \tag{6.19}$$

where w_0 is the maximum aperture. For an equivalent volume to a constant aperture fracture, w_0 is a factor 3/2 larger than the constant aperture case. If the injection and production well are aligned along the centerline, drawdown will occur faster because the flow will be concentrated in the region with the largest

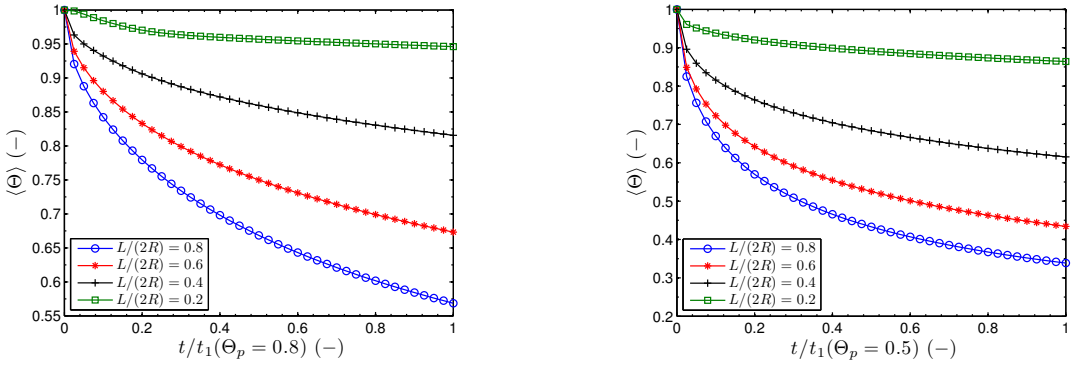

(a) (b)

Figure 6.8: Mean dimensionless fracture surface temperature $\langle\Theta\rangle$ for various wellbore spacings $L/(2R)$. Time for each curve has been nondimensionalized by the duration of extraction t_1 for its respective wellbore spacing value so that all curves range from zero to one. (a) Extraction to $\Theta_p = 0.8$. (b) Extraction to $\Theta_p = 0.5$.

aperture. To avoid solving for the analytical flow field, the FEM was used to solve for the velocity in the fracture using a mesh that represents the wellbores as circles rather than a single node. Running equivalent simulations of a constant aperture fracture with both the finite wellbore mesh and the analytical and the FEM derived velocities showed fractional percent error, compared to using a point well mesh with the analytical velocity field.

Figure 6.9 shows the dimensionless production temperature as a function of time for an elliptical and constant aperture field. The elliptical aperture field fracture exhibits more flow channeling than the constant aperture fracture, which leads to a lower production temperature, since the injection and production well are located in the high aperture region of the fracture. As such, flow has a greater tendency to follow in a straight path to the production well, as opposed to the regions closer to the edge where the aperture is more constricted. Instead of 200 days to reach $\Theta_p = 0.8$, the fracture with the elliptical aperture field takes 100 days, and instead of 2000 days to reach $\Theta_p = 0.5$, it takes just 745 days. Figure 6.10 compares the dimensionless temperature field of the elliptically shaped

fracture with that of the constant aperture fracture. As expected, the temperature field for the fracture with the elliptical aperture field extracts thermal energy in a narrower region than the constant aperture fracture, reducing the effective heat transfer area of the system.

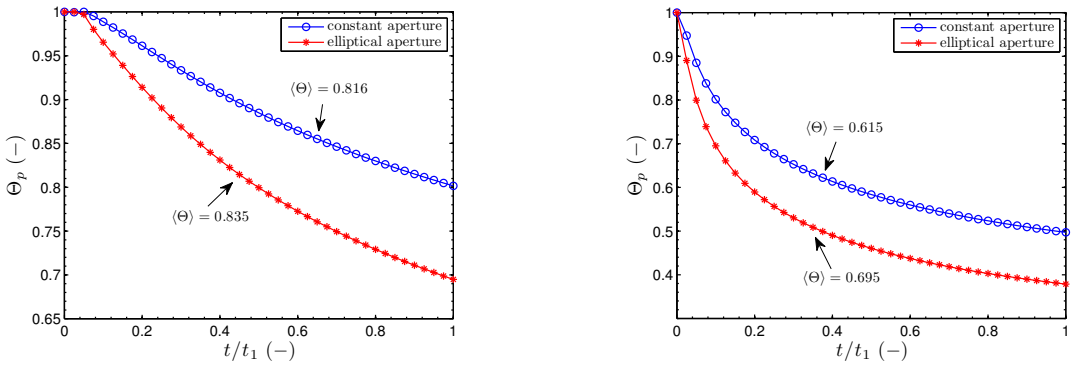

Figure 6.9: Dimensionless drawdown curves for an elliptically shaped fracture and a constant aperture fracture for two different extraction times. The $\langle\Theta\rangle$ at the end of extraction are reported. Time t is normalized by the end time of extraction t_1 (a) 200 day extraction. (b) 2000 day extraction.

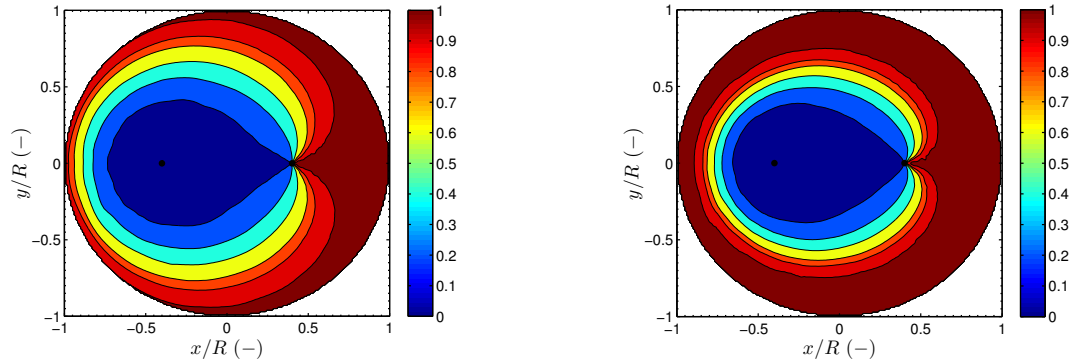

Figure 6.10: Dimensionless temperature surface temperature Θ for $L/(2R) = 0.4$ after 2000 days for both an elliptical and constant aperture field. The Θ contours are 0, 0.2, 0.4, 0.6, 0.8, 0.9, and 0.99. The black marker refers to the injection (-0.4, 0) and production well (0.4, 0). (a) Constant aperutre fracture (b) Elliptical aperture field.

6.3.2 Thermal Recovery

The developed numerical mode can simulate thermal recovery in depleted reservoirs. As was the case for the rectangular fracture in Chapter 4, a Green's function can be used to describe the temperature of the system during thermal recovery. The Green's function formulation for the temperature field is

$$T(x,y,z,t) = T_r + \int_0^{t_1} \int_A G(x-x', y-y', z, t-t') \frac{q_s(x',y',t')}{\rho_r c_r} \, \mathrm{d}x' \, \mathrm{d}y' \, \mathrm{d}t', \quad (6.20)$$

where t_1 is the duration of extraction. During recovery, $q_s = 0$ and the bounds of integration only range from 0 to t_1, instead of 0 to t. By storing the surface heat flux for different times during extraction, the integral in Eq. (6.20) can be numerically evaluated for any position and time.

Using the outlined procedure for determining thermal recovery, we have modeled the thermal recovery for various circular fractures with different wellbore spacings. The extraction duration differs for each wellbore spacing and is based on when the dimensionless production temperature reaches 0.8 and 0.5. Figure 6.11 shows the recovery curves at the location of the production well for various wellbore spacings. The duration of the recovery phase was four times the extraction period. The curves shown in Figure 6.11 resemble those from the single rectangular fractures in Chapter 4; early on there is rapid recovery, which subsequently is followed by a slow, asymptotic recovery. The curves also suggest there is little to be gained for allowing the reservoir to recover after four times the extraction time. The dimensionless temperature contours of the fracture surface for various recovery times is depicted in Figure 6.12. Both figures show that the recovery curves are nearly indistinguishable and are neither a function of the wellbore spacing nor a function of the amount of thermal energy extracted during drawdown. If we consider the dimensionless mean fracture surface temperature, we observe that larger wellbore

spacings and higher levels of extraction lead to lower $\langle\Theta\rangle$ values at the end of recovery; $\langle\Theta\rangle$ is equal to 0.967, 0.905, 0.864, and 0.844 at the end of the recovery period for values of $L/(2R)$ equal to 0.2, 0.4, 0.6, and 0.8, respectively. Thus, while the temperature at the production well recovers at the same relative rate, recovery at different points in the reservoir vary for different wellbore spacing.

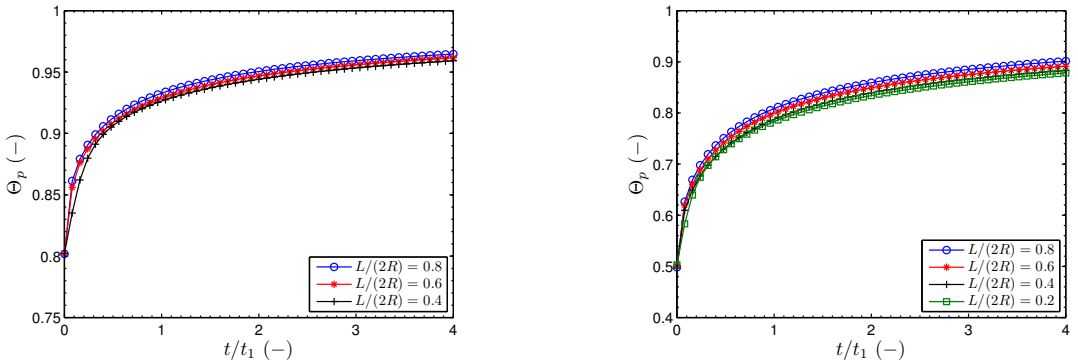

(a) (b)

Figure 6.11: Thermal recovery curves at the production well for different wellbore spacings $L/(2R)$. The recovery period lasts for four times the extraction time t_1. Recovery starts when $t = 0$ and $t/t_1 = 1$ refers to a recovery time equal to that of extraction. (a) Recovery starting when $\Theta_p = 0.8$ at the end of the extraction phase. (b) Recovery starting when $\Theta_p = 0.5$ at the end of the extraction phase.

After twice the extraction time, the curves in Figure 6.11 after twice the extraction time exhibit a fit of $1 - a/\sqrt{t}$ as in Eq. (4.31). Using Eq. (4.31), the thermophysical properties of the host rock and the cumulative heat flux during extraction at the production well Q_p, for each different $L/(2R)$ value, the values for a should be in the range of 1260 to 5640 $\mathrm{s}^{1/2}$. By using a linear fit of $1/\sqrt{t}$ on the results, the slopes for the fit vary from 1600 to 7000 $\mathrm{s}^{1/2}$, much like those derived by Eq. (4.31).

Using the definition of the dimensionless mean fracture surface temperature and the first term of the recovery solution found in by Eq. (4.31), $\langle\Theta\rangle = 1 + O(1/\sqrt{t})$

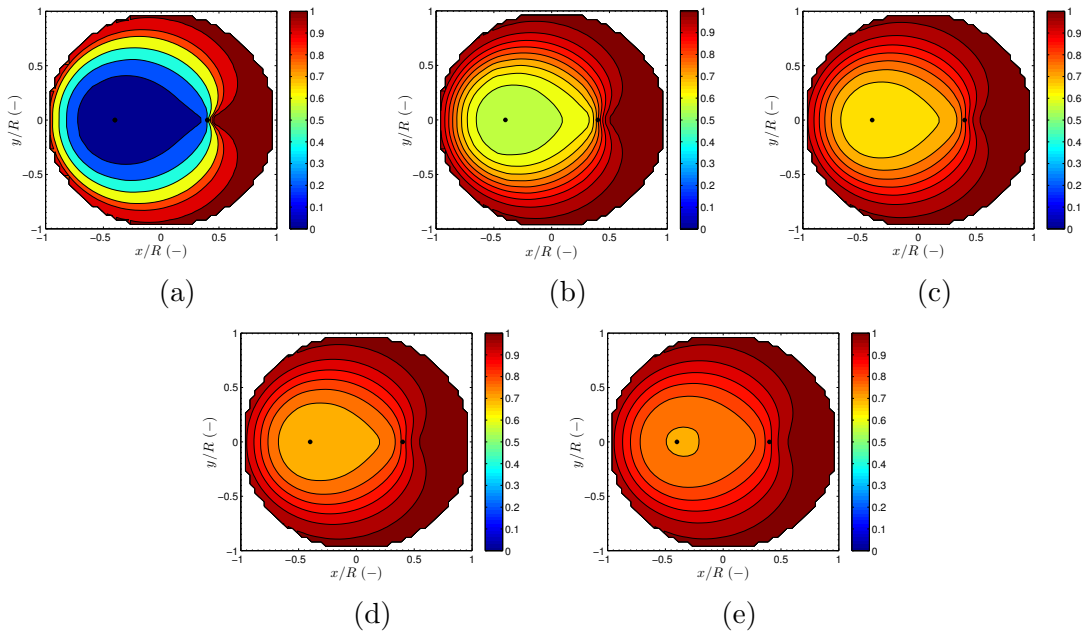

Figure 6.12: Dimensionless fracture surface temperature Θ for $L/(2R) = 0.4$ at different recovery times. The x and y axes are nondimensionalized by R and the black markers represent the injection (-0.4, 0) and production well (0.4, 0). (a) $t/t_1 = 0$. (b) $t/t_1 = 1$. (c) $t/t_1 = 2$. (d) $t/t_1 = 3$. (e) $t/t_1 = 4$.

and is given by

$$\langle \Theta \rangle = 1 + \left(\frac{Q_{ex}}{\sqrt{k_r \rho_r c_r}} \right) \frac{1}{\sqrt{t}}, \tag{6.21}$$

where Q_{ex} is the total amount of heat extracted during the extraction phase. The total amount of energy extracted from the reservoir is linearly proportional to the product of mass flow and the integral of production temperature with time. The amount of thermal energy extracted for the drawdown criteria of $\Theta_p = 0.5$ is 9.2, 6.6, 3.3, and 0.40 PJ for $L/(2R)$ of 0.8, 0.6, 0.4, and 0.2, respectively. Using the total extracted energy and the thermopysical properties of the reservoir in Eq. (6.21) to calculate the dimensionless mean fracture surface temperature, the resulting values of $\langle \Theta \rangle$ are 0.967, 0.892, 0.866, and 0.849 for $L/(2R)$ of 0.2, 0.4, 0.6, and 0.8, respectively. These values closely agree with the previously reported values from the simulations. Since the total energy extracted during the production phase can be readily calculated for a real geothermal field, one can easily determine the

mean fracture surface temperature during recovery by knowing the thermophysical properties of the host rock, specifically, the thermal conductivity, density, and heat capacity.

For a single rectangular fracture examined in Chapter 4, only conduction normal to the flow was considered and $\Theta = 1+O(1/\sqrt{t})$ for recovery. Because recovery in the circular fracture with dipole flow also followed the $O(1/\sqrt{t})$ behavior for the temperature, it experiences quasi 1D conduction. As in Chapter 4, β represents the ratio of the heat flux in the plane of the fracture to the direction normal to the plane, we have

$$\beta \equiv \frac{q_{x,y}}{q_z} \sim \frac{\delta_z}{\delta_{x,y}}, \tag{6.22}$$

where $\delta_{x,y}$ and δ_z represents the length scale of the depleted thermal field in their respective directions. In the transient conduction partial differential equation, the strength of the equatorial conduction is on the order of β^2. Since $\delta_z \approx 2\sqrt{\alpha t}$, and according to the fracture surface temperature shown in Figure 6.5, $\delta_{x,y}$ is on the order of the fracture radius R,

$$\beta \sim \frac{2\sqrt{\alpha t}}{R}. \tag{6.23}$$

For a 2000 day extraction period and a fracture radius of 500 m, $\beta = 0.05$ and $\beta^2 = 2.5 \times 10^{-3}$. Since $\beta^2 \ll 1$, heat conduction in the two equatorial directions is negligible compared to the axial heat flux, therefore, using the 1D Green's function to simulate thermal recovery is appropriate.

6.3.3 Natural Convection

Temperature gradients formed in the subsurface have the capability to induce natural convection caused by density differences. Natural convection will subsequently

alter the base flow and affect heat transport in the subsurface. The characteristic buoyancy induced velocity scales as

$$U_b \sim \frac{w^2 g \cos(\theta) \beta_T \Delta T}{12\nu}, \tag{6.24}$$

where ν is the kinematic viscosity, ΔT is the characteristic temperature disparity, β_T is the thermal expansion coefficient, g is the acceleration due to gravity, and θ is the angle the fracture makes with the vertical axis, the axis parallel to gravity. The characteristic buoyancy induced velocity assumes the Boussinesq approximation. If the characteristic velocity for the pressure driven dipole flow is

$$U_p \sim \frac{\dot{Q}}{wL}, \tag{6.25}$$

then the ratio of buoyancy to pressure driven velocity is

$$\mathcal{F} \equiv \frac{U_b}{U_p} = \frac{w^3 g L \beta_T \Delta T}{12\dot{Q}\nu}. \tag{6.26}$$

For typical values explored in the simulations, $\mathcal{F} \sim 1$ and we should expect buoyancy to play an important role in fractures that are primarily vertically oriented. Although some researchers like to use the Boussinesq approximation, the volumetric expansion coefficient β_T changes significantly with the typical temperature range seen in a reservoir undergoing energy extraction. For example, $\beta_T = 2 \times 10^{-4}$ 1/°C at $T = 20$ °C but is equal to 1.38×10^{-3} 1/°C at $T = 200$ °C, an order of magnitude larger. The effect of buoyancy on the production temperature is dependent on orientation and the positioning of the injection and production well. For example, a horizontal fracture will not experience any natural convection and the injection well will need to be placed below the production well to benefit from natural convection. For a horizontal fracture, there will still be density dependent effects because the mass flow and convective flux are directly proportional to the density of water as seen in Eq. (6.4) and Eq. (6.7). We should expect a reduction in energy extraction since less mass will travel and less energy will convect

in the hotter regions because density decreases as temperature increases. However, fractures are predominantly aligned vertically, modeling buoyancy is important.

With respect to dimensionless groups, Θ is no longer a function of four dimensionless variables; there will be an additional dimensionless parameter to the system when buoyancy is considered. Since β_T varies significantly over typical reservoir temperatures, the mean value of β_T over the temperature range of T_w and T_r is a more appropriate value to use. The dimensionless value $\mathcal{F}$ derived earlier determines the importance of buoyancy driven flow. From $\mathcal{F}$, we should expect buoyancy to play a bigger role in the system as times goes on since more of the reservoir is characterized by the vertical temperature disparity ΔT that drives natural convection.

Figure 6.13 shows the results of the additional buoyancy driven flow for a wellbore spacing of $L/(2R) = 0.4$ for different fracture orientations. The dimensionless fracture surface temperature for the cases with and without buoyancy are displayed in Figure 6.14. The angle effects the level of buoyancy because the driving force is proportional to $\mathbf{g} = -g\cos(\theta)\hat{y}$, where θ is the angle that the fracture forms with the vertical direction $\hat{y}$. The density at different temperatures was obtained from the NIST database and it was assumed that the fluid is sufficiently pressurized in order to avoid vaporization. The pressure has a negligible effect on the density of liquid water. Modeling natural convective couples the velocity and temperature field are coupled w ; an iterative scheme was used until the average deviation from the temperature from the last iteration to the one before is less than 0.001 °C. As in the Soultz fracture network shown in Figure 6.1, the fractures may be predominantly aligned vertically, but some form angles with the vertical are greater than zero. From the fracture surface temperature plots, we can see that buoyancy

has the effect of spreading out the mass flow and accessing greater parts of the reservoir, a desirable effect. What is apparent from the results is that buoyancy can greatly improve heat extraction. If the surface installation is highly sensitive to temperature drop, for example, no less than $\Theta_p = 0.95$ can be tolerated, then buoyancy can improve the reservoir life by a factor of three. The effect natural convection has on expanding the swept fracture area will be more pronounced for smaller wellbore spacings. As was seen earlier, fractures with the wells close together did not efficiently sweep the entire fracture. Conversely, the fractures with the wells spread farther apart were better able to retrieve the stored thermal energy in the subsurface. The additional buoyancy induced velocity will move fluid further below the injection well and increase the heat transfer area.

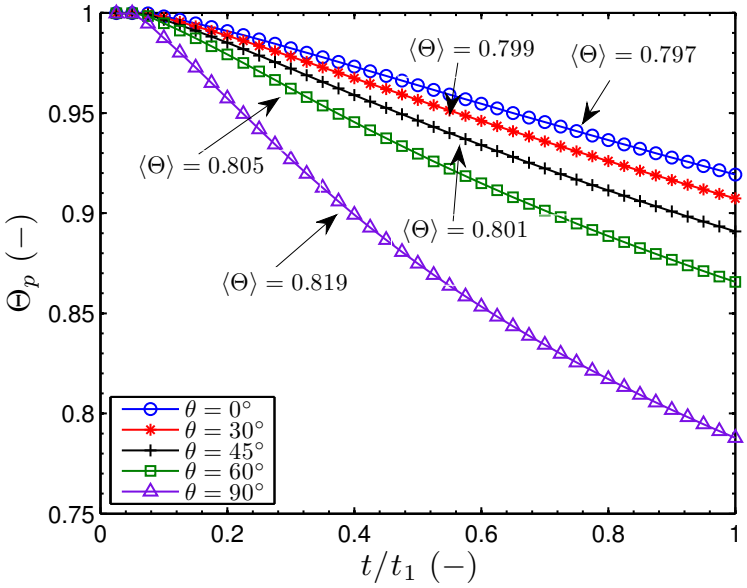

Figure 6.13: Dimensionless production temperature Θ_p for several different fracture angles θ. The mean dimensionless fracture surface temperature $\langle\Theta\rangle$ is reported for each curve. Time t has been nondimensionalized by the end time of extraction t_1, 200 days.

As extraction continues, the disparity between the different strengths of buoyancy increases with time and buoyancy becomes increasingly significant because

buoyancy is driven by the temperature deficit in the fracture. We can also see that the production temperature is more strongly influenced by angle shifts around the horizontal as opposed to around the vertical. In other words, there is a larger production temperature difference from shifting the fracture from the horizontal than from shifting the fracture by the same angle from the vertical axis.

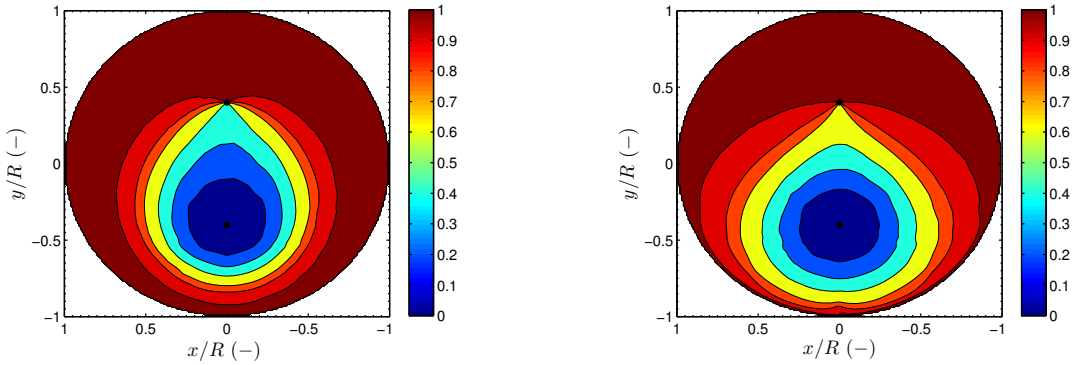

(a) (b)

Figure 6.14: Dimensionless fracture surface temperature for with and without buoyancy effects when $L/(2R) = 0.4$ and after 200 days of extraction. The Θ contours are 0, 0.2, 0.4, 0.6, 0.8, 0.9, and 0.99. The x and y axes are nondimensionalized by the radius R and the black marker refers to the injection (0, -0.4) and production well (0, 0.4) (a) Without buoyancy (b) With buoyancy. Notice the widening of the depleted thermal field.

6.3.4 Intersecting Fractures

The Soultz fracture network depicted in Figure 6.1 shows that the reservoir is not only consists of multiple fractures, but these fractures intersect with each other. Intersections cause changes in the flow structure, compared to if they were modeled as independent fractures and consequently, affect the thermal exchange in the subsurface. If one considers the fracture intersection as a line source or sink, then one would expect that intersections will lead to improved thermal exchange as the intersection will help spread the flow in the fracture.

A simple system by which explore the effect of intersecting fractures on a reservoir's thermal performance is a two fracture system, where the injection well is located in one fracture and production well in the other. Two different reservoirs are modeled in this study, differing in the form of the fracture intersection. One system has the intersection line parallel to a line connecting the injection well and the mid point of the intersection line and the second has the intersection perpendicular to the aforementioned connecting line. The described line can be considered as the mean direction of the flow. The fractures are circular with a radius of 500 m, where the fracture with the injection well is referred to as fracture A and the fracture with the production well is referred to as fracture B. The injection well placement in fracture A is the same as the placement of the injection well in the one fracture scenario, when $L/(2R) = 0.4$. The same is true with regard to fracture B and the placement of the production well. Both intersection lines are the same length, 200 m.

Figure 6.15 and 6.16 show the fracture system configuration and the fracture surface temperature for both the parallel and perpendicular intersection systems. The temperature field in each of the systems is different as a consequence of different flow structures in the fracture. In fracture A, for both intersection types, the intersection causes the flow to efficiently sweep out most of the fracture. However, the temperature fields in fracture B are considerably different between the two systems because the flow structures are not the same. For the perpendicular intersection, the flow is able to access most of the fracture surface below the production well, but the region above the production well is still close to the original rock temperature. The parallel intersection system had a better thermal performance; the dimensionless production temperature was 0.8 after 13.6 years, compared to 0.72 for the perpendicular system. Although there is a central region where the fracture

surface remains close to the original rock temperature, the flow is able to access the peripheral regions of the fracture. The fluid existing the intersection line fans out, as opposed to following straight to the production well, as is the case for the perpendicular intersection.

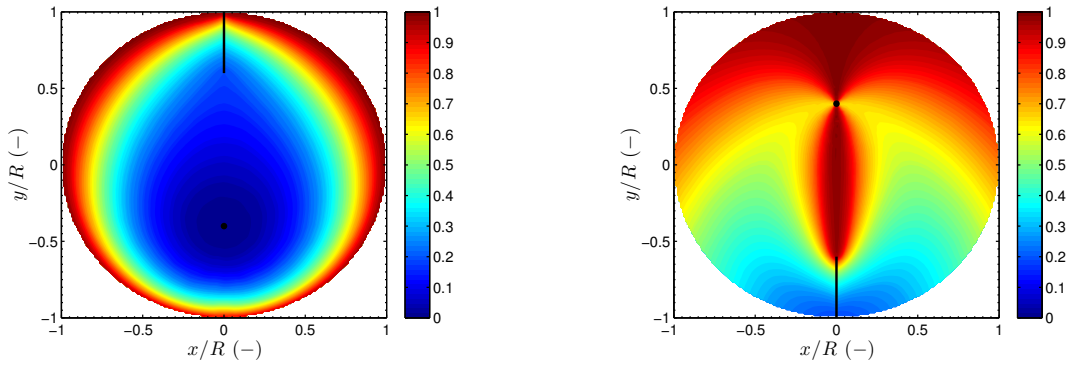

(a) (b)

Figure 6.15: Dimensionless fracture surface temperature for a two fracture system where the intersection line is parallel to the y axis. The temperature field corresponds to 13.55 years of extraction. The x and y axes are nondimensionalized by the radius R. The black marker refers to the injection (0, -0.4) and production well (0, 0.4) and the black line represents the intersection line formed by the fractures. The intersection is 200 m long. (a) Fracture A with the injection well. (b) Fracture B with the production well.

Figure 6.17 shows the drawdown curves for the two different fracture systems in addition to two additional systems. The additional systems represent two independent fractures with the flow split evenly between the two fractures. One system has a dimensionless wellbore spacing $L/(2R)$ of 0.4, while the second system has a value of 0.8. The independent system with $L/(2R) = 0.4$ performed the worst; the dimensionless production temperature reaches 0.8 in about 3 years, while the parallel intersection system performed the best. The dipole flow in the independent fracture system concentrates the flow in the region surrounding the wellbores and the wells need to be sufficiently spread apart so that the region surrounding the wellbores is on the same order of the entire fracture area in order to mitigate

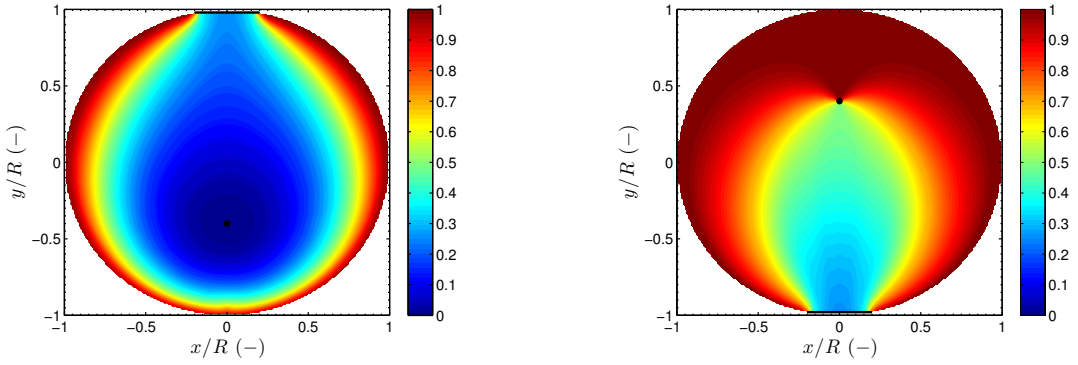

(a) (b)

Figure 6.16: Dimensionless fracture surface temperature for a two fracture system where the intersection line is perpendicular to the y axis. The temperature field corresponds to 13.55 years of extraction. The x and y axes are nondimensionalized by the radius R. The black marker refers to the injection (0, -0.4) and production well (0, 0.4) and the black line represents the intersection line formed by the fractures. The intersection is 200 m long. (a) Fracture A with the injection well. (b) Fracture B with the production well.

the problem of flow concentration. For a reservoir life defined as the time when Θ_p drops to 0.8, the perpendicular intersection system had a reservoir life of about 1.3 times shorter than the parallel intersection case, however, its thermal performance is significantly better than the the independent system when $L/(2R) = 0.4$. The drawdown curve for the independent system with $L/(2R) = 0.8$ is slightly lower than the parallel intersection system, suggesting that effective heat transfer area in both fractures is similar.

The two fracture intersection cases presented just represent two possible ways fractures can intersect. With respect to a system with independent, non-intersecting fractures, fracture intersections can either enhance or inhibit heat exchange, depending on the resulting flow field caused by the intersection. If fracture intersections are able to "stretch" out the flow and make it more uniform, the fluid will more effectively harvest the thermal energy in the host rock. The fluid flow resulting from the fracture intersection depends on the location of the wellbores

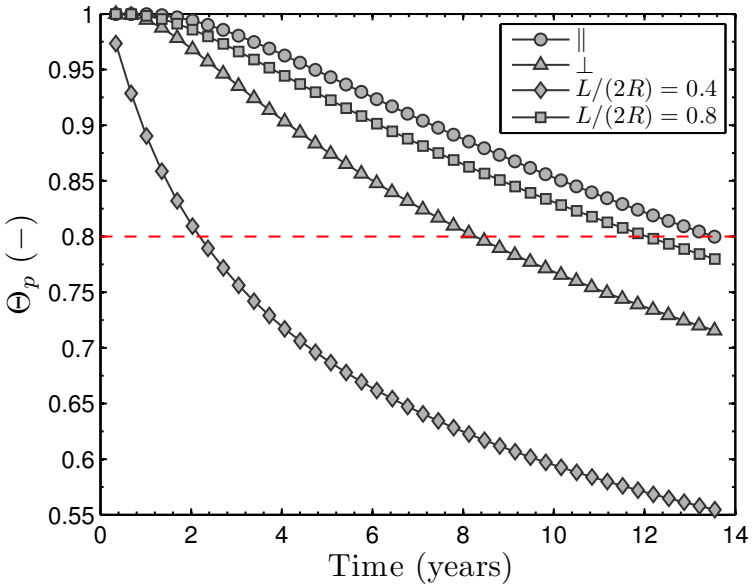

Figure 6.17: Dimensionless production temperature Θ_p for several different fracture systems with different fracture intersections, parallel and perpendicular, and for two systems with independent non-intersecting fractures, each with a different wellbore spacing. The extraction period is 13.55 years. The dashed red line presents the $\Theta_p = 0.8$ drawdown criteria.

with respect to intersection, as well as the angle formed by a line connecting one wellbore/intersection to another wellbore/intersection. For example, if the perpendicular intersection occurred closer to the injection or to the production well, then the flow will be cutoff from a large region of the fracture, thereby reducing the effective heat transfer area. The results presented here show the wide range of reservoir thermal performance and proves how important it is to model fracture intersection accurately.

6.4 Conclusion

A numerical model for simulating fluid flow, heat transport, and particle transport in discretely fractured geothermal systems was developed using the finite element

method for the fluid flow, particle transport, as well as a coupling of finite element and boundary integral equations for heat transport. This numerical model has the capabilities to simulate fractures with varying aperture field, thermal recovery, natural convection, and fracture intersections. The developed code was used on several case studies in order to demonstrate its capabilities. All of these case studies modeled the fractures as circles, although, this is not a requirement for the code.

The first case study modeled the heat transport in a one fracture reservoir, where dipole flow was induced by an injection well and production well. Several values of the wellbore separation distance were modeled, and the results showed how increasing the separation distance of the wells caused the flow to spread across the fracture surface and to extract more thermal energy. A fracture with an elliptical aperture field was also simulated in order to model fractures with a spatially varying aperture. The elliptical aperture field led to greater thermal drawdown, compared to the constant aperture case, because the wellbores were located in the region of the fracture with the largest aperture values, causing the flow to be more channeled.

The second case study investigated thermal recovery for several depleted reservoirs, varying in the length of the wellbore spacing. For the different wellbore spacings investigated, the recovery phase started when the production temperature was the same and when the duration of recovery was four times the length of its respective extraction phase. The temperature at the production well recovered at the same relative rate for all the reservoirs with different wellbore spacing values. The simulations showed that the recovery of the reservoirs followed an inverse square root law with respect to time, suggesting that recovery is primarily driven

by one dimensional heat conduction. As a result, there is little advantage for allowing the reservoir recovery beyond four times the duration of the extraction phase. The mean fracture surface temperature during the recovery phase was shown easily determined given the total amount of energy extracted and the thermophysical properties of the host rock.

Natural convection was studied in vertically orientated fractures, resulting in the the velocity and the temperature field to be coupled. Compared to a fracture with no natural convection, the mixed forced and natural convection created a better sweep of the fracture surface area and enhanced the thermal performance of the system. Fractures that were not perfectly aligned with the vertical direction still exhibited a benefit in thermal performance, albeit to a lesser degree.

For the case study of modeling intersecting fractures, two different reservoirs were modeled, differing in how two fractures intersect each other. The first intersection formed a line that was vertical to the line formed by connecting the wellbore to the midpoint of the intersection line. The second system had the intersection line perpendicular to the aforementioned line. Both intersecting systems had higher production temperatures, compared to a system with two independent fractures that do not intersect each other. The intersection allowed for the flow in the system to be more spread out, compared to dipole flow, and accessed more of the reservoir, which improved thermal performance. However, there could be fracture intersections that cut off large areas of the fracture to flow, reducing the heat transfer area and, thereby, the thermal performance. In general, the manner in which fractures intersect has a significant impact on the fluid flow and thermal performance of a reservoir.

This chapter has demonstrated the capabilities of the model to simulate the

thermal performance of different geothermal reservoirs and to study the effect several reservoir features and characteristics have on thermal performance. The developed numerical model will be used as the basis for work in subsequent chapters. Any additions or modifications to the numerical framework will be stated and explained.

Bibliography

Brown, S. R. (1987). Fluid flow through rock joints: The effect of surface roughness. *Journal of Geophysical Research: Solid Earth*, 92(B2):1337–1347.

Cheng, A. H.-D., Ghassemi, A., and Detournay, E. (2001). Integral equation solution of heat extraction from a fracture in hot dry rock. *International Journal for Numerical and Analytical Methods in Geomechanics*, 25:1327–1338.

Deen, W. (1998). *Analysis of Transport Phenomena*. Oxford University Press, New York, NY.

Fox, D. B., Sutter, D., Beckers, K. F., Lukawski, M. Z., Koch, D. L., Anderson, B. J., and Tester, J. W. (2013). Sustainable heat farming: Modeling extraction and recovery in discretely fractured geothermal reservoirs. *Geothermics*, 46(0):42–54.

Ghassemi, A. and Kumar, G. S. (2007). Changes in fracture aperture and fluid pressure due to thermal stress and silica dissolution/precipitation induced by heat extraction from subsurface rocks. *Geothermics*, 36(2):115–140.

Ghassemi, A., Nygren, A., and Cheng, A. (2008). Effects of heat extraction on fracture aperture: A porothermoelastic analysis. *Geothermics*, 37(5):525–539.

Ghassemi, A., Tarasovs, S., and Cheng, A.-D. (2007). A 3-D study of the effects of thermomechanical loads on fracture slip in enhanced geothermal reservoirs. *International Journal of Rock Mechanics and Mining Sciences*, 44(8):1132–1148.

Ghassemi, A., Tarasovs, S., and Cheng, A. H.-D. (2005). Integral equation solution of heat extraction-induced thermal stress in enhanced geothermal reservoirs. *International Journal for Numerical and Analytical Methods in Geomechanics*, 29(8):829–844.

Ghassemi, A., Tarasovs, S., and H.-D. Cheng, A. (2003). An integral equation solution for three-dimensional heat extraction from planar fracture in hot dry rock. *International Journal for Numerical and Analytical Methods in Geomechanics*, 27(12):989–1004.

Ghassemi, A. and Zhou, X. (2011). A three-dimensional thermo-poroelastic model for fracture response to injection/extraction in enhanced geothermal systems. *Geothermics*, 40(1):39–49.

Greengard, L. and Rokhlin, V. (1997). A fast algorithm for particle simulations. *Journal of Computational Physics*, 135(2):280–292.

Hertzsch, J.-M., Sturman, R., and Wiggins, S. (2007). DNA microarrays: Design principles for maximizing ergodic, chaotic mixing. *Small*, 3(2):202–218.

Lachat, J. C. and Watson, J. O. (1976). Effective numerical treatment of boundary integral equations: A formulation for three-dimensional elastostatics. *International Journal for Numerical Methods in Engineering*, 10(5):991–1005.

Méheust, Y. and Schmittbuhl, J. (2001). Geometrical heterogeneities and permeability anisotropy of rough fractures. *Journal of Geophysical Research: Solid Earth*, 106(B2):2089–2102.

Sausse, J., Dezayes, C., Dorbath, L., Genter, A., and Place, J. (2010). 3D model of fracture zones at Soultz-sous-Forêts based on geological data, image logs, induced microseismicity and vertical seismic profiles. *Comptes Rendus Geoscience*, 342(7–8):531–545.

Sneddon, I. N. (1946). The distribution of stress in the neighbourhood of a crack in an elastic solid. *Proceedings of the Royal Society of London. Series A, Mathematical and Physical Sciences*, 187(1009):229–260.

Stehfest, H. (1970a). Algorithm 368: Numerical inversion of Laplace transforms [d5]. *Commun. ACM*, 13(1):47–49.

Stehfest, H. (1970b). Remark on algorithm 368: Numerical inversion of Laplace transforms. *Commun. ACM*, 13(10):624.

Taron, J. and Elsworth, D. (2009). Thermal-hydrologic-mechanical-chemical processes in the evolution of engineered geothermal reservoirs. *International Journal of Rock Mechanics and Mining Sciences*, 46(5):855–864.

Taron, J. and Elsworth, D. (2010). Coupled mechanical and chemical processes in engineered geothermal reservoirs with dynamic permeability. *International Journal of Rock Mechanics and Mining Sciences*, 47(8):1339–1348.

Taron, J., Elsworth, D., and Min, K.-B. (2009). Numerical simulation of thermal-hydrologic-mechanical-chemical processes in deformable, fractured porous media. *International Journal of Rock Mechanics and Mining Sciences*, 46(5):842–854.

Watanabe, N., Hirano, N., and Tsuchiya, N. (2008). Determination of aperture structure and fluid flow in a rock fracture by high-resolution numerical modeling

on the basis of a flow-through experiment under confining pressure. *Water Resources Research*, 44(6).

Zhou, X. X., Ghassemi, A., and Cheng, A. H.-D. (2009). A three-dimensional integral equation model for calculating poro- and thermoelastic stresses induced by cold water injection into a geothermal reservoir. *International Journal for Numerical and Analytical Methods in Geomechanics*, 33(14):1613–1640.

Zimmerman, R. W. and Bodvarsson, G. S. (1996). Hydraulic conductivity of rock fractures. *Transport in Porous Media*, 23(1):1–30.

CHAPTER 7

THE EFFECT OF SPATIAL APERTURE VARIATIONS ON THE THERMAL PERFORMANCE OF DISCRETELY FRACTURED GEOTHERMAL RESERVOIRS

7.1 Introduction

Variations in fluid velocity on various flow paths in discretely fractured geothermal reservoirs like those found in Enhanced/Engineered Geothermal Systems (EGS) have a significant effect on the thermal performance of a reservoir. One source of variations in fluid flow is from spatial aperture variations in the fractures. EGS reservoirs are developed in hot rock with low permeability and porosity to extract a portion of the stored thermal energy contained in the rock mass. A reservoir is stimulated by pressurizaton to open existing sealed fractures (hydro-shearing) or induce new ones by hydraulic fracturing where water may be pumped into and out of the fractured reservoir using a connected set of injection and production wells to "farm" or extract the stored thermal energy. While convective heat transport is the dominant mode of transport within the fractures, it is inherently coupled to conductive heat transport from the surrounding bulk rock. Because of the low thermal diffusivity of the host rock (of order 10^{-6} m^2/s), only a small region surrounding the fracture network is effective for heat extraction. Given the finite areal extent of the fracture network, extended use will locally cool down the reservoir. The mass loading per unit area usually expressed as the total flow rate per unit fracture surface area is a critical parameter that often scales directly with the rate of thermal drawdown. Drawdown is a major concern for geothermal developers who must forecast reservoir performance and consider its effect in their techno-

economic analysis. This study seeks to determine the effect of fracture aperture variations on the thermal performance of discretely fractured geothermal reservoirs

Because fractures do not have smooth surfaces, spatial aperture variations can lead to maldistributed flow within the fracture network adding a degree of thermal performance uncertainty. Fracture core samples have revealed fracture apertures to have a self-affine spatial correlation governed by a roughness or Hurst coefficient (Brown et al., 1986; Glover et al., 1998; Schmittbuhl et al., 1993, 1995; Plouraboué et al., 1995; Boffa, J. M. et al., 1999; Ponson et al., 2007). A self-affine spatial correlation is one characterized by long range correlations. The aperture undulations in the core samples are found on all length scales but the aperture variance is dominated by the largest scale. Often self-affine fracture surface variations are referred to as fracture roughness despite the fact that roughness implies variations on small rather than large length scales. In this paper, we have avoided using "rough and roughness" as descriptors as much as possible and instead use terms like aperture or surface variations.

To determine the effect fracture surface variations have on fluid flow and on a reservoir's thermal performance, a dipole flow in circular fractures between a single injector and producer was selected. Dipole flow is not uniform and is characterized by streamlines where the fluid velocity is faster near the injection and production wells. For simplicity, effects like temperature dependent properties and buoyancy were not considered. We are interested in modeling reservoirs with different degrees of fracture surface variations, roughness/Hurst coefficients, wellbore spacings, and multiple fractures. Our focus is to determine how fracture aperture variations affect reservoir parameters like the production temperature and the likelihood a reservoir will exhibit thermal enhancement or decline through statistical

parameters involving an ensemble set of fracture realizations. Through these statistical values, we hope to 1. infer how the extent of aperture variations aid or hinder thermal performance, 2. characterize the degree of reservoir performance uncertainty due to aperture variations, and 3. determine under what scenarios aperture variations need to be modeled. Furthermore, modeling spatial aperture variations provides a method to systematically generate variations in flow fluid rates and their pathway through the fracture system.

While little work has been done on the coupled convective-conductive heat transport of the fracture and surrounding rock in a reservoir with spatial aperture variations, researchers have modeled fluid flow and other transport properties using a self-affine aperture field. They have observed that self-affine aperture fields lead to flow channeling where most of the fluid will travel through several preferential channels (Brown, 1987; Tsang and Tsang, 1989; Glover et al., 1998; Drazer and Koplik, 2000; Méheust and Schmittbuhl, 2001, 2003; Auradou et al., 2006). Méheust and Schmittbuhl (2001) determined that three parameters are required to model the flow, the mean aperture, the root mean square of the aperture, and the Hurst coefficient. They further showed how the mean flow rate was either enhanced or inhibited, depending on the orientation of the applied pressure drop. Transport properties such as dispersion have also been studied in self-affine fractures (Plouraboué et al., 1998; Drazer and Koplik, 2002; Auradou et al., 2010). Numerical studies exhibit non-Gaussian transit time distribution with long tails (Drazer and Koplik, 2002) and experiments with Newtonian and shear thinning fluids showed that geometric/hydraulic dispersion is dominant at low Péclet numbers with the dispersion coefficient on the order of the Péclet number (Auradou et al., 2010). Other researchers have used flow channeling to reduce numerical computation by reducing flow in 2D fractures to an equivalent 1D flow (Cacas et al.,

1990; Nordqvist et al., 1992; Bruel et al., 1994) or to reduce 3D flow into an equivalent 2D system (Bruderer-Weng et al., 2004). The above mentioned studies have focused on the effects fracture surface variations have on hydraulic performance and particle/solute transport and do not cover the consequence on convective heat transport. However, these studies mention preferential flow paths which suggest that surface variations may have a negative impact on thermal exchange.

Kolditz (1995) suggested that local aperture variations may play a strong role in a reservoir's thermal performance. Jupe et al. (1995) attempted to model spatial aperture variations by modeling separate flow paths. They used the multifracture parallel rectangular reservoir model described by Nicol and Robinson (1990) and treated the different flow paths as separate fractures. Their work focused on determining the wellbore spacing needed to obtain an economic EGS reservoir. By incorporating multiple flow paths, the wellbore spacing needed to obtain their desired performance criteria went from 700 m (no channeling) to 1080 m.

The thermal effect of surface variations has recently been investigated in a rectangular fracture where the base flow is uniform (Neuville et al., 2010b,a). However, Neuville et al. (2010b,a) used a simplified heat transfer model that only considers the heat transfer in the fracture and not in the surrounding rock; the surrounding rock was assumed to be permanently at the original reservoir temperature. As a consequence, their results can be interpreted as the early thermal behavior of the reservoir and not the behavior after extended reservoir use. The assumption of constant rock temperature is valid for the time scale of w^2/α, where w is the fracture aperture and α is the thermal diffusivity of the rock. For an aperture value from 1 to 5 mm and a thermal diffusivity of 1×10^{-6} m^2/s, the time scale will be on the order of 1 to 10 seconds. Neuville et al. (2010b) work focused on de-

veloping relationships between a reservoir's hydraulic performance and its thermal performance. They concluded heat exchange in self-affine fractures is less efficient compared to a constant aperture case. As a case study, Neuville et al. (2010a) modeled the Soultz-sous-Forêts EGS reservoir as a single fracture and concluded that merely knowing the mean aperture is not sufficient to determine the thermal heat exchange and that fracture surface variations always led to inhibited thermal exchange. Although Neuville et al. (2010b,a) have modeled variations in convective heat transport in the presence of aperture undulations, there is still a need to model the coupled convective heat transport in the fracture with that of the conductive transport in the surrounding rock.

Our approach fully couples the heat transfer in the fracture to the surrounding bulk rock by using a finite element method in the fracture and boundary integral equations to describe the temperature in the bulk rock. Additionally, our study aims to determine how much deviation in production temperature in the absence of aperture undulations is anticipated after prolonged reservoir utilization. The use of statistical values of an ensemble of realizations including the mean and standard deviation of production temperatures will offer a better and more practical understanding of the effects fracture surface variations have on discretely fractured geothermal reservoirs.

7.2 Modeling of Mass, Momentum, and Heat Transport

The following section discusses the mathematical description and generation algorithm of self-affine aperture fields. The fluid flow and heat transport in the reservoir are solved using the developed FEM/BIE numerical model. Please refer

to Chapter 6 for more details on the FEM/BIE numerical model.

7.2.1 Self-affine Aperture Field

A spatially varying aperture field fluctuates with a value of $h(x, y)$ from a mean value of $\langle w \rangle$ to give

$$w(x, y) = \langle w \rangle + h(x, y). \tag{7.1}$$

The spatial mean aperture $\langle w \rangle$ is given by

$$\langle w \rangle \equiv \frac{\int_A w(x, y)\ \mathrm{d}A}{\int_A\ \mathrm{d}A}, \tag{7.2}$$

where A is the fracture surface area and the variance or mean square of the aperture field is given by

$$\sigma_h^2 \equiv \langle h^2 \rangle = \frac{\int_A h^2(x, y)\ \mathrm{d}A}{\int_A\ \mathrm{d}A}. \tag{7.3}$$

The spatial correlation of an aperture field can be described by the variogram function γ, which is twice the difference of the aperture variance and the two-position autocorrelation function:

$$\gamma(\mathbf{r}') \equiv \langle [h(\mathbf{r}) - h(\mathbf{r} + \mathbf{r}')]^2 \rangle = 2 \left[\langle h^2 \rangle - \langle h(\mathbf{r}) h(\mathbf{r} + \mathbf{r}') \rangle \right], \tag{7.4}$$

where $\mathbf{r}'$ is the displacement from point $\mathbf{r}$ and $\mathbf{r}$ is a point on the surface of the fracture. The autocorrelation function is a measure of the correlation of the aperture at point $\mathbf{r}$ with that at point $\mathbf{r} + \mathbf{r}'$. If the variogram function follows

$$\gamma(\mathbf{r}') = C|\mathbf{r}'|^{2\zeta}, \tag{7.5}$$

it has a scaling behavior of $\gamma(\lambda \mathbf{r}') = \lambda^{2\zeta} \gamma(\mathbf{r}')$, where λ is a scaling parameter and the field is said to have a self-affine geometry governed by the Hurst or roughness coefficient, ζ (Feder, 1988; Falconer, 2003). For this study, we have chosen to

model fracture aperture variations as having a self-affine geometry. By measuring a surface profile, many materials have been shown to have a self-affine geometry (Bouchaud, 1997). From fracture core samples, the Hurst coefficient has been determined to be from 0.7 to 0.8 (Brown et al., 1986; Glover et al., 1998) and, specifically, equal to 0.8 for granite (Schmittbuhl et al., 1993, 1995; Plouraboué et al., 1995), the typical rock type of deep geothermal systems. Sandstone, on the other hand, has been shown to have a lower value of ζ at around 0.5 (Boffa, J. M. et al., 1999; Ponson et al., 2007). Although it is difficult to determine whether a fracture will exhibit a self-affine behavior at the length scale of geothermal fractures, it has been observed up to the meter scale (Brown and Scholz, 1985).

With a self-affine behavior, larger scale variations in h (small frequencies, long wavelengths) are more important than small scale (large frequencies, short wavelengths) variations. The large scale variations become more strongly dominant when ζ is increased. However, the large scale variations are the primary determinant of the aperture variations for any positive ζ. A self-affine aperture field is analogous to fractional Brownian motion, if one views the spatial displacement $|\mathbf{r}'|$ as a time-like variable and the change of aperture with displacement as equivalent to the spatial step of the Brownian motion. With this analogy, $\zeta < 1/2$ corresponds to a subdiffusive or antipersistent process, $\zeta = 1/2$ corresponds to a normal diffusive process, and $1/2 < \zeta < 1$ corresponds to a super diffusive process with $\zeta = 1$ representing ballistic motion (Mandelbrot and Ness, 1968).

The algorithm used to generate spatially varying aperture fields, which was adapted from Méheust and Schmittbuhl (2001), uses random seeding and Fast Fourier Transforms to obtain isotropic self-affine fracture aperture fields on rectangular fractures. In order to generate circular fractures with a self-affine aperture

field, a square fracture of length $2R$ was first generated and only the area of an inscribed circle was used for the analysis. Any shaped fracture could have been generated by first generating a large enough rectangular fracture to inscribe the desired shape of the fracture. Only the inscribed area formed by the arbitrary shaped fracture is used for the analysis. To obtain the desired σ_h of the fracture, the aperture value h is rescaled. A more detailed description of the algorithm used can be found in Appendix B.

7.2.2 Fluid Flow and Heat Transport

The fluid flow and heat transport in the self-affine fractures are solved using the developed numerical model in the previous chapter. The pressure and velocity field are first solved and the velocity field is used in determining the temperature field in the fracture. The dimensionless temperature in the reservoir is defined as $\Theta \equiv (T(x,y) - T_w)/(T_r - T_w)$, where T is the temperature of the fracture surface at point (x,y), T_w is the temperature of the injected water and T_r is the initial rock temperature which remains constant in the far-field. The value of Θ ranges from zero to one. A value of zero refers to complete thermal exhaustion of the reservoir as the temperature in the fracture is now equal to the injected water temperature. If $\Theta = 1$, there is no drawdown since the temperature in the fracture is still at the initial reservoir rock temperature. The variable Θ_p refers to the dimensionless production temperature. If $\beta^2 \ll 1$ (1D conduction), then the dimensionless temperature is a function of the dimensionless wellbore spacing and dimensionless time:

$$\Theta = f\left(\frac{L}{2R}, \frac{t}{\tau}\right), \tag{7.6}$$

where $\tau \equiv L^4 k_r \rho_r c_r / (\dot{m} c_w)^2$. The dimensionless wellbore spacing is constrained to range from zero to one. The results for one mass flow rate and a set of times for a given dimensionless wellbore spacing are the same as for a different mass flow rate and a set of extraction times corresponding to the same dimensionless times. By adding self-affine aperture fluctuations, the statistical values of the dimensionless temperature become functions of two additional parameters, $\sigma_h / \langle w \rangle$ and ζ. For this study, we have used a radius R of 500 m and an injected mass flow $\dot{m}$ of 40 kg/s. The injection and production wells are modeled as circles radius 0.15 m in the mesh. The thermophysical property values used were $k_r = 2.4$ W/(m °C), $\rho_r = 2300$ kg/m^3, $c_r = 1000$ J/(kg °C), and $c_w = 4184$ J/(kg °C). The value of τ is 2.1×10^7 s or 0.16 years for a wellbore spacing of 400 m and for the previously listed values of the thermophysical properties and mass flow rate.

7.3 Results for One Fracture

For an idealized single circular fracture with self-affine aperture variations, our modeling provides the statistical distribution of the dimensionless production temperatures as a function of wellbore spacing, duration of extraction, the variance of fracture aperture variations, and the Hurst coefficient. The extraction time for geothermal production selected for our study corresponded to a particular level of the thermal performance. In our study, this occurred when the dimensionless production temperature reached 0.8 for the case without aperture variations, which we call the base case. The variable $\Theta_{p,0}$ refers to the base case production temperature. The drawdown criteria will vary depending on the end-use of the thermal energy; direct thermal use operations can afford a greater drawdown compared to electricity production. However, using $\Theta_{p,0} = 0.8$ is a realistic value for the

drawdown criteria in many practical situations.

For $\sigma_h/\langle w \rangle$, ζ, and $L/(2R)$, we chose a range of possible values for these parameters to model their impacts on thermal performance. The range of $\sigma_h/\langle w \rangle$ was chosen to be from 0.015 to 0.35. Granite core samples have been shown to have a value of $\sigma_h/\langle w \rangle$ of 0.42 (Hakami and Larsson, 1996) but also low values around 5×10^{-4} (Sausse, 2002). Because of the uncertainty in the standard deviation of the local aperture values and the difficulty in concluding how representative core sample values will be of practical in situ conditions in geothermal reservoirs, we believe the range chosen is adequate for simulating a large class of fractures. Above $\sigma_h/\langle w \rangle = 0.35$, it becomes difficult to generate fractures that do not have zero or negative aperture values. Thus, the aperture realizations generated represent fractures that have been sufficiently propped open due to the combination of "self-propping" due to shear displacement and inflation as a result of higher fluid pressures within the fracture. As previously reported, the Hurst coefficient has been observed to be always above 0.5 and is often reported to be around 0.8. However, the Hurst coefficient is a model specific parameter and is not often reported. It is plausible to think that there are instances where the Hurst coefficient is less than 0.5. Given its theoretical range of 0 to 1, the range of the Hurst coefficient chosen was from 0.1 to 1. The dimensionless wellbore spacing $L/(2R)$ can vary anywhere from 0 to 1, depending on where the injection and production wells have been placed relative to the fracture size. In this study, we investigated the range from 0.2 to 0.8.

We first present the results where the standard deviation of the aperture is varied. For the range of values investigated, five thousand fracture realizations were generated for each value of $\sigma_h/\langle w \rangle$ with $L/(2R)$ and ζ kept constant at 0.4

and 0.8, respectively. In a second set of simulations, we repeated the process but now varying the Hurst coefficient and keeping $L/(2R) = 0.4$ and $\sigma_h/\langle w \rangle = 0.25$. Finally, in a third set, the wellbore spacing was varied and $\sigma_h/\langle w \rangle$ and ζ are set to 0.25, and 0.8, respectively. The statistical values of the thermal performance of most interest are the mean dimensionless production temperature $\bar{\Theta}_p$ of the ensemble, the standard deviation of production values σ_Θ, and the fraction of cases with a higher production temperature than the base case F. Five-thousand was chosen to have an adequate sample size but also to be able to generate results in a timely manner. Using ten-thousand fracture realizations did not result in any significant change in the derived results.

7.3.1 Varying Strength of Aperture Fluctuations

For a range of $\sigma_h/\langle w \rangle$ from 0.015 to 0.35, five thousand fracture realizations were generated for each value of $\sigma_h/\langle w \rangle$. For each five thousand fracture realization data set, the values of $\bar{\Theta}_p$, σ_Θ, and F are reported based on the thermal performance for all realizations at the time when the dimensionless production temperature reached 0.8 in the absence of aperture variations. A depiction of the fracture surface temperature for the base case, thermally under performing, and thermally over performing (compared with the base case) and their corresponding aperture fields is shown in Figure 7.1. The dimensionless heat transfer area accessed at a certain time is defined as $\int(1-\Theta)\ \mathrm{d}A/A = 1 - \langle\Theta\rangle$. Thus, the mean fracture surface temperature $\langle\Theta\rangle$ is a measure of the thermally accessed area of the fracture at a given extraction time. Comparing $\langle\Theta\rangle$ for different fracture aperture distributions, a fracture with a lower value of $\langle\Theta\rangle$ was able to access more area of the reservoir for heat transfer. For dipole flow, the majority of the flow occurs in the

region surrounding the injection and production wells with less flow in the periphery of the fracture. The base case mean value for $\langle\Theta\rangle$ is 0.816 when $\Theta_{p,0} = 0.8$. For a fracture with smaller apertures in the region between the wells, the fluid is pushed to higher aperture regions in the periphery and the effective heat transport area increases, $\langle\Theta\rangle = 0.787$ when the dimensionless production temperature reaches 0.8. As expected, this less channeled, beneficial flow field leads to a higher production temperature and slows the rate of thermal drawdown. On the other hand, when there exists a high aperture region in between the wells, the flow is further channeled from the injection to production well and the effective heat transfer area becomes narrower than the base case; the mean dimensionless fracture surface temperature is 0.854 when the dimensionless production temperature is 0.8. Consequently, the production well cools down rapidly. How the low and high aperture regions are arranged in the fracture is clearly important in determining whether the reservoir will exhibit poor or good thermal performance.

Figure 7.2 shows the distribution of thermal performance when $\sigma_h/\langle w\rangle = 0.25$. Although a Gaussian curve does not fit the histogram perfectly, it does an adequate job of describing the behavior. A Gaussian distribution of Θ_p is expected for a Gaussian aperture fluctuations with small amplitude variations. Inserting $\langle w\rangle + h$ into the governing equations for fluid velocity and fracture surface temperature and considering a regular perturbation expansion for small $\epsilon = \sigma_h/\langle w\rangle$, one obtains $\Theta_p = \Theta_0 + \epsilon\Theta_1 + \epsilon^2\Theta_2 + O(\epsilon^3)$ for w, where Θ_0 is the production temperature for the constant aperture case and Θ_1 is a linear functional of the field $h(\mathbf{r})/\sigma_h$. A linear functional of a Gaussian field is a Gaussian variable. Figure 7.2 also reveals that we sometimes encounter enhanced thermal performance but more often encounter poor performing fractures with a dimensionless production temperature less than the base case. Figures 7.3 and 7.4 show how the strength of

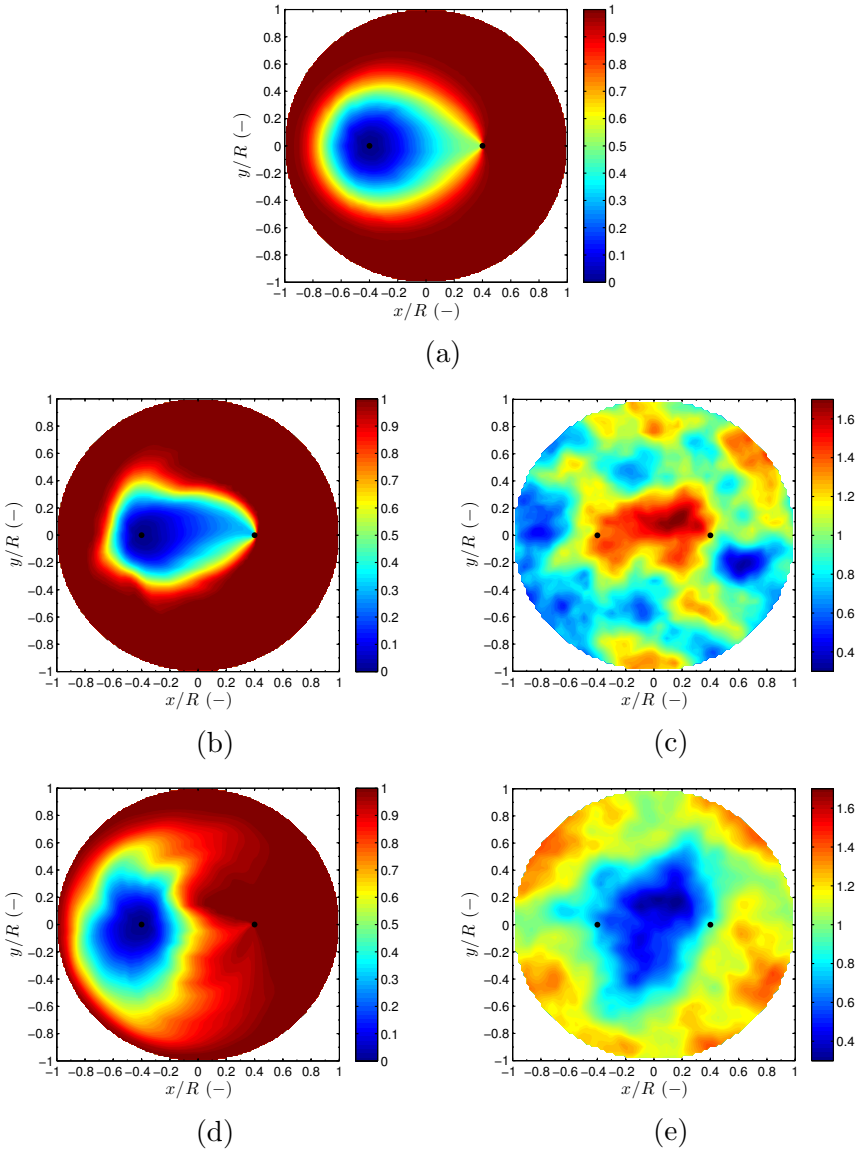

Figure 7.1: Dimensionless fracture surface temperature for the base case (a) and fractures exhibiting poor (b) and good (d) thermal performance (left hand side) with their respective aperture fields ((c) and (e); right hand side). The aperture field is normalized by the mean aperture value $\langle w \rangle$ and the dimensionless aperture standard deviation $\sigma_h / \langle w \rangle$ and the Hurst coefficient ζ are equal to 0.25 and 0.8, respectively. The wellbore separation value is $L/(2R) = 0.4$ and the injection and production wells are located at (-0.4,0) and (0.4,0), respectively (marked by a black dot). All figures represent the same production period of 203 days, the time it takes for the base case to reach a dimensionless production temperature of $\Theta_{p,0} = 0.8$.

aperture variations affects the mean and standard deviation of the production temperature. As $\sigma_h/\langle w \rangle$ increases, the mean production temperature decreases quadratically and the standard deviation increases linearly. The trends reveal that as the aperture fluctuations increase, the thermal performance declines on average and is more variable. In effect, figure 7.4 says that predicting the reservoir's thermal performance becomes more difficult with increasing values of $\sigma_h/\langle w \rangle$.

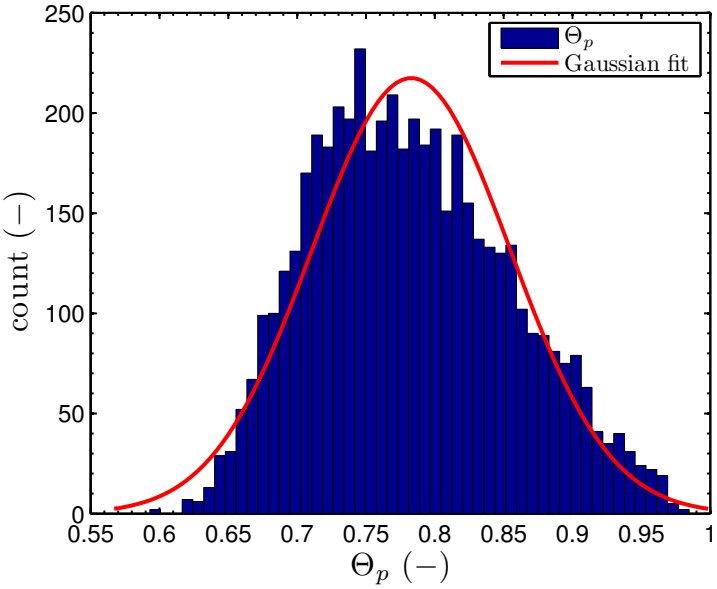

Figure 7.2: Histogram of the dimensionless production temperature Θ_p when the dimensionless wellbore spacing $L/(2R)$ is equal 0.4, the dimensionless standard deviation of the aperture $\sigma_h/\langle w \rangle$ is equal to 0.25, and the Hurst coefficient ζ is equal to 0.8. The results are for the production period when the base case (no aperture variations) reaches $\Theta_{p,0} = 0.8$. A Gaussian fit results in a mean and standard deviation of 0.783 and 0.072, respectively.

The linear behavior of Figure 7.4 is expected due to the before mentioned linear behavior of Θ_p to small variations of h. In particular, Θ_0 has zero standard deviation, while Θ_1 has an $O(1)$ standard deviation so that the standard deviation of $\Theta_p \approx \Theta_0 + \epsilon\Theta_1$ is proportional to σ_h. The quadratic relationship between the mean production temperature and the aperture standard deviation is also expected owing to the fact that $\bar{\Theta}_1$ must be zero based on linearity. Thus, $\bar{\Theta} - \Theta_0 =$

$(\sigma_h/\langle w\rangle)^2\bar{\Theta}_2$, where $\bar{\Theta}_2$ is a constant of proportionality.

Geothermal operations are sensitive to temperature drawdown and a premature drop in production temperature would reduce the economic attractiveness of the project. Each fracture in the ensemble has a lifetime corresponding to the time when Θ_p reaches 0.8. When $\sigma_h/\langle w\rangle = 0.1$, which resulted in $\sigma_\Theta = 0.031$, the 25% and 75% quantiles of the distribution of the ratio of reservoir life to the reservoir life of the base case are equal to 0.83 and 1.16, respectively. For $\sigma_h/\langle w\rangle = 0.35$, corresponding to $\sigma_\Theta = 0.092$, the results are more drastic as the 25% and 75% quantiles become 0.47 and 1.28, respectively. On the other hand, aperture variations are less important for lower values of $\sigma_h/\langle w\rangle$; when $\sigma_h/\langle w\rangle = 0.05$, the 25% and 75% quantiles of reservoir life are closer together and equal to 0.91 and 1.08, respectively.

For a normally distributed production temperature, the probability density function is equal to

$$f(\Theta_p) = \frac{1}{\sqrt{2\pi}\sigma_\Theta} \exp\left[\frac{(\Theta_p - \bar{\Theta}_p)^2}{2\sigma_\Theta^2}\right]. \tag{7.7}$$

From Figure 7.2, it is reasonable to model the production temperature using a normal (Gaussian) distribution. The fraction of fractures that exhibit enhanced thermal performance is equal to one minus the integral of Eq. (7.7) with respect to Θ_p form 0 to $\Theta_{p,0}$. The result is

$$F = \frac{1}{2}\text{erfc}\left[\frac{\Theta_{p,0} - \bar{\Theta}_p}{\sqrt{2}\sigma_\Theta}\right]. \tag{7.8}$$

As discussed earlier, the mean and standard deviation of the production temperature distribution have a quadratic and a linear behavior, respectively:

$$\Theta_{p,0} - \bar{\Theta}_p = C_1\left(\frac{\sigma_h}{\langle w\rangle}\right)^2, \tag{7.9}$$

and

$$\sigma_\Theta = C_2 \left(\frac{\sigma_h}{\langle w \rangle} \right). \tag{7.10}$$

Using Eq. (7.9) and (7.10), the fraction of fractures that exhibit enhanced thermal performance compared to the base case can be expressed in terms of the standard deviation of the aperture fluctuations,

$$F = \frac{1}{2} \text{erfc} \left(\frac{K \sigma_h}{\sqrt{2} \langle w \rangle} \right), \tag{7.11}$$

where K is the ratio of C_1/C_2. Since the error function is linear for small values of $K\sigma_h/(\sqrt{2}\langle w \rangle)$, Eq. (7.11) can be approximated as

$$F \approx \frac{1}{2} - \frac{K}{\sqrt{2\pi}} \left(\frac{\sigma_h}{\langle w \rangle} \right). \tag{7.12}$$

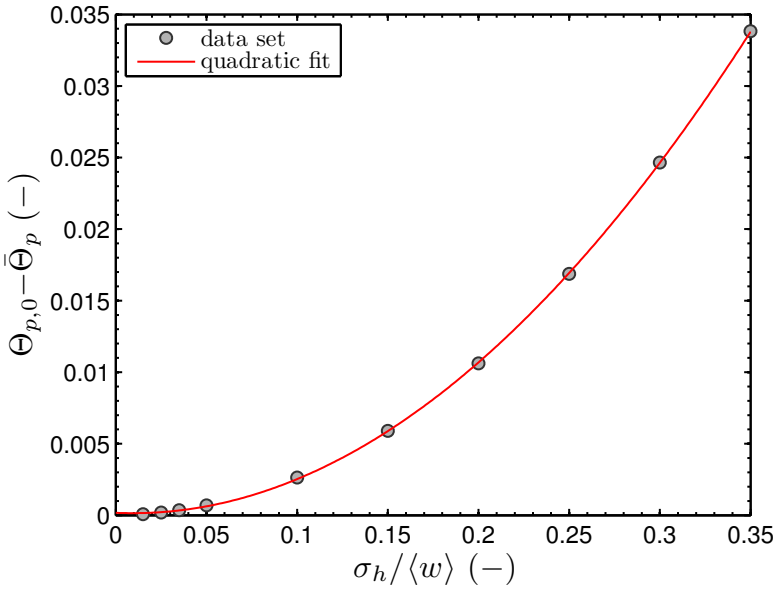

Figure 7.3: Deviation of the mean dimensionless production temperature from the base case value $\Theta_{p,0} - \bar{\Theta}_p$ as a function of the dimensionless standard deviation of the aperture $\sigma_h/\langle w \rangle$. The Hurst coefficient ζ is equal to 0.8, the wellbore spacing $L/(2R)$ is equal to 0.4, and the base case production temperature $\Theta_{p,0}$ is equal to 0.8 (reference value of no aperture variations). A quadratic fit is also shown.

Figure 7.5 displays the linear decrease of F as a function of $\sigma_h/\langle w \rangle$. The linear behavior of F results because the argument of the error function is small for the

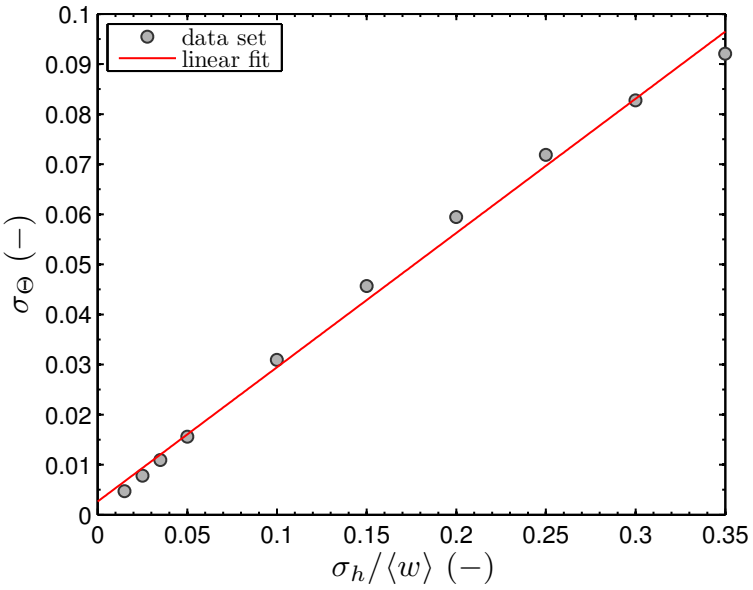

Figure 7.4: Standard deviation of the dimensionless production temperature σ_Θ for the ensemble of fracture realizations as a function of dimensionless standard deviation of the aperutre $\sigma_h/\langle w\rangle$ when $\zeta = 0.8$ and $L/(2R) = 0.4$. The production end time of interest is when the dimensionless production temperature Θ_p of the base case (no aperture variations) reaches 0.8. A linear fit is also shown.

range studied ($K = 1.03$). The theoretical prediction for F matches well with the simulation results and is consistent with assuming that the distribution of Θ_p is Gaussian. The theoretical and simulated curves only deviate about 0.015 at the end of the range investigated. The fraction of fractures exhibiting adverse flow channeling was not observed to be a function of dimensionless time as F only varied temporally by less than 1%. Thus, choosing a different dimensionless temperature stopping criteria will not change the reported values of F.

The results shown indicate that the magnitude of aperture variations has a large effect on the thermal performance of the reservoir. For a specified standard deviation, the production temperature can be modeled as a Gaussian distribution. The fraction of fracture whose thermal performance benefits from a self-affine aperture field monotonically decreases with respect to the strength of the aperture

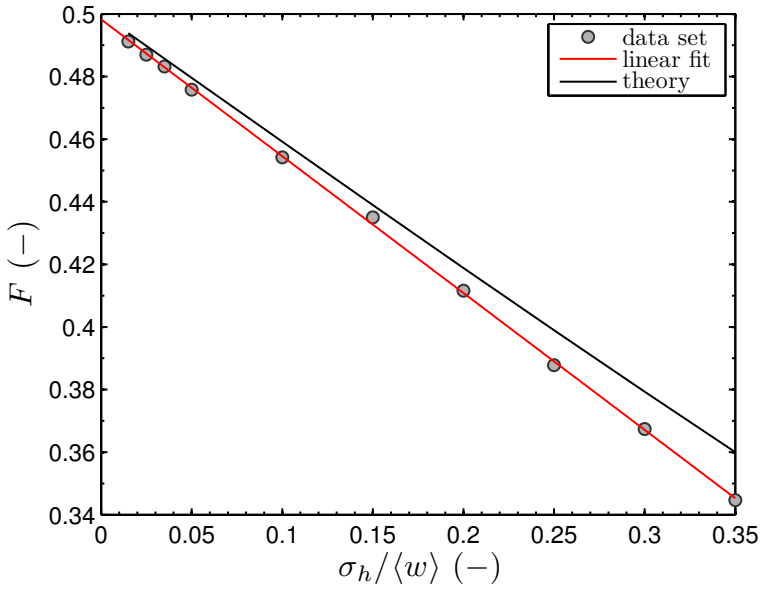

Figure 7.5: The fraction of fractures exhibiting thermal performance enhancement F as a function of dimensionless standard deviation of the aperture $\sigma_h/\langle w \rangle$. The Hurst coefficient ζ is equal to 0.8 and the wellbore spacing $L/(2R)$ is equal to 0.4. A best fit line (dashed red) was added as well as the theoretical prediction (solid black) using a Gaussian distribution and the fitted parameters for the relationship of σ_Θ and $\bar{\Theta}_p$.

variations and is never higher than 0.5. It ranged from 0.49 to 0.34 for the range of $\sigma_h/\langle w \rangle$ investigated. Thus, there are more ways to arrange isotropic self-affine aperture fluctuations that lead to a flow field which produces adverse rather than beneficial thermal performance.

7.3.2 Varying the Hurst Coefficient

To investigate the effect of the Hurst coefficient ζ on thermal performance, simulations were performed for ten sets of five thousand fractures. Each set had a different value of ζ in the range from 0.1 to 1 and $\sigma_h/\langle w \rangle$ was kept constant at 0.25. Figure 7.6 displays 1D fracture aperture profiles for various values of ζ.

Table 7.1: Thermal performance with varying the Hurst coefficient. The statistical values are reported with a 95% confidence interval determined using resampling based on the bootstrapping method.

ζ	$\bar{\Theta}_p$	σ_Θ	F
0.1	0.786 ± 0.002	0.063 ± 0.001	0.41 ± 0.01
0.2	0.785 ± 0.002	0.065 ± 0.001	0.40 ± 0.01
0.3	0.784 ± 0.002	0.067 ± 0.001	0.40 ± 0.01
0.4	0.784 ± 0.002	0.069 ± 0.001	0.40 ± 0.01
0.5	0.784 ± 0.002	0.069 ± 0.001	0.39 ± 0.01
0.6	0.784 ± 0.002	0.071 ± 0.001	0.40 ± 0.01
0.7	0.783 ± 0.002	0.072 ± 0.001	0.39 ± 0.01
0.8	0.783 ± 0.002	0.072 ± 0.001	0.39 ± 0.01
0.9	0.784 ± 0.002	0.073 ± 0.001	0.40 ± 0.01
1	0.784 ± 0.002	0.073 ± 0.001	0.40 ± 0.01

Increasing ζ yields aperture fields with strong large scale correlations. In other words, the profile for $\zeta = 1$ is smoother than the profile for $\zeta = 0.1$, which is characterized by many "peaks" and "valleys". Table 7.1 summarizes the statistical results of the ensembles for each value of ζ, with a 95% confidence interval derived by resampling based on the bootstrapping method (Efron and Tibshirani, 1994).

Table 7.1 indicates that the Hurst coefficient has little effect on the thermal performance given the confidence intervals of the statistical quantities. Zimmerman and Bodvarsson (1996) and Méheust and Schmittbuhl (2001) have shown that changing the Hurst coefficient had little affect on fluid flow. Since heat transport is mathematically an integral process that is dependent on large length scale fluid flow variations and even the variance of the aperture is governed by the large scale, it is not surprising that varying the Hurst coefficient has little impact on the distribution of thermal performance. Of the statistical values from the ensemble, only σ_Θ changes appreciably, ranging from 0.063 to 0.073 with increasing ζ. If the aperture field is more correlated (larger value of ζ), the region between the wells is more likely to have either a single peak or a single valley (low or high aperture

regions). Having either a single peak or valley results in a more drastic difference in thermal performance than would be induced by the many peaks and valleys occurring for smaller ζ. The standard deviation of the production temperature does not change much for $\zeta > 0.6$ because for these values the diameters of the peaks and valleys are likely to be equal or larger than the wellbore spacing.

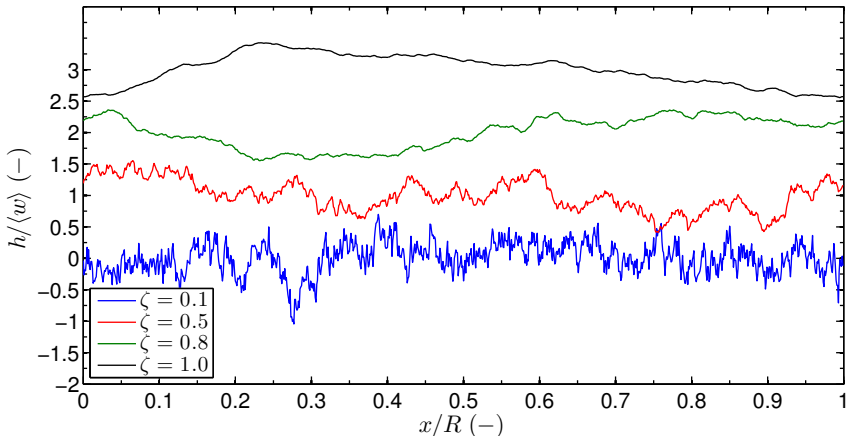

Figure 7.6: The fracture aperture h profile for various values of the Hurst coefficient ζ with the dimensionless standard deviation of aperture fluctuations $\sigma_h/\langle w \rangle$ kept at 0.25. For values of ζ of 0.1, 0.5, 0.8, and 1, the profiles were shifted upward by $\langle w \rangle$, $2\langle w \rangle$, and $3\langle w \rangle$ to prevent them from overlapping.

7.3.3 Varying Wellbore Separation

The effect of self-affine aperture variations on different base flows can be understood by changing the value of the wellbore separation value, $L/(2R)$. As $L/(2R)$ gets smaller the streamlines becomes more varied and diverse. On the other hand, the streamlines become more uniform as the injection and production wells are pulled apart. For values of $L/(2R)$ of 0.2, 0.4, 0.5, 0.6, and 0.8, the thermal performance of the five thousand fracture simulations for each value of $L/(2R)$ were all performed for an end time when the respective $L/(2R)$ base case production temperature reaches 0.8. To reach the $\Theta_p = 0.8$, the dimensionless time t/τ for $L/(2R)$ of 0.2,

Table 7.2: Thermal performance with varying wellbore spacing $L/(2R)$. The statistical values are reported with a 95% confidence interval determined using resampling based on the bootstrapping method.

$L/(2R)$	$\bar{\Theta}_p$	σ_Θ	F
0.2	0.793 $\pm$0.002	0.057 $\pm$0.001	0.42 $\pm$0.01
0.4	0.783 $\pm$0.002	0.072 $\pm$0.001	0.39 $\pm$0.01
0.5	0.779 $\pm$0.002	0.073 $\pm$0.001	0.38 $\pm$0.01
0.6	0.774 $\pm$0.002	0.068 $\pm$0.001	0.36 $\pm$0.01
0.8	0.763 $\pm$0.002	0.053 $\pm$0.001	0.28 $\pm$0.01

0.4, 0.5, 0.6, and 0.8 is equal to 4.7, 3.5, 2.8, 2.2, and 1.2 respectively. Although increasing the wellbore spacing increases the time to reach the drawdown criteria, the dimensionless time t/τ to reach the drawdown criteria drops for increasing values of wellbore spacing because τ is proportional to L^4. The values of ζ and $\sigma_h/\langle w \rangle$ were kept constant at 0.8 and 0.25, respectively.

Boxplots for the distribution of thermal performance for the different values of $L/(2R)$ are plotted in Figure 7.7. The boxplots show that the distribution of dimensionless production temperatures becomes more varied with increasing values of the wellbore spacing but peaks at $L/(2R) = 0.4$; the standard deviation of the dimensionless production temperature is greatest for this value. The mean value of the distribution and F decreases as $L/(2R)$ decreases. Table 7.2 summarizes the statistical values of the data sets, with a 95% confidence interval derived by resampling based on the bootstrapping method (Efron and Tibshirani, 1994).

The mean dimensionless production temperature is closest to the base case value when the wellbore spacing is small and there is less opportunity for the conductance to vary in the inter-wellbore region. The thermal performance distribution is most varied when $L/(2R) = 0.4$ because it corresponds to the typical length scale of one "peak" or "valley", as can be see in Figure 7.6. When the dimensionless wellbore spacing is smaller than 0.4, then the region in between the

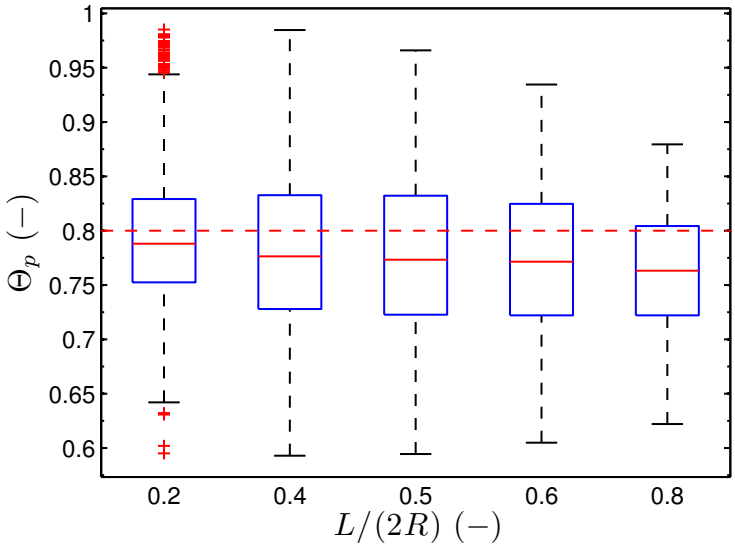

Figure 7.7: Boxplot of dimensionless production temperatures for various values of wellbore spacing $L/(2R)$. The dimensionless standard deviation $\sigma_h/\langle w \rangle$ is equal to 0.25 and the Hurst coefficient ζ is equal to 0.8. The lower and upper edge of the box represents the first and third quartiles while the solid red line represents the median value. The lower and upper whiskers of the boxplot are defined as 1.5 times the first and third quartile value, respectively, and the red plus signs represent the outliers. The dashed red line represents the base case (no aperture variations) value of 0.8.

wells will have less aperture variations which results in a lower σ_Θ. The trend of lower values of F for larger values of wellbore spacing can be rationalized by considering the heat transfer area. The mean fracture surface temperature $\langle \Theta \rangle$ is a measure of the accessed area for heat transfer at a point in time; smaller values of $\langle \Theta \rangle$ mean more area has been accessed. The base case values for $\langle \Theta \rangle$ are 0.95, 0.82, 0.74, 0.67 and 0.57 for $L/(2R) = 0.2, 0.4, 0.5, 0.6$, and 0.8, respectively. For larger wellbore spacing values, the base case is already harvesting energy from a large portion of the fracture and any deflection of the base flow caused by aperture variations will tend to decrease the heat transfer area as seen in the results for F, the fraction of fractures with better performance than the base case. In contrast, smaller wellbore spacing values, the base case heat transfer area is small and

perturbations of the flow field are more likely to increase the heat transfer area.

7.4 Results for Multiple Fractures

The previous section described the effect of a self-affine aperture field on the thermal performance when there is only one fracture. A relevant situation to further model would be a reservoir consisting of two fractures. We consider a reservoir consisting of two fractures with equal radii that do not intersect with one another, but rather are hydraulically connected via the injection and production well. The pressure drop along the wellbore is assumed negligible because $w/r \ll 1$, where the wellbore radius r is around 10 cm and the aperture is around 1 mm. The mass flow was doubled to 80 kg/s, but the value of $\dot{m}/A$ remains the same as that in the one fracture system because the total surface area of the system is twice as large.

With two fractures the flow field exhibits both inter- and intrafracture flow variations. As has been seen in the one fracture reservoir, local aperture variations disturb the baseflow creating intrafracture flow variations. However, aperture variations can also modify the ratio of the mean flow rate between fractures through altering the flow impedance or resistance to mean flow of each fracture and affect the reservoir's overall pressure drop. The flow impedance of the fractures in the reservoir is what drives the global distribution of flow in the reservoir.

Since the pressure drop ΔP is linear with the flow rate, $\Delta P \propto \dot{m}$, the flow split fractions for fracture A and B are

$$\phi_A = \frac{I_B}{I_A + I_B}, \tag{7.13}$$

$$\phi_B = 1 - \phi_A, \tag{7.14}$$

where $I_i \equiv \Delta P/\dot{m}_i$ and represents the flow impedance of fracture i. The system can be viewed as two "resistors" in parallel where the pressure drop is the same between the two fractures. The above equation demonstrates how fracture aperture variations modify the interfracture flow. Since it does not matter whether a fracture is labeled fracture A or B, the labels used in Eq. (7.13) and (7.14) are arbitrary and we may define the variable ϕ as $\max(\phi_A, \phi_B)$, which ranges from 0.5 to 1.

The hydraulic aperture is another way to view the varying pressure drop for each fracture. In terms of the pressure drop of a fracture ΔP, the hydraulic aperture is defined as

$$w_H \equiv w_0 \left(\frac{\Delta P_0}{\Delta P} \right)^{1/3}, \tag{7.15}$$

where ΔP_0 is the reference pressure drop in a smooth fracture for an aperture value of w_0 receiving the same mass flux. The cube root is a result of the cubic law described in Eq. (6.4). The hydraulic aperture is the aperture value needed in a smooth fracture to have the same pressure drop in a fracture with aperture variations. The hydraulic aperture is a useful metric in quantifying how spatial aperture variations control the pressure drop and affect interfracture flow variations.

The effects of fracture aperture variations in two and three fracture systems was studied by determining the thermal performance of an ensemble of fracture realizations. The wellbore spacing and the Hurst coefficient were kept constant and the standard deviation of the aperture was varied over the same range considered before. Finally, we examined the efficacy of flow control methods in minimizing any negative effects aperture variations have on the thermal performance of multifracture systems.

7.4.1 Varying Strength of Aperture Fluctuations

Two thousand five hundred fracture pairs with $L/(2R) = 0.4$ and $\zeta = 0.8$ were generated and their thermal performance was simulated. Reassigning the pairing had an insignificant effect on the results presented. Figures 7.8 and 7.9 show the histogram of the production temperature and the flow split fraction when $\sigma_h/\langle w \rangle = 0.25$. It is apparent that the flow split can be modeled as a Gaussian distribution and compared to Figure 7.2, the thermal performance is closer to Gaussian than that of the one fracture system.

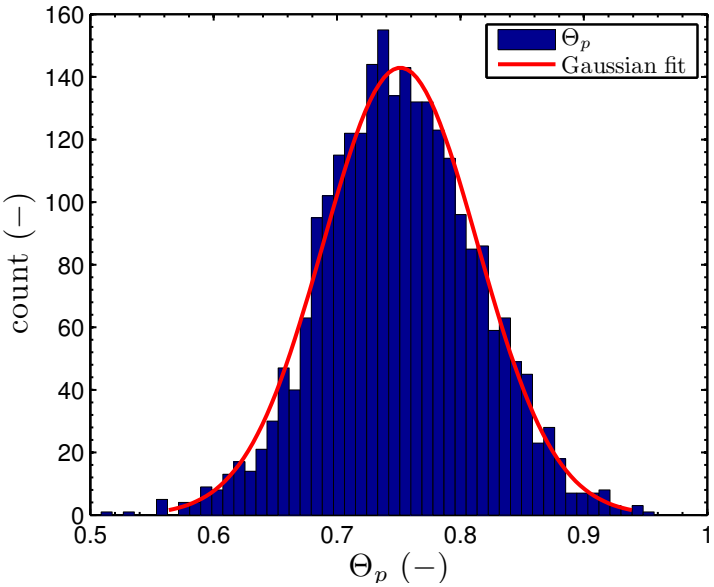

Figure 7.8: Histogram of the thermal performance of the two fracture system when $L/(2R) = 0.4$, $\sigma_h/\langle w \rangle = 0.25$, and $\zeta = 0.8$. A Gaussian fit results in a mean and standard deviation of 0.751 and 0.0625, respectively.

Figure 7.10 shows that larger ϕ values, corresponding to more unequal flow splits, are likely to result in lower production temperatures. Also, plotted in the figure is the production temperature as a function of the flow split if the fractures had no surface variations. In the absence of aperture variations, Θ_p is always monotonically decreasing with respect to ϕ. There are simulation outcomes that

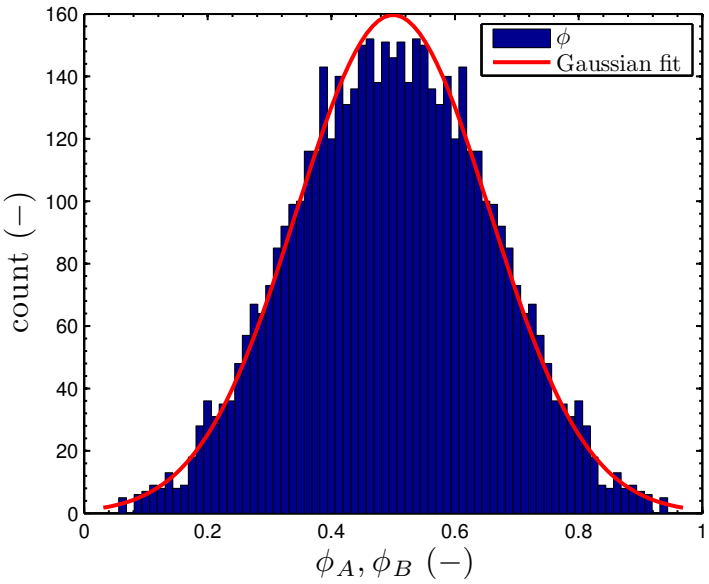

Figure 7.9: Histogram of the fractional flow split of the two fracture system when $L/(2R) = 0.4$, $\sigma_h/\langle w \rangle = 0.25$, and $\zeta = 0.8$. By definition the mean is 0.5 and standard deviation is 0.156, respectively.

lie above the smooth case curve, but systems that exhibit a boost in thermal performance for larger flow split fractions become increasingly rare. In general, having a flow split deviate from equality is likely to result in undesirable thermal performance. As plotted in Figure 7.11, the uncertainty in thermal performance has a linear relationship with the uncertainty in ϕ.

As with the single fracture reservoir, the fraction of reservoirs that benefit from aperture variations decreases with increasing mean square of aperture variations. The fraction of reservoirs with a production temperature higher than the base case, F, as a function of the dimensionless standard deviation, is plotted in Figure 7.12. For comparison, the single fracture results are plotted in the same figure. The theoretical fit was obtained by using Eq. (7.11) along with the fits of σ_Θ and $\bar{\Theta}_p$. Compared to the single fracture case, the values of both σ_Θ and $\bar{\Theta}_p$ are smaller. The curve is no longer linear since K is now equal to 3.00 and as a result, the

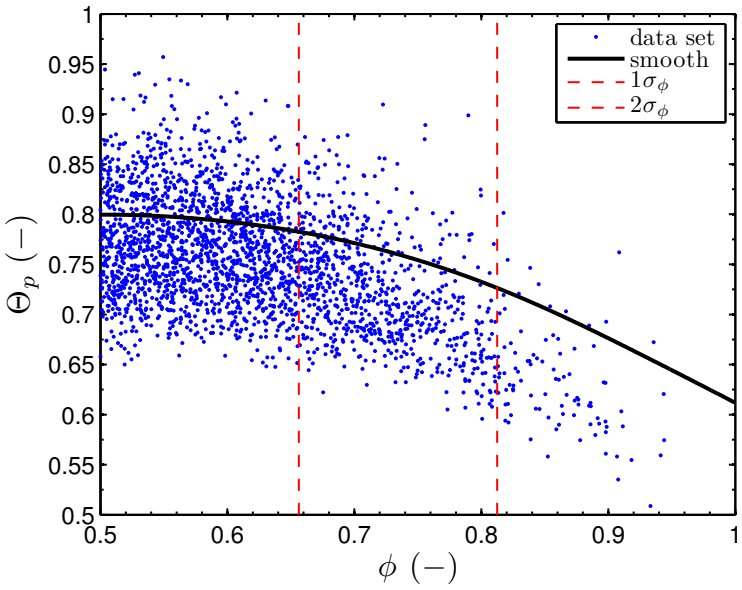

Figure 7.10: Dimensionless production temperature as a function of fractional flow split when $L/(2R) = 0.4$, $\sigma_h/\langle w \rangle = 0.25$, and $\zeta = 0.8$. The solid black line represents the production temperature for smooth fractures when the flow split varies. One and two standard deviations from the mean are plotted to help visualize how the data is distributed.

linear approximation of the error function breaks down.

A portion of the decreased thermal performance in the two fracture reservoir results solely from the existence of an unequal flow split between the fractures. The reduction in the production temperature for two smooth fractures with increasing flow split ratio is indicated by the solid line in Figure 7.10 and we will refer to this function as $g(\phi)$. A metric of the additional loss of thermal performance in the two fracture reservoir compared with the case of two smooth fractures with unequal apertures is F^*, which we define as the fraction of two fracture reservoirs with $\Theta_p > g(\phi)$, i.e., the fraction that beat the smooth fracture reservoir with the same flow split. The results for F^* are higher than F because the smooth case thermal performance drops with respect to increasing ϕ. However, F^* is closer to the results of F for the two fracture results than to the single fracture results. These

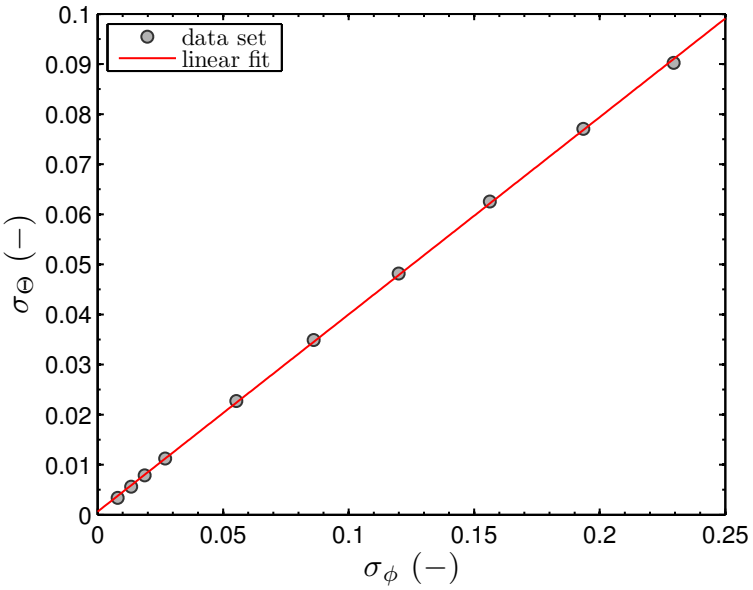

Figure 7.11: The standard deviation of the dimensionless production temperature σ_θ as a function of the standard deviation of the fraction flow split σ_ϕ when $L/(2R) = 0.4$ and $\zeta = 0.8$. A linear fit is also shown.

results demonstrate that the primary determinant of the diminished performance of the two fracture system is the aperture variation and flow channeling within each reservoir rather than being simply a result of the difference of hydraulic aperture of the two fractures.

The reduced thermal performance compared to a one fracture system can be explained by the relationship between pressure drop and the thermal performance in an individual fracture. In general, a fracture with a small aperture region in between the injection and production wells will exhibit enhanced thermal performance because the flow will expand and sweep through the reservoir more effectively. The reverse is true; a high aperture region in between the wells will promote flow short circuiting and the flow will primarily harvest thermal energy in a narrow area. This behavior was illustrated in Figure 7.1, where the temperature of the fracture surface was plotted along side their respective aperture fields.

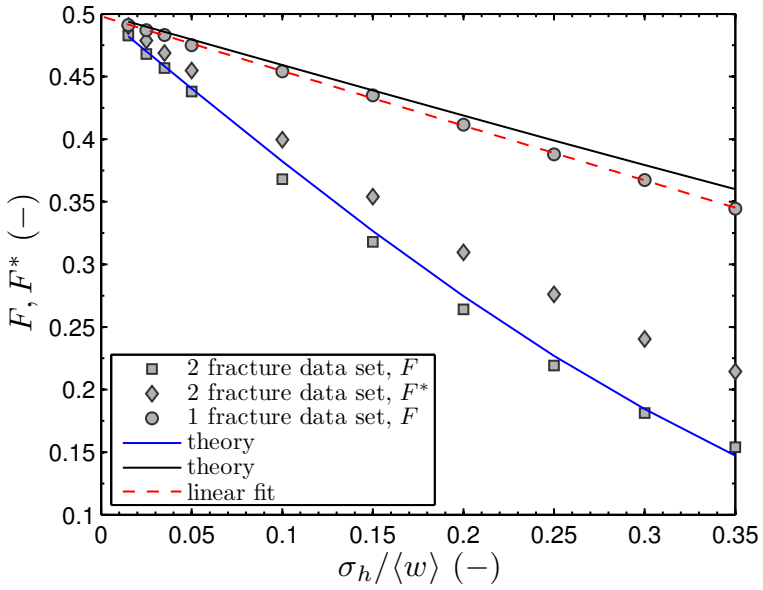

Figure 7.12: The fraction of two fracture system exhibiting thermal performance enhancement as a function of $\sigma_h/\langle w \rangle$. The Hurst coefficient ζ is equal to 0.8 and the wellbore spacing $L/(2R)$ is equal to 0.4. The curves give theoretical predictions based on a Gaussian distribution of Θ_p. The squares are the fraction of reservoirs that outperform a base case with an equal flow split, F. The diamonds are the fraction of reservoirs that outperform a base case with a constant aperture within each fracture but the same flow split as observed in the simulations, F^*. The one fracture results and the theoretical fit was also plotted.

Furthermore, a low aperture wellbore region requires a higher pressure drop to push the fluid through the constricted region surrounding both the injection and production wells. The covariance of w_H and Θ_p for the single fracture is -0.65 when $L/(2R) = 0.4$, $\zeta = 0.8$, and $\sigma_h/\langle w \rangle = 0.25$, which supports our qualitative argument.

For single fracture reservoirs, poor performing fractures exhibit a smaller pressure drop. However, in a two fracture reservoir, the poor thermally performing reservoir will receive a larger portion of the flow and the reservoir with good thermal performance receives a smaller portion of the flow. Thus, it is not simply the existence of an unequal flow split but the fact that the higher flow goes preferentially

to the fracture with more channeling that accounts for the poorer performance of two fracture reservoirs compared with single fracture reservoirs. However, the negative impact on thermal performance can be mitigated if the flow split between the reservoirs can be manipulated.

7.4.2 Three Fracture System

We can extend the analysis to a three fracture system, following the same method used for the two fracture reservoir. The system is treated as three resistors in parallel, all with the same pressure drop. Plotted in Figure 7.13 are the fitted Gaussian probability distribution of the production temperature for one, two, and three fracture reservoir systems for when $L/(2R) = 0.4$, $\sigma_h/\langle w \rangle = 0.25$, and $\zeta = 0.8$. With the addition of more fractures, the distribution of thermal performance becomes less varied and the mean shifts to lower values. As expected, the thermal performance of the system gets worse for increasing values of the mean square of aperture fluctuations. For the range of $\sigma_h/\langle w \rangle = 0.015 - 0.35$, F monotonically decreases from 0.49 to 0.074. The three fracture system has the worst thermal performance among the cases investigated. Using the same argument as the two fracture system, it is more likely that a low impedance fracture has individually poor thermal performance and diverts most of the fluid into that fracture. With three fractures, the probability of having the aforementioned outcome increases and thermal performance suffers to a greater extent than the one or two fracture reservoirs.

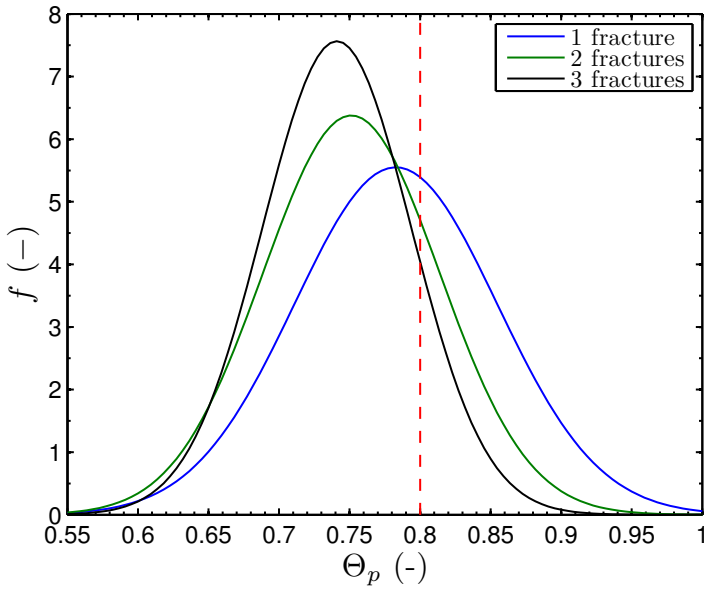

Figure 7.13: Fitted Gaussian probabilty density function of dimensionless production temperature for one, two, and three fracture system when $L/(2R) = 0.4$, $\sigma_h/\langle w \rangle = 0.25$, $\zeta = 0.8$, and with the base case value of $\Theta_{p,0} = 0.8$. The Gaussian distributions were chosen to match the mean and standard deviation of the simulated temperature results.

7.4.3 Flow Control

To mitigate the adverse impact of fracture surface variations on the interfracture flow variations, flow control methods can modify the flow split and reduce the negative effects associated with flow split disparity. In a real reservoir, flow control is achieved by using interflow control devices (ICD). An ICD works by increasing the resistance of flow from the wellbore to the formation or fracture. The increased resistance is achieved using nozzles, orifices, and helical channels on the base pipe. For more information on ICD, please refer to Al-Khelaiwi et al. (2010) and Birchenko et al. (2010).

Figure 7.14 shows the boxplot of the dimensionless production temperature distribution of the two fracture system when $L/(2R) = 0.4$, $\zeta = 0.8$, and $\sigma_h/\langle w \rangle =$

0.25 for three cases: no flow control (untreated), 50/50 flow split, and the optimal flow split. A 50/50 flow split was chosen as a good guess on how to best distribute the flow. The optimal flow split represents the value of ϕ that optimizes the production temperature. In practice, the optimal flow split would be very difficult to predict, as one would first need to know the structure of the reservoir from solving an inverse problem based on tracer tests. Nonetheless, it is calculated to be used as an upper bound on thermal performance. The boxplot of the 50/50 and the optimal flow scenario show that there is only a marginal increase in thermal performance when the optimal value is used. The 25%, 50% (median), and 75% quantiles of the distribution for the change in production temperature for the equal split are 0.0023, 0.0149, and 0.0458, respectively. For the optimal split, the 25%, 50% (median), and 75% quantiles of the distribution are 0.0043, 0.0194, and 0.0554, respectively.

Another way to view the flow control results is to plot the change in dimensionless production temperature $\Delta\Theta_p$ versus the flow split fraction. For the 50/50 flow split scenario, the results for $\Delta\Theta_p$ versus ϕ are plotted in Figure 7.15. The equal flow split strategy does result in worse thermal performance 13% of the time compared to no flow control. However, 75% of these cases only saw a minimal drop in the production temperature, less than 0.004. Additionally, using the optimal flow split in these cases led to an increase in Θ_p of no more than 0.0019 with improvement occurring in only 75% of the cases. The figure reveals that as the flow split fraction moves away from a 50/50 split, the improvements of applying flow control increases; the covariance of ϕ and $\Delta\Theta_p$ is 0.88. When the fracture surface is less varied, the distribution of thermal performance is also less varied. Consequently, flow control will become less important. When $\sigma_h/\langle w\rangle = 0.05$, 75% of the cases only had a $\Delta\Theta_p$ of less than 0.002 when the optimal value of ϕ was

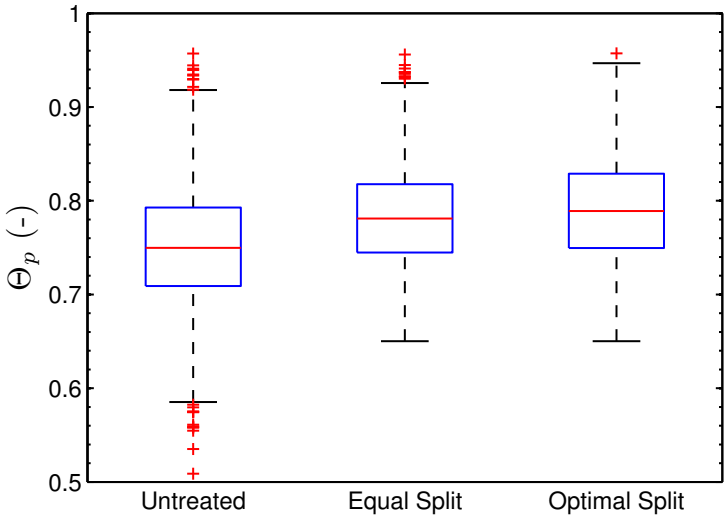

Figure 7.14: Boxplot of dimensionless production temperatures for three cases: no flow control (untreated), 50/50 flow split, and the optimal flow split. The dimensionless standard deviation of the aperture $\sigma_h/\langle w \rangle$ is kept at 0.25, the Hurst coefficient ζ is equal to 0.8, and the wellbore spacing $L/(2R)$ is equal to 0.4. The lower and upper edge of the box represents the first and third quartiles while the solid red line represents the median value. The lower and upper whiskers of the boxplot are defined as 1.5 times the first and third quartile value, respectively, and the red plus sign represents the outliers.

used.

Compared to the F value for the one fracture reservoir, applying flow control for the range of $\sigma_h/\langle w \rangle$ investigated was capable of increasing F to a range of 0.50 to 0.31, which represents 100% to 89% of the value of the one fracture reservoir. Plotted in Figure 7.16 are the F values for the 50/50 flow split as well as the values for the one and two fracture cases (no flow control). It is only when $\sigma_h/\langle w \rangle > 0.25$ that F of the equal flow split is appreciably lower than the one fracture reservoir.

The fact that flow control was able to bring F near the single fracture results indicates that interfracture flow variations inhibit thermal performance more than intrafracture flow variations. The results in Figure 7.12 showed that these detri-

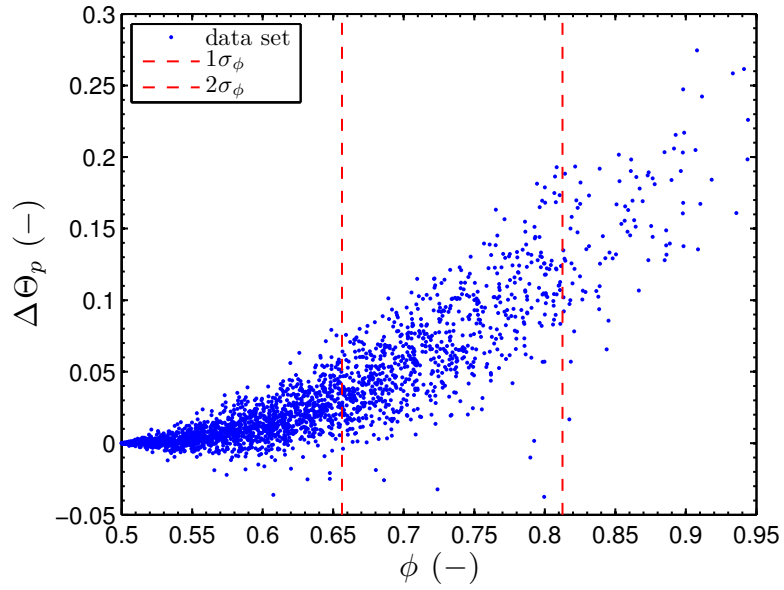

Figure 7.15: The change of production temperature $\Delta\Theta_p$, using an equal flow split strategy as a function of the original flow split fraction when $L/(2R) = 0.4$, $\sigma_h/\langle w \rangle = 0.25$, and $\zeta = 0.8$. The original flow split is normally distributed and one and two standard deviations from the mean are plotted to help visualize how $\Delta\Theta_p$ is distributed.

mental interfracture flow variations consist of flow preferentially going to poor thermal performing fractures rather than simply involving unequal flow splits. Nonetheless a comparison of our two flow control strategies indicates that an effort to divert flow preferentially away from fractures exhibiting channeling yields only a marginal improvement over a flow control strategy that yields an equal flow split.

The flow control results reveal that for equally sized fractures, a 50/50 flow split is good practice. Knowing the optimal split does not result in a large improvement in thermal performance. Flow control would be limited if the reservoir consists of fracture-to-fracture intersections as ICD can only control flow in the fractures that are directly connected to the wellbore. Fracture-to-fracture intersections, therefore, open up new possible flow paths rather than just partitioning the flow between two independent flow paths where the path with the least impedance takes

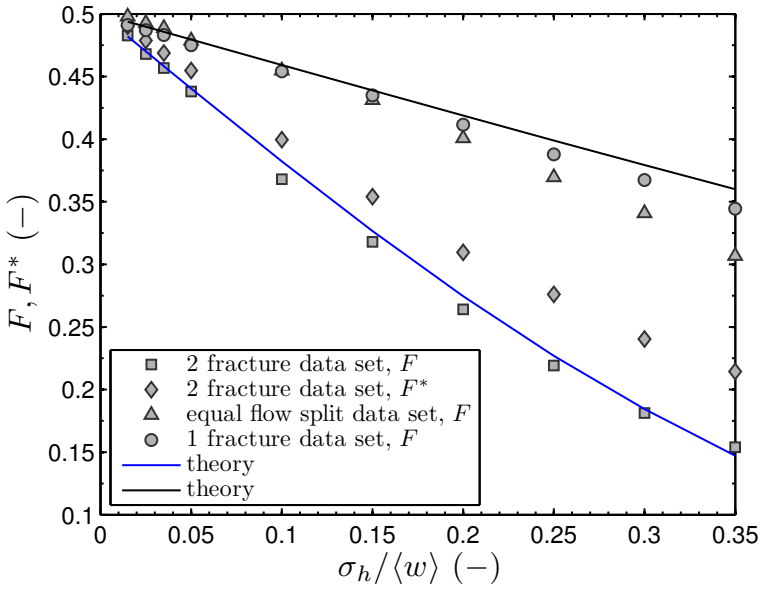

Figure 7.16: The fraction of two fracture system exhibiting thermal performance enhancement as a function of $\sigma_h/\langle w \rangle$ for the case of equal flow split. The Hurst coefficient ζ is equal to 0.8 and the wellbore spacing $L/(2R)$ is equal to 0.4. The results for the one fracture, and untreated two fracture cases are also plotted.

the majority of the flow. Thus, the presence of fracture-to-fracture intersections may not result in a diminished thermal performance, as was shown in the case of multiple fractures only hydraulically connected via the wellbores.

7.5 Conclusion

Isotropic self-affine fracture aperture variations limit a reservoir's thermal performance. There are more ways to arrange aperture variations that causes flow paths that lead to premature drawdown than flow pathways that enhance heat transfer. We have shown that the dimensionless standard deviation of the aperture $\sigma_h/\langle w \rangle$ is more important in controlling thermal performance than the Hurst coefficient ζ. Specifically, both the uncertainty in thermal performance, σ_Θ, and the number

of fracture realizations that benefit from aperture variations have linear relationships to the root mean square of the aperture variations. However, the effects of aperture variations become nearly insignificant when $\sigma_h/\langle w \rangle < 0.1$. For the investigated range of $\sigma_h/\langle w \rangle$ from 0.015 to 0.35, 34 to 49% of the fracture realizations benefited from aperture variations. Reservoirs with a larger wellbore separation have more uniform base flow, flow in the absence of aperture variations, that is more negatively affected by aperture variations. A reservoir with a large wellbore separation already accesses a larger area of the fracture for heat exchange and any flow channeling induced by aperture variations will more likely decrease the effective heat exchange area. Our finding that aperture variations will lead to adverse thermal performance, more often than not, is in agreement with the previous work of Neuville et al. (2010b,a), despite the fact that their study did not couple heat transport in the fracture with that in the surrounding rock and used a uniform base flow in a rectangular fracture. Additionally, our use of statistical values for an ensemble of realizations, including the mean and standard deviation of production temperatures, offers a better and more practical understanding of the effects fracture aperture variations have on discretely fractured geothermal reservoirs.

We also demonstrated that fracture aperture variations alter the interfracture flow split in a system with multiple parallel fractures. The number of reservoirs exhibiting diminished thermal performance increased compared a reservoir with one fracture and the same mass flow per fracture area. Simply having a higher flow rate in one fracture will more than likely lead to a worse thermal performance because the fracture receiving most of the flow will experience thermal breakthrough more quickly. Further deterioration in thermal performance arises because fractures with a larger flow impedance usually have better thermal performance but receive a smaller portion of the flow. However, applying flow control can alleviate

the problems with undesirable flow splits.

Our analysis suggests that a major cause of poor thermal performing reservoirs is due to interfracture flow variations. With more fractures, the reservoir is more susceptible to adverse thermal performance. In general, more fractures in the reservoir lead to a drop in the variability of thermal performance but also leads to a higher likelihood of having a worse production temperature compared to the base case scenario of no aperture variations. The multiple fracture systems simulated in this study were only hydraulically connected via the injection and production well. Real EGS reservoirs, however, like the one at Soultz-sous-Forêts will have fractures that intersect with each other (Sausse et al., 2010). With fracture-fracture intersections, flow control devices become less effective because they can only control well-to-fracture flow.

The present study dealt only with a static reservoir where the spatially varying aperture field stayed constant with time. Real reservoirs, however, will experience thermal, hydraulic, mechanical, and chemical (THMC) changes that may substantially alter the aperture field. In addition to THMC effects, fracture shearing/slipping during heat extraction will also change the aperture field. In general, aperture change due to THMC effects will increase permeability/aperture in the region enclosed by the injection and production well (Taron and Elsworth, 2009; Ghassemi and Zhou, 2011). Fracture slippage will lead to an increase in the standard deviation of the aperture fluctuations and result in preferential flow channeling in the direction perpendicular to the shear displacement (Yeo et al., 1998; Plouraboué et al., 2000; Watanabe et al., 2008). Although our work did not incorporate fracture slippage and THMC effects it, nonetheless, provides a framework through which to understand how spatial aperture fluctuations affect thermal per-

formance. It shows that fracture surface variations are a reservoir characteristic that researchers should consider in modeling discretely fractured geothermal reservoirs and performing techo-economic analysis (Beckers et al., 2014; Held et al., 2014). Our systematic approach for generating spatially varying apertures can be used in conjunction with modeling the effects that THMC and fracture slippage have on reservoir thermal performance, by providing a base aperture field that already has a spatially varying aperture field.

Bibliography

Al-Khelaiwi, F. T., Birchenko, V. M., Konopczynski, M. R., and Davies, D. (2010). Advanced wells: A comprehensive approach to the selection between passive and active inflow-control completions. *SPE Production and Operations*, 25:305–326.

Auradou, H., Boschan, A., Chertcoff, R., DAngelo, M.-V., Hulin, J.-P., and Ippolito, I. (2010). Miscible transfer of solute in different model fractures: From random to multiscale wall roughness. *Comptes Rendus Geoscience*, 342(7–8):644–652.

Auradou, H., Drazer, G., Boschan, A., Hulin, J.-P., and Koplik, J. (2006). Flow channeling in a single fracture induced by shear displacement. *Geothermics*, 35(5–6):576–588.

Beckers, K. F., Lukawski, M. Z., Anderson, B. J., Moore, M. C., and Tester, J. W. (2014). Levelized costs of electricity and direct-use heat from Enhanced Geothermal Systems. *Journal of Renewable and Sustainable Energy*, 6(1).

Birchenko, V., Muradov, K., and Davies, D. (2010). Reduction of the horizontal

well's heeltoe effect with inflow control devices. *Journal of Petroleum Science and Engineering*, 75:244–250.

Boffa, J. M., Allain, C., Chertcoff, R., Hulin, J. P., Plouraboué, F., and Roux, S. (1999). Roughness of sandstone fracture surfaces: Profilometry and shadow length investigations. *European Physical Journal B*, 7(2):179–182.

Bouchaud, E. (1997). Scaling properties of cracks. *Journal of Physics: Condensed Matter*, 9(21):4319–4344.

Brown, S. R. (1987). Fluid flow through rock joints: The effect of surface roughness. *Journal of Geophysical Research: Solid Earth*, 92(B2):1337–1347.

Brown, S. R., Kranz, R. L., and Bonner, B. P. (1986). Correlation between the surfaces of natural rock joints. *Geophysical Research Letters*, 13(13):1430–1433.

Brown, S. R. and Scholz, C. H. (1985). Broad bandwidth study of the topography of natural rock surfaces. *Journal of Geophysical Research: Solid Earth*, 90(B14):12575–12582.

Bruderer-Weng, C., Cowie, P., Bernabé, Y., and Main, I. (2004). Relating flow channelling to tracer dispersion in heterogeneous networks. *Advances in Water Resources*, 27(8):843–855.

Bruel, D., Cacas, M. C., Ledoux, E., and de Marsily, G. (1994). Modelling storage behaviour in a fractured rock mass. *Journal of Hydrology*, 162(3–4):267–278.

Cacas, M. C., Ledoux, E., de Marsily, G., Tillie, B., Barbreau, A., Durand, E., Feuga, B., and Peaudecerf, P. (1990). Modeling fracture flow with a stochastic discrete fracture network: Calibration and validation 1. The flow model. *Water Resources Research*, 26(3):479–489.

Drazer, G. and Koplik, J. (2000). Permeability of self-affine rough fractures. *Physical Review E*, 62(6):8076–8085.

Drazer, G. and Koplik, J. (2002). Transport in rough self-affine fractures. *Physical Review E*, 66:026303.

Efron, B. and Tibshirani, R. (1994). *An Introduction to the Bootstrap*. Chapman & Hall, New York, NY.

Falconer, K. (2003). *Fractal Geometry: Mathematical Foundations and Application*. John Wiley & Sons, Chichester, England, 2nd edition.

Feder, J. (1988). *Fractals*. Physics of Solids and Liquids. Plenum Press, New York, NY.

Ghassemi, A. and Zhou, X. (2011). A three-dimensional thermo-poroelastic model for fracture response to injection/extraction in enhanced geothermal systems. *Geothermics*, 40(1):39–49.

Glover, P. W. J., Matsuki, K., Hikima, R., and Hayashi, K. (1998). Fluid flow in synthetic rough fractures and application to the Hachimantai geothermal hot dry rock test site. *Journal of Geophysical Research: Solid Earth*, 103(B5):9621–9635.

Hakami, E. and Larsson, E. (1996). Aperture measurements and flow experiments on a single natural fracture. *International Journal of Rock Mechanics and Mining Sciences & Geomechanics Abstracts*, 33(4):395–404.

Held, S., Genter, A., Kohl, T., Koelbel, T., Sausse, J., and Schoenball, M. (2014). Economic evaluation of geothermal reservoir performance through modeling the complexity of the operating EGS in Soultz-sous-Forêts. *Geothermics*, 51(0):270–280.

Jupe, A., Bruel, D., Hicks, T., Hopkirk, R., Kappelmeyer, O., Kohl, T., Kolditz, O., Rodrigues, N., Smolka, K., Willis-Richards, J., Wallroth, T., and Xu, S. (1995). Modelling of a European prototype HDR reservoir. *Geothermics*, 24(3):403–419.

Kolditz, O. (1995). Modelling flow and heat transfer in fractured rocks: Dimensional effect of matrix heat diffusion. *Geothermics*, 24(3):421–437.

Mandelbrot, B. B. and Ness, J. W. V. (1968). Fractional Brownian motions, fractional noises and applications. *SIAM Review*, 10(4):422–437.

Méheust, Y. and Schmittbuhl, J. (2001). Geometrical heterogeneities and permeability anisotropy of rough fractures. *Journal of Geophysical Research: Solid Earth*, 106(B2):2089–2102.

Méheust, Y. and Schmittbuhl, J. (2003). Scale effects related to flow in rough fractures. *Pure and Applied Geophysics*, 160(5–6).

Neuville, A., Toussaint, R., and Schmittbuhl, J. (2010a). Fracture roughness and thermal exchange: A case study at Soultz-sous-Forêts. *Comptes Rendus Geoscience*, 342(7–8):616–625.

Neuville, A., Toussaint, R., and Schmittbuhl, J. (2010b). Hydrothermal coupling in a self-affine rough fracture. *Physical Review E*, 82:036317.

Nicol, D. A. and Robinson, B. A. (1990). Modelling the heat extraction from the Rosemanowes HDR reservoir. *Geothermics*, 19(3):247–257.

Nordqvist, A. W., Tsang, Y. W., Tsang, C. F., Dverstorp, B., and Andersson, J. (1992). A variable aperture fracture network model for flow and transport in fractured rocks. *Water Resources Research*, 28(6):1703–1713.

Plouraboué, F., Hulin, J.-P., Roux, S., and Koplik, J. (1998). Numerical study of geometrical dispersion in self-affine rough fractures. *Physical Review E*, 58:3334–3346.

Plouraboué, F., Kurowski, P., Boffa, J.-M., Hulin, J.-P., and Roux, S. (2000). Experimental study of the transport properties of rough self-affine fractures. *Journal of Contaminant Hydrology*, 46(3–4):295–318.

Plouraboué, F., Kurowski, P., Hulin, J.-P., Roux, S., and Schmittbuhl, J. (1995). Aperture of rough cracks. *Physical Review E*, 51(3):1675.

Ponson, L., Auradou, H., Pessel, M., Lazarus, V., and Hulin, J.-P. (2007). Failure mechanisms and surface roughness statistics of fractured fontainebleau sandstone. *Physical Review E*, 76(3):036108.

Sausse, J. (2002). Hydromechanical properties and alteration of natural fracture surfaces in the Soultz granite (Bas-Rhin, France). *Tectonophysics*, 348(1–3):169–185.

Sausse, J., Dezayes, C., Dorbath, L., Genter, A., and Place, J. (2010). 3D model of fracture zones at Soultz-sous-Forêts based on geological data, image logs, induced microseismicity and vertical seismic profiles. *Comptes Rendus Geoscience*, 342(7–8):531–545.

Schmittbuhl, J., Gentier, S., and Roux, S. (1993). Field measurements of the roughness of fault surfaces. *Geophysical Research Letters*, 20(8):639–641.

Schmittbuhl, J., Schmitt, F., and Scholz, C. (1995). Scaling invariance of crack surfaces. *Journal of Geophysical Research: Solid Earth*, 100(B4):5953–5973.

Taron, J. and Elsworth, D. (2009). Thermal-hydrologic-mechanical-chemical processes in the evolution of engineered geothermal reservoirs. *International Journal of Rock Mechanics and Mining Sciences*, 46(5):855–864.

Tsang, Y. W. and Tsang, C. F. (1989). Flow channeling in a single fracture as a two-dimensional strongly heterogeneous permeable medium. *Water Resources Research*, 25(9):2076–2080.

Watanabe, N., Hirano, N., and Tsuchiya, N. (2008). Determination of aperture structure and fluid flow in a rock fracture by high-resolution numerical modeling on the basis of a flow-through experiment under confining pressure. *Water Resources Research*, 44(6).

Yeo, I., de Freitas, M., and Zimmerman, R. (1998). Effect of shear displacement on the aperture and permeability of a rock fracture. *International Journal of Rock Mechanics and Mining Sciences*, 35(8):1051–1070.

Zimmerman, R. W. and Bodvarsson, G. S. (1996). Hydraulic conductivity of rock fractures. *Transport in Porous Media*, 23(1):1–30.

CHAPTER 8

IDENTIFYING SPATIALLY VARYING APERTURE FIELDS AND PREDICTING GEOTHERMAL PRODUCTION TEMPERATURES IN FRACTURES USING INVERSION METHODS WITH CONSERVATIVE AND REACTIVE TRACERS

8.1 Introduction

Geothermal energy is the stored thermal energy within the earth. One method to extract the stored thermal energy is to create an Enhanced/Engineered Geothermal System (EGS) with an active reservoir by opening existing weakly sealed fractures or inducing new ones. This facilitates the circulation of water into and out of the fractured reservoir to "farm" or extract a portion of the thermal energy. EGS is often implemented in areas with low permeability and/or dry rock with small amounts of in situ water or steam to provide a means for extracting the earth's stored thermal energy. The thermal hydraulic behavior, or the flow of fluid in the reservoir and the temporal evolution of the subsurface temperature, of a geothermal reservoir is strongly dependent on the subsurface. One of the goals of modeling a geothermal system is to be able to forecast the production temperature throughout the operational lifetime of the reservoir, which requires knowledge of the structure of the reservoir and the flow paths. Wellbore imaging techniques can only characterize the reservoir near the wells by identifying locations of fracture and flow zones but cannot determine the overall structure of the reservoir. For discretely fractured geothermal reservoirs like those of EGS, one reservoir characteristic that affects the thermal hydraulic performance is a heterogeneous spatial aperture in the fractures. These spatial aperture variations result in flow paths

that differ from those that would have occurred if the reservoir had a uniform aperture. Consequently, the production temperature is also altered from that for an idealized uniform aperture fracture.

One method to ascertain the flow behavior in the subsurface is to conduct tracer tests by injecting a known mass of a compound or a particle in the inlet fluid and measuring the concentration of the compound at the production well with time. A tracer test yields a residence time distribution in the form of a concentration profile versus time that is a result of the flow distribution in the system. The purpose of this study is to determine the flow paths in a target fracture using an inverse search that looks for an aperture field whose tracer curve best matches the simulated tracer profile for the target fracture. The spatially varying aperture field is the manner in which variable flow paths are induced inside the fracture. The reservoir's anticipated thermal performance is predicted using the aperture field obtained from the inverse search in a numerical forward model of heat transfer between fluid circulating in the fracture and the rock surrounding it.

Our study is motivated by the desire to create an improved analysis of tracer data to infer reservoir structure that captures both the hydraulic and thermal behavior of the reservoir. The approach used in this study has three parts: (1) to develop an inverse procedure that uses tracer measurements to arrive at a reservoir structure that best matches the data, (2) to understand the extent to which tracer data can be used to predict the flow paths in the reservoir, and (3) to quantify how well tracer data can be used to determine a reservoir's production temperature. The study differs from previous tracer analysis efforts which rely on heuristic interpretation methodologies by determining the tracer RTD for simulated reservoirs for which the true nature of the reservoir configuration and thermal performance is

known. Validation is obtained by comparing the simulated model's thermal performance with measured performance in a real reservoir whose geometry is completely characterized.

Tracers can be used to ascertain the subsurface environment and understand the flow in a geothermal reservoir. There are two kinds of tracers, conservative and reactive. Conservative tracers such as Br^{82} and I^{131} have been used to characterize physical quantities of the reservoir such as volume, sweep area, increase in volume with time, and flow paths (Tester et al., 1982; Robinson and Tester, 1984, 1986). These works used residence time distribution curves from field tests at the Fenton Hill EGS project, along with analytical models and statistical analysis to arrive at estimations about the size and configuration of the reservoir. Tester et al. (1989) used the results of tracer tests at different stages of the Fenton Hill project to suggest that the reservoir was not only growing, but growing in areas that were not part of the main flow conduit of the reservoir, increasing the reservoir's capability to provide more energy throughout its lifetime. Our study also aims at determining the subsurface structure. The aforementioned studies described the reservoir coarsely, by estimating the volume of the reservoir or by describing the reservoir as being composed of two or three dominant flow paths of a certain size. Instead, we seek a more detailed description of the subsurface by revealing the aperture field of the fracture. Despite using simple reservoir models, these early tracer studies were crucial in establishing the importance of tracers as a subsurface investigative tool.

Tracer tests have also been conducted in more recent testing of EGS reservoirs, such as the Soultz-sous-Forêts project in France. Tracers have been used to propose the flow structure of the Soultz reservoir. Researchers there performed

six different tracer tests between 2000 and 2005, using sodium benzoate, various naphthalene disulfonate isomers, and fluorescein (Sanjuan et al., 2006). Radilla et al. (2012) modeled the system as having three flow paths, each path modeled as a heterogeneous porous medium. They used an analytical expression for the concentration to fit the tracer data by modifying the flow fraction, standard deviation of the permeability, and mean arrival time for each of the three flow paths. The researchers were able to accurately fit the data with their model and their flow model is consistent with the fracture zone mapping at Soultz. However, the study did not consider if the fits were unique or if they can be described by another set of model parameters that describe a distinct flow model. Vogt et al. (2012a) used a more sophisticated approach in matching the Soultz field data. Modeling the reservoir as a heterogeneous porous medium, they generated an ensemble of ten-thousand reservoir models and used each realization's respective tracer curve to determine the models that best matched the field data, using three different misfit functions that quantified how far the tracer test of the model reservoir was from the true result. Their methodology yielded forty-nine best-fitting realizations that can be classified into three different groups, with each group representing a different characterization of the reservoir flow structure. Vogt et al. (2012b) used an ensemble Kalman filter to match the tracer data. Furthermore, they determined the anticipated production temperature with time for the reservoir models that matched the tracer data. After 50 years of operation, their results showed the reservoir will not experience a drop in temperature, an overly optimistic outcome for conduction limited geothermal reservoirs. The long predicted reservoir life may be due to modeling the reservoir's thermal performance using a porous medium model rather than as discrete fractures. Unfortunately, their prediction of the production temperature throughout the current operational life of the Soultz reservoir

cannot be verified. The current study's use of simulated data of both tracer measurements and reservoir production temperatures addresses the problem of past research efforts not being able to validate reservoir thermal behavior predictions.

Reactive tracers are capable of thermally mapping the reservoir and provide information of the evolving cooling fronts that will eventually lead to thermal breakthrough of the reservoir. Since chemical kinetics are a function of temperature, the amount of unreacted tracer coming out of the production well is a function of the residence time and of the temperature along the paths the tracer followed. By knowing the thermal map of a reservoir, one would be able to make conclusions on the progress of thermal breakthrough and the anticipated level of temperature decline in the reservoir, information important for the surface plant design and operation. Early reactive tracers candidates have been organic esters and amides undergoing hydrolysis (Robinson et al., 1988) while quantum dots (Rose et al., 2011) and tin-bismuth alloys and silica nanoparticles have been recently proposed (Alaskar et al., 2012). Phenolic ester hydrolysis reactions kinetics are also a set of promising reactive tracers because their kinetics can be modified by altering the steric hindrance groups (Nottebohm et al., 2012). Although this study is not concerned with identifying specific reactive tracer compounds as possible candidates, it is essential to understand the current state of reactive tracer candidate research to justify our idealistic approach in modeling the behavior of reactive tracers in a simulated reservoir environment.

Reactive tracer field experiments have been limited, due to a lack of kinetic and reservoir characterization or little reactivity of the tracer. Ethyl acetate has been used in the Rosemanowes EGS pilot project in England (Kwakwa, 1988) while thermal degradation of injected sodium fluorescein in the Fenton Hill EGS project

was measured (Du Teaux and Callahan, 1996), with both studies concluding that an increase in tracer reactivity in the reservoir was due to opening of new fluid pathways that have not been cooled by the circulation of water. Polyaromatic sulfonate compounds were tested at several hydrothermal reservoirs, but behaved like conservative tracers due to a lack of reactivity caused by low reservoir fluid temperatures (Rose et al., 2001).

With such limited experimental validation, the potential of reactive tracers as a reliable subsurface interrogator has been limited to theoretical studies focused on proof of concept or compound candidate selection. Chemburkar et al. (1991) used a plug flow velocity field to derive integral expressions for a hypothetical reactive tracer profile given an analytical expression for the temperature profile and the reactive tracer's activation energy and pre-exponential factor. They used the concentration integral expressions to determine the temperature profile in the system, noting the existence of multiple solutions and the advantage in using at least two different tracers. Plummer et al. (2012) used the analytical temperature profiles for a single rectangular fracture and a porous media to determine a reactive tracer's sensitivity as a function of the reservoir temperature and residence time, governed by its Arrhenius equation parameters. The sensitivity parameter was defined as the change of tracer concentration per degree change of the temperature of a flow path. The sensitivity helped determine the ideal set of Arrhenius equation parameters for a reactive tracer to be used in a reservoir with certain temperature and residence time. Ames et al. (2015) conducted investigations using hypothetical "threshold" reactive tracers. These threshold reactive tracers would be encapsulated in a nanoparticle that would disassociate and release the tracers at a certain threshold temperature. Ames et al. (2015) produced theoretical reactive tracer results using a multiparallel rectangular fracture model. If the threshold tempera-

ture is set to the initial reservoir temperature, the location of the cooling front with respect to the production can be better predicted. These studies have been useful in demonstrating the potential for reactive tracers to predict a reservoir's thermal performance and have established procedures in the deployment of reactive tracer tests and interpretations of the results. However, they usually require simple reservoir models with analytical solutions for the transient temperature distribution. In contrast, the present study will not be restricted to analytical reservoir models, but instead use a numerical reservoir model that incorporates variable flow paths to achieved the outlined goals.

Using both conservative and reactive tracers in a simulated environment, the objective of this study is to determine the spatially varying aperture field in a single, circular fracture. A method of generating reservoirs with variable flow paths is needed to produce target reservoirs to determine the spatial distribution of apertures contained in the fractures. A self-affine geometry where large scale variations dominate over shorter scales was chosen as the method to generate the target reservoirs. The finite element method is used to solve for both the fluid flow and the transport of the tracer in the fracture. Although the single fracture model can be considered simplistic, the spatially varying aperture field captures the multiple flow paths typically present in geothermal systems as was documented in Chapter 7. In addition, the numerical model provides a more realistic description of the subsurface that analytical models cannot fully capture.

The problem of determining the aperture field using tracer tests is posed as an inversion problem, rather than a forward search that prescribes a range of reservoir parameters, such as the flow distribution, to find the best reservoir candidate. An inverse search is more computationally efficient as the search algorithm is guided

by the previously visited states to arrive at the optimal solution more readily. Principal component analysis (PCA) is used to determine the dominant spatial correlations of fracture aperture variations, reducing a complicated description of the aperture field to a simplified model that is governed by several modes. PCA has been extensively used in the field of groundwater flow and oil reservoir modeling (van Doren et al., 2006; Li and Jafarpour, 2010; Cui et al., 2015). Instead of trying to determine the aperture at each node in the computational mesh, the inverse search algorithm targets the coefficients associated with the first eight to twenty-four PCA modes. The genetic algorithm, a meta-heuristic global optimizer, is chosen for the inversion scheme to minimize discrepancies between the predicted tracer based on the reservoir realizations and the target reservoir. Metaheuristic search optimizers are ideal for problems with multiple local minima and a large number of degrees of freedom.

The strategy implemented does not eliminate non-uniqueness of the solution for the aperture field. This reflects the fact that the tracer information is inadequate to determine a unique aperture field. The non-uniqueness of the solution is addressed by running the inversion algorithm multiple times to populate a set of various models that adequately describe the tracer data. The set of possible solutions then yield a range of predictions for the heat transfer that are consistent with the tracer measurements. The ultimate goal in using tracers is to forecast the reservoir's thermal performance. Since the study uses simulated reservoirs, the inversion algorithm's ability to match the tracer curve and predict a reservoir's thermal performance can be evaluated using the thermal performance computed for a target reservoir with a specified aperture distribution.

First, the problem of solving for the flow in a spatially varying aperture field is

introduced (Section 8.2), with a description of how the aperture field is modeled and how tracer results are generated for a given fracture description. Next, the inversion algorithm is introduced by discussing the application of reduced order modeling with PCA and the usage of the genetic algorithm in solving for a fracture's aperture field (Section 8.3). The predicted RTD using a conservative tracer is first presented (Section 8.4), which includes the results using different numbers of PCA modes. Finally, the results using reactive tracers are shown and the effectiveneness of reactive tracers for predicting thermal performance is compared against that for conservative tracers (Section 8.5).]

8.2 Inverse Problem Description

An inverse problem is a formulation where one attempts to calculate the parameters that describe a system making use of a set of data or observations. It is the reverse of a forward model where one calculates the response of a system for a given set of parameter values. Mathematically, the inverse problem is formulated as

$$d_i = F(x_j), \tag{8.1}$$

where d_i is the vector of data or observations and F is a model often comprised of algebraic and/or differential equation or sets of equations which depend on x_j. The inverse problem is solved by determining the x_j given d_i. Through an inverse problem formulation, the goal of this study is to determine the spatially varying aperture field of a fracture by comparing tracer data generated for a postulated trial aperture distribution to that for the actual aperture distribution using a forward model of transport in a fracture. An additional goal is to predict the thermal performance of the reservoir using the output aperture field from the

inversion scheme. For this problem, x_j are the local aperture values of a fracture, F is a numerical model describing the behavior of the injected tracer particles, and d_i is the measured concentration of the tracer at the production well as a function of time. The description of the fracture aperture field is first discussed, followed by the explanation of how the tracer RTD (concentration versus time or volume throughput) is calculated. Finally, we show how to model the heat transfer between the circulating fluid and the surrounding rock to determine the thermal performance of a reservoir for a given aperture field.

8.2.1 Fracture Aperture Field

Variable flow paths in a single circular fracture are achieved by using fractures with a spatially fluctuating aperture field. The chosen model for aperture variations is a self-affine description, where larger scale variations in the aperture (small frequencies, long wavelengths) are more important than small scale (large frequencies, short wavelengths) variations (Feder, 1988; Falconer, 2003). The primary purpose of the self-affine model is to systematically generate target reservoirs with different flow structures, but a different model could have been adopted instead. Fracture core samples have revealed fracture apertures to have a self-affine spatial correlation (Brown et al., 1986; Glover et al., 1998; Plouraboué et al., 1995; Schmittbuhl et al., 1995; Boffa, J. M. et al., 1999; Ponson et al., 2007), and was the impetus for deciding on using the self-affine description. Below is a detailed description of the varying aperture field with a self-affine spatial correlation.

The spatially varying aperture field is described as

$$w(x, y) = \langle w \rangle + h(x, y), \tag{8.2}$$

where $\langle w \rangle$ is the mean aperture value and h is the local aperture fluctuation. The spatial correlation of an aperture field can be described by the variogram function γ, which is twice the difference of the aperture variance and the two-position autocorrelation function:

$$\gamma(\mathbf{r}') \equiv \langle [h(\mathbf{r}) - h(\mathbf{r}+\mathbf{r}')]^2 \rangle = 2\left[\langle h^2 \rangle - \langle h(\mathbf{r})h(\mathbf{r}+\mathbf{r}') \rangle\right], \tag{8.3}$$

where $\mathbf{r}'$ is the displacement from point $\mathbf{r}$ and $\mathbf{r}$ is a point on the surface of the fracture. The autocorrelation function is a measure of the correlation of the aperture at point $\mathbf{r}$ with that at point $\mathbf{r}+\mathbf{r}'$. If the variogram function follows

$$\gamma(\mathbf{r}') = C|\mathbf{r}'|^{2\zeta}, \tag{8.4}$$

it has a scaling behavior of $\gamma(\lambda\mathbf{r}') = \lambda^{2\zeta}\gamma(\mathbf{r}')$, where λ is a scaling parameter and the field is said to have a self-affine geometry governed by the Hurst or roughness coefficient, ζ (Feder, 1988; Falconer, 2003). Fracture core samples of granite have been shown to have a Hurst coefficient equal to 0.8 (Schmittbuhl et al., 1993, 1995; Plouraboué et al., 1995), the typical rock type of deep geothermal systems. A self-affine aperture field was chosen to systematically generate fractures with different aperture configurations drawn from the same statistical ensemble.

The algorithm used to generate spatially varying aperture fields, which was adapted from Méheust and Schmittbuhl (2001), uses random seeding and Fast Fourier Transforms to obtain isotropic self-affine fracture aperture fields on rectangular fractures. In order to generate circular fractures with a self-affine aperture field, a square fracture of length $2R$ was first generated and only the area of an inscribed circle was used for the analysis. Any shaped fracture could have been created by first generating a large enough rectangular fracture to circumscribe the desired shape of the fracture. Only the inscribed area formed by the arbitrary shaped fracture is used for the analysis. To obtain the desired σ_h of the fracture,

the aperture value h is rescaled. A more detailed description of the algorithm used can be found in Appendix B.

For this study, the reservoir was modeled as a circular fracture, with all buoyancy effects neglected, with a radius of 500 m and a wellbore separation L of 400 m. The injection and production well are located at (-200 m, 0) and (200 m, 0), respectively, where the origin of the system is the center of the fracture. The Hurst coefficient was set to 0.8 and the dimensionless standard deviation of the aperture fluctuations $\sigma_h/\langle w \rangle$ was 0.25, with the mean aperture equal to 1 mm. By specifying the same mean aperture, the volume and mean fluid residence time for all simulated fractures are the same.

8.2.2 Tracer Test

The transport of the tracer particles in the fracture follows the governing equation

$$w\frac{\partial C}{\partial t} + w\mathbf{v} \cdot \boldsymbol{\nabla} C = wr, \tag{8.5}$$

where C is the concentration of the tracer, t is time, $\mathbf{v}$ is the velocity averaged across the aperture, and r is the reaction rate of any chemical reaction or decay. The above equation neglects dispersion. The velocity field is derived by the finite element method treatment of

$$-\boldsymbol{\nabla} \cdot \left(\frac{w^3}{12\mu} \boldsymbol{\nabla} P \right) = 0, \tag{8.6}$$

as described in Chapter 7, and with the velocity given by

$$\mathbf{v} = -\frac{w^2}{12} \boldsymbol{\nabla} P. \tag{8.7}$$

In the above equations, P refers to the pressure of the fluid, and μ is the viscosity. The flow is induced by an injection and production of fluid from two wells and there

is a no flux condition on the boundaries of the fracture. The wells are modeled as an internal boundary rather than a point to avoid singularities in velocity. The total flux across the internal boundaries representing the wells is equal to the volumetric flow rate $\dot{Q}$. To model a pulse injection tracer test, the initial condition is

$$C(x, y, 0) = 0, \tag{8.8}$$

and the boundary condition at the injection well $\mathbf{r}_I$ is

$$C(\mathbf{r}_I, t) = \frac{m_p \delta(t - t_0)}{\dot{Q}}, \tag{8.9}$$

where m_p is the mass of the injected tracers, $\delta(t)$ is the Dirac delta function, t_0 is the time of the tracer injection, and $\mathbf{r}_I$ is the location of the injection well. Additionally, there is a no mass flux boundary condition along the edge of the circular fracture. The pulse test represents the introduction of a known quantity of tracer for a differentially small time step. The concentration of tracer at the production well with time produces a tracer breakthrough curve that is a result of the aperture field and resulting flow in the fracture. By simulating a pulse tracer test, the concentration curve represents the residence time distribution (RTD) of the reservoir. The concentration is nondimensionalized by the reservoir volume V and the mass of the injected tracer,

$$\chi \equiv \frac{C(t)V}{m_p}, \tag{8.10}$$

and time is nondimensionalized by the volumetric flow rate and the reservoir volume,

$$\tau \equiv \frac{\dot{Q}t}{V}. \tag{8.11}$$

Under these definitions, the integral $\int_0^\infty \chi(\tau)\, \mathrm{d}\tau$ is equal to one and $\tau = 1$ represents the mean residence time.

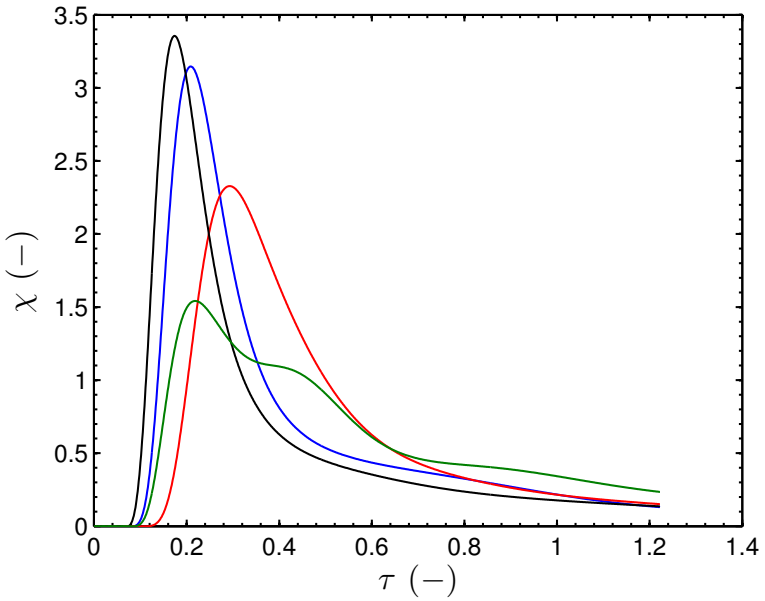

Figure 8.1: Examples of residence time distributions for four different equally sized fractures with spatial aperture variations. The aperture variations have a self-affine correlation with a dimensionless standard deviation of the aperture $\sigma_h/\langle w \rangle$ of 0.25 and a Hurst coefficient of 0.8.

The duration of the tracer test was set to $6L^2\langle w \rangle/\dot{Q}$, where $L^2\langle w \rangle/\dot{Q}$ is an estimate of the modal time, the time for the peak concentration in a tracer test. The estimate of the modal time is derived by calculating the transit time of a particle with a characteristic velocity of $U_c \sim \dot{Q}/(wL)$ traveling a distance L. The volumetric flow rate in the system is 40 L/s. The number six in $6L^2\langle w \rangle/\dot{Q}$, the duration of the tracer test, is arbitrary but it effects what concentration values are recorded. The duration needs to be long enough to have the RTD reflect a sufficient integration of the subsurface, but not too long where the RTD has too many points that are associated with flow paths that do not contribute significantly to the heat transport in the fracture. For a constant aperture fracture, the mass fraction collected from the production well for the specified duration of the tracer test is 0.77. Several examples of RTDs are plotted in Figure 8.1 for different fracture realizations, all with the same volume, and with $\sigma_h/\langle w \rangle = 0.25$ and $\zeta = 0.8$.

8.2.3 Thermal Performance of a Reservoir

After the aperture field from the inverse search has been obtained, it is used in the simulation of energy extraction to determine the production temperature as a function of time. The comparison of the production temperature for a target reservoir with that of the inversion algorithm output reservoir is used to determine how effective the inversion scheme was in predicting a reservoir's thermal performance using tracer data. The temperature field of the fracture is determined using the numerical model presented in Chapter 6. It models the heat transport within the fracture using the finite element method and couples it to a boundary integral description of the heat conduction in the surrounding bulk rock. The dimensionless temperature in the reservoir is defined as $\Theta \equiv (T(x,y) - T_w)/(T_r - T_w)$, where T is the temperature of the fracture surface at point (x,y), T_w is the temperature of the injected water and T_r is the initial rock temperature. The value of Θ ranges from zero to one. A value of zero refers to complete thermal exhaustion of the reservoir as the temperature in the fracture is now equal to the injected water temperature. If $\Theta = 1$, there is no drawdown since the temperature in the fracture is still at the initial reservoir rock temperature. The variable Θ_p refers to the dimensionless production temperature. The duration of extraction simulated was 203 days, which corresponds to when the dimensionless production temperature reaches 0.8 for the case of a constant aperture field, a wellbore spacing of 400 m, and a mass flow of 40 kg/s.

8.3 Inversion Algorithm

To solve for the aperture field of a fracture, an inversion algorithm was developed using reduced order modeling and a global optimization algorithm. The optimization algorithm is used to reduce the error against a simulated tracer RTD curve, expressed as an objective function. The objective function used is the l^2-norm error of the tracer curve for the true fracture and the output of the inversion algorithm. The l^2-norm error for a variable is defined as

$$l_y^2 = \|\hat{y}_i - y_i\|_2, \tag{8.12}$$

where $\|z_i\|_p = (\sum |z_i|^p)^{1/p}$ with summation over all the entries of the vector, y_i is the vector of the actual observations or data, and $\hat{y}_i$ is output of the model. For both conservative and reactive tracers, y_i is the vector of concentration data as a function of time of the target reservoir while $\hat{y}_i$ is the result of reservoir candidate of the inverse search. The l^2-norm error is a standard objective function used in minimization problems and is an adequate choice for this study.

A reduced order model of the aperture field is obtained using principal component analysis, an algorithm that determines the dominant modes of a system. The genetic algorithm is used for the optimization. The description and application of the principal component analysis for the problem is first presented, followed by the explanation of how the genetic algorithm is used in solving the inverse problem.

8.3.1 Principal Component Analysis

Principal component analysis (PCA) is a statistical tool that determines a set of orthogonal basis functions for a given data set (Chatterjee, 2000). The goal of PCA

is to identify the dominant behavior of the data set by revealing the key modes that best describe the data. PCA has been used to analyze turbulent flows by identifying the dominant flow structures (Berkooz et al., 1993) and for reduced order modeling (Kerschen et al., 2005; van Doren et al., 2006; Li and Jafarpour, 2010; Cui et al., 2015). van Doren et al. (2006) used PCA to reduce the computation costs by 35% in modeling water flooding in secondary oil recovery. In addition, reduced order modeling has been used in conjunction with inverse searches; Cui et al. (2015) used PCA to solve an inverse problem of determining the two dimensional permeability field. Li and Jafarpour (2010) solved the spatially varying rock permeability of an oil reservoir by matching its nonlinear dynamic flow data with that of a reduced order model described by discrete wavelet and cosine transforms. PCA is also called proper orthogonal decomposition and Karhunen-Loéve transforms, among other names (Hua and Liu, 1998; Chatterjee, 2000).

For a data set X_{ih} of mean zero, the PCA modes are the eigenvectors of the covariance matrix

$$C_{ih} = \sum_{k=1}^{m} X_{ik} X_{hk}. \tag{8.13}$$

The data set X_{ih} is an $n \times m$ matrix with m being the number of "trials" or "samples" and n being the number of components or degrees of freedom of each sample or trial. For the aperture field on a computation mesh or grid, the degrees of freedom are the aperture values at all the nodes on the mesh and the number of trials or samples is the number of fracture realizations used to generate the PCA modes. The eigenvalues represent the relative importance of their respective eigenvectors. With the basis functions identified, the values of any sample or trial can be constructed by knowing the coefficients for all the modes,

$$u_i = \sum_{j=1}^{n} \Phi_{ij} \alpha_j, \tag{8.14}$$

where Φ_{ij} is the matrix containing the basis functions or PCA modes and α_j are the coefficients for the modes. The matrix Φ_{ij} is an $n \times n$ matrix, where n is the number of degrees of freedom, in this case, the number of nodes on the mesh describing the aperture field. Each column of Φ_{ij} represents one basis function or PCA mode and each row corresponds to an aperture nodal value. To generate a reduced order model, Eq. (8.14) is truncated to p terms,

$$\hat{u}_i = \sum_{j=1}^{p} \Phi_{ij}\alpha_j, \tag{8.15}$$

where $\hat{u}_i$ denotes the reduced order model. The modes are arranged by their respective eigenvalues, the mode with the largest eigenvalue being designated as the first mode. The PCA algorithm derives the modes that minimize the l^2-norm error of reduced order model of the samples or trials contained in data set X_{ih}. The ideal number of modes to use is not certain as one must consider the trade off of using more modes and increasing the complexity of the system but increasing the accuracy of the aperture field for the reduced order model.

The PCA algorithm will be applied to determine the dominant aperture structures in fractures with spatially varying aperture fields. Large length scale variations of the aperture dominate over small length scale aperture variations for fractures with a self-affine geometry. The first few modes should capture the large scale aperture variations, while the higher modes progressively capture smaller scale variations. To create the modes, five thousand fractures are randomly generated using the algorithm described in the previous section, all with the same standard deviation of the aperture variations, mean aperture, and Hurst coefficient. Each fracture realization represents a "snapshot" of a possible structure of the aperture field. Several of the modes are plotted in Figure 8.2. Any fracture surface can be described by the PCA modes by modulating the modes through the

coefficient α_j for each mode. The expression of the reduced order model for the aperture field using p modes is

$$\hat{w}_i = \langle w \rangle + \sum_{j=1}^{p} \Phi_{ij} \alpha_j, \tag{8.16}$$

where w_i is the nodal values of the aperture field on a computational mesh.

PCA can be used in conjunction with an inverse search by using the inversion to determine the coefficients of the a reduced order model of the aperture field. Instead of trying to determine the nodal aperture value in the mesh, only the coefficients of the dominant p modes will be determined, greatly reducing the computational cost and making the inverse problem more tractable. As discussed previously, if the aperture field is described by a self-affine geometry, the field is composed of dominant small wave number (large wavelength) variations. Because the aperture field has this inherent behavior, PCA will be capable of adequately describing the system using a reduced order model. Figure 8.2 illustrates various modes obtained from the PCA analysis. Note that as the mode number increases, the modes increasingly describe larger frequencies. The first set of modes are sinusoidal curves with a period of one while higher modes exhibit larger frequency sinusoidal features.

The PCA modes for the aperture field shown in Figure 8.2 were derived for $\sigma_h/\langle w \rangle = 0.25$ and $\zeta = 0.8$. However, using a different value for the standard deviation of the aperture or a different Hurst coefficient will yield the same PCA modes. The PCA modes are invariant to changes in σ_h because the parameter α_j controls properties like the standard deviation of the aperture field. For example, σ_h can be doubled by multiplying all α_j values by two. The Hurst coefficient controls how much more important large scale variations are than smaller scale variations. As such, the same PCA modes for one value of the Hurst coefficient

will be the same for another. The only thing the Hurst coefficient controls is the number of modes needed to achieve a level of accuracy. Fractures with smaller Hurst coefficients require more modes because higher wave number modes are more important than they are in fractures with a higher Hurst coefficient. Schmittbuhl et al. (2008) modeled viscous flow through a fracture with a self-affine aperture field and demonstrated how only the first four Fourier modes are sufficient to describe the flow in the system. Neuville et al. (2011) showed that the l^2-norm error of the aperture field for rectangular fractures with self-affine aperture field is $l^2 = O(n^{-\zeta})$, where n is the number of modes used to describe the aperture field.

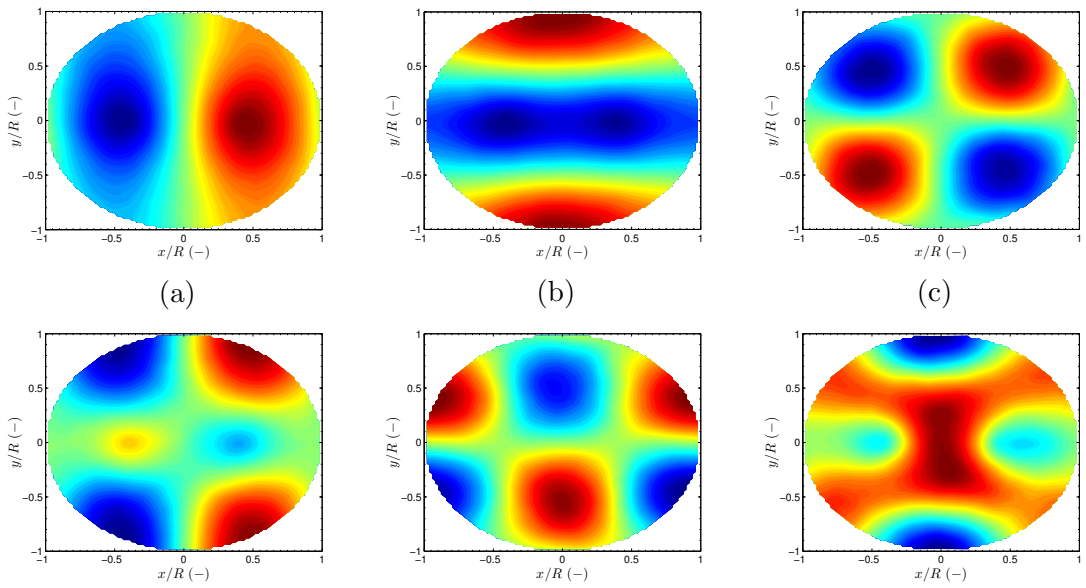

Figure 8.2: Principal component modes for a circular fracture. The color scale is arbitrary as the strength of the modes are modulated by the coefficient α_j. (a) First mode (b) Second mode (c) Fifth mode (d) Sixth mode (e) Seventh mode (f) Eighth mode.

The reduced order model for the aperture field using various number of modes is shown in Figure 8.3. With only four modes, the large scale features of the fracture are captured; there is a large aperture region near the top and narrow region near the bottom. As the number of modes used to describe the system

increases, the aperture field gains more details since the higher modes flesh out more of the smaller scale variations. The l^2-norm error of the aperture field goes down with more modes, 0.16, 0.11, 0.10. 0.085, 0.074, and 0.065, for four, eight, twelve, sixteen, twenty, and twenty-four modes, respectively.

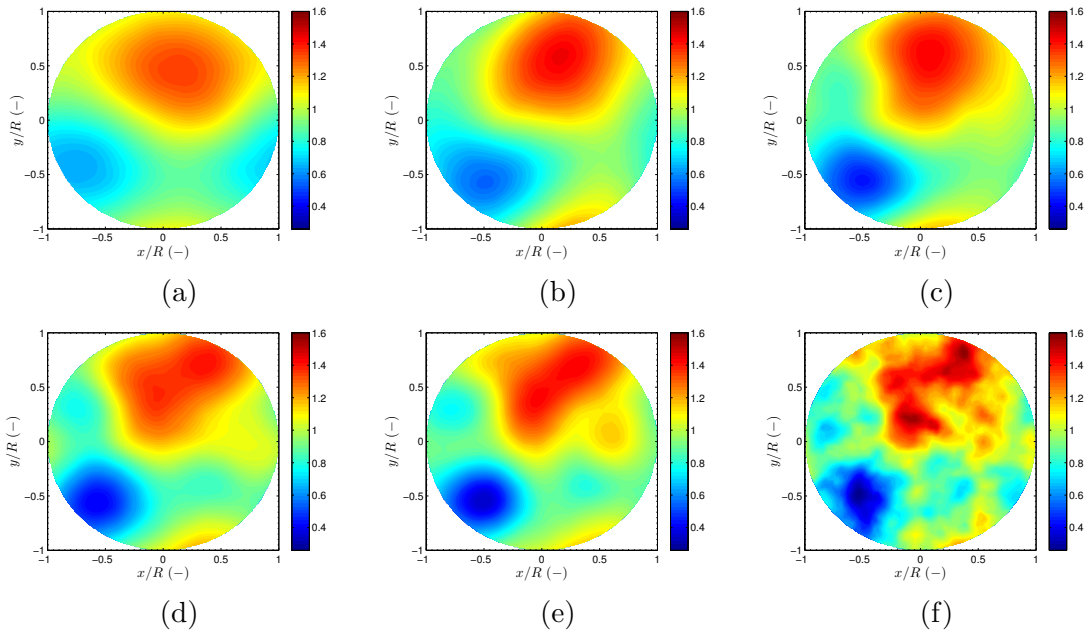

Figure 8.3: Different depictions of a fracture aperture field using various number of PCA modes. (a) Four modes. (b) Eight modes. (c) Twelve modes. (d) Twenty modes. (e) Twenty-four modes. (f) full order model (all modes used).

8.3.2 Genetic Algorithm

The genetic algorithm is a metaheuristic stochastic global optimizer. It mimics the process of natural selection to reach the optimal value of a problem. The genetic algorithm has been used to solve a wide range of problems such as finding the optimal antenna design for aerospace applications (Hornby et al., 2011), improving vehicle routing involving simultaneous pickup and delivery (Tasan and Gen, 2012), and optimizing land use considering multiple objectives (Cao et al., 2012).

To optimize an objective function $f(x_j)$ where x_j is a set of parameter values or "genes", N "individuals" are randomly created to form a population, with each individual representing a set of parameter values. For each individual, a "fitness" score is assigned based on the evaluation of the objective function. A new set of individuals are formed in each generation by breeding parent pairs and by mutation. The process for selecting parent pairs will preferentially choose individuals with better fitness values. A set of new individuals are created through a crossover function that uses the two sets of genes of the parents to form two new individuals for a new generation, replacing the parents. Mutations in the population are also modeled by taking the individuals with the worst fitness scores and replacing their genes with a new set of randomly generated values. The algorithm is terminated either by reaching a preset number of generations or when the value of the objective function reaches a predetermined tolerance value. The individual with the best fitness score is the optimal answer. For this study, x_j is α_j, the coefficients for the PCA modes and the genetic algorithm is tasked to determine α_j with the mean aperture specified, mathematically,

$$\min f(\alpha_j) = \frac{\|\chi_i - \hat{\chi}_i\|_2}{\|\chi_i\|_2}, \tag{8.17}$$

with,

$$\hat{\chi}_i = F(\langle w \rangle, \alpha_j), \tag{8.18}$$

where χ_i and $\hat{\chi}_i$ are the modeled tracer data for the true fracture and the reduced order simulated model, respectively, and F is the forward model that produces a tracer curve from the velocity field given the mean aperture and the PCA coefficients.

The genetic algorithm was chosen over other search algorithms for several reasons. Determining the fracture aperture field is non-unique, as various aperture

fields can yield tracer curves that describe the observed tracer curve equally well. Additionally, the search space of the tracer error may have many local minima. Deterministic searches have difficulty dealing with local minima and may stop after finding one, while methods like the genetic algorithm are adept at dealing with many local minima and explore a wide function space. The evaluation of the fitness of each individual is independent of the others, and as a result, the genetic algorithm can be easily parallelized, taking advantage of computers with multiple cores and processors. Parallelization provides advantages over other metaheuristic optimizations like simulated annealing. As a heuristic optimization, the genetic algorithm allows one to modify the process for a given problem, however, this is also a disadvantage because one may need to experiment with different sets of parameters and options to get the best results. Another limitation of metaheuristic searches is that they often lack guaranteed convergence or a theoretical description of the rate of convergence.

For this study, fifty individuals and ten generations were used for the genetic algorithm. After ten generations had been reached, the best individual was kept and all others were replaced with forty-nine new, random individuals. This new population was used as the starting population for another implementation of the genetic algorithm with ten generations. Genetic diversity was ensured by periodically starting with a fresh population which also avoids a dominant phenotype that may negatively restrict the algorithm into a smaller search space. This approach is similar to micro-genetic algorithms (Krishnakumar, 1990; Madadi and Balaji, 2008) but those approaches use about five individuals in each generation. After the optimal coefficients had been determined, a deterministic search using the Nelder-Mead algorithm (Nelder and Mead, 1965; Lagarias et al., 1998) was applied using the optimal coefficients as the initial guess. The Nelder-Mead algorithm further

refined the result by looking for the local minimum near the output of the genetic algorithm.

The most important parameters of the genetic algorithm are the crossover function, the size of the population, and the number of generations. The crossover function determines how the offspring are produced from a selected parent pair. The population size and number of generations control the total number of function evaluations. An efficient and accurate use of the genetic algorithm requires the user to experiment with different sets of parameters to arrive at the optimal configuration. It is recommended to start with typical algorithm configurations, like those reported by Buljak (2012). When comparing runs with different parameter specifications, it is important to look at the value of the objective function for the optimal answer and the mean value of the objective function of all individuals for each generation. If the mean and optimal objective function values of a generation are too close, then the population consists of individuals that are genetically similar and the population needs more genetic diversity. The number of generations needs to be large enough that the optimal value of the objective function is much smaller (for minimization problems) than the optimal value at early generations but the number of generations should not be so large that the optimal value for each generation remains stagnant for several generations. Please refer to Appendix C for more information on the parent selection, crossover functions, and other details of the genetic algorithm used for this study.

8.4 Inversion Results Using Conservative Tracers

The inversion algorithm was tested by applying the algorithm to ten different target fractures, all with the same size, wellbore separation, and aperture statistics. The mean aperture is 1 mm and the dimensionless standard deviation and Hurst coefficient is 0.25 and 0.8, respectively. A pulse conservative tracer test was simulated for each of the ten fracture realizations, and is the curve the inverse method must match in the results presented here. We also performed inverse searches using a step tracer test and obtained results equivalent to those for the pulse test as might be expected since the step test concentration is the cumulative integral of a pulse test (Fogler, 2006). The inverse algorithm searches through a space of fracture aperture fields, seeking to minimize the error between the simulated tracer curve for a target fracture realization and the tracer curve associated with an aperture field in the algorithm search space. The inversion algorithm was applied to determine the best number of modes to use that would lead to the lowest error of not only the tracer residence time distribution, but also of the aperture field and the expected production temperature. The inversion algorithm used eight, twelve, sixteen, twenty, and twenty-four modes for the analysis, being applied to ten different fractures. More than twenty-four modes could have been used for the study, however, it would increase the number of degrees of freedom and the difficulty for the inversion algorithm to converge to a satisfactorily minimum answer. The resulting increase in the convergence time requires more generations and a larger population, which will increase the computational time. Since additional modes will only describe small scale aperture variations, it is unclear whether these additional modes beyond twenty-four would affect the simulated tracer curve. The genetic algorithm was run five times for each fracture to produce five replicates. The result is a total of fifty runs per mode value investigated. Since the genetic

algorithm is a stochastic optimization scheme, different runs will yield different results. Instead of taking the best inversion run that yielded the lowest error in matching the tracer curve, all five replicates are considered to obtain a measure of uncertainty in predicting the reservoirs' thermal performance. Having a measure of uncertainty partially addresses the problem of non-unique solutions, a common problem when solving inverse problems. The l^2-norm error is reported for the tracer curve, the aperture field, and the production temperature drawdown curve for each run of the inversion algorithm.

The error of the tracer curve, aperture field, and production temperature each represent different evaluations of the inverse process. The error associated with matching the tracer curves measures the effectiveness of the inversion scheme. On the other hand, the error of the aperture field and the production temperature reveal how effective the tracer results were at producing the correct reservoir model and thermal performance. The production temperature error is dependent on the output aperture field. If the inversion algorithm is able to closely match a given tracer curve but does a poor job predicting the aperture field and thermal performance, then the tracer measurements failed to provide the necessary information to predict a reservoir's structure and thermal hydraulic behavior. The results of the tracer curve error is first examined, before analyzing the inversion methodology's capability of predicting both the reservoir's production temperature and aperture field.

The aim of analyzing the usage of various number of PCA modes is to understand what level of detail of the aperture field is required to produce reservoirs with a tracer signal that is a close match to that of a target reservoir. The boxplots of the l^2-norm error for the tracer curve, aperture field, and production temperature

are plotted in Figure 8.4. From Figure 8.4, there is a substantial drop in error from twelve to sixteen modes, with the boxplots of the l^2-norm error for higher modes similar to each other. The results for the for sixteen, twenty, and twenty-four modes are too close together to say that the difference is statistically significant. The boxplots also show the variability of the l^2-norm error. Apart from the eight and twelve mode results, the tracer error was least variable and the aperture field and production temperature l^2-norm error were comparable. For comparison and to better interpret the l^2-norm errors reported in the boxplots, Figure 8.5 compares several tracer and production drawdown curves for the output aperture field from the genetic algorithm. From Figure 8.5a, the two sets of RTDs are indistinguishable when l^2-norm error is equal to 0.02 and 0.04. Thus, for most of the results when sixteen or more modes are used, the tracer curves of the target fracture and the output of the genetic algorithm are virtually identical. The inversion algorithm, when using sixteen or more modes, has no difficulty in producing a reservoir with a tracer signal that closely matches that of the target fracture and there is little advantage in terms of accuracy of using smaller scale aperture features than what is representative of sixteen to twenty-four PCA modes.

The inversion scheme was capable of producing an aperture field that resulted in a close match of the tracer curve of the target reservoir. However, it is not evident whether a smaller error in the tracer RTD correlates to better predictions of both the aperture field and production temperature. Understanding the correlation of the error is vital in assessing replicate runs of the inversion scheme. If error of tracer measurement and either the production temperature of aperture field are well correlated, then it becomes important to strongly weight the inversion run that yielded the lowest tracer error. The correlation coefficient is a measure of how correlated two variables are and ranges from zero to one, with zero denoting

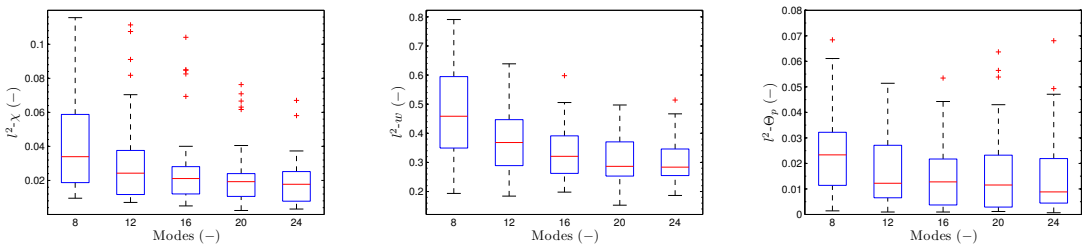

(a) (b) (c)

Figure 8.4: Boxplots of the l^2-norm error of the genetic algorithm output using various numbers of PCA modes in the inverse search. The inverse search was applied to ten different fractures with five replicates for each fracture. (a) l^2-norm error for tracer concentration. An outlier for eight modes at $l^2 = 0.16$ is not plotted to better show the range of results for the other boxplots. (b) l^2-norm error for the aperture field. (c) l^2-norm error for the dimensionless production temperature drawdown curve. An outlier for eight modes at $l^2 > 0.2$ is not plotted to better show the range of results for the other boxplots.

no correlation between the two variables. The correlation coefficient of the l^2-norm error of the tracer and the aperture field is 0.4, and is 0.25 for the correlation of the error of the tracer and production temperature. The values were evaluated by pooling all the l^2-norm error values for all the modes, but Table 8.4 breaks down the results by the number of modes used. The correlation coefficients when the modes are not pooled tend to be lower, ranging from 0.21 to 0.34 and 0.07 to 0.23, for corr(l^2_χ, l^2_w) and corr$(l^2_\chi, l^2_{\Theta_p})$, respectively, and where corr signifies the function evaluating the correlation coefficient. The low correlation values are attributed to the good fidelity with which the inversion algorithm matches the tracer curve. Most of the inversion runs produced a tracer curve that was nearly identical to the true data and any improvement in matching the tracer data will result in negligible change in the both error of the aperture field and production temperature. The correlation results suggest using multiple inversion runs to obtain a range of likely values for the reservoir aperture field and thermal performance consistent with the tracer data instead of solely relying on the run with the lowest l^2-norm error of

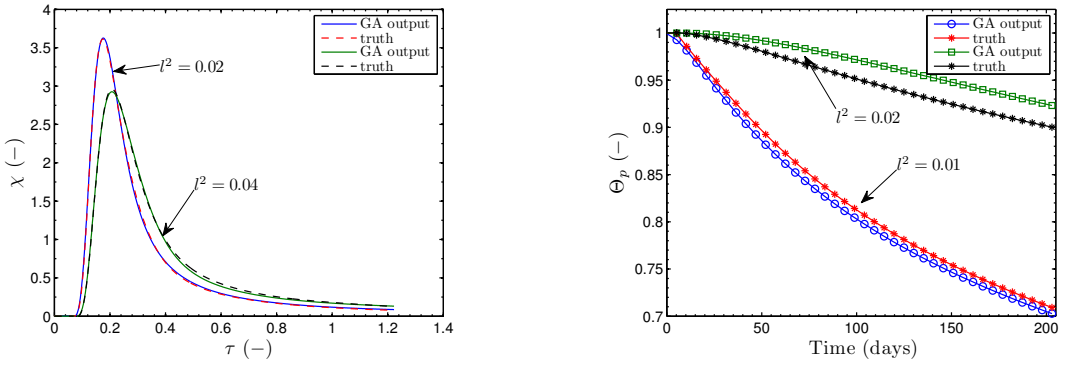

(a) (b)

Figure 8.5: Comparison of the genetic algorithm output results for the tracer curves and the production temperature, for different values of the l^2-norm error (a) Tracer RTD comparison. The first set of curves have a l^2-norm error of 0.02 while the second has 0.04. Twenty PCA modes were used for the first set and sixteen modes for the second. (b) Dimensionless production temperature comparison. The first set of drawdown curves has an l^2-norm error of 0.01, while the second has an error of 0.02. The difference between the dimensionless production temperature for the last time step is 0.007 and 0.013, for the first and second set of curves, respectively. Twenty-four PCA modes were used for the first set and sixteen modes for the second.

Table 8.1: The correlation coefficient of the l^2-norm error of tracer and aperture field and the tracer and the production temperature, broken down by the number of modes used in the inversion scheme.

modes	$\text{corr}(l^2_\chi, l^2_w)$	$\text{corr}(l^2_\chi, l^2_{\Theta_p})$
eight	0.27	0.21
twelve	0.28	0.07
sixteen	0.31	0.23
twenty	0.34	0.21
twenty-four	0.21	0.22
all	0.40	0.25

the tracer RTD.

The production temperature drawdown curves between the full order model and those derived from the genetic algorithm output do not have the same level of agreement as the tracer curves, which were nearly identical. Figure 8.5b shows two different predicted drawdown curves along side the true production temperature

curve, each with a different value of the l^2-norm error for the thermal performance prediction. When $l^2 = 0.01$, there is little difference between the two drawdown curves and the difference between the dimensionless temperature at the end time is only 0.007, however, there is a notable separation between the curves when the l^2-norm error is doubled. The boxplots in Figure 8.4c show that most of the results do not have the level of accuracy shown in Figure 8.5b for $l^2 = 0.01$, except for the case of twenty-four modes which has a median l^2-norm error value of 0.009. Less than 75% of the results have an l^2-norm error of less than 0.02.

Figure 8.6 shows the accuracy and precision of the dimensionless production temperature of each of the ten fractures investigated for the results using sixteen or more modes, with a total of fifteen replicates for each target fracture. Accuracy is a measure of how close the inversion output matches the true answer while precision describes how close the replicate inversion results are from each other. The true dimensionless production temperature is represented by Θ_p, the mean dimensionless production for the five thousand fracture ensemble is $\bar{\Theta}_p$, while the dimensionless production temperature for the aperture field from the inversion algorithm is $\hat{\Theta}_p$. A slope of one plotted on the figure indicates no error as corresponds to when the true production temperature is equal to the production temperature of the aperture field from the inversion scheme. Points below the line of slope one represent an under prediction in production temperature, while negative values on the x-axis signify that the production temperature is lower than the mean of the five thousand fracture ensemble. The error bars in the figure represent the precision of the inversion results using the interquartile range.

The inversion scheme is able to handle reservoirs with different thermal performance without loss in both precision and accuracy. The results do not show a

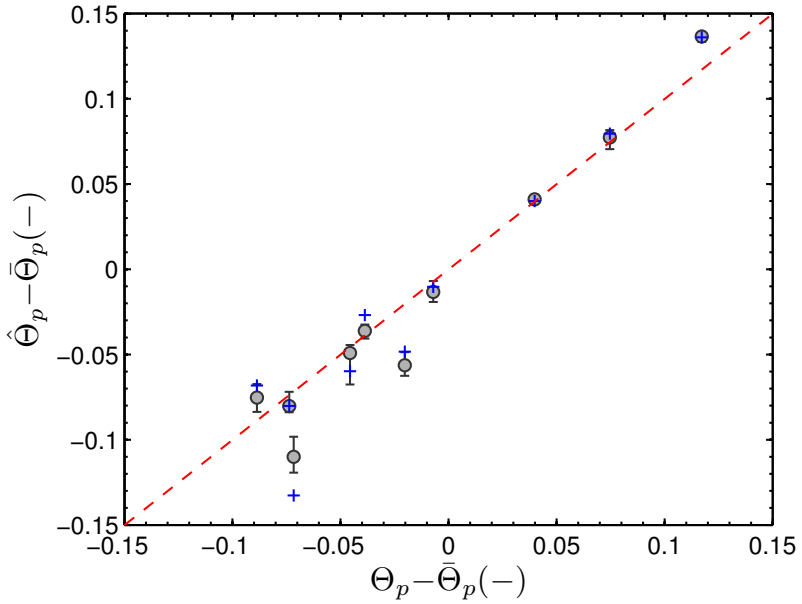

Figure 8.6: The accuracy and precision of the dimensionless production temperature for each of the ten fractures investigated. The true dimensionless production temperature is represented by Θ_p, the mean dimensionless production for the five thousand fracture ensemble is $\bar{\Theta}_p$, while the dimensionless production temperature for the aperture field from the inversion algorithm is $\hat{\Theta}_p$. The circles are the median value while the error bars represent the interquartile range, the 25% to 75% quantile. The dashed red line represents a slope of one which corresponds to no error. The blue plus markers represent the value of $\hat{\Theta}_p - \bar{\Theta}_p$ for the inversion run that produced the lowest l^2-norm error of the tracer measurement for each fracture.

trend of lower precision associated with less probable thermal performances, fractures with production temperatures farther away from the mean. A majority of the points are close to zero error line, with an equal number of points that represent under and over predictions. However, not all the results' interquartile range cross over the zero error line, with some that are either situated entirely on one side or the other. The ideal situation would be that the median points reside near the zero error line with the distribution from the replicate runs being symmetrically distributed below and above indicating positive and negative deviation. The value of $\hat{\Theta}_p - \Theta_p$ for the inversion run that produced the lowest l^2-norm error of

the tracer measurement for each fracture is also plotted on Figure 8.6. Compared to the median value, three results of predicted production temperature with the lowest tracer error were more accurate, while three were just as accurate. These results show that it is a better practice to consider all inversion model outputs rather than simply taking the result with that had the lowest error in matching the tracer measurement.

As an aggregate of the data points of the ten fracture cases, the median value of production temperature deviation from the truth $\hat{\Theta}_p - \Theta_p$ is nearly zero, -6×10^{-4}. The 50% and 95% probability range of $\hat{\Theta}_p - \Theta_p$ centered around the median is -0.014 to 0.0079 and -0.048 to 0.03, respectively. A method to measure the effectiveness of the inversion methodology to predict a reservoir's thermal performance is to consider the case in which no inversion methodology was applied. For $\sigma_h/\langle w \rangle = 0.25$ and $\zeta = 0.8$, the dimensionless production temperature at the end of the extraction for an ensemble of five thousand fracture realizations has a mean value of 0.783 and a standard deviation σ_Θ of 0.072, with a Gaussian like distribution. There is a 50% and 95% probability that a randomly sampled fracture will have $\Theta_p = 0.783 \pm 0.1$, and $\Theta_p = 0.783 \pm 0.14$, respectively. There is an increase in precision by a factor of seven to twelve and three to five for the 50% and 95% interquartile error range, respectively, by using the inversion scheme. For the limited number of fractures investigated, the optimization procedure was capable of accurately and precisely predicting the dimensionless production temperature of fractures that are both common and uncommon.

For the analysis of the aperture error, the key questions to answer are to what extent the output aperture fields from the inversion methodology resemble the target reservoirs, whether the error of the aperture field is correlated to the error

of the production temperature, and if the information of the aperture field from the inversion scheme is reliable enough to make decision like future placement of wells for reservoir expansion. The l^2-norm error for the aperture field was the largest among the quantities measured. For the entire dataset representing fifty runs, the lowest l^2-norm error for the aperture field was 0.15, when twenty modes were used. For that particular fracture, the lowest possible error is 0.068, which occurs when the genetic algorithm correctly determines α_j for the reduced order model. The mean of the lowest possible l^2-norm error of the ten target fractures is 0.13, 0.11, 0.096, 0.085, and 0.079, for eight, twelve, sixteen, twenty, and twenty-four modes, respectively. The genetic algorithm output for several fracture aperture fields is shown in Figure 8.7, along with the full order model of the target fracture. The first pair is the result with the lowest error of the aperture field, the second pair depicts the aperture field for the lowest error for the aperture field for only the twenty-four mode dataset, while the last pair is the output with the lowest production temperature error in the entire dataset. In all three cases the large scale features and thus the major flow channels in the system are captured. The location and relative size of low and high aperture regions of the full order order model are present in the reduced order aperture fields. The aperture fields depicted in the figure had thermal drawdown curves that also matched well with the true values. The dimensionless temperature after 203 days of extraction was off by about 0.002, 0.01, and 0.0001, for the system shown in Figures 8.7a-8.7c, respectively.

While the previous results demonstrated examples that highlight the capacity of the inversion algorithm to closely reproduce the aperture field of the target reservoir, they are the exception rather than the norm. Typical results of the aperture field are shown in Figure 8.8, consisting of the five output aperture fields from the inversion algorithm for one of the ten target fractures when using twenty-four

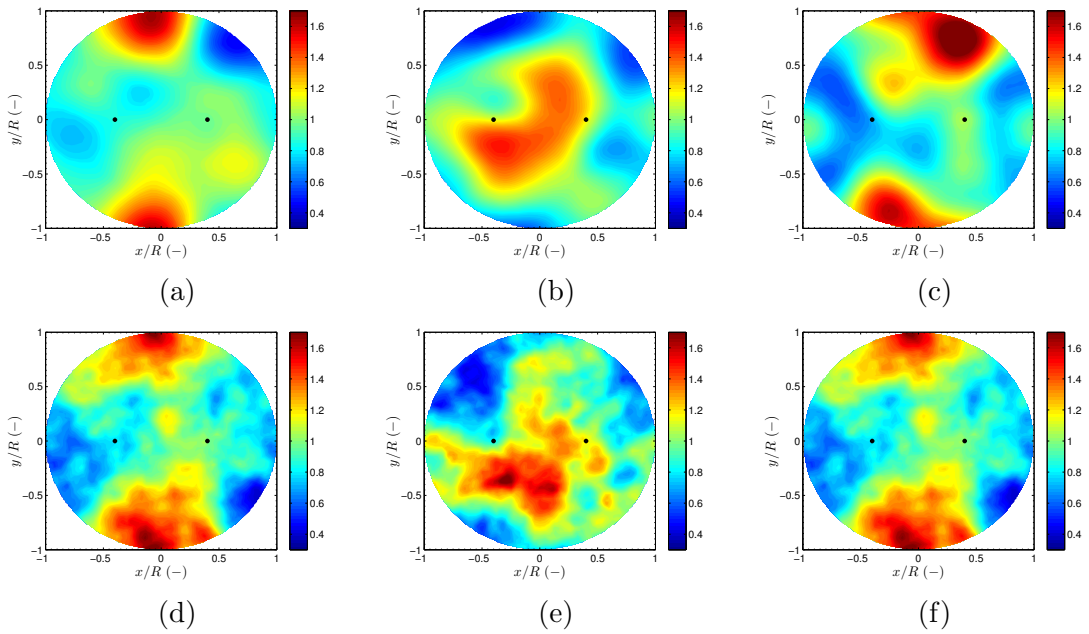

Figure 8.7: Comparison of the output aperture field from the inversion algorithm with the true, full order, aperture field. The black dots represent the location of the wells. (a) The aperture field with the lowest l^2-norm error of the aperture field among the entire dataset, which occurred when using twenty modes. (b) The aperture field with the lowest l^2-norm error of the aperture field when twenty-four modes were used. (c) The aperture field that had the lowest l^2-norm error of the dimensionless production temperature of the entire dataset, which occurred when using twenty-four modes. (d)-(f) The true, full order model, aperture fields for (a), (b), and (c), respectively. Note that (d) and (f) are the same reservoir.

modes. None of the five fractures resemble the target fracture. The fracture in Figure 8.8d is possibly the closest match if it were reflected across the x-axis. The inversion algorithm cannot distinguish between mirror images of the target fracture, as mirror images result in the same tracer curve and thermal performance due to the symmetry of the problem. The aperture fields displayed in Figure 8.8 suggest that it is impractical for the results to be used for reservoir management considerations like the placement of additional wells. Plotted in Figure 8.8 are examples of possible additional well placements to expand the system by considering the output aperture field. The placements were chosen simply by sight, considering areas where the aperture field is small to avoid flow channeling and to target areas

of the reservoir that would have not seen significant drawdown. All the placements chosen would be areas of high aperture in the real system, and thus poor choices for well placement. Given the results of the aperture field from the inversion algorithm, using the resulting aperture field to implement a drilling strategy is not feasible.

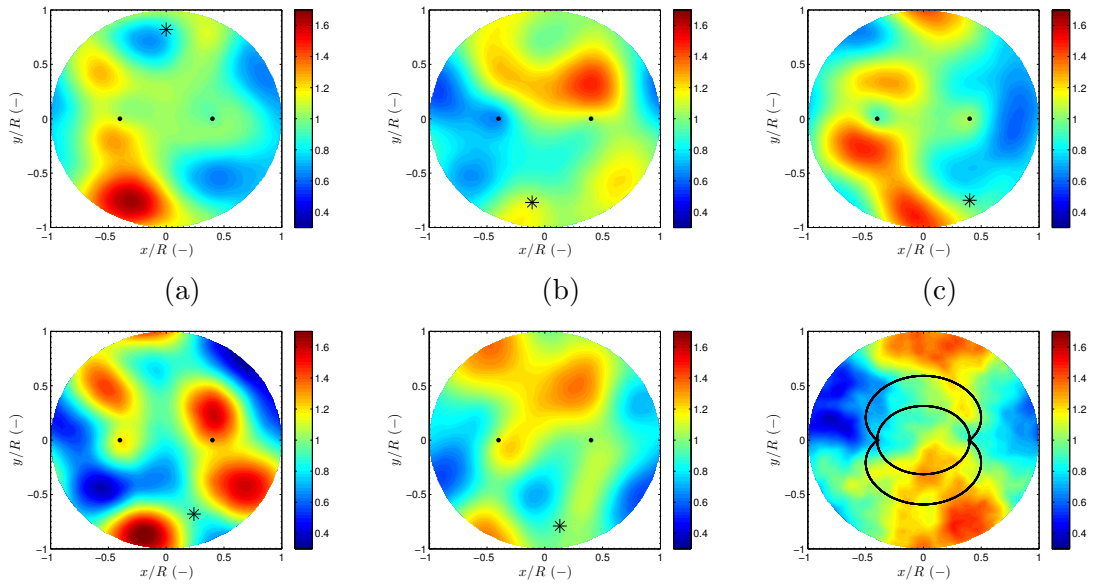

Figure 8.8: Comparison of the output aperture field from the inversion algorithm with the true, full order, aperture field. The black dots represent the location of the wells while the black asterisk signifies a possible location for an additional well in the system. (a)-(e) Five different aperture field results from the inversion algorithm, using twenty-four modes. (f) The full order aperture field. The two sets of black lines represent the streamlines that coincide with the arrival of 50% and 77% of the tracer, with the inner lines corresponding to the lower percentage.

The difference in performance of the inversion scheme to predict the thermal performance compared to the aperture field suggests that error of the production temperature and aperture field is poorly correlated. Fracture apertures that do a poor job of representing the spatial aperture structure can accurately and precisely model the thermal performance. All the reservoirs shown in Figure 8.8 had a l^2-norm error for the dimensionless production temperature drawdown curve of

less than 0.009, corresponding to a close match of the drawdown curves with that of the full order model. The correlation coefficient for the l^2-norm error of the aperture field and dimensionless production temperature is 0.31, when considering the results for sixteen or more modes. Furthermore, the fractures do not resemble each other; several different reservoir configurations can result in similar thermal behavior and produce similar tracer RTDs. These results illustrate how the formulated inverse problem is ill posed, which is often the case for inverse problems. An ill posed problem is one in which either no solution exists, the solution is not unique, or the solution is highly sensitive to differences in the observation.

The failure of the inversion methodology to generate aperture fields resembling the true aperture field is further illustrated in Figure 8.9. The figure displays the output aperture field and the resulting fracture surface temperature for five target fractures, when using twenty-four modes. Also plotted for comparison are the production temperature and the aperture field for the true reservoir. Of the five cases, two results predicted the production temperature to a high degree of accuracy, two were moderately accurate, while one did a poor job. Looking at the output aperture fields, the inversion algorithm did an inadequate job at matching the aperture field. Streamlines are drawn on the figures for the fracture surface temperature, and they reveal how the shape of the streamlines are reflected in the shape of the depleted thermal field in the fracture. Overall, the temperature field of the output model more closely resembled the true result compared to aperture field.

The inversion algorithm might be minimizing the error of a subset of the aperture field and this error may be better correlated to the error of the production temperature. The correlation coefficient of the l^2-norm error of the dimensionless

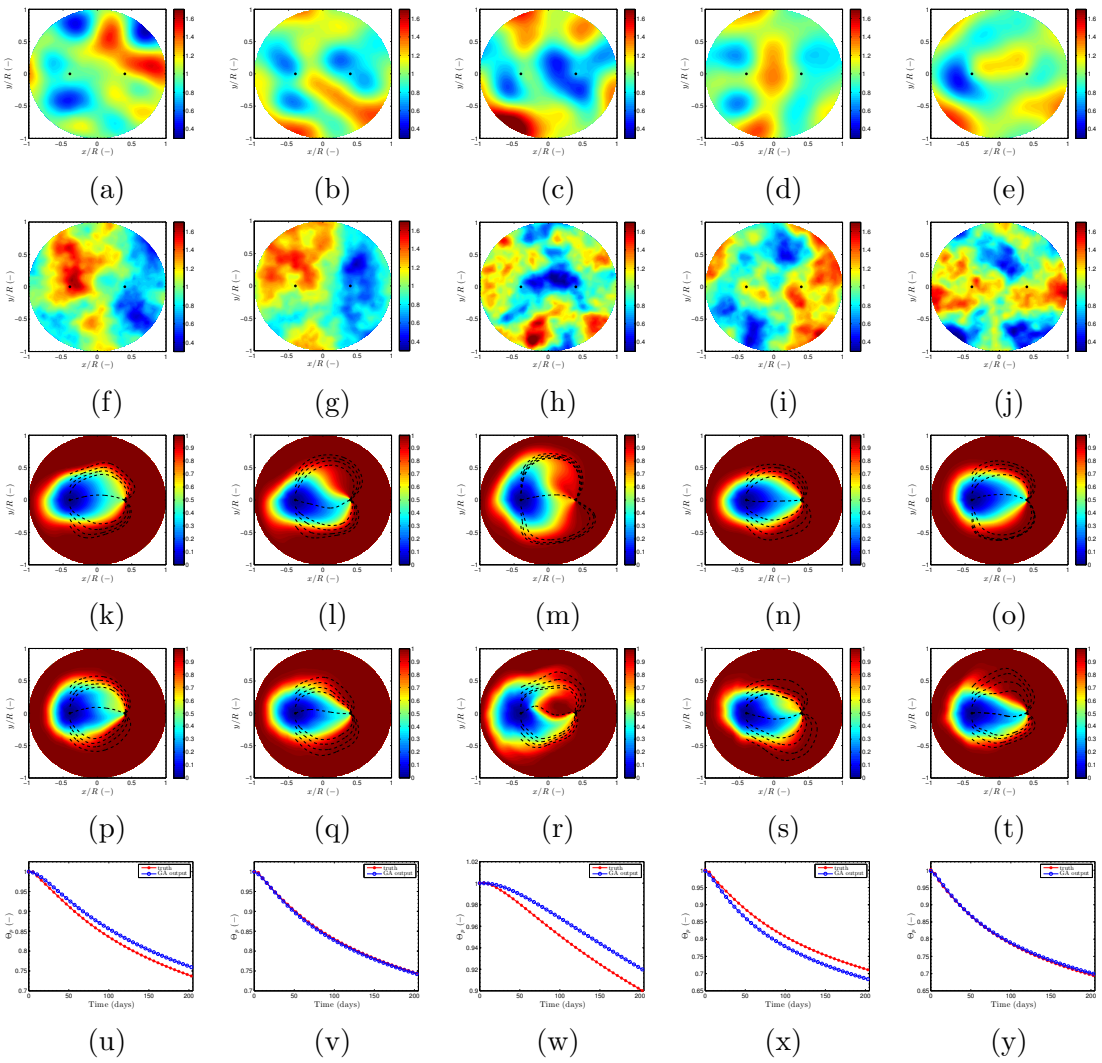

Figure 8.9: Inversion algorithm results, using twenty-four modes, for five different target fractures. The first and second rows contain the output aperture fields and the corresponding true aperture fields, respectively, the third and fourth rows contain the fracture temperature fields (the black dashed lines are streamlines) for the output aperture fields and the target fractures, respectively, and the production temperature curve comparisons between the output and true values are in the fifth row.

production temperature and that of a subset of the aperture field was calculated. Since most of the flow is contained within the region in between the injection and production well, the area enclosed by a circle centered around the wellbores with a radius of 100, 150, 200, 250, 300, 350, and 400 m was used. In addition to the

Table 8.2: Correlation coefficient of the l^2-norm error of the aperture field and dimensionless temperature drawdown for various subsets of the aperture field.

Radius (m)	Correlation Coefficient
100 m	0.74
150 m	0.66
200 m	0.40
250 m	0.34
300 m	0.36
350 m	0.39
400 m	0.43
500 m	0.40
50% streamline	0.64
77% streamline	0.35

circles, the area enclosed by the streamlines that correspond to the arrival of 50% and 77% of the tracer particles was considered. For a constant aperture fracture, 77% of the tracer has arrived at the production well for the chosen duration of the test. The shapes of the streamlines are plotted in Figure 8.8f, with the 50% and 77% streamlines roughly the shape of a circle with a radius 150 m and 300 m, respectively. The results of the correlation coefficient are presented in Table 8.4. The greatest correlation occurred for the smallest area analyzed, a circle with a 100 m radius. Since the aperture area in between the wellbores strongly controls the reservoir's thermal performance, the error of the aperture field for this region is more correlated to the production temperature.

For the range of eight to twenty-four PCA modes, there is little improvement in the performance of the inversion scheme when using more than sixteen modes. The inverse algorithm is capable of finding an aperture field that will satisfy the tracer RTD, but it may not accurately solve for the aperture field, despite correctly forecasting the reservoir's thermal performance. The formulated inverse problem is ill posed because the solution is not unique. Although predicting the thermal performance is the ultimate objective, a lack of knowledge of the spatially vary-

ing aperture field will make it difficult to use the results to make decisions that require correctly identifying the aperture field, such as determining the optimal placement of additional wells. The non-uniqueness of the inverse problem can be partly addressed by running multiple replicates. For the production temperature, each replicate forms a distribution of possible reservoir temperatures, and the statistical analysis from the distribution should guide one in determining the level of uncertainty in predicting a reservoir's thermal performance based on tracer data.

8.5 Inversion Results Using Reactive Tracers

Temperature sensitive reactive tracers provide an additional tool to interrogate the subsurface. Since the reaction rate of thermally degrading tracers are a function of temperature, a reactive tracer test will contain information of the subsurface temperature field, in addition to information about the fluid residence time distribution. This is an advantage over conservative tracers. The inversion algorithm was applied using a simulated reactive tracer test. The inversion scheme was run for ten different fracture realizations, with five replicates, and the results of the l^2-norm error for the aperture field and the dimensionless production temperature drawdown are compared to the results from the conservative tracer study. The objective of this section is to determine whether, and to what extent, reactive tracers are more effective in predicting a reservoir's thermal performance than conservative tracers. Twenty-four PCA modes were used for the inversion scheme.

In modeling chemically reactive tracers, the Damköhler number, Da, is a useful nondimensional number to calculate. The Damköhler number is the ratio of the tracer's residence time to the time scale of the chemical reaction. For a first

order reaction, the time scale of the reaction is the inverse of the reaction rate constant k. If $\mathrm{Da} \ll 1$, then little reaction occurs during the time the particles are in the reservoir and the tracer will behave like a conservative tracer. When the opposite occurs, most of the tracer particles will react in the subsurface and very little unreacted tracer will be recovered. The ideal reactive tracer should have a reaction rate where $\mathrm{Da} \sim 1$ in order to get tracer results that will be most beneficial in determining the subsurface temperature. Since deploying reactive tracers at a different stage of the geothermal operation will result in different amount of reactivity, the Damköhler number will also change and the same reactive tracer candidate may no longer be suitable. The derivative $\mathrm{d(Da)}/\mathrm{d}T$ can be considered as the sensitivity of the reactivity of the tracer to changes in reservoir temperature and can be used to further gauge the candidate's potential as a reactive tracer.

The reactive tracer kinetics were modeled as a first order reaction, with the reaction rate constant k a function of temperature. The reaction rate is equal to $-kC$, where C is the concentration of the tracer. The typical Arrhenius equation is equal to

$$k(T) = A \exp\left[-\frac{E_a}{RT}\right], \tag{8.19}$$

where A is the pre-exponential factor, E_a is the activation energy, R is the universal gas constant, and T is the temperature in an absolute scale. Because the temperature field in the fracture varies spatially, the reaction rate will as well. In order to simulate a reactive tracer experiment, the kinetic parameters need to be defined and the temperature throughout the fracture surface is required.

The choice of ideal Arrhenius parameters will depend on the reservoir temperature and the injected fluid residence time. The deployment of reactive tracers is more difficult than that of conservative tracers because one reactive tracer candi-

date may not be suitable for different geothermal reservoirs. For a desired extent of reaction or Damköhler number, there will not be a unique set of activation energies and pre-exponential factors to use. Plummer et al. (2012) looked into different pairings of the Arrhenius parameters for the ideal tracer for the Raft River, Idaho geothermal reservoir. They derived a contour plot of tracer sensitivity as a function of $\log(A)$ and E_a to be able to identify the best set of Arrhenius parameters to use. Plummer et al. (2012) mention the enthalpy-entropy compensation limit that fixes the range of possible activation energies and pre-exponential factors for a class of compounds (Liu and Guo, 2001). Fortuitously, the range of activation energies and pre-exponential factors for amide hydrolysis researched by Robinson and Tester (1990) fall within a desired band on the tracer sensitivity map, suggesting they are good candidates for the Raft River geothermal field. Reimus et al. (2011) performed a similar analysis to conclude that a set of Ea and A values should result in a first order rate constant of $2/t_{\text{resd}}$, where t_{resd} is the residence time. Without making mention of the Damköhler number, Reimus et al. (2011) suggests to use a reactive tracer that will yield a Damköhler number of order one.

The reactive tracer test was administrated at two different times during the energy extraction phase. The first time was early in the extraction phase when there was no measurable drop in production temperature. The early time corresponds to only after 10 days of extraction, which represents about 5% of the duration when the dimensionless production temperature reaches 0.8. Although the dimensionless production temperature is still equal to one, the area around the injection well has cooled down and the mean fracture surface temperature is 0.95 for a constant aperture case. The later reactive tracer test is conducted after 85 days which corresponds to when the production temperature of the uniform aperture reservoir has reached $\Theta_p = 0.9$. We should expect the thermal perfor-

mance predictions for the later reactive tracer test to be better than the early time test because a larger region around the wellbores would have experienced drawdown, creating more differentiation among the reservoirs. Because the tracer residence time is on the order of an hour, the temperature of the reservoir will not change appreciably during the reactive tracer experiment. It is valid to assume that the fracture surface temperature remains constant during the duration of the tracer run.

The extent of reaction and the log of the Damköhler number as a function of the activation energy and the pre-exponential factor are plotted in Figure 8.10. The results were calculated for a constant aperture fracture after 10 days of extraction. The extent of reaction is defined as the mass of tracer that has reacted normalized by the total injected mass. The Damköhler number is defined using the spatial average of the reaction constant in the fracture and a residence time defined as $L^2\langle w\rangle/\dot{Q}$. The figure was used as a guide to determine what values of the activation energy and pre-exponential factor should be used. For an extent of reaction from 25% to 75%, the Damköhler number ranges from 0.12 to 1. For a desired extent of reaction or log of the Damköhler number, there is a line that describes the required pairing of the activation energy and the natural log of the pre-exponential factor. For this study, the reactive tracer kinetic parameters were $A = 10$ s^{-1} and $E_a/R = 5000$ J/mole/K, which corresponds to Da $= 0.94$ and 72% extent of reaction for the reservoir conditions used throughout the study and after 10 days of reservoir operation. For the reactive tracer test at the later stage of operation, the Damköhlher number and extent of reaction are 0.79 and 46%, respectively. The objective function was the l^2-norm error of the tracer concentration with time of the output reservoir model and the target reservoir.

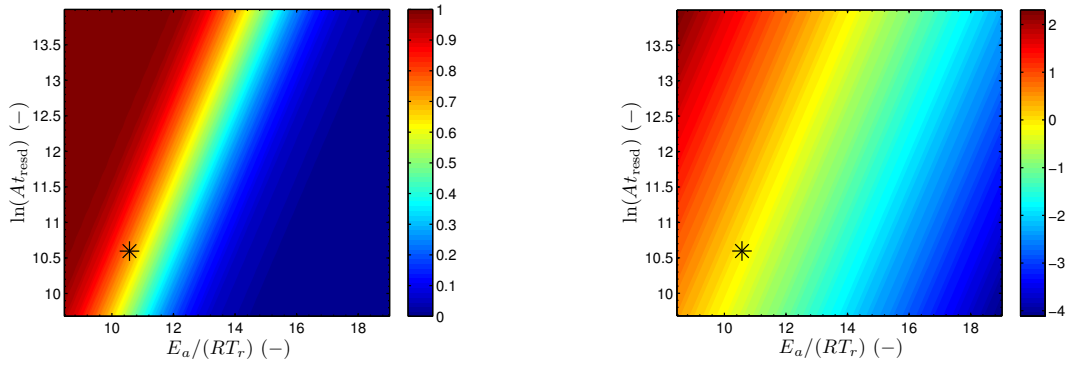

(a) (b)

Figure 8.10: The extent of reaction and the Damköhler number for a reactive tracer test with varying activation energy E_a and pre-exponential factor A. The reactive tracer test was conducted for constant aperture fracture after only 10 days of energy extraction. The activation energy was nondimensionalized using the universal gas constant R and the original reservoir rock temperature T_r. The pre-exponential factor was nodimensionalized by the tracer's residence time t_{resd}, estimated as $L^2\langle w\rangle/\dot{Q}$, where L is the wellbore spacing, $\langle w\rangle$ is the mean aperture, and $\dot{Q}$ is the volumetric flow. (a) The extent of reaction, defined as the fraction of tracer particles that have reacted during the duration of the tracer test. (b) The base ten log of the Damköhler number, defined as $\langle k\rangle t_{\text{resd}}$ with $\langle k\rangle$ being equal to the spatial average of the reaction constant.

The boxplots of the l^2-norm error for both the aperture field and the dimensionless production drawdown curve are found in Figure 8.11. For comparison, the conservative test results are shown along side the reactive tracer results. Using reactive tracers, the inversion scheme was able to obtain improved results for the aperture field for the early reactive tracer test. For the later reactive tracer test, the error of the aperture field is qualitatively different, as the error range is smaller than the conservative tracer results.

Both sets of reactive tracers test yielded better predictions of the reservoir's thermal performance, with more improvements from the reactive tracer test administered at the later time. The improvements were expected since the reactive tracer test relies on the fracture surface temperature field, in addition to the flow

field. As noted earlier, the reactive tracer results belonging to the later test time had a lower and less variable error because the subsurface thermal profile will be more variable among reservoirs after an extended period of energy extraction. While there will be improved results by waiting a longer period of time to carry out a reactive tracer test, one would like to know earlier on during the extraction phase the anticipated level of thermal performance of the reservoir.

The prediction of the thermal performance among the tracer tests can be analyzed using two different metrics, the standard deviation of the error for the production temperature at a specified time, after 203 days of extraction, and the reservoir lifetime, defined when the reservoir production temperature reaches $\Theta_p = 0.8$. The error of the reservoir lifetime is normalized by the true reservoir lifetime of the target reservoir. Under both metrics, the reactive tracer results for the later time was twice as effective compared to the conservative tracer. The standard deviation of the error $|\hat{\Theta}_p - \Theta_p|$ is 0.017 and 0.010, for the early and later time, respectively, lower than the conservative tracer test value of 0.021. For the reservoir life metric, the standard deviation of the error is 0.11 and 0.07, while the conservative tracer results yielded a value of 0.13.

As discussed earlier in the previous section, the conservative tracer test had difficulty correlating the error of the aperture field with that of the temperature drawdown. For reactive tracers, the problem still exists, the correlation coefficient of l^2-norm error for the aperture field and dimensionless temperature drawdown are 0.33 and 0.15 for the early and later reactive tracer tests, respectively. The small correlation coefficient for the later reactive tracer test is a result of having lower error of the production temperature and the less variable aperture error.

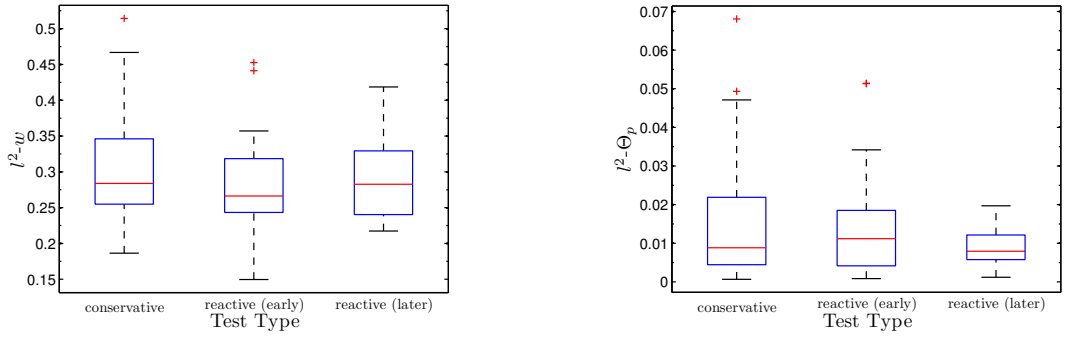

(a) (b)

Figure 8.11: Boxplots comparing of the l^2-norm error of the aperture field and the dimensionless temperature drawdown curve when minimizing the l^2-norm error when using either a conservative or reactive tracer test (at two different times). (a) l^2-norm error of the aperture field (b) l^2-norm error of the dimensionless production temperature drawdown curve.

8.6 Conclusion

An inverse methodology was created to determine a fracture's spatially varying aperture field and thermal performance using the temporal variation of the concentration at the production well of both conservative and reactive tracers. The fracture was modeled as a circle with a self-affine aperture correlation. Principal component analysis (PCA) was used to obtain reduced order modeling of the aperture field, creating a set of modes that can describe the aperture with a coefficient associated with each mode. The genetic algorithm, a metaheuristic global optimizer, was chosen to determine the PCA mode coefficients that will result in the best fit tracer curve compared to that of a full order, target fracture. By using tracer data from simulated reservoirs, our approach has an advantage by being able to verify whether our resulting model of the subsurface matches both the true aperture configuration and the thermal performance.

The inversion algorithm was applied using eight to twenty-four PCA modes

with a simulated conservative pulse tracer test. The results of the different modes were compared using the l^2-norm error for the tracer curve, aperture field, and the anticipated dimensionless production temperature versus time. While the results improved when using more than eight modes, there was little difference between results using sixteen or twenty-four modes. Results derived from a step tracer test did not differ significantly from those for a pulse tracer test. The output fracture surfaces from the inverse scheme were used in a forward model to simulate the production temperature with time. The accuracy and precision of the inverse methodology was contrasted with a "blind" approach where one uses the mean and standard deviation of the dimensionless production temperature of an ensemble of fracture realization. Under this approach, the mean temperature is the best guess while the standard deviation is the measure of the error. Against this comparison, the results of the prediction of the production temperature from the inversion exceeded that of the approach of using the statistics of an ensemble of fracture realizations.

Although the primarily goal using tracers is to anticipate the reservoir's thermal performance, knowing the aperture field is valuable in making decisions on expanding the system through placement of additional wells. The inversion scheme had trouble matching the true aperture field. Certain fractures from the inversion matched the location and size of high and low aperture regions in the target fracture but other results did not. Additionally, a spatial aperture field that does not match the target fracture can still predict the decline in the production temperature with time for the target fracture. For the results of the inversion, the error of the aperture field did not correlate strongly with the error of the production temperature, but the two were more correlated when only the error of the aperture field for a region surrounding the wells was considered instead of the entire frac-

ture. The results reveal non-uniqueness in the posed inverse problem. The results indicate that tracer signals contain limited information when trying to derive a reservoir structure that closely matches the truth, despite being capable in predicting the reservoir's thermal performance. Compared to the fracture aperture, the inversion scheme was better at predicting fracture surface temperature and streamlines.

A hypothetical candidate for a reactive tracer was chosen by determining the extent of reaction of the tracer in a constant aperture fracture, as a function of the activation energy and pre-exponential factor. The level of reactivity is not only governed by the Arrhenius parameters, but by the tracer's residence time in the reservoir. For a desired level of reactivity, there is a line describing the required value of the natural log of the pre-exponential factor and the activation energy to achieved the specified extent of reaction. The prediction of a reservoir's thermal performance was better when using reactive tracers administrated for two different times during energy extraction. The concentration of the reactive tracer is dependent on the temperature of the fracture surface, and by matching the reactive tracer signal, the thermal performance of the fracture from the inversion process will more than likely be similar to the target reservoir. The reactive tracer test carried out further along the extraction process was about twice as effective at predicting reservoir production temperature and lifetime. The reactive tracer application did not result in any significant improvement in predicting the reservoir's aperture field, as the l^2-norm error of the aperture field was similar to the conservative tracer results.

The developed inversion methodology and analysis will be applied to a field laboratory at the Altona Flat Rocks, located in the William H. Miner Experimental

Station near Plattsburgh, New York. The Altona reservoir represents a meso-scale field site, larger than a bench scale, artificial reservoir but smaller than a full sized geothermal reservoir. The Altona reservoir consists of Cambrian Potsdam Sandstone formation, where a five spot well system has been drilled in a 10 m by 10 m area, intersecting an isolated horizontal fracture 7.6 m deep (Becker and Tsoflias, 2010). Ground penetrating radar has been used to determine the spatial aperture of the fracture (Tsoflias and Becker, 2008), creating a reservoir with a characterized subsurface. The site has been used to conduct tracer tests, demonstrating the presence of flow channelizations caused by the spatially varying aperture field (Becker et al., 2015; Castagna et al., 2011; Hawkins et al., 2015). Additionally, the spatially varying aperture field in Altona, NY shows a self-affine configuration. To determine the Hurst coefficient, the Fourier transform of the aperture fluctuations is taken and the power spectrum is plotted against the inverse of the wave number. This results in a Hurst coefficient of 0.44. The variable band method, an alternate approach, results in a value of 0.51. The measured Hurst coefficient range from 0.44 to 0.51 is close to the reported values of 0.5 for sandstone (Boffa, J. M. et al., 1999; Ponson et al., 2007). For the current study, the Hurst coefficient was set to 0.8 because it is the reported value for granite, the rock typically encountered in deep EGS reservoirs.

The results of the current study revealed the difficulty of matching the target aperture field while showing one can more closely reproduce the tracer curve and accurately predict the thermal performance of the reservoir. Experiments at the Altona field site will be directed to both validate the methods developed and improve on the shortcomings of the current study. Future experimentation at the field site will include deployment of thermally degrading and sorbing tracers. Reservoir heating through injection of hot water will provide an analog of

the geothermal energy extraction process. The presence of multiple wells is an advantage as it provides the possibility of generating multiple tracer curves that can be used to help reproduce the GPR derived aperture field using an inverse search methodology. Future work will focus on how to best use and interpret results from multiple tracer tests from the field site to determine both the reservoir's aperture field and thermal performance, methodologies that can be applied to full scale EGS reservoirs.

Bibliography

Alaskar, M., Ames, M., Liu, C., Connor, S., Horne, R., Li, K., and Cui, Y. (2012). Nanoparticle and microparticle flow in porous and fractured media-An experimental study. *SPE*, 17(4):1160–1171.

Ames, M., Li, K., and Horne, R. (2015). The utility of threshold reactive tracers for characterizing temperature distributions in geothermal reservoirs. *Mathematical Geosciences*, 47(1):51–62.

Becker, M. W. and Tsoflias, G. P. (2010). Comparing flux-averaged and resident concentration in a fractured bedrock using ground penetrating radar. *Water Resources Research*, 46(9).

Becker, M. W., Tsoflias, G. P., Baker, M., and Hawkins, A. (2015). Confirmation of hydraulic, tracer, and heat transfer characterization of a fractured bedrock using ground penetrating radar. In *Proceedings of the Fortieth Workshop on Geothermal Reservoir Engineering, Stanford University, January 26-January 28, 2015*, Stanford, CA.

Berkooz, G., Holmes, P., and Lumley, J. L. (1993). The proper orthogonal de-

composition in the analysis of turbulent flows. *Annual Review Fluid Mechanics*, pages 539–575.

Boffa, J. M., Allain, C., Chertcoff, R., Hulin, J. P., Plouraboué, F., and Roux, S. (1999). Roughness of sandstone fracture surfaces: Profilometry and shadow length investigations. *European Physical Journal B*, 7(2):179–182.

Brown, S. R., Kranz, R. L., and Bonner, B. P. (1986). Correlation between the surfaces of natural rock joints. *Geophysical Research Letters*, 13(13):1430–1433.

Buljak, V. (2012). *Inverse Analyses with Model Reduction: Proper Orthogonal Decomposition in Structural Mechanics*. Springer, Berlin, Germany.

Cao, K., Huang, B., Wang, S., and Lin, H. (2012). Sustainable land use optimization using boundary-based fast genetic algorithm. *Computers, Environment and Urban Systems*, 36(3):257–269.

Castagna, M., Becker, M. W., and Bellin, A. (2011). Joint estimation of transmissivity and storativity in a bedrock fracture. *Water Resources Research*, 47(9).

Chatterjee, A. (2000). An introduction to the proper orthogonal decomposition. *Current Science*, 78(7):808–817.

Chemburkar, R. M., Brown, L. F., Travis, B. J., and Robinson, B. A. (1991). Numerical determination of temperature profiles in flowing systems from conversions of chemically reacting tracers. *Chemical Engineering Science*, 46(5):1349–1360.

Cui, T., Marzouk, Y. M., and Willcox, K. E. (2015). Data-driven model reduction for the Bayesian solution of inverse problems. *International Journal for Numerical Methods in Engineering*, 102(5):966–990.

Du Teaux, R. and Callahan, T. (1996). Comparing reactive and non reactive tracers to measure changes in liquid dominated, fractured geothermal reservoirs. *Geothermal Resources Council Transactions*, 20:447–451.

Falconer, K. (2003). *Fractal Geometry: Mathematical Foundations and Application*. John Wiley & Sons, Chichester, England, 2nd edition.

Feder, J. (1988). *Fractals*. Physics of Solids and Liquids. Plenum Press, New York, NY.

Fogler, H. (2006). *Elements of Chemical Reaction Engineering*. Prentice Hall PTR, Upper Saddle River, NJ, 4th edition.

Glover, P. W. J., Matsuki, K., Hikima, R., and Hayashi, K. (1998). Fluid flow in synthetic rough fractures and application to the Hachimantai geothermal hot dry rock test site. *Journal of Geophysical Research: Solid Earth*, 103(B5):9621–9635.

Hawkins, A., Fox, D., Zhao, R., Tester, J., Cathles, L., Koch, D., and Becker, M. (2015). Predicting thermal breakthrough from tracer tests: Simulations and observations in a low temperature field laboratory. In *Proceedings of the Fortieth Workshop on Geothermal Reservoir Engineering, Stanford University, January 26-January 28, 2015*, Stanford, CA.

Hornby, G. S., Lohn, J. D., and Linden, D. S. (2011). Computer-automated evolution of an X-band antenna for NASA's Space Technology 5 Mission. *Evolutionary Computation*, 19(1):1–23.

Hua, Y. and Liu, W. (1998). Generalized Karhunen-Loeve transform. *Signal Processing Letters, IEEE*, 5(6):141–142.

Kerschen, G., Golinval, J.-C., Vakakis, A. F., and Bergman, L. A. (2005). The method of proper orthogonal decomposition for dynamical characterization and

order reduction of mechanical systems: An overview. *Nonlinear Dynamics*, 41(1–3):147–169.

Krishnakumar, K. (1990). Micro-genetic algorithms for stationary and non-stationary function optimization. In *Proceedings of SPIE, Intelligent Control and Adaptive Systems*, volume 1196, pages 289–296, Philadelphia, PA.

Kwakwa, K. (1988). Tracer measurements during long-term circulation of the Rosemanowes HDR geothermal system. In *Proceedings of the Thirteenth Workshop on Geothermal Reservoir Engineering, Stanford University, January 19-February 21, 1988*, Stanford, California.

Lagarias, J. C., Reeds, J. A., Wright, M. H., and Wright, P. E. (1998). Convergence properties of the Nelder–Mead simplex method in low dimensions. *SIAM Journal on Optimization*, 9(1):112–147.

Li, L. and Jafarpour, B. (2010). Effective solution of nonlinear subsurface flow inverse problems in sparse bases. *Inverse Problems*, 26(10):105016.

Liu, L. and Guo, Q.-X. (2001). Isokinetic relationship, isoequilibrium relationship, and enthalpy-entropy compensation. *Chemical Reviews*, 101(3):673–696.

Madadi, R. R. and Balaji, C. (2008). Optimization of the location of multiple discrete heat sources in a ventilated cavity using artificial neural networks and micro genetic algorithm. *International Journal of Heat and Mass Transfer*, 51(9–10):2299–2312.

Méheust, Y. and Schmittbuhl, J. (2001). Geometrical heterogeneities and permeability anisotropy of rough fractures. *Journal of Geophysical Research: Solid Earth*, 106(B2):2089–2102.

Nelder, J. A. and Mead, R. (1965). A simplex method for function minimization. *The Computer Journal*, 7(4):308–313.

Neuville, A., Toussaint, R., and Schmittbuhl, J. (2011). Hydraulic transmissivity and heat exchange efficiency of open fractures: a model based on lowpass filtered apertures. *Geophysical Journal International*, 186(3):1064–1072.

Nottebohm, M., Licha, T., and Sauter, M. (2012). Tracer design for tracking thermal fronts in geothermal reservoirs. *Geothermics*, 43(0):37–44.

Plouraboué, F., Kurowski, P., Hulin, J.-P., Roux, S., and Schmittbuhl, J. (1995). Aperture of rough cracks. *Physical Review E*, 51(3):1675.

Plummer, M. A., Palmer, C. D., Hull, L. C., and Mattson, E. D. (2012). Sensitivity of a reactive-tracer based estimate of thermal breakthrough in an EGS to properties of the reservoir and tracer. In *Proceedings of the Thirty-Seventh Workshop on Geothermal Reservoir Engineering, Stanford University, January 30-February 1, 2012*, Stanford, CA.

Ponson, L., Auradou, H., Pessel, M., Lazarus, V., and Hulin, J.-P. (2007). Failure mechanisms and surface roughness statistics of fractured Fontainebleau sandstone. *Physical Review E*, 76(3):036108.

Radilla, G., Sausse, J., Sanjuan, B., and Fourar, M. (2012). Interpreting tracer tests in the enhanced geothermal system (EGS) of Soultz-sous-Forêts using the equivalent stratified medium approach. *Geothermics*, 44(0):43–51.

Reimus, P. W., Watson, T., Vermeul, V., Newell, D., and Williams, M. (2011). Laboratory testing and modeling to evaluate perfluorocarbon compounds as tracers in geothermal systems. In *Proceedings of the Thirty-Sixth Workshop on Geother-*

mal Reservoir Engineering, Stanford University, January 31-February 2, 2011, Stanford, California.

Robinson, B. A. and Tester, J. W. (1984). Dispersed fluid flow in fractured reservoirs: An analysis of tracer-determined residence time distributions. *Journal of Geophysical Research*, 89:10374–10384.

Robinson, B. A. and Tester, J. W. (1986). Characterization of flow maldistribution using inlet-outlet tracer techniques: An application of internal residence time distributions. *Chemical Engineering Science*, 41(3):469–484.

Robinson, B. A. and Tester, J. W. (1990). Kinetics of alkaline hydrolysis of organic esters and amides in neutrally-buffered solution. *International Journal of Chemical Kinetics*, 22(5):431–448.

Robinson, B. A., Tester, J. W., and Brown, L. (1988). Reservoir sizing using inert and chemically reacting tracers. *SPE Formulation Evaluation*, 3:227–334.

Rose, P., Riasetto, D., Siy, J., Bartl, M., Reimus, P., Mella, M., Leecaster, K., and Petty, S. (2011). Quantum dots as tracers in geothermal and EGS reservoirs. In *Proceedings of the Thirty-Sixth Workshop on Geothermal Reservoir Engineering, Stanford University, January 31-February 2, 2011*, Stanford, California.

Rose, P. E., Benoit, W. R., and Kilbourn, P. M. (2001). The application of the polyaromatic sulfonates as tracers in geothermal reservoirs. *Geothermics*, 30(6):617–640.

Sanjuan, B., Pinault, J.-L., Rose, P., Gérard, A., Brach, M., Braibant, G., Crouzet, C., Foucher, J.-C., Gautier, A., and Touzelet, S. (2006). Tracer testing of the geothermal heat exchanger at Soultz-sous-Forêts (France) between 2000 and 2005. *Geothermics*, 35(5-6):622–653.

Schmittbuhl, J., Gentier, S., and Roux, S. (1993). Field measurements of the roughness of fault surfaces. *Geophysical Research Letters*, 20(8):639–641.

Schmittbuhl, J., Schmitt, F., and Scholz, C. (1995). Scaling invariance of crack surfaces. *Journal of Geophysical Research: Solid Earth*, 100(B4):5953–5973.

Schmittbuhl, J., Steyer, A., Jouniaux, L., and Toussaint, R. (2008). Fracture morphology and viscous transport. *International Journal of Rock Mechanics and Mining Sciences*, 45(3):422–430.

Tasan, A. S. and Gen, M. (2012). A genetic algorithm based approach to vehicle routing problem with simultaneous pick-up and deliveries. *Computers & Industrial Engineering*, 62(3):755–761.

Tester, J., Murphy, H., Grigsby, C., Potter, R., and Robinson, B. (1989). Fractured geothermal reservoir growth induced by heat extraction. *SPE Reservoir Engineering*, 4(1):97–104.

Tester, J. W., Bivins, R. L., and Potter, R. M. (1982). Interwell tracer analyses of a hydraulically fractured granitic geothermal reservoir. *SPE*, 22:537–554.

Tsoflias, G. P. and Becker, M. W. (2008). Ground-penetrating-radar response to fracture-fluid salinity: Why lower frequencies are favorable for resolving salinity changes. *Geophysics*, 73(5):J25–J30.

van Doren, J. F., Markovinović, R., and Jansen, J.-D. (2006). Reduced-order optimal control of water flooding using proper orthogonal decomposition. *Computational Geosciences*, 10(1):137–158.

Vogt, C., Kosack, C., and Marquart, G. (2012a). Stochastic inversion of the tracer experiment of the enhanced geothermal system demonstration reservoir

in Soultz-sous-Forêts - Revealing pathways and estimating permeability distribution. *Geothermics*, 42(0):1–12.

Vogt, C., Marquart, G., Kosack, C., Wolf, A., and Clauser, C. (2012b). Estimating the permeability distribution and its uncertainty at the EGS demonstration reservoir Soultz-sous-Forêts using the ensemble Kalman filter. *Water Resources Research*, 48(8).

CHAPTER 9

CONCLUSIONS AND RECOMMENDATIONS

9.1 Summary of Research

The overall goals of my research is to develop a better understanding of the thermal hydraulic behavior of fractured geothermal reservoirs like those often encountered in Enhanced/Engineered Geothermal Systems (EGS). The approach used to address these goals included five major components as presented in Chapter 2:

1. Determine the domestic market for the expansion of geothermal energy for direct thermal use
2. Quantify the renewability of EGS by determining how the temperature field recovers after a period of no sustained heat extraction in model reservoir systems
3. Develop analytical and numerical models to probe how fundamental reservoir characteristics including aperture distribution, fracture intersections, and other rock properties affect thermal hydraulic performance
4. Develop the methodology of using conservative and reactive tracers to determine flow characteristics
5. Validate the role of tracer modeling to predict thermal behavior

In the first component, the U.S. thermal energy spectrum was analyzed to estimate the potential for using geothermal energy to meet the total thermal energy demand for applications that require temperatures below 260 °C. More than 30%

of the U.S. energy demand is used for direct thermal use applications at temperatures below 260 °C, about 34 EJ annually. Of the 34 EJ, 80% was used for applications below 150 °C, of which 55% came from the residential sector. The U.S. thermal energy spectrum quantifies the domestic heat market for the expansion of renewable energy sources like geothermal and the potential of displacing fossil fuel energy sources.

In the second area of study, the thermal recovery of a depleted model geothermal reservoir was analyzed, using both analytical and numerical methods. The model reservoir, whose geometry was specified, was shown to initially recover very quickly, but over longer times recovered asymptotically, with an inverse square root with respect to time. The recovery curves indicate that the ideal recovery duration is two to four times the duration of heat extraction or production. Although the ideal ratio of extraction to recovery would be less than or equal to one, the results in Chapter 4 demonstrate that discretely fractured geothermal reservoirs are renewable and can be operated in a sustainable fashion.

Analytical and numerical models describing transport in discrete fractures were presented in Chapters 5 and 6. These models were used to explore the sensitivity of reservoir network structure on fluid production temperature and how spatially varying aperture fields affect a reservoir's thermal performance. The studies conducted using the developed models showed a strong link between flow and thermal performance, which further reinforced the importance of characterizing the subsurface. Uncertainties in reservoir characteristics were addressed by stochastically generating reservoir realizations and subsequently simulating their thermal behavior to obtain a distribution of possible reservoir production temperature histories.

Relying on the numerical code developed in Chapter 6, the last two components of the research program were addressed by solving an inverse problem to obtain a spatially varying aperture field in a fractured reservoir using conservative and reactive tracer data. Given the complexity of a reservoir, reduced order modeling was used to simplify the description of the aperture variations to make the inverse problem tractable. The results illustrated how it is possible to use tracers to identify the major flow channels in the fracture and predict the reservoir's production temperature with time. However, difficulties were encountered with non-unique solutions appearing, where several different fracture aperture fields matched the tracer curves. Tracer tests are an important part of characterizing a geothermal reservoir, but they do have limitations. In order to specify reservoir structure with more confidence, additional information is needed, such as geophysical data and wellbore imaging.

9.2 Recommended Future Work

Below are several areas that warrant further research based on the research presented in this dissertation. Specific topics for the suggested future research resulted by considering the lessons learned from the modeling carried out and through identification of gaps in what was studied in detail in my dissertation.

Thermal Spectrum Analysis on Different Systems

The methodology developed to characterize the thermal spectrum of energy use in the U.S. could be applied to other countries or groups of countries, like the Eu-

ropean Union, or to municipalities with substantial industrial and manufacturing sectors. Heat and power integration has been extensively researched to optimize the energy usage of industrial and manufacturing processes, but without consideration of the the appropriate energy source to use. The thermal spectrum of manufacturing processes like paper mills (Klugman et al., 2009; Ruohonen et al., 2010) or agricultural processes like dairy farms (Upton et al., 2013; Houston et al., 2014) can unearth opportunities for heat integration using low temperature geothermal or solar energy utilizing a cascaded approach over a range of end-use temperatures.

Economic Modeling of the Heat Farming Strategy

The heat farming study did not consider the potential long term economic benefits of implementing a thermal recovery strategy. Using a sustainable heat farming strategy could be economically beneficial since it would extend the usable lifetime of reservoirs and will cut down on drilling costs, the most expensive capital cost of a geothermal project (Blankenship et al., 2005; Tester et al., 2012). However, it is not obvious what the economic savings or the optimal recovery time of a reservoir would be. Future work should consider the economics of the heat farming strategy in EGS reservoirs by minimizing project costs, constrained by supplying the energy demand of a process for periods twenty or thirty years.

To evaluate the economic benefit of a heat farming strategy, the base case for comparison would be one where no reservoirs are reused. Different reservoir usage strategies could then be considered and compared with the base case. For example, a preheater strategy involves continually pumping fluid through the first partially depleted reservoir, which has reached its thermal drawdown criteria limit, to preheat fluid before it is injected into one or more active, non-depleted reservoirs.

As a result, the thermal drawdown rate in the other reservoirs will be reduced. An alternative strategy, the diverted flow strategy works by over producing fluid from a second reservoir and injecting the excess, hot fluid into a depleted reservoir, thereby, forcing the depleted reservoir to recover faster. For the economic modeling, different end use applications could be explored, since this variable impacts the thermal drawdown criteria of the reservoir. Furthermore, the type of application will govern the depth of the required reservoir in a specific region which controls the cost of the drilled wells. A more complex scenario would consider multiple applications; reservoirs that have been used for several cycles may not sustain high enough temperatures for the original application, but can still adequately supply the energy for lower temperature processes.

Natural Convection Effects during Extraction and Recovery

Simulating natural convection in the fracture involves coupling the fluid flow and heat transport because the buoyancy force is a function of temperature. At the moment, the numerical code is limited in its ability to model natural convection for longer extraction times and larger wellbore separations than what was modeled in Chapter 6. The iteration scheme implemented was not able to converge and resulted in numerical instability; the error between two successive iterations grew, which resulted in erroneous temperature values. Although modeling natural convective flow in geothermal systems is nothing new, having a robust treatment of the process for the developed code will allow for future work that investigates the effect natural convection has on systems with spatially varying aperture fields and intersecting fractures.

The temperature sensitivity of the viscosity of water will also affect the flow

within the fracture. The viscosity is greatly affected by temperature. For instance, from 20 °C to 200 °C, the viscosity decreases by a factor of seven. The flow in the fracture is viscous, pressure driven and a lower viscosity will reduce the resistance to flow in the hotter regions of the fractures, increasing the fluid flow in these regions and, as a result, enhancing the thermal performance. Although the numerical code was able to model viscosity as a function of temperature separately from natural convection, it was not able to model both effects simultaneously.

The problems with solving for the coupled velocity and temperature field might be fixed by using a more robust iteration scheme. At the moment, the code employs a fixed-point iteration scheme where an initial guess of the velocity field, usually the velocity without the buoyancy force, is used to generate a temperature field. The buoyancy force is calculated using the resulting temperature field and then used to solve for a new velocity field. A new temperature field is calculated using the new velocity field. The process iterates until the difference of the temperature field in successive iterations is below a predefined tolerance. The fixed-point iteration may be too simple to solve for natural convection when it becomes comparable to the induced dipole flow. Additionally, temperature dependency of the flow becomes more strongly coupled when temperature effects of viscosity are taken into account. Longer extraction times will have strong natural convection because of the larger temperature deficits in the fracture. Using a more sophisticated and robust algorithm like Newton-Raphson may alleviate the numerical issues faced when modeling natural convection. Xiaoxue Huang, a visiting Ph.D. student from Tianjin University, has started working on improving the code to better handle the velocity and temperature field coupling. Professor Koch, who is on my dissertation committee, is supervising her.

The study on reservoir thermal recovery considered conduction as the only means of recovery. However, fluid is still left inside the fracture after the extraction phase, creating the possibility for natural convection in vertically oriented fractures. After extraction, there will be cooler, denser fluid near the injection well, causing induced flow currents and altering the rate of recovery of the reservoir. Using the characteristic buoyancy induced velocity, we can determine the time scale for convective mixing in the reservoir with the length scale equal to the fracture diameter. Mixing in the reservoir would be beneficial if it brings in hotter fluid from the edges of the fracture and heats up the cooled zone surrounding the injection well and production well. It is important to investigate under what conditions foster natural convection during recovery and how these conditions would affect the recovery process.

More Modeling on Systems with Intersecting Fractures

In this dissertation, little work was done on modeling systems with fracture intersections using the numerical model developed in Chapter 6; only two different two fracture systems were analyzed. The systems differed by how fractures intersected with each other and represented two extreme cases, resulting in two systems where the intersection lines were perpendicular to each other. The results of these two systems suggest that more work needs to be done in the area of fracture intersections. The systems studied had different levels of thermal drawdown and had a better thermal performance, compared to a system with two independent fractures. A future study could build on this by simulating a variety of two fracture systems that intersect differently. The systems should differ in the length of the formed intersection line, as well as, orientation of the resulting intersection with respect to

the fractures. Additionally, it is important to model systems with more than two fractures, in particular, systems that have multiple flow paths from the injection well to production well. One hypothetical system would have the injection well connected to the first fracture, which intersects two fractures, splitting the flow and creating two flow paths. Those two fractures intersect another fracture that contains the production well. The purpose of this proposed study is to explore the importance of accurately modeling fracture intersections.

The multiple fracture reservoirs investigated in the spatial aperture study only considered systems where the fractures are equally sized and do not intersect each other. The fractures were only hydraulically connected via the injection and production wells. It is important to further investigate the effect aperture fluctuations have on the thermal performance of geothermal systems with intersecting fractures. The investigations should simulate reservoirs with different levels of fracture connectivity, flow complexity, and flow paths. It would be useful to know what kinds of reservoirs will be more affected by local aperture fluctuations in order to determine the level of susceptibility a real reservoir would be to aperture fluctuations.

Spatial Aperture Variations Caused by Fracture Shearing/Slipping

Fracture shearing or slippage will result in a spatially varying aperture field that will be different than the isotropic self-affine field used in Chapter 7. Shearing is to be expected under the stimulation process and throughout the operation of the geothermal reservoir (Ghassemi et al., 2007). Evans et al. (2005) estimated the average slip in the Soultz EGS project to be 0.3 mm. Wang et al. (1988) and

Matsuki et al. (2006) both developed analytical equations for the spatial aperture fluctuations given a direction and distance of shearing. Numerical and laboratory experiments in both unidirectional and radial flow have been performed that illustrated that shear displacement leads to an increase in the standard deviation of the aperture fluctuations and results in preferential flow channeling in the direction perpendicular to the shear displacement (Yeo et al., 1998; Plourabouré et al., 2000; Watanabe et al., 2008). Thus, research has shown that not only will shearing increase channeling, but that channeling will occur preferentially in the direction perpendicular to shear and provides an alternative in modeling spatially varying aperture fields. Knowing how the extent and direction of shearing affects a reservoir's thermal performance would help contribute to the understanding of discretely fractured geothermal systems.

Application of the Inversion Scheme at Meso-scale Field Sites

Our research group has access to the Altona Flat Rocks in Plattsburgh, New York, a meso-scale field site, as described in Chapter 8. The site provides an ideal test bed for validating our developed inverse search methodology because the spatially varying aperture field has been mapped using ground penetrating radar (Tsoflias and Becker, 2008; Becker and Tsoflias, 2010). Packers were installed at the site, creating an isolated single, horizontal fracture. A five spot well configuration was placed at the site, which is advantageous since using different wells as injectors and producers results in different tracer curves due to the heterogeneity of the aperture field. Non-uniqueness is major problem in an inverse search, but the number of possible answers can be reduced by using more tracer curves, as the

optimal answer will best match all the curves. The presence of a background flow at the Altona field site provides an additional complexity. Currently, both the strength and direction of the hydraulic gradient is not precisely known, but the numerical model described in Chapter 6 has already been adapted to consider background flow in simulating both heat and mass transport. Adam Hawkins, an Earth and Atmospheric Sciences Ph.D. student in our group, will continue with numerical modeling of the Altona meso-scale field site.

Using the same methodology for deriving the temperature of a discrete fracture network as shown in Chapter 5, it is possible to derive the concentration profile of a tracer throughout the fractured reservoir. Another research effort would be to use the derived concentration equation for tracer analysis at the Mirror Lake field site. The Mirror Lake field is the bedrock of the Hubbard Brook Experimental Forest, located in New Hampshire, that is composed of granite and schist in a 120 m by 120 m area, 60 to 230 m deep (Becker and Shapiro, 2000). Apart from the Altona field site, Adam Hawkins, plans to conduct conservative and reactive tracer test at the site.

Inverse Search Using the Analytical Discrete Fracture Network Model

The analytical solution for the flow and heat transport for discrete fracture networks is ideal for studies that rely on model evaluations on the order of thousand to hundreds of thousands. The derived analytical temperature model for the fractures is currently being used by Morgan Ames, a Ph.D. from Stanford University working for Professor Roland Horne's group, to solve for reservoir structures using

reactive tracers. I have assisted Morgan Ames on how to use the analytical model and how to best integrate it into their inversion scheme using reactive tracers.

Bibliography

Becker, M. W. and Shapiro, A. M. (2000). Tracer transport in fractured crystalline rock: Evidence of nondiffusive breakthrough tailing. *Water Resources Research*, 36(7):1677–1686.

Becker, M. W. and Tsoflias, G. P. (2010). Comparing flux-averaged and resident concentration in a fractured bedrock using ground penetrating radar. *Water Resources Research*, 46(9).

Blankenship, D., Wise, J., Bauer, S., Mansure, A., Normann, R., Raymond, D., and LaSala, R. (2005). Research efforts to reduce the cost of well development for geothermal power generation. In *40th U.S. Symposium on Rock Mechanics, June 25-29, 2005*, Anchorage, AL.

Evans, K. F., Moriya, H., Niitsuma, H., Jones, R. H., Phillips, W. S., Genter, A., Sausse, J., Jung, R., and Baria, R. (2005). Microseismicity and permeability enhancement of hydrogeologic structures during massive fluid injections into granite at 3 km depth at the Soultz HDR site. *Geophysical Journal International*, 160(1):389–412.

Ghassemi, A., Tarasovs, S., and Cheng, A.-D. (2007). A 3-D study of the effects of thermomechanical loads on fracture slip in enhanced geothermal reservoirs. *International Journal of Rock Mechanics and Mining Sciences*, 44(8):1132–1148.

Houston, C., Gyamfi, S., and Whale, J. (2014). Evaluation of energy efficiency and

renewable energy generation opportunities for small scale dairy farms: A case study in Prince Edward Island, Canada. *Renewable Energy*, 67:20–29.

Klugman, S., Karlsson, M., and Moshfegh, B. (2009). A Swedish integrated pulp and paper mill-Energy optimisation and local heat cooperation. *Energy Policy*, 37(7):2514–2524.

Matsuki, K., Chida, Y., Sakaguchi, K., and Glover, P. (2006). Size effect on aperture and permeability of a fracture as estimated in large synthetic fractures. *International Journal of Rock Mechanics and Mining Sciences*, 43(5):726–755.

Plouraboué, F., Kurowski, P., Boffa, J.-M., Hulin, J.-P., and Roux, S. (2000). Experimental study of the transport properties of rough self-affine fractures. *Journal of Contaminant Hydrology*, 46(3–4):295–318.

Ruohonen, P., Hippinen, I., Tuomaala, M., and Ahtila, P. (2010). Analysis of alternative secondary heat uses to improve energy efficiency-case: A Finnish mechanical pulp and paper mill. *Resources, Conservation and Recycling*, 54(5):326–335.

Tester, J. W., Drake, E. M., Golay, M. W., Driscoll, M. J., and Peters, W. A. (2012). *Sustainable Energy: Choosing Among Options*. The MIT Press, Cambridge, MA, 2nd edition.

Tsoflias, G. P. and Becker, M. W. (2008). Ground-penetrating-radar response to fracture-fluid salinity: Why lower frequencies are favorable for resolving salinity changes. *Geophysics*, 73(5):J25–J30.

Upton, J., Humphreys, J., Koerkamp, P. G., French, P., Dillon, P., and Boer, I. D. (2013). Energy demand on dairy farms in Ireland. *Journal of Dairy Science*, 96(10):6489–6498.

Wang, J. S. Y., Narasimhan, T. N., and Scholz, C. H. (1988). Aperture correlation of a fractal fracture. *Journal of Geophysical Research: Solid Earth*, 93(B3):2216–2224.

Watanabe, N., Hirano, N., and Tsuchiya, N. (2008). Determination of aperture structure and fluid flow in a rock fracture by high-resolution numerical modeling on the basis of a flow-through experiment under confining pressure. *Water Resources Research*, 44(6).

Yeo, I., de Freitas, M., and Zimmerman, R. (1998). Effect of shear displacement on the aperture and permeability of a rock fracture. *International Journal of Rock Mechanics and Mining Sciences*, 35(8):1051–1070.

APPENDIX A

FEM FORMULATION

The following appendix describes the finite element formulation for the governing equations for the fluid flow, heat transport, and particle transport in discretely fractured geothermal reservoirs. For this work, bilinear quadrilateral elements (Q4) were used.

A.1 Fluid Flow

For the governing equation for fluid flow,

$$-\boldsymbol{\nabla}\cdot\left(\frac{\rho_w w^3}{12\mu}\left[\boldsymbol{\nabla}P-\rho_w\mathbf{g}\right]\right)=\sum_l \dot{m}_l\delta(\mathbf{r}-\mathbf{r}_l), \tag{A.1}$$

the FEM formulation before applying essential boundary conditions in index notation is

$$D_{ij}P_j = f_{D,i}+f_{B,i}, \tag{A.2}$$

and

$$[D]\{P\}=\{f_D\}+\{f_B\}, \tag{A.3}$$

in matrix/vector representation. The terms for the matrices and vectors are

$$D^e_{ij}=\int_{\Omega^e}\left(\frac{\rho_w w^3}{12\mu}\right)\frac{\partial N_i}{\partial r_k}\frac{\partial N_j}{\partial r_k}\,\mathrm{d}\Omega \quad [D^e]=\int_{\Omega^e}\left(\frac{\rho_w w^3}{12\mu}\right)\boldsymbol{\nabla}[N]^T\cdot\boldsymbol{\nabla}[N]\,\mathrm{d}\Omega, \tag{A.4}$$

$$f_{B,i}=\int_{\Omega^e}\left(\frac{\rho_w^2 w^3}{12\mu}\right)g_k\frac{\partial N_i}{\partial r_k}\,\mathrm{d}\Omega \qquad \{f_B\}=\int_{\Omega^e}\left(\frac{\rho_w^2 w^3}{12\mu}\right)\mathbf{g}\cdot\boldsymbol{\nabla}[N]\,\mathrm{d}\Omega, \tag{A.5}$$

$$f_{D,i}=\dot{m}_i \qquad \{f_D\}=\dot{m}_i. \tag{A.6}$$

The vector $f_{D,i}$ is only nonzero at the nodes of the injection/production well and the nodes along fracture intersections. The vector $f_{B,i}$ represents the buoyancy force.

A.2 Heat Transfer

The Laplace transform of the heat balance in the fracture given by

$$\rho_w c_w w \langle \mathbf{v} \rangle \cdot \boldsymbol{\nabla} \bar{T} = \bar{q}_s, \tag{A.7}$$

has the FEM formulation before applying essential boundary conditions is

$$(C_{ij} + S_{ij})\bar{T}_j = M_{ij}\bar{q}_j, \tag{A.8}$$

in index notation and

$$([C] + [S])\{\bar{T}\} = [M]\{\bar{q}\}, \tag{A.9}$$

in matrix/vector representation. The terms for the matrices and vectors are

$$M^e_{ij} = \int_{\Omega^e} N_i N_j \, \mathrm{d}\Omega \qquad [M^e] = \int_{\Omega^e} [N]^T [N] \, \mathrm{d}\Omega, \tag{A.10}$$

$$C^e_{ij} = \int_{\Omega^e} \rho_w c_w w v_k \frac{\partial N_i}{\partial r_k} N_j \, \mathrm{d}\Omega \quad [C^e] = \int_{\Omega^e} \rho_w c_w w [N]^T (\{v\}^T \boldsymbol{\nabla}[N]) \, \mathrm{d}\Omega, \tag{A.11}$$

$$S^e_{ij} = \int_{\Omega^e} \rho_w c_w w \tau v_k^2 \frac{\partial N_i}{\partial r_k} \frac{\partial N_j}{\partial r_k} \quad [S^e] = \int_{\Omega^e} \rho_w c_w w \tau \mathbf{v} \cdot \boldsymbol{\nabla}[N]^T \mathbf{v} \cdot \boldsymbol{\nabla}[N] \, \mathrm{d}\Omega. \tag{A.12}$$

S_{ij} is the stability parameter for the pure/strong convective systems whose form is found in Donéa and Huerta (2003), and the expression for stabilization parameter τ is described by Codina (2000).

The nodal discretization of the Green's function formulation,

$$\bar{T}(x, y, z, s) = \bar{T}_r + \int_A \bar{G}(x - x', y - y', z, s) \frac{\bar{q}_s(x', y', s)}{\rho_r c_r} \, \mathrm{d}x' \, \mathrm{d}y', \tag{A.13}$$

in index notation is

$$\bar{T}_i = \bar{T}_{r,i} + \bar{G}_{ij}\bar{q}_j, \tag{A.14}$$

and

$$\{\bar{T}\} = \{\bar{T}_r\} + [\bar{G}]\{\bar{q}\}, \tag{A.15}$$

in matrix/vector representation. The terms for $\bar{G}_{ij}$ are

$$\bar{G}_{ij} = \int_{A^e} \frac{\exp\left[-\sqrt{\frac{s}{\alpha}}\sqrt{(x_i - x')^2 + (y_i - y')^2}z^2\right]}{4\pi k_r \sqrt{(x_i - x')^2 + (y_i - y')^2 + z^2}} N_j \, \mathrm{d}x'\mathrm{d}y'. \tag{A.16}$$

Any singular integrals are resolved using the Lachat-Watston transformations (Lachat and Watson, 1976; Beer et al., 2008). For simplification, one can use the one dimensional conduction Green's function instead of the computationally expensive three dimensional form:

$$\bar{G}_{ij} = \frac{1}{\sqrt{4\pi k_r \rho_r c_r s}} \exp\left[-|z|\sqrt{\frac{s}{\alpha}}\right]. \tag{A.17}$$

The main difference between the one and three dimensional Green's function is that the one dimensional formulation lacks the area integral, making it computationally less intensive and easier to numerical implement.

A.3 Particle Transport

For the governing equation

$$w\frac{\partial C}{\partial t} + w\mathbf{v}\cdot\boldsymbol{\nabla}C - w\boldsymbol{\nabla}\cdot\nu\boldsymbol{\nabla}C = rw, \tag{A.18}$$

the FEM formulation of the above equation is

$$\left(\frac{1}{\Delta t}M_{ij} + \theta K_{ij}\right)c_j^{n+1} = \left(\frac{1}{\Delta t}M_{ij} - (1-\theta)K_{ij}\right)c_j^n \tag{A.19}$$

in index notation and

$$\left(\frac{1}{\Delta t}[M] + \theta[K]\right)\{c^{n+1}\} = \left(\frac{1}{\Delta t}[M] - (1-\theta)[K]\right)\{c^n\}, \tag{A.20}$$

in matrix/vector representation. The time step Δt comes from the temporal discretization scheme governed by the parameter θ, which ranges from zero to one,

and n represents the current time step for the scheme. When θ is equal to 0, 1/2, and 1, the discretization scheme represents, forward Euler, Crank-Nicolson, and backward Euler time discretization, respectively. The matrix K_{ij} is a convenient grouping defined as

$$K_{ij} = C_{ij} + S_{ij} + D_{ij} + R_{ij}, \tag{A.21}$$

where R_{ij} is the reaction matrix due to the chemical reaction or decay and is defined as

$$R^e_{ij} = \int_{\Omega^e} kwN_iN_j \, \mathrm{d}\Omega \qquad [R^e] = \int_{\Omega^e} kw[N]^T[N] \, \mathrm{d}\Omega, \tag{A.22}$$

$$\tag{A.23}$$

where k is the first order reaction constant. The matrices M_{ij}, C_{ij}, S_{ij}, and D_{ij} are similarly defined as before except for the M_{ij} requires the parameter w inside the integral, C_{ij} and S_{ij} require the removal of $\rho_w c_w$, and the parameter grouping $(\rho_w w^3/12/\mu)$ is replaced by $w\nu$ for the matrix D_{ij}.

A.4 Applying Essential Boundary Conditions

For a FEM formulation of the form

$$K_{ij}P_j = f_i, \tag{A.24}$$

the above system of equations becomes

$$K^*_{ij}P_j = \Lambda_{ij}f_j - \Lambda_{ij}m_j + \gamma_i, \tag{A.25}$$

after applying essential boundary conditions (EBC). If p are the nodes where the EBCs are applied and u_p the values of the EBCs, then

$$K^*_{ij} = \begin{cases} K_{ij}, & ij \neq pj \text{ or } ip \\ 1, & ij = pp \\ 0, & ij = pj \text{ or } ip, \end{cases} \quad \Lambda_{ij} = \begin{cases} \delta_{ij}, & ij \neq pp \\ 0, & ij = pp, \end{cases} \quad \gamma_i = \begin{cases} u_p, & i = p \\ 0, & i \neq p, \end{cases} \quad m_i = \sum_p K_{ip} u_p. \tag{A.26}$$

For the temperature field, after applying EBCs, the nodal heat flux becomes

$$\bar{q}_i = \frac{\gamma_i - \Lambda_{ij} m_j - (C_{ij} + S_{ij}) \bar{T}_{r,j}}{(C_{ik} + S_{ik}) \bar{G}_{kj} + \Lambda_{ik} M_{kj}}. \tag{A.27}$$

Bibliography

Beer, G., Smith, I., and Duenser, C. (2008). *The Boundary Element Method with Programming: For Engineers and Scientists*. Springer.

Codina, R. (2000). On stabilized finite element methods for linear systems of convection-diffusion-reaction equations. *Computer Methods in Applied Mechanics and Engineering*, 188(1-3):61–82.

Donéa, J. and Huerta, A. (2003). *Finite Element Methods for Flow Problems*. John Wiley & Sons.

Lachat, J. C. and Watson, J. O. (1976). Effective numerical treatment of boundary integral equations: A formulation for three-dimensional elastostatics. *International Journal for Numerical Methods in Engineering*, 10(5):991–1005.

APPENDIX B

GENERATING SELF-AFFINE APERTURE VARIATIONS

To generate a 2D self-affine aperture field $w(x, y)$ in a fracture with a Hurst exponent of ζ and standard deviation of σ_h:

1. Generate white Gaussian noise on an evenly spaced N x N grid.
2. Take the discrete 2D Fourier transform of the white Gaussian noise.
3. Calculate the modulus of the Fourier transform $|F(\mathbf{k})|$ for each wave number $\mathbf{k}$.
4. Calculate the phase φ of the Fourier transform for each wave number $\mathbf{k}$.
5. Apply the power law on the modulus of the Fourier transform, $|H(\mathbf{k})| = |F(\mathbf{k})|\,|\mathbf{k}|^{-1-\zeta}$.
6. Filter out any modes if the lower and upper $\mathbf{k}$ cutoffs are defined.
7. Calculate the modified Fourier transform $H(\mathbf{k})$ by using the modified modulus but the same phase values, $H(\mathbf{k}) = |H(\mathbf{k})|\,e^{i\varphi}$.
8. Set $H(\mathbf{0})$ to zero to yield a mean fluctuation of zero.
9. Take the inverse discrete Fourier transform of $H(\mathbf{k})$ to obtain the aperture fluctuations $h(x, y)$.
10. If modeling fractures that are not squares, inscribed the desired shape in the square and only take the aperture values within the inscribed shape.
11. Rescale $h(x, y)$ to obtain the desired standard deviation of aperture fluctuations σ_h by using $\sigma_h^2 = (\int_A h^2(x, y)\ \mathrm{d}A)/(\int_A\ \mathrm{d}A)$, where A is the area of the fracture surface.
12. Add $h(x, y)$ to the desired mean aperture $\langle w \rangle$ to get $w(x, y)$.

An example of a self-affine aperture field derived using the algorithm described above is shown in Figure B.1.

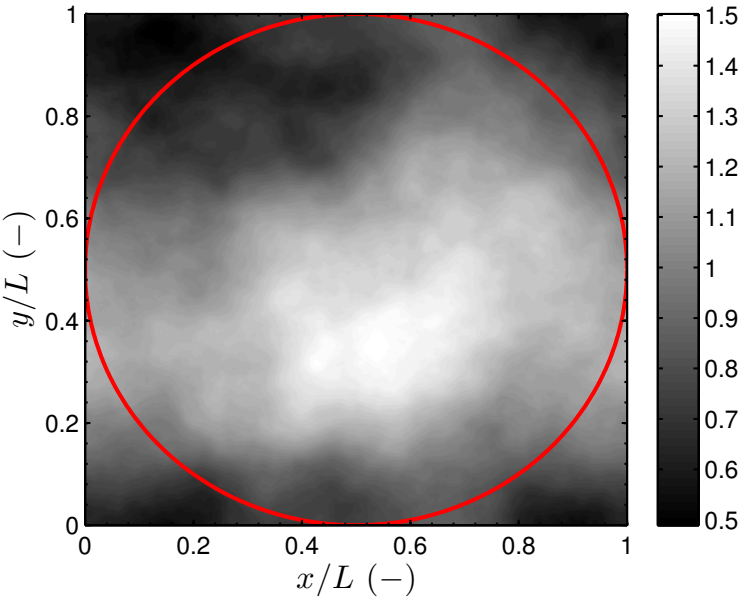

Figure B.1: Generated fracture with a self-affine aperture field on a 512 x 512 point grid. The mean aperture $\langle w \rangle$ is 1 mm, the standard deviation of the fluctuations σ_h is 2.5×10^{-4}, and the Hurst coefficient is 0.8. The aperture values are nondimensionalized by the mean aperture. An inscribed circle is drawn to show the excluded region when the desired fracture shape is a circle.

APPENDIX C

GENETIC ALGORITHM

The genetic algorithm is composed of five processes: population initialization, fitness evaluation, parent selection, crossover function, and mutation function. The algorithm starts by initializing a population of possible solutions, called individuals, and evaluating their fitness, which is the value of their objective function. The selection process follows by determining which individuals will become parents. The parents produce new individuals for the next generation to replace the individuals in the old generation, using the crossover and mutation functions to create the new population. The fitness function for all the individuals in the new generation are evaluated and the process repeats until the termination criteria is reached. The flowchart of the genetic algorithm is shown in Figure C.1. The description of each of the steps in the algorithm is provided below.

Population Initialization: N individuals are generated by randomly sampling the genes of the individuals using a uniform distribution for each gene given a defined range of values. The genes α_j are the parameter values for the forward model. For this study, the genes are the PCA mode coefficients. A typical population size would be from twenty to hundred, with problems with more degrees of freedom requiring a larger population size. The population size for this study was fifty.

Fitness Evaluation The fitness of each individual is determined by evaluating the objective function for each member of the population. The objective function used was the l^2-norm error, the sum of the square of the residuals.

Selection Process: The number of parents selected for each generation is equal to the population size minus the elite count times the crossover fraction. For example, if there are fifty individuals in the population, the elite count is two, and the crossover fraction is 0.8, thirty-eight parents need to be selected. A number of the most fit individuals equal to the elite count are automatically copied over to the next generation. For instance, if the elite count is two, then the next generation will have two individuals with the same genetic makeup as the top two fittest individuals in the previous generation. The elite individuals can be selected as parents, which will often be the case because the selection process preferentially picks parents with high fitness scores. The crossover fraction is recommended to range from 0.5 to 0.8 and the elite count of about 2 to 5% of the population size (Buljak, 2012). This study used a crossover fraction of 0.8 and an elite count of two.

The parents are chosen via the tournament process. Four individuals are randomly sampled with replacement and the individual with the best fitness function among the selected four is chosen as a parent. The process is repeated until all required parents have been selected, with the possibility of one individual being a parent more than once due to sampling with replacement.

Crossover Function: The parents are randomly put into pairs, with each parent pair designated to produce two offspring. The genes of the offspring are determined by employing the intermediate crossover function which uses a weighted average of the parents by applying the formula

$$\alpha'_j = \alpha_{1,j} + r(\alpha_{2,j} - \alpha_{1,j}), \tag{C.1}$$

where α_j are the genes with the subscript 1 and 2 referring to the first and second parent, respectively, the prime denoting the genes of the offspring, and r being a random number sampled from a uniform distribution from zero to one. Each parent pairing produces two offspring that will form part of the population of the next generation, replacing the parent candidates. For the example used, the thirty-eight selected parent candidates are replaced by thirty-eight offspring formed by the selected nineteen parent pairings. The intermediate crossover function was chosen because it can generate values of α_j that are a blend of the two parents, which is not the case for other crossover functions like the single and double point crossover. The single and double point crossover functions yield offspring whose entries of α_j either come from one parent or another.

Mutation Function: The remaining offspring are created by mutating the genes of the least fitted individuals. If the population size is fifty, the number of selected parents are thirty-eight, and the elite count is two, then the ten individuals with the lowest fitness score are replaced by ten mutation offspring. The mutation process replaces the genes by resampling the parameter values given the initial range used for the population initialization step. The mutation process can be viewed as creating entirely new individuals whose genetic makeup are not derived on the current generation. Mutated individuals increase the genetic diversity of the population to allow the algorithm to continually search a larger area of the function space.

Termination Criteria: The algorithm continues until the predefined number of generations have been reached. The optimal answer from the search is the indi-

vidual with the highest fitness score in the last generation. Ten generations were used for this study.

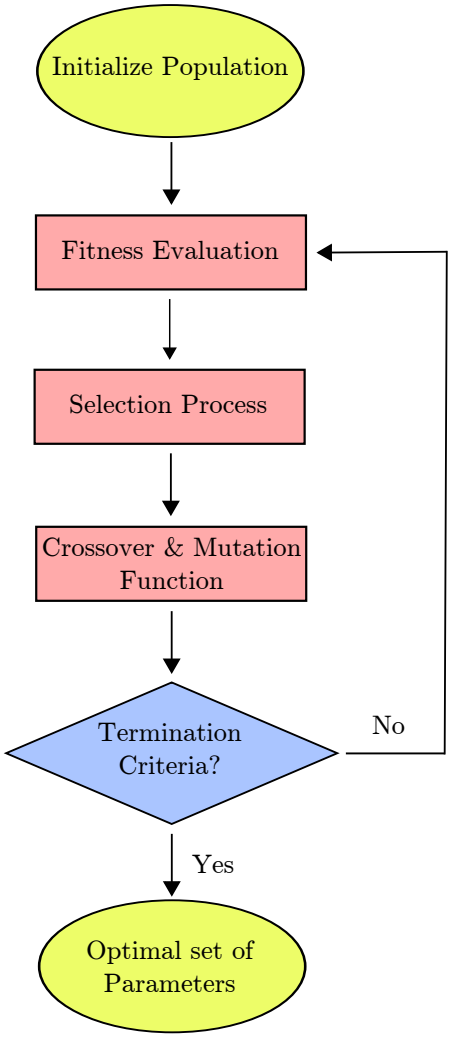

Figure C.1: Flowchart showing the steps involved in the genetic algorithm.

Bibliography

Buljak, V. (2012). *Inverse Analyses with Model Reduction: Proper Orthogonal Decomposition in Structural Mechanics*. Springer, Berlin, Germany.